

Stony Brook University



OFFICIAL COPY

The official electronic file of this thesis or dissertation is maintained by the University Libraries on behalf of The Graduate School at Stony Brook University.

© All Rights Reserved by Author.

Advancing numerical prediction of physical and biological processes in Long Island Sound

A Dissertation Presented

by

Ling Liu

to

The Graduate School

in Partial Fulfillment of the

Requirements

for the Degree of

Doctor of Philosophy

in

Marine and Atmospheric Sciences

Stony Brook University

December 2015

Stony Brook University
The Graduate School

Ling Liu

We, the dissertation committee for the above candidate for the
Doctor of Philosophy degree, hereby recommend
acceptance of this dissertation.

Kamazima M.M. Lwiza – Dissertation Advisor
Associate Professor, School of Marine and Atmospheric Sciences,
Stony Brook University

Minghua Zhang - Chairperson of Defense
Professor, School of Marine and Atmospheric Sciences, Stony Brook University

Dong-Ping Wang, Professor
School of Marine and Atmospheric Sciences, Stony Brook University

Robert E. Wilson, Associate Professor
School of Marine and Atmospheric Sciences, Stony Brook University

Lie-Yauw Oey, Professor
Atmospheric & Oceanic Sciences, Princeton University

Pierre F. J. Lermusiaux, Associate Professor
Dept. of Mechanical Engineering, Massachusetts Institute of Technology

This dissertation is accepted by the Graduate School

Charles Taber
Dean of the Graduate School

Abstract of the Dissertation

Advancing numerical prediction of physical and biological processes in Long Island Sound

by

Ling Liu

Doctor of Philosophy

in

Marine and Atmospheric Sciences

Stony Brook University

2015

The occurrence and spread of hypoxia in coastal waters is known to depend strongly on nutrients, primary production, water column structure, wind and tidal mixing. Accurate prediction of the onset, intensity and areal extent of hypoxia remains a challenge. Previous modeling efforts have needed to ‘tune’ vertical mixing or phytoplankton respiration in order to obtain results that agree with field observations of dissolved oxygen (DO). We use a one-dimensional physical model coupled with a biogeochemical model to establish mechanistic links between factors involved in the evolution of seasonal hypoxia in western Long Island Sound.

The coupled model includes bacterial dynamics, which allows accurate prediction of the onset of late summer hypoxia and subsequent recovery. The cost of not including the bacterial dynamics in the model is an overestimation of bottom DO by as much as 700% in summer. By including bacterial dynamics, we eliminate the need to distort vertical mixing or phytoplankton respiration rate to simulate observed seasonal variability in DO. Along with the importance of the bacterial

dynamics, it is instructive to conduct a thorough examination of other mechanisms influencing hypoxia. These mechanisms may include DO production by plankton growth and surface oxygen supply, DO consumption by organic matter remineralization both in the water column and the sediment, DO transport by vertical mixing and horizontal advection. In order to explore these mechanisms and quantify their individual impacts on seasonal hypoxia, we analyze the rates of DO consumption/production, which include the surface flux of DO, detritus remineralization or bacterial consumption, sedimentary DO consumption, as well as horizontal advection of DO. By quantifying these dynamic terms in DO control equation, we are able to demonstrate that DO consumption rate associated with bacterial activities has significantly the largest influence. We also find that perturbing wind mixing contributes at most 30% to the late summer DO variability. Advection plays a non-trivial role in hypoxia development. Ignoring horizontal advection leads to up to 40% of under-estimation of DO during low DO season. DO variability is sensitive to horizontal advection during low DO season. An examination of DO consumption/ventilation rates indicates that horizontal advection has same order of impact as planktonic photosynthesis in terms of oxygen generation, but it is on three orders less than bacterial DO consumption.

Table of Contents

List of Figures	viii
List of Tables	xiii
Acknowledgments	xiv
Chapter 1: Introduction	1
1.1 Background and motivation	1
1.2 Objectives and Approach	4
References	7
Chapter 2: Importance of the bacterial dynamics in model simulations of seasonal hypoxia	12
Abstract	12
2.1 Introduction	13
2.2 Study Area	16
2.3 Methods	17
2.3.1 Data	17
2.3.2 Model	18
2.3.2.1 General Ocean Turbulence Model (GOTM).....	18
2.3.2.2 Biogeochemical model	19
2.3.2.3 Oxygen dynamics in the coupled model	22
2.3.2.4 Adding bacterial dynamics into the 1-D coupled model	25
2.4 Results	30
2.4.1 Water column properties	30
2.4.2 Sensitivity test of minimum kv with respect to temperature	45
2.4.3 Seasonal variability in simulated bacterial biomass	48
2.4.4 DO variability from the bacterial dynamics-excluded model	56
2.5 Discussions	60
2.5.1 Water column properties	61
2.5.2 Seasonal variability in bacterial biomass	62
2.5.3 The importance of bacterial dynamics in simulating seasonal hypoxia	62
2.5.4 Comparison of DO variability produced by hyperbolic and Q10 thermal controls of bacterial metabolism	63
2.5.5 Missing mechanisms in the model	65
2.6 Conclusion	65
References	67

Chapter 3: Estimation of exchange transport in the East River and the western Narrows in LIS with high-resolution 3-D model	74
Abstract	74
3.1 Introduction	74
3.2 Study Area	78
3.3 Methods.....	78
3.3.1 Model configuration	78
3.3.2 Tidal validation	84
3.3.3 Estimation of exchange and net transports.....	87
3.3.4 Momentum balance analysis	89
3.3.5. Estimation of Ekman number	90
3.4 Results	90
3.4.1 Tidal validation results	90
3.4.2 Water transport across the western Narrows of LIS and the East River	102
3.4.3 Vertical eddy viscosity and Ekman number	112
3.4.4 Momentum balance analysis	115
3.5 Discussions	125
3.5.1 Current structure analysis	125
3.5.2 Exploration of dynamics controlling the general current structure	128
3.5.3 Exchange transport	128
3.5.4 Momentum analysis	129
3.5.5 Model error analysis	130
3.6 Conclusion	131
References	133
Chapter 4: Exploration of physical and biological mechanisms affecting seasonal hypoxia using the enhanced 1-D and 3-D model results	139
Abstract	139
4.1 Introduction	141
4.2 Study Area.....	145
4.3 Methods	148
4.3.1 Examination of mechanisms leading to further DO reduction due to added bacterial dynamics.....	148
4.3.2 Examination of the role of wind-induced vertical mixing.....	148
4.3.3 Exploring the importance of horizontal advection to DO variation.....	149
4.3.4. Estimating the nutrient flux due to surface nudging of nutrient concentration	159
4.4 Results	159
4.4.1 Mechanisms controlling DO variability	159
4.4.2 Roles of vertical mixing on the recovery of hypoxia	164
4.4.3 Roles of horizontal advection on hypoxia development	168
4.4.4. Estimating nutrient flux generated by nudging surface nutrient	174

4.5 Discussions	181
4.5.1 The mechanisms leading to DO reduction with added bacterial dynamics	181
4.5.2 The importance of vertical mixing in simulating seasonal hypoxia	184
4.5.3 The importance of horizontal advection in simulating seasonal DO variability.....	184
4.5.4 Impact of nudging surface nutrient	186
4.5.5 Implications on coastal hypoxia modeling	188
4.5.6 Missing mechanisms and future direction	189
4.6 Conclusions	190
References	192
Chapter 5: Conclusion	197

List of Figures

Chapter 2

Figure 2-1. Bathymetry of Long Island Sound (SS, Stratford Shoal; CA, Cable and Anchor Reef; MS, Mattituck Sill; SB, Smithtown Bay)	15
Figure 2-2. Model structure of GOTM/ERGOM.....	27
Figure 2-3. (a) Simulated seasonal variability of vertical temperature structure (Celcius) in 2008. (b) Observations of vertical temperature structure (Celcius) in 2008. (c) Observed surface temperature in Celcius (red) compared to model simulation (blue). (d) Observed temperature below thermocline (red) versus model simulation (blue). (e) Observed bottom temperature (red) compared to model simulation (blue) in 2008.....	32
Figure 2-4. (a) Simulated seasonal variability of salinity profile (g/kg). (b) Observations of vertical salinity structure (g/kg).....	38
Figure 2-5. Simulated seasonal variability of the density profile (kg m^{-3}).....	41
Figure 2-6 (a) Brunt vaisala frequency profile in February. (b) Brunt vaisala frequency profile in July.....	42
Figure 2-7 (a) Richardson number profile in February. (b) Richardson number profile in July.....	44
Figure 2-8. Target diagram of sensitivity test of K_{min} with respect to water temperature. X-axis shows the bias and y-axis indicates RMSE.....	47
Figure 2-9. Seasonal variability of temperature profiles associated with multiple k_{min} values shown in the Target diagram by Figure 2-8	48
Figure 2-10 (a) Simulated seasonal evolution of surface bacteria compared to the observations. (b) Simulated seasonal variation of bacterial profile (mmol N m^{-3}).....	50
Figure 2-11 (a) Simulated Dissolved Oxygen (DO) variability with daily frequency produced by the model with hyperbolic control on bacterial growth rate in comparison to the observations. (b) Simulated seasonal variability of DO profile produced by the model with hyperbolic control on bacterial growth rates (mg/L).....	53
Figure 2-12. Simulated bottom DO produced by the model with Q10 control on bacterial growth rate in comparison to the observations (mg/l) in 2008.....	56
Figure 2-13. (a) Simulated bottom DO concentration from the original model without microbial loop compared to observations in 2008. (b) Simulated seasonal variability of DO profile from the original model without bacterial activity (mg/L). (c) Ratio of the bottom DO	

from the original model without microbial loop over the bottom DO from the model with microbial loop.....58

Chapter 3

Figure 3-1. (a) Grid points in the model domain (sub-sampled by 2 grid points). (b) zooming-in view of the highlighted section.....81

Figure 3-2. Topography of model domain.....82

Figure 3-3. Buoy stations in LIS with wind and climatology observations. Blue dots indicate CTDEEP all-year round water quality monitoring stations. Red squares show MYSound buoy stations operated by UCONN.....83

Figure 3-4. Locations of 14 tidal stations in the western LIS operated by CO-OPS are indicated by red star and numbers. Blue stars indicate tidal stations extracted from ADCIRC tidal data base. The stations are labeled the same as in Table 3.185

Figure 3-5. P.T. Barnum ferry LIS transects for ADCP observations between Port Jefferson, NY and Bridgeport, CT between July 20 and August 11, 2008 (after Wilson 2007).....86

Figure 3-6. Transects T1, T2, T3 and T4 between the western end of the East River in the west and Sands Point in the Narrows of western LIS in the east. Transects T1, T2 and T3 are located in the East River, and T4 is the transect in the western LIS. Transect T1 lies to the south of Belmont Island; Transect T2 is across the Bronx-Whitestone Bridge; Transect T3 is close to the Throgs Neck Bridge; Transect T4 goes through the Execution Rocks lighthouse located in the western LIS.....88

Figure 3-7. (a) M2 tidal amplitude from the 3-D model. (b) Modeled M2 phase from the 3-D model92

Figure 3-8. (a) Simulated M2 amplitude of the current velocity. (b) M2 amplitude derived from the ferry observations.....97

Figure 3-9. (a) Modeled M2 phase lag of current velocity in radians. (b) M2 Phase derived from the ferry observations in 2008.....99

Figure 3-10. Tidal ellipses comparison between model (red) and observations (blue). Stations are labeled according to Table 3-2 Site numbers.....101

Figure 3-11. Plot of depth-averaged horizontal residual current velocity in LIS. Color plot represents the depth-averaged longitudinal residual current velocity u103

Figure 3-12. (a) Vertical structures of longitudinal residual current across T2 (Whitestone), (b) Vertical structures of longitudinal residual current across T3 (Willet Point) transect. (c) Vertical structures of longitudinal residual current across T4 (Execution Rocks) transect

in Long Island Sound. (d) Cross-section structure of long-term residual current isotachs in cm/s across same transect as T4 in Vieira (2000).....105

Figure 3-13 (a). The net transport integrated for the component of residual currents perpendicular to T2, T3 and T4 in Long Island Sound for winter, 2008. (b). The net transport integrated for the component of residual currents perpendicular to T2, T3 and T4 in Long Island Sound for summer, 2008. (c). The net transport integrated for the component of residual currents perpendicular to T4 in Long Island Sound for 2008.108

Figure 3-14. Mean exchange transport in the East River and the Narrows in LIS. Positive values stand for eastward flow; Negative values are westward transport.....111

Figure 3-15. Vertical eddy viscosity for LIS derived from ROMS.....113

Figure 3-16. Ekman number for LIS estimated from vertical viscosity shown by Figure 3-17 and Eq 3.4.....114

Figure 3-17. Longitudinal momentum terms derived from the momentum balance equation 3.3 in ROMS for transect T1, July, 2008. Blue line indicates the variability of the Coriolis acceleration term; Green line shows the variability of the advection term; Red line represents the barotropic pressure gradient; Cyan indicates baroclinic pressure gradient; Magenta line is the local acceleration; Yellow and black lines show surface and bottom stress, respectively117

Figure 3-18. Longitudinal momentum terms derived from the momentum balance equation 3.3 in ROMS for transect T2, July, 2008. Line colors indicate the same terms as Figure 3-17.118

Figure 3-19. Longitudinal momentum terms derived from the momentum balance equation 3.3 in ROMS for transect T3, July, 2008. Line colors indicate the same terms as Figure 3-17.119

Figure 3-20. Longitudinal momentum terms derived from the momentum balance equation 3.3 in ROMS for transect T4, July, 2008. Line colors indicate the same terms as Figure 3-17.120

Figure 3-21. Lateral direction momentum terms derived from the momentum balance equation 3.3 in ROMS for transect T1, July, 2008. Line colors indicate the same terms as Figure 3-17.....121

Figure 3-22. Lateral direction momentum terms derived from the momentum balance equation 3.3 in ROMS for transect T2, July, 2008. Line colors indicate the same terms as Figure 3-17.....122

Figure 3-23. Lateral direction momentum terms derived from the momentum balance equation 3.3 in ROMS for transect T3, July, 2008. Line colors indicate the same terms as Figure 3-17.....123

Figure 3-24. Lateral direction momentum terms derived from the momentum balance equation 3.3 in ROMS for transect T4, July, 2008. Line colors indicate the same terms as Figure 3-17.....124

Figure 3-25. Wind stress variation of the Execution Rocks station during year 2008.....127

Chapter 4

Figure 4-1. Long Island Sound Bathymetry (Lee 2009).....146

Figure 4-2. Percent of Hypoxia between 1991 and 2011 in Long Island Sound (Long Island Sound Study).....147

Figure 4-3. Map of the shoreline of western Long Island Sound showing the location of the Execution Rocks Buoy and western LIS Station (EX and WS on the map) used to estimate horizontal DO gradient (O’Donnell et al. 2008).....152

Figure 4-4 (a) NEIWPC-IEC District western LIS sampling stations. Levels of oxygen were estimated from Mid-July Survey of 2014 (NEIWPC 2014), (b) NEIWPC-IEC District 2014 western LIS sampling stations. Levels of oxygen were estimated from Late-July, (c) NEIWPC-IEC District 2014 western LIS sampling stations. Levels of oxygen were estimated from August, (d) NEIWPC-IEC District 2014 western LIS sampling stations. Levels of oxygen were estimated from Early September, (e) NEIWPC-IEC District 2014 western LIS sampling stations. Levels of oxygen were estimated from Middle of September.153

Figure 4-5. Along channel non-tidal transport estimated from the u momentum equation. Positive transport is toward the east.....158

Figure 4-6. DO dynamics from a model excluding bacterial dynamics in mmol O m⁻³ hr⁻¹ for the Execution Rocks Station in 2008. From top to bottom and left to right, are rates of DO consumption by detritus remineralization, DO production due to nutrient uptake by phytoplankton, DO consumption due to respiration of phytoplankton and zooplankton, sedimentary DO consumption and surface oxygen flux, respectively. Surface flux, detritus remineralization and sedimentary DO consumption, are three major processes in controlling DO variability.....161

Figure 4-7. DO dynamics from a bacterial dynamics-included model in mmol O m⁻³ hr⁻¹ for the Execution Rocks Station in 2008. From top to bottom and left to right are rates of DO consumption by bacteria decomposition of detritus, DO production due to nutrient uptake by phytoplankton, DO consumption due to respiration of phytoplankton and zooplankton, sedimentary DO consumption and surface oxygen flux, respectively.162

Figure 4-8. Ratio of oxygen consumption rate within the water column and the sediment in the models with and without bacterial dynamics in 2008.....163

Figure 4-9. Simulated bottom DO (dashed green) forced by the observed wind speed (solid blue) between February and October, 2008, at the Execution Rocks Station165

Figure 4-10. Simulated bottom DO (dashed green) under the wind speed lagged behind observations for one month (solid blue) for year 2008, at the Execution Rocks Station.166

Figure 4-11. The ratio of bottom DO forced with the lagged wind forcing (Figure 4-5) divided by DO forced by observed wind forcing (Figure 4-6). It shows that perturbing wind forcing contributes to at most 30% of the total DO variability.....167

Figure 4-12. Modeled DO variation plotted against the observations. This figure shows time series of DO concentration before adding advection for year 2008, at Execution Rocks Station.....170

Figure 4-13. Modeled DO variation plotted against the observations. This figure shows seasonal variability of DO concentration after adding advection for year 2008, at Execution Rocks Station.....171

Figure 4-14. The ratio between the seasonal DO variation from the model without the horizontal DO advection and the seasonal DO variation from the model with the horizontal DO advection.....172

Figure 4-15. The rate of DO increase (positive sign) due to horizontal advection in 2008. The time shown in this figure is when the measured horizontal DO gradient is available from O'Donnell et al. 2008.....173

Figure 4-16. (a) Case I experiment results with microbial loop. Figure shows the nutrient concentration comparison between nudging and no-nudging experiments (mmol N m^{-3}) for 2008. (b) The comparison between nudging and no-nudging of nutrient concentration (mmol N m^{-3}) for Case II (without microbial loop).....175

Figure 4-17. Percentage of nutrient concentration difference due to nudging compared for Case I: with microbial loop, and Case II: without microbial loop, for 2008.....177

Figure 4-18. (a) Individual nutrient component flux ($\text{mmol N m}^{-2} \text{h}^{-1}$) due to nudging in Case I experiment with microbial loop for 2008. (b) Individual nutrient component flux ($\text{mmol N m}^{-2} \text{h}^{-1}$) due to nudging in Case II experiment without microbial loop178

Figure 4-19. Comparison of total nutrient flux ($\text{mmol n m}^{-2} \text{h}^{-1}$) due to nudging between Cases I and Case II.....180

Figure 4-20. DO consumption rates in $\text{mmol O m}^{-3} \text{hr}^{-1}$ as bacterial decomposing labile detritus into inorganic nitrogen (top and middle panel) from the bacterial dynamics-included model. For comparison, bottom panel shows the rates during detritus remineralization from the bacterial dynamics-excluded model. Bacteria induced inorganic matter

production during summer leads to further increase of the rates by $0.07 \text{ mmol N m}^{-3} \text{ hr}^{-1}$ (middle panel) in the bacterial dynamics-included model, which is approximately 37% of the total DO consumption rate.....182

List of Tables

Chapter 2

Table 2-1. Major parameters applied in the modified model.....23

Chapter 3

Table 3-1. Tidal amplitude and phase comparison with tidal gauges.....94

Acknowledgements

I would like to express my deepest gratitude to my advisor, Dr. Kamazima M.M. Lwiza, for his excellent and patient guidance, caring, and strong support during my research and study at Stony Brook University. I would like to thank Dr. Dong-Ping Wang, for great lecture series on ocean dynamics and always being ready and willing to help with my research. I would also like to thank Drs. Robert E. Wilson and Charles N. Flagg for teaching me physical oceanography and providing data for my research. Many thanks to Dr. Minghua Zhang, Dr. Leo Oey and Dr. Pierrre Lermusaux for being my committee members and providing important guidance on the approaches applied in my research.

I am very thankful to Ms. Carol Dovi. Her goodness, kindness and caring always motivate and inspire me to become a better person.

Lastly, I would like to thank all people who have helped me during my doctoral study in the School of Marine and Atmospheric Sciences.

Advancing numerical prediction of physical and biological processes in Long Island Sound

Chapter 1

General Introduction

1.1 Background and Motivation

The coastal ocean is a shallow water area with depth less than 200 m, and it covers approximately 7% of the global ocean surface. It holds for at least 15% of oceanic primary production, 90% of the world fish catch, 40% of the value of ecosystem services in the world, and thus it is the most critical habitat for most marine organisms, and is one of the most important and dynamic areas for the world's habitat (Alongi 2998). Coastal habitat is strongly affected by physical conditions, such as wind, river discharge, topography of sea floor and shape of the coastline. Coastal biomasses and their community structure are affected by the changes of these physical conditions (Lee 2009; Anderson et al. 2001). As part of the coastal ocean, an estuary is defined to be a partially enclosed body of water, where freshwater from rivers, streams, and groundwater mixes with the salty seawater. Estuaries are the coastal areas being affected mostly by anthropogenic activities such as pollution and eutrophication. For example, land debris is transported into estuaries by storm sewers and tidal current. The debris comes from disposal of land trash, storm water runoff, ship vessels and oil platforms, and could cause severe threats to the estuary ecosystem (Browne et al. 2015). In addition to coastal debris, fertilizers and sewage discharged from the land pollute the estuaries through 'eutrophication' process, which

lead to persistent algal bloom, and affect the supply and uptake processes of dissolved oxygen (DO) (Friedrich et al., 2014).

Eutrophication is a process that brings excessive nutrients into estuaries, fuels phytoplankton production and increases organic carbon transport to the seabed (Welsh and Eller 1991). Below the euphotic zone and at the seabed, oxygen is utilized during microbial degradation of organic matter. Deep-water oxygen levels therefore decrease. As a consequence, hypoxia can occur when DO concentration in the water column falls below 3 mg/l (Diaz et al. 1995; Ritter et al. 1999). If oxygen levels in bottom water column drops further, the coastal environments could eventually become permanently anoxic environments. In that case, coastal life will collapse, which leads to a dramatic decline in biodiversity and causes big economic loss (Friedrich et al., 2014).

Both hypoxia and anoxia significantly affects ecosystem functioning, including the ecosystem bio-diversity and sustainability, capability of organic and inorganic matter cycling. This is because oxygen level may affect the behavior, physiology, and mortality of coastal organisms (Friedrich et al., 2014; Levin et al 2009). To understand hypoxia, we need to know how oxygen has been depleted in the coastal environments. The seasonal evolution of oxygen depletion in estuaries is shaped by interactions among physical and biogeochemical processes. These processes include air-sea exchange, nutrient input, vertical mixing, horizontal advection, primary productivity, sedimentation and organic matter decomposition by microbial loop, as well as sediment oxygen demand (Welsh and Eller 1991; Jensen et al. 1990; Lee and Lwiza 2008; Officer et al. 1984; Pokryfikil and Randall 1987; Rabalais et al. 1991; Ritter et al. 1999).

The microbial loop is defined to be the flow of energy, organic matter and nutrients through unicellular organisms, including bacteria, predatory protists and parasitic viruses, to multicellular organisms and dissolved pools (Pomeroy et al. 2007). Previous studies analyze the microbial

loop activities by applying conceptual model approach. These conceptual models describe trophic carbon transfer and regeneration of inorganic N and P through bacterial degradation of organic matter and its subsequent remineralization through bacterial ammonification and predator's excretion (e.g., Taylor 1982; Thingstad and Giske 2008).

Although conceptual models have been developed to study the microbial loop processes, there are very few studies on microbial loop with numerical modeling approach. This study applies numerical modeling method to explore interactions between physical and biological processes including microbial activity in Long Island Sound (LIS). LIS is an estuary that suffers from eutrophication and hypoxia for decades. Since the early 1970s, the western Narrows of LIS has exhibited seasonally developed hypoxia in the bottom waters (Anderson et al. 2001). During the fall seasons between 1998 and 1999, the severe die-off of the American lobsters (*Homarus americanus*) caused huge ecological losses (CTDEP, 2000). Harmful algal bloom (*Alexandrium fundyense*) that has profoundly impacted the northeastern coast of North America has recently expanded to LIS, and caused complete closure of shellfish beds during its bloom season (Zhuang et al. 2015). In addition to biological processes, there is no doubt that the physical processes in the water column have large impacts on the coastal environment in LIS. However, it is still unclear how these physical processes vary temporally and spatially, and how they interact with the biogeochemical processes to influence oxygen depletion/recovery. Therefore, it is important to investigate the Sound as a whole and integrate the knowledge discovered from individual processes, so that we can address current and future environmental issues in conjunction with physical-biogeochemical variability, e.g., ecological regime shifts, carbon cycling, algal bloom, physical transport and hypoxic condition, etc.

1.2 Objectives and Approach

The main goals of this research is, to

- (1) Examine seasonal variability of water column properties including water column density and dissolved oxygen (DO) in western LIS;
- (2) Quantify variability of exchange transport in the East River and western LIS;
- (3) Explore mechanisms leading to seasonal hypoxia in western LIS.

A modeling approach is required in order to achieve the above goals. The specific objectives of this research is, to

- (1) Parameterize bacterial dynamics including bacterial biomass growth, respiration, regeneration of inorganic nitrogen and phosphate, and grazing by zooplankton;
- (2) Link oxygen variability with the physical and biological processes;
- (3) Examine the seasonal variability of exchange transport, current structure and momentum balance throughout the East River and the western LIS;
- (4) Quantify the contributions of the bacterial activity, vertical mixing and horizontal advection leading to seasonal hypoxia;
- (5) Discuss the outcome of this research and suggest on decision making for coastal management.

To meet these objectives, it is required to modify a coupled physical-biological model and set up a high resolution 3-D model in the East River and western LIS. The objectives are achieved through several approaches. A coupled 1-D physical-biogeochemical model (GOTM/ERGOM) is applied to study the variability of water column properties and variation of DO concentration. The coupled model is modified to include a microbial loop represented by bacterial dynamics, including bacterial biomass growth, respiration, regeneration of inorganic nitrogen and phosphate, and grazing by zooplankton. With the microbial-loop-inclusive model, DO variability is compared to the modeled DO variation without the microbial loop. The impact of the microbial loop on DO variability is determined (Chapter 2).

To estimate the exchange transport in the East River and western Narrows of LIS, a high-resolution 3-D ROMS is run on SoMAS Linux Cluster Cloud and Xsede Gordon National supercomputer. The seasonal variability of exchange transport across four transects between the East River and the western LIS is addressed by using this model. ROMS is applied to simulate stratification, residual circulation and exchange transport between the East River and western LIS for one year period (2008). The model results are validated with observations, i.e., tidal elevation, tidal currents and mean currents, etc. The residual current structures and the momentum balance across the four transects are shown and analyzed (Chapter 3).

The mechanisms leading to seasonal hypoxia is analyzed in a comprehensive way: the impacts of added bacterial dynamics (Chapter 2), vertical mixing (Chapter 3), horizontal advection (Chapter 4, derived from Chapter 3) on seasonal hypoxia are analyzed and compared. In order to explore why adding microbial loop leads to further reduction of DO concentration, DO dynamic terms from the model excluding and including bacterial dynamics are plotted and analyzed. The

horizontal advection derived from high-resolution 3-D ROMS in Chapter 3 are used in the 1-D coupled GOTM/ERGOM in Chapter 4, so that the effect of non-local oxygen transport to seasonal hypoxia could be examined.

References

- Alongi D. M., 1998. Coastal ecosystem processes. 419 p. Boca Raton: CRC Press.
- Anderson, T. H. and Taylor, G. T., 2001. Nutrient pulses, plankton blooms, and seasonal hypoxia in western Long Island Sound. *Estuaries*. 24(2), 228-243.
- Blumberg, A. F. and Pritchard, D. W., 1997. Estimates of the transport through the East River, New York. *J. Geophys Res-Oceans*. 102(C3), 5685-5703.
- Blumberg, A. F., Khan L. A. and John, J. P. St. Three-Dimensional Hydrodynamic Model of New York Harbor Region. *Journal of Hydraulic Engineering*, Vol. 125, No. 8, August 1999, pp. 799-816
- Boon, N. A., 2008. Nutrient Dynamics of Long Island Sound. Master's thesis. Wesleyan University.
- Browne, Mark Anthony; Chapman, M. Gee; Thompson, Richard C.; et al. 2015. Spatial and Temporal Patterns of Stranded Intertidal Marine Debris: Is There a Picture of Global change? *Environmental Science & Technology*. Volume: 49 Issue: 12 Pages: 7082-7094
- Crowley, H. A. 2005. The seasonal evolution of thermohaline circulation in Long Island Sound. Ph.D. Thesis. Stony Brook University. Stony Brook, New York, USA.
- CTDEP, 2000. Information Regarding the Impacts of 1999 Lobster Mortalities in Long Island Sound. Connecticut Department of Environmental Protection (CTDEP), Hartford, Connecticut.
- Diaz, R. J. and Rosenberg, R., 1995. Marine benthic hypoxia: A review of its ecological effects and the behavioural responses of benthic macrofauna. *Oceanography and Marine Biology: an Annual Review* 33, 245-303.

- Friedrich, J., Janssen, F., Aleynik, D., Bange, H. W., Boltacheva, N., Çagatay M. N., Dale, A. W. et al. 2014. Investigating hypoxia in aquatic environments: diverse approaches to addressing a complex phenomenon. *Biogeosciences*, 11, 1215–1259
- Hardy, C.D. 1972. Hydrographic data report : Long Island Sound, 1970, Part II. Marine Sciences Research Center, State University of New York, Stony Brook, with support from Nassau-Suffolk Regional Planning Board.
- Jensen, L. M., Sand-Jensen, K., Marcher, S. and Hansen, M., 1990. Plankton community respiration along a nutrient gradient in a shallow Danish estuary. *Marine Ecology Progress Series*. 61, 75-85.
- Lee, Y. J. and Lwiza, K. M. M., 2008. Characteristics of bottom dissolved oxygen in Long Island Sound, New York, *Estuar. Coast Shelf. S.*, 76(2), 187-200, doi:DOI 10.1016/j.ecss.2007.07.001
- Lee, Y. 2009. *Mechanisms Controlling Variability in Long Island Sound*. Stony Brook University.
- Levin, L. A., Ekau, W., Gooday, A. J., Jorissen, F., Middelburg, J. J., Naqvi, S.W. A., Neira, C., Rabalais, N. N., and Zhang, J. 2009. Effects of natural and human-induced hypoxia on coastal benthos, *Biogeosciences*, 6, 2063–2098, doi:10.5194/bg-6-2063-2009.
- O'Donnell, J., Dam, H. G., Bohlen, W. F., Fitzgerald, W., Gay, P. S., Houk, A. E., Cohen, D. C. and Howard-Strobel M. M., 2008. Intermittent ventilation in the hypoxic zone of western Long Island Sound during the summer of 2004. *Journal of Geophysical Research: Oceans* DOI: 10.1029/2007JC004716.

O'Donnell, J., Dam, H. G., McCardell, G. and Fake, T., 2010. Long Island Sound Study EPA Assistance Award Final Report.

O'Donnell, J., Wilson, R. E., Lwiza, K., Whitney, M., Bohlen, W. F., Codiga, D., Fake, T., Bowman, M., and Varekamp, J., 2013. The Physical Oceanography of Long Island Sound, in Swanson, R.5 yarish, C. and Latimer, J. (eds), "Long Island Sound". Springer-Verlag Publishing company.

Officer, C. B., Biggs, R. B., L. T. J, Cronin, L. E., Tyler, M. A., and Boynton, W. R., 1984. Chesapeake Bay anoxia: Origin, development, and significance., *Science* 223, 22-27.

Pokryfki, L. and Randall, R. E., 1987. Nearshore hypoxia in the bottom water of the northwestern Gulf of Mexico from 1981 to 1984, *Marine Environmental Research* 22:75-90.

Pomeroy, L. R., Williams, P. J. I., Azam, F. and Hobbie, J. E., 2007. The microbial loop., *Oceanography* 20(2):28-33.

Rabalais, N. N., Turner, R. E., Wiseman, W. J. and Boesch, D. F., 1991. A brief summary of hypoxia on the northern Gulf of Mexico continental shelf: 1985-1988, p. 35-47. In R. V.

Ritter, C. and Montagna, P. A., 1999. Seasonal hypoxia and models of benthic response in a Texas bay, *Estuaries* 22:7-20.

Swanson, R.L., Wilson, R.E., Crowley, H.A., 2008. Perspectives on long-term variations in hypoxic conditions in western Long Island Sound. DOI: 10.1029/2007JC004693.

Thingstad, T.F. and Giske, J., 2008. Models and functioning of marine ecosystems. In: *Oceanography*, (J.C.J. Nihoul and C.-T. A. Chen, Eds.), *Encyclopedia of Life Support Systems* Vol. 2, 88-105.

- Torgersen, T., Deangelo, E., O'Donnell, J., 1997. Calculations of horizontal mixing rates using ^{222}Rn and the controls on hypoxia in western Long Island Sound, 1991. *Estuaries* 20, 328–345.
- Valle-Levinson, A. and R. E. Wilson. 1998. Effects of rotation and vertical mixing on volume exchange in eastern Long Island Sound. *Estuarine Coastal and Shelf Science*, 46:573-585.
- Vieira, M. E. C. 1990. Observations of Currents, Temperature and Salinity in Long Island Sound, 1988. A Data Report. , Data Report #6. Marine Sciences Research Center, State University of New York, Stony Brook, New York.
- Vieira, M. E. C. 2000. The long-term residual circulation in Long Island Sound, *Estuaries*, 23(2), 199-207, doi:10.2307/1352827.
- Wilson, R.E. , 1976. Gravitational circulation in Long Island Sound: Estuarine and Coastal Marine Science, v. 4, p. 443-453.
- Wilson, R.E., R.L. Swanson and H.A. Crowley , 2008. Perspectives on long-term variations in hypoxic conditions in Western Long Island Sound. *Journal of Geophysical Research*, 113, C12011, doi:10.1029/2007JC004693.
- Welsh, B.L., Eller, F.C., 1991. Mechanisms Controlling Summertime Oxygen Depletion in Western Long Island Sound. *Estuaries* 14, 265-278.
- Wong, K.-C., The effect of East River on the barotropic motions in Long Island Sound, *J. Mar. Res.*, 49, 321-337, 1991.

Zhuang, Y., Zhang, H. Hannick, L., Lin, S. 2015. Metatranscriptome profiling reveals versatile N-nutrient utilization, CO₂ limitation, oxidative stress, and active toxin production in an *Alexandrium fundyense* bloom. *Harmful Algae*. 42 (2015) 60–70

Chapter 2

Importance of the bacterial dynamics in model simulations of seasonal hypoxia

Abstract

The occurrence and spread of hypoxia in coastal waters is known to depend strongly on nutrients, primary production, water column structure, wind and tidal mixing. Accurate prediction of the onset, intensity and areal extent of hypoxia remains a challenge. Previous modeling efforts have needed to ‘tune’ vertical mixing or phytoplankton respiration in order to obtain results that agree with field observations of dissolved oxygen (DO). In this chapter, we use a one-dimensional physical model coupled with a biogeochemical model to establish mechanistic links between factors involved in the evolution of seasonal hypoxia in western Long Island Sound. The coupled model includes bacterial dynamics, which allows accurate prediction of the onset of late summer hypoxia and subsequent recovery. Model results indicate that a hyperbolic temperature response function represents temperature control on bacterial community growth rate better than the traditional Q_{10} function. The cost of not including the bacterial dynamics in the model is an overestimation of bottom DO by as much as 700% in summer. By including bacterial dynamics, we eliminate the need to distort vertical mixing or phytoplankton respiration rate to simulate observed seasonal variability in DO. In order to accurately model DO dynamics under normal wind forcing, therefore, coastal ecosystem models need to explicitly include terms for major components of the microbial loop.

2.1 Introduction

Eutrophication is a process that brings excessive nutrients into coastal estuaries, fuels phytoplankton production and increases organic carbon transport to the seabed (Welsh and Eller 1991). As a consequence, seasonal hypoxia can occur when DO concentration in the water column falls below 3 mg/l (Diaz et al. 1995; Ritter et al. 1999). The seasonal evolution of DO depletion in coastal embayments and estuaries is shaped by interactions among physical and biogeochemical processes. These processes include air-sea exchange, nutrient input, vertical mixing, horizontal advection, primary productivity, sedimentation and organic matter decomposition, as well as sediment DO demand (Welsh and Eller 1991; Jensen et al. 1990; Lee and Lwiza 2008; Officer et al. 1984; Pokryfikil and Randall 1987; Rabalais et al. 1991; Ritter et al. 1999).

Observational analysis of the interplay among these processes responsible for eutrophication and hypoxia has always been confounded by logistical difficulties presented by conducting systematic and comprehensive field measurements with sufficient temporal resolution. However, with the piece-meal information gathered from field experiments, responses of seminal processes can be evaluated using a modeling approach. In LIS, several generations of water quality models have been developed since 1987 to examine the mechanisms leading to seasonal hypoxia. The first two generations (LIS1.0 and LIS2.0) were steady-state 2-D models. The third generation model LIS3.0 is 3-D and time-varying (LISS 2003; Science and Technical Advisory Committee 2003). In 2001, a system-wide eutrophication model called SWEM was developed for LIS with the eutrophication module of Row Column Aesop (RCA) (HydroQual 2001; LISS 2003; Science and Technical Advisory Committee 2003).

One major problem associated with the SWEM model is that vertical mixing has to be artificially forced to go to near zero in order to obtain a reasonable representation of hypoxia (Hydroqual 2003; O'Donnell et al. 2010). In addition, phytoplankton respiration rates have to be increased to force adequate DO consumption (O'Donnell et al. 2010). This, however, leads to a distorted simulation of the phytoplankton system, and implies that mechanisms other than vertical mixing and phytoplankton respiration are required in order to explain depletions in bottom DO. One of these mechanisms is most certainly respiration by bacteria, which consume large amounts of DO when decomposing organic matter. We further note that field observations reveal large bacterial biomasses, nearly matching phytoplankton biomasses in western LIS (Suter 2011). This means that in order to understand DO variability and the mechanisms leading to hypoxia, it is important to incorporate bacterial dynamics into coastal models (Fenchel 2008; Jahnke and Craven 1995; Lee and Lwiza 2008), and carefully examine how the microbial loop controls remineralization processes, driving significant DO consumption in near-bottom waters.

In this chapter we represent microbial loop by parameterizing bacterial dynamics which includes aerobic bacterial biomass growth, respiration, regeneration of inorganic nitrogen and phosphate, and grazing by zooplankton. It also includes the relative contributions of bacterial remineralization and zooplankton excretion to inorganic nutrient regeneration. The mechanisms leading to seasonal hypoxia and recovery of bottom DO are investigated by applying a coupled 1-D physical-biogeochemical model to a western LIS station (i.e., A4, Execution Rocks, Figure 2-1).

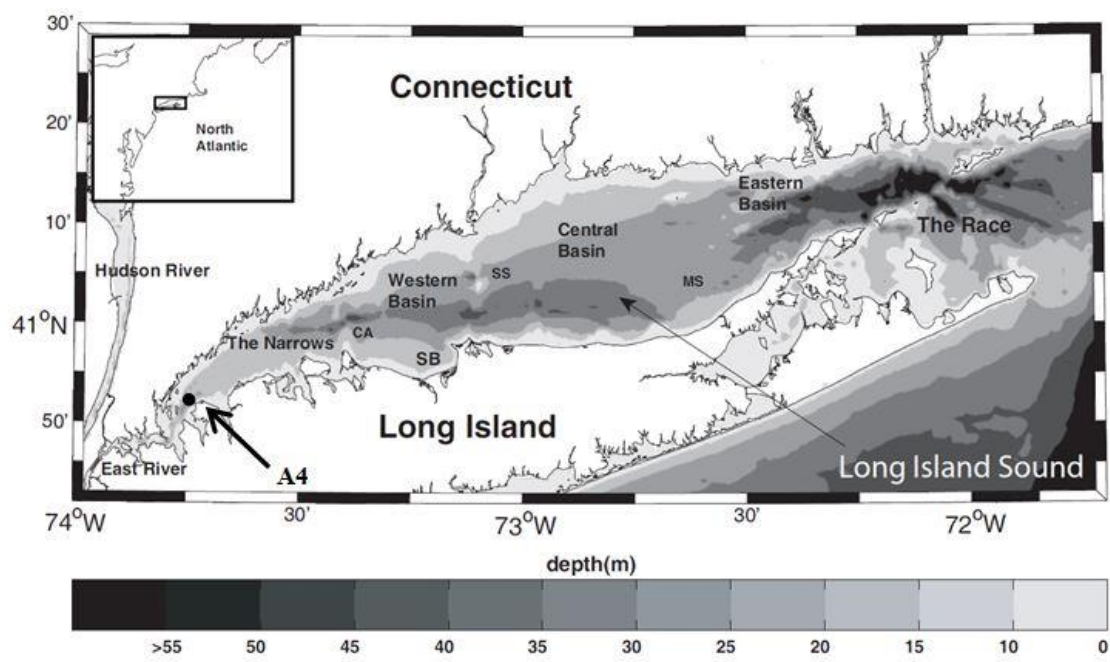


Figure 2-1. Bathymetry of Long Island Sound (SS, Stratford Shoal; CA, Cable and Anchor Reef; MS, Mattituck Sill; SB, Smithtown Bay) (Lee 2009).

This chapter is organized in the following manner. Section 2.2 introduces the study area. Section 2.3 describes the data and the 1-D coupled model applied in this chapter and the modification of the 1-D coupled model to include bacterial dynamics. Important physical and biological results are presented in Section 2.4. The importance of bacterial dynamics on DO variability is discussed in Section 2.5. Also discussed in Section 2.5 is the sources of errors of the biogeochemical model setup and the comparison to the Q10 controlled bacterial growth curve, as well as the future directions of eutrophication modeling. Conclusions from this chapter are presented in Section 2.6.

2.2 Study area

LIS is a 20x150 km estuary with an average depth of 20 m. In the eastern end of the Sound, the Connecticut River enters the Sound from the north and the ocean enters at the mouth. The western end of LIS is connected to the lower Hudson River via the East River (Blumberg and Pritchard 1997; O'Donnell et al. 2013). LIS is made up of four major basins (i.e., the Eastern Basin, the Central Basin, the Western Basin and the Narrows) separated by several sills and shoals (Figure 2-1). Among those four major basins, the western Basin, with a deep channel continuing to the eastern part of the Narrows, is separated by Cable and Anchor Reef (Vieira 2000). Freshwater enters the Sound from runoff and drainage along the coast of Long Island, New York, and Connecticut. Freshwater discharge reaches its maximum during the spring freshet. Up to 90% of the freshwater input into the Sound comes from the discharge of three major rivers, namely, Thames River, Housatonic River, and Connecticut River, among which Connecticut River contributes 74% of the total freshwater discharge. Sewage treatment plants also contribute approximately 1% of the total annual freshwater input (Boon 2008). Since at least

the early 1970s, the western narrows of Long Island Sound has exhibited hypoxia during warm seasons in the bottom waters (Parker and O'Reilly 1991). Despite efforts of modeling and observational managements, the discharges from the sewage treatment works still supply high nutrient loadings into western narrows, which continue to fuel seasonal hypoxia. Station A4 in this chapter (40°52.3'N, 73°44.1'W) is located to the south of Execution Rocks lighthouse between New Rochelle and Manhasset, New York in approximately 32 m of water depth (Figure 2-1).

2.3 Methods

2.3.1 Data

To monitor water quality in LIS, the Connecticut Department of Energy and Environmental Protection (CTDEEP) has conducted biweekly to monthly surveys since 1991 collecting data on distributions of salinity, temperature, DO and inorganic nutrients throughout the Sound. These data were used for nudging and verification of model results in this chapter. In addition, the CTDEEP also monitors phytoplankton community composition by pigment analysis, which they report as percent contribution to total Chlorophyll *a* (Chl*a*). Pigment analyses were performed using High Performance Liquid Chromatography (HPLC). Each phytoplankton taxonomic group's contribution to the community was estimated using the CHEMTAX program to compare measured pigment concentrations to known photopigment ratios of phytoplankton populations in LIS, and abundance of each group was normalized to predicted units of $\mu\text{g Chl/L}$ (CTDEEP 2005). We converted observed phytoplankton biomass (total Chl*a*) to nitrogen-based biomass (mmol N m^{-3}) in order to compare with model outputs because the model uses nitrogen as its

currency. To do this, Chl a was converted to C using a C:Chl a ratio of 30 g C g $^{-1}$ Chl a , which is at the lower end of Taylor et al.'s, (1997) range of 20 to 160 g C g $^{-1}$ Chl a , and C was converted to N using a constant C:N ratio of 6.625:1 (Redfield ratio). Monthly data for two phytoplankton groups, i.e., diatom and dinoflagellates in Station A4 surface waters in 2008 were used to validate the modeled surface phytoplankton biomasses.

Bacterial biomass was obtained by converting bacterial cell abundances with a conversion ratio of 37.0 femtograms C/cell (Suter 2011). Cell abundances were enumerated using epifluorescent microscopy in water samples from the surface, bottom, upper and lower pycnocline of the water column collected on 23 June, 14 July, 11, 16 and 28 August, 10 and 15 September, 1 October 2008 (Suter 2011). These data were converted from $\mu\text{g C/L}$ to mmol N m^{-3} using the Redfield C:N ratio of 6.625:1 for lack of an empirically determined alternative.

Meteorological data collected at Station A4 in 2008 by the Long Island Sound Integrated Coastal Observing System (LISICOS) were used to force the model (data available at <http://LISICOS.uconn.edu>). These data include wind speed and direction; air pressure, temperature and humidity. Hourly cloud cover was measured at LaGuardia Airport, Queens, New York and data are archived at the National Climatic Data Center (NCDC) of National Oceanic and Atmospheric Administration (NOAA).

2.3.2 Model

2.3.2.1 General Ocean Turbulence Model (GOTM)

The physical model applied in this study is the General Ocean Turbulence Model (GOTM), originally described by Burchard et al. (1999), which has been revised several times since (see Burchard et al. 2006; Umlauf et al. 2005). GOTM is a 1-D water column model for

hydrodynamical processes with vertical mixing. The core of the model solves the 1-D transport equations of heat, momentum and salt with mean and turbulent fluxes (Burchard et al. 2006).

The turbulent closure applied in this study is k-ε model with second-order moment closure (Canuto et al. 2001), as described by Burchard et al. (2001). The stability function introduced by Schumann and Gerz (1995) is applied in the model. The momentum and turbulent equations for GOTM were described in more detail in Burchard et al. (2006) and Umlauf et al. (2005). For brevity's sake, the equations are not provided here. Please refer to Table 2-1 for major model parameters applied in this study.

The temperature equation of the model is expressed by:

$$\frac{\partial T}{\partial t} - \nu' \frac{\partial^2 T}{\partial z^2} + \frac{\partial}{\partial z} \langle w' T' \rangle = \frac{1}{c_p \rho_0} \frac{\partial Q}{\partial z} \quad (2-1)$$

in which ν' indicates the heat molecular diffusivity, and c_p represents the heat capacity. The source term on the right hand side of the temperature equation, is the vertical divergence of short-wave radiation Q .

Similarly, the salinity equation in GOTM is given by:

$$\frac{\partial S}{\partial t} - \nu'' \frac{\partial^2 S}{\partial z^2} + \frac{\partial}{\partial z} \langle w' S' \rangle = \tau_R^{-1} (S_R - S) \quad (2-2)$$

where ν'' is the salt molecular diffusivity. The right side of the equation represents the relaxation of salinity towards the observation S_R with the relaxation time period τ_R .

2.3.2.2 Biogeochemical model

The biogeochemical model, viz., ERGOM ecosystem model (Neumann et al. 2002) is governed by the general equation:

$$\frac{\partial c_i}{\partial t} + \frac{\partial}{\partial z} < m_i c_i - K_v \frac{\partial c_i}{\partial z} > = P_i(c) - D_i(c), \quad i = 1, \dots, I \quad (2-3)$$

in which c_i denotes concentrations of 10 state variables (i.e. $I = 10$), m_i represents the autonomous motion of the state variable c_i (e.g. sinking or active swimming), and K_v represents eddy diffusivity. Note that the physical model GOTM to which ERGOM is coupled is an Eulerian type model with all ten state variables in ERGOM in nitrogen units, i.e., mmol N m^{-3} . Although the model is capable of simulating three groups of phytoplankton (i.e., diatoms, dinoflagellates and cyanobacteria), we chose to represent phytoplankton by data on diatoms (indicated by c_1) and dinoflagellates (c_2), because cyanobacterial biomass in LIS is negligible (Capriulo et al. 2002). Zooplankton biomass is represented by c_4 , and c_5 indicates detritus, which comprise non-living labile particulate organic material. Ammonium (c_6), nitrate (c_7) and phosphate (c_8) represent three nutrient state variables, in which the production/consumption of phosphate is estimated from that of nitrogen based on the stoichiometric ratio, which is assumed to be constant (0.0625). Further, c_9 and c_{10} indicate DO and sedimentary detritus, respectively (Burchard et al. 2006). Sedimentary detritus accumulates as debris as reaching the seabed. Diatoms represent large cell phytoplankton, which favor nutrient-rich turbulent environments, while dinoflagellates represent relatively smaller sized phytoplankton favoring stratified conditions (Burchard et al. 2006; Capriulo et al. 2002). The two groups of phytoplankton are grazed on by zooplankton. Dead phytoplankton and zooplankton are included in the detritus state variable, which are assumed to be labile and can be microbially remineralized into dissolved

ammonium and phosphate. The dynamics of DO are coupled to biogeochemical processes (i.e., photosynthesis, respiration, excretion, remineralization) via stoichiometric ratios. DO concentrations in turn control biochemical processes including denitrification and nitrification.

To summarize, the ERGOM model simulates phytoplankton uptake of ammonium, nitrate and phosphorus; zooplankton grazing on phytoplankton groups; respiration of the phytoplankton; phytoplankton and zooplankton mortality; detritus remineralization; zooplankton excretion; nitrification; denitrification; surface flux of DO; DO production/consumption due to photosynthesis, phytoplankton respiration, detritus remineralization and sedimentary processes.

Between ERGOM and GOTM, there is a two-way coupling. The biogeochemical processes modeled by ERGOM depend on the physical processes provided by GOTM. All the biogeochemical variables are subject to vertical mixing. Temperature is the primary controlling factor on most biogeochemical processes including uptake, grazing, respiration and nitrification; photosynthesis is a function of temperature, light and nutrient availability. The water column structure modeled by GOTM is modified by the feedback loop provided by ERGOM's biogeochemical processes, e.g., water turbidity may be modified by biogeochemical properties and change the light absorption in the water column; Viscosity and density may be modified due to biogeochemical properties. The model also includes self-shading effect of the biological biomass. Q in Equation (2-1) includes short wave radiation, which is parameterized by,

$$I(z) = I_0 \left\{ a \exp\left(\frac{z}{\eta_1}\right) + (1-a) \exp\left(\frac{z}{\eta_2}\right) B(z) \right\} \quad (2-4)$$

where the first term in parentheses on the right hand side corresponds to the absorption of the red part of the light spectrum, and the second term to the blue-green light, which is subject to further absorption by phytoplankton c_p and detritus c_D . The biological biomass $B(z)$ is written by,

$$B(z) = \exp(-k_c \int_z^0 (c_p(\xi) + c_D(\xi)) d\xi) \quad (2-5)$$

The variables in Equations. (2-4) and (2-5) are the surface radiation, I_0 , the absorption length scales for the red and the blue-green part of the light spectrum, η_1 and η_2 , respectively, the weighting parameter, a , and the attenuation constant for self-shading, k_c .

2.3.2.3. Oxygen dynamics in the coupled model

Oxygen dynamics in the coupled model has three main components: Surface oxygen flux, oxygen production due to photosynthesis (i.e., $d_{nutrient,phy}$), and oxygen consumption due to planktonic respiration (i.e., $d_{phy/zoo,amm}$), detritus and sediment remineralization (i.e., $d_{det,amm}$ and $d_{sed,amm}$). The surface flux of oxygen is modeled as:

$$F_9^s = p_{vel}(O_{sat} - c_9) \quad (2-6)$$

where

$$O_{sat} = a_0(a_1 - a_2T) \quad (2-7)$$

Please refer to Table 2-1 for values applied to parameters.

In addition, oxygen produced by phytoplankton (i.e., photosynthesis) under ammonium and nitrate limitation is represented as:

$$p_{DO,amm/nit} = s_2(d_{amm/nit,dia} + d_{amm/nit,fla}) \quad (2-8)$$

Oxygen consumed due to respiration of phytoplankton and zooplankton can be written as:

$$P_{DO,phy} = -s_2(d_{phy/zoo,amm}) \quad (2-9)$$

Also, oxygen consumed when detritus is remineralized into ammonium is represented by:

$$P_{DO,det} = -s_2(L_+^+ + L_-^-)d_{det,amm} \quad (2-10)$$

with L_+^+ and L_-^- being the switches between oxic and anoxic states.

Oxygen demand during sediment remineralization into ammonium is formulated as follows:

$$P_{DO,sed} = -(s_4 + s_2(L_+^+ + L_-^-)) \frac{d_{sed,amm}}{h_1} \quad (2-11)$$

With h_1 representing the depth of the bottom, s_2 and s_4 indicating stoichiometric and remineralization coefficients, respectively. It is important to recognize that in reality detritus can be remineralized into several chemical pools, and ammonium can be released merely by hydrolysis. Table 2-1 contains all coefficient values used in the model. Please also refer to (Burchard et al. 2006) for more detail of these equations. The oxygen produced in ERGOM was redistributed in the water column by turbulent mixing in the physical model (GOTM) as described by Equation (2-3).

Table 2-1. Major parameters applied in the modified model.

Name	Description	Values wLIS	Units
Prandtl0_fix	Turbulent Prandtl-number	0.74	
kappa	Von Karman constant	0.4	
Ri_st	Steady-state Richardson number	0.25	
k_min	Minimum TKE	10^{-5}	J kg^{-1}
eps_min	Minimum dissipation rate	10^{-12}	W kg^{-1}
kb_min	Minimum buoyancy variance	10^{-10}	s^{-2}
epsb_min	Minimum buoyancy variance destruction rate	10^{-14}	s^{-2}
α_1	Half saturation of nutrients for diatoms	1.35	mmol N m^{-3}
α_2	Half saturation of nutrients for flagellates	0.675	mmol N m^{-3}
c_{\min}^4	Minimum zooplankton concentration	0.0045	mmol N m^{-3}
g_1^{\max}	Maximum grazing rate on diatoms	0.5	d^{-1}
g_2^{\max}	Maximum grazing rate on dinoflagellates	0.5	d^{-1}
I_{\min}	Minimum photosynthetically active radiation	25	W m^{-2}
I_v	Ivlev constant	0.244	mmol N m^{-3}
I_{AN}	Nitrification constant	0.004	d^{-1}
I_{DA}	Detritus mineralization constant	0.008	d^{-1}
I_{DS}	Net rate of detritus sinking into sediment	3.5	m d^{-1}
I_{PA}	Phytoplankton respiration rate	0.01	d^{-1}
I_{PD}	Phytoplankton mortality Rate	0.02	d^{-1}
I_{ZA}	Zooplankton excretion rate	0.067	$\text{m}^3\text{d}^{-1}(\text{mmol N})^{-1}$
I_{ZD}	Zooplankton mortality rate	0.133	$\text{m}^3\text{d}^{-1}(\text{mmol N})^{-1}$
p_{vel}	Piston velocity	5.0	m d^{-1}
r_1^{\max}	Maximum growth rate of diatoms	2.0	d^{-1}
r_2^{\max}	Maximum growth rate of flagellates	0.7	d^{-1}
s_2	Stoichiometric ratio (i.e., O/ N)	6.625	
s_R	Stoichiometric ratio (i.e., PO/ N)	0.0625	
T_{DA}	Temperature control of diatom	13	$^{\circ}\text{C}$

T_f	Temperature control of dinoflagellates	10	$^{\circ}\text{C}$
T_{opt}	Temperature control of bacteria	20	$^{\circ}\text{C}$
W_{de}	Vertical velocity of detritus	-3	m d^{-1}
W_{p1}	Vertical velocity of diatoms	-0.5	m d^{-1}
V_b	Maximum bacteria growth rate	2	d^{-1}
g_{11}^{max}	Maximum grazing rate on bacteria	0.5	d^{-1}
L_{ba}	Bacterial respiration rate	0.34	d^{-1}
L_{bd}	Bacterial mortality rate	0.18	d^{-1}
a_0	oxygen saturation parameter	24.25	$\text{mmol O}_2 \text{ m}^{-3}$
a_1	oxygen saturation parameter	14.6	
a_2	oxygen saturation parameter	0.1	$(^{\circ}\text{C})^{-1}$

2.3.2.4 Adding bacterial dynamics into the 1-D coupled model

In order to determine the mechanistic links between DO variability, bacterial dynamics and vertical mixing, the 1-D coupled model was modified to include bacterial dynamics and the associated DO consumption processes. Adding bacterial dynamics to ERGOM is important because we eliminate simulating remineralization by proxy (i.e., phytoplankton tuning) and simulate more closely what occurs in nature. In addition, bacterial dynamics terms capture feedback and nonlinear processes, which were missing in previous models. Furthermore, we used monthly data for surface temperature, salinity, ammonium, nitrate, phosphate to nudge the corresponding variables in surface waters in the coupled model with a one-month relaxation time

scale. The spin-up time for the model was 6 years and the results from the seventh year were used for analysis. All model outputs were set to daily time scales.

After setting up the original model and making sure it stably ran on our system, we added bacterial biomass into ERGOM as an additional component (c_{11}). The relationships between bacterial dynamics and the variability in DO concentration were also added (see Figure 2-2 for the complete structure of 1-D GOTM/ERGOM and Table 2-1 for major parameters applied in the model). Bacteria assimilate ammonium for growth, and they degrade and remineralize labile detritus into ammonium. They, in turn, are grazed upon by microzooplankton which excrete ammonium. A temperature control factor was applied to bacterial growth and respiration processes in addition to substrate control (i.e., labile detritus) due to the observed dependence of these processes on temperature (Hall et al. 2008). The detritus remineralization process in the original model without bacterial dynamics was replaced by bacterial degradation of labile detritus and releasing inorganic nitrogen.

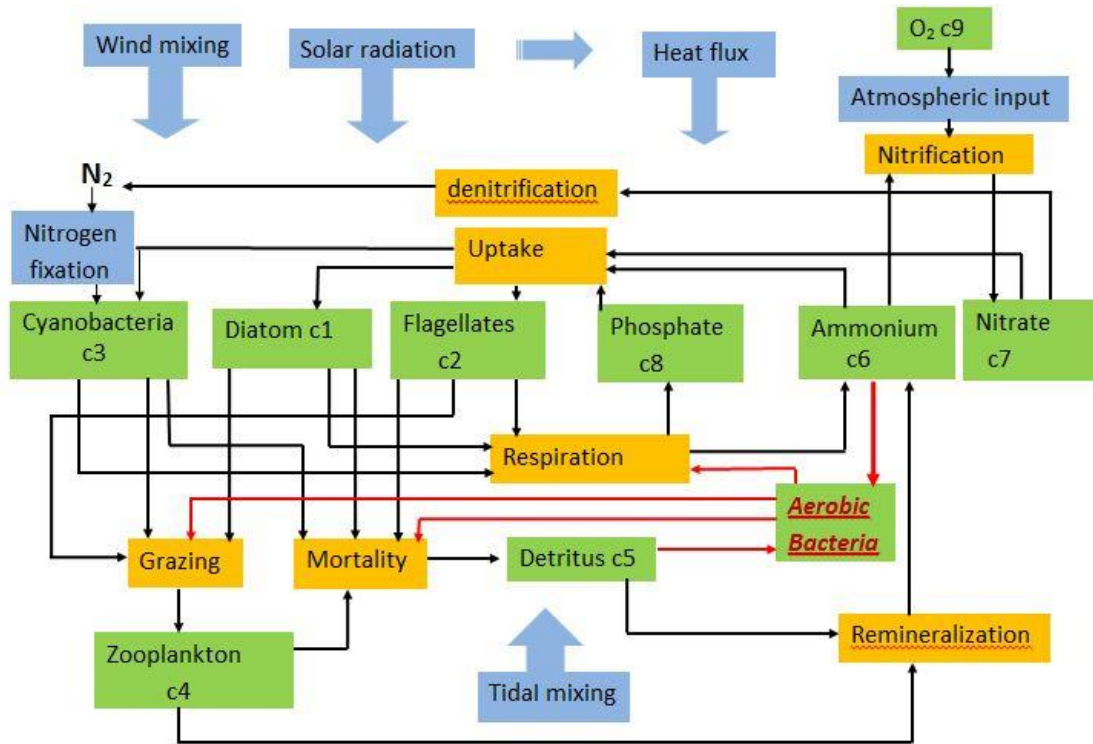


Figure 2-2. Model structure of GOTM/ERGOM.

The dynamics of bacterial decomposition of labile detritus are described by:

$$d_{\text{det},\text{bac}} = vb * Y(td, t) * c_{\text{det}} / (c_{\text{det}} + c_{\text{amm}}) * c_{\text{bac}} \quad (2-12)$$

in which Y is a hyperbolic temperature function with the square of temperature t as numerator and sum of squares of temperature t and a constant temperature td as denominator (Neumann et al. 2002), formulated as:

$$Y(td, t) = \frac{t^2}{td^2 + t^2} \quad (2-13)$$

In equation (2-12), bacterial decomposition rate of labile detritus varies hyperbolically with temperature increase. td controls the rate of change of the hyperbolic curve, and we set td in (2-12) to be 20°C so that the change in decomposition rate is nearly linear.

Alternatively, growth rate responses of individual marine poikilotherms to temperature change have been shown to follow a Q_{10} function (Van't Hoff 1884) and are described by:

$$Q_{10} = \left(\frac{R_2}{R_1} \right)^{10/(T_2 - T_1)} \quad (2-14)$$

where R_1 and R_2 are growth rates at two temperatures T_1 and T_2 , respectively. Most biological processes follow this function over short term exposures to changing temperature, often with a Q_{10} near 2 for phytoplankton growth and near 3 for microbial activity (Shiah and Ducklow 1994).

The Q_{10} function described by (2-14) could be inverted to a more generalized representation of growth rate as a function of temperature:

$$R = R_1 * Q_{10}^{\frac{T - T_1}{10}} \quad (2-15)$$

Thermal responses in bacterial growth rate following a Q_{10} function are exponential and thus growth responds more to temperature than other control factors (e.g., detritus concentration and bacterial biomass). This may distort prediction of timing of hypoxia since bottom DO concentration is controlled by bacterial dynamics. We compared the effects of these two functions on predictions of hypoxia, and presented the comparisons in the Results section.

Next we considered the relationship between bacteria and ammonium in the model. We assume under steady state, the amount of ammonium consumed by heterotrophic bacteria depends on the concentrations of ammonium, labile detritus, heterotrophic bacteria, and temperature. It must be noted that the amount of ammonium consumed by bacteria is also determined by detrital quality (i.e., C:N ratio) such that if detritus is rich in proteins and nucleic acids, bacteria may not need a NH_4 subsidy. However, if detritus is rich in lipids and carbohydrates, then NH_4 subsidy is required by bacteria. Since ERGOM uses nitrogen as model currency and C:N ratio is assumed to be constant, the formula below does not include detrital quality:

$$d_{amm,bac} = vb * Y(td, t) * c_{amm} / (c_{det} + c_{amm}) * (c_{bac} + ba0) \quad (2-16)$$

Bacteria are consumed by microzooplankton through grazing process. The process was represented by:

$$d_{bac,zoo} = g_{11}^{max} \left(1 + \frac{T^2}{T_{opt}^2} \exp\left(1 - \frac{2T}{T_{opt}}\right)\right) * \left(1 - \exp\left(-I_v^2 \left(\sum_{j=1}^2 c_j + c_{bac}\right)^2\right)\right) * \frac{c_{bac}}{\sum_{j=1}^2 c_j + c_{bac}} (c_{zoo} + c_{zoo}^{min}) \quad (2-17)$$

$\sum_{j=1}^2 c_j$ represents the total biomass of phytoplankton and c_{bac} is the bacterial biomass density.

Here, zooplankton was considered to be an aggregation of organisms from heterotrophic protists to copepods that prey on both phytoplankton and bacteria. Zooplankton grazing preferences are not only functions of the prey proportions (i.e., proportions of phytoplankton and bacteria, parameterized explicitly in the model) and relative size differences between prey and predator (not explicitly parameterized in this model), and assigned such that they change dynamically

with time (Fasham et al. 1990). In Equation (2-17), $\frac{c_{bac}}{\sum_{j=1}^2 c_j + c_{bac}}$ represents the preference or

proportion of zooplankton grazing on bacteria. Equation (2-17) states that the process of zooplankton grazing on bacteria is a function of grazing rate, seasonal cycle of temperature, zooplankton biomass and proportion of zooplankton grazing on bacteria.

In addition, bacterial respiration is formulated as a function of temperature (Hall et al., 2008):

$$d_{bac,amm} = lba * c_{bac} * (0.15 + Y(td, t)) \quad (2-18)$$

DO is consumed by bacteria as they remineralize labile detritus and release ammonium. We did not need to define the DO consumed by zooplankton and ammonium released by zooplankton because it is included in the original ERGOM. The amount of DO consumed is also controlled by the stoichiometric ratio s_2 (i.e., O:N):

$$p_{oxy,bac} = -s_2 * d_{det,bac} - s_2 * d_{bac,amm} \quad (2-19)$$

2.4 Results

2.4.1 Water column properties

Modeled sea surface temperature (SST) reached a minimum value of 2.5°C in mid-February of 2008 (Figure 2-3a). It increased gradually to reach the maximum of 22°C in early September, after which it decreased linearly toward December. Bottom water temperature increased from 14°C to 22°C from June until early September, while surface waters warmed from 18°C to 22°C (Figure 2-3a), and so deeper water warmed faster than the surface water during the same period. The thermocline started to develop at approximately 10 m from late April, then deepened slightly to reach 12 m until end of June, then shoaled gradually and was shallowest (i.e., 4 m) in late August. After which the thermocline deepened until the water column became well mixed again between September and December. The observed temperature profiles show sharper thermocline in June and July than the simulation, possibly due to monthly sampling frequency (Figure 2-3b). Otherwise, the modeled seasonal variation of temperature profiles generally agreed with the observations. Also shown are the modeled seasonal temperatures at surface, depth below pycnocline, and bottom (Figure 2-3(c-e)) compared to the observations. The comparison shows that the model captured the main features of the observed seasonal cycle of temperature at different depths. This demonstrates that vertical diffusion is correctly prescribed in the model.

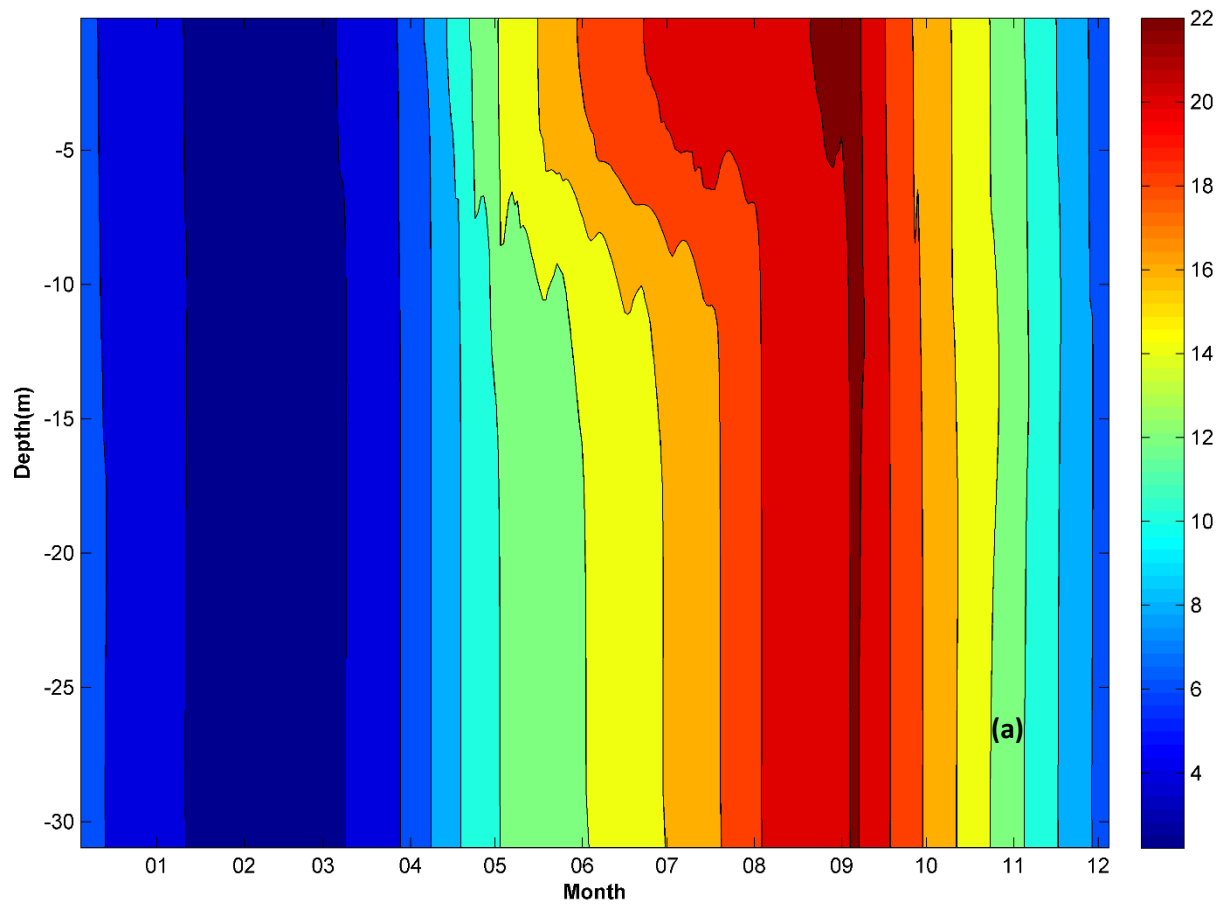


Figure 2-3. (a) Simulated seasonal variability of vertical temperature structure (Celcius) in 2008.

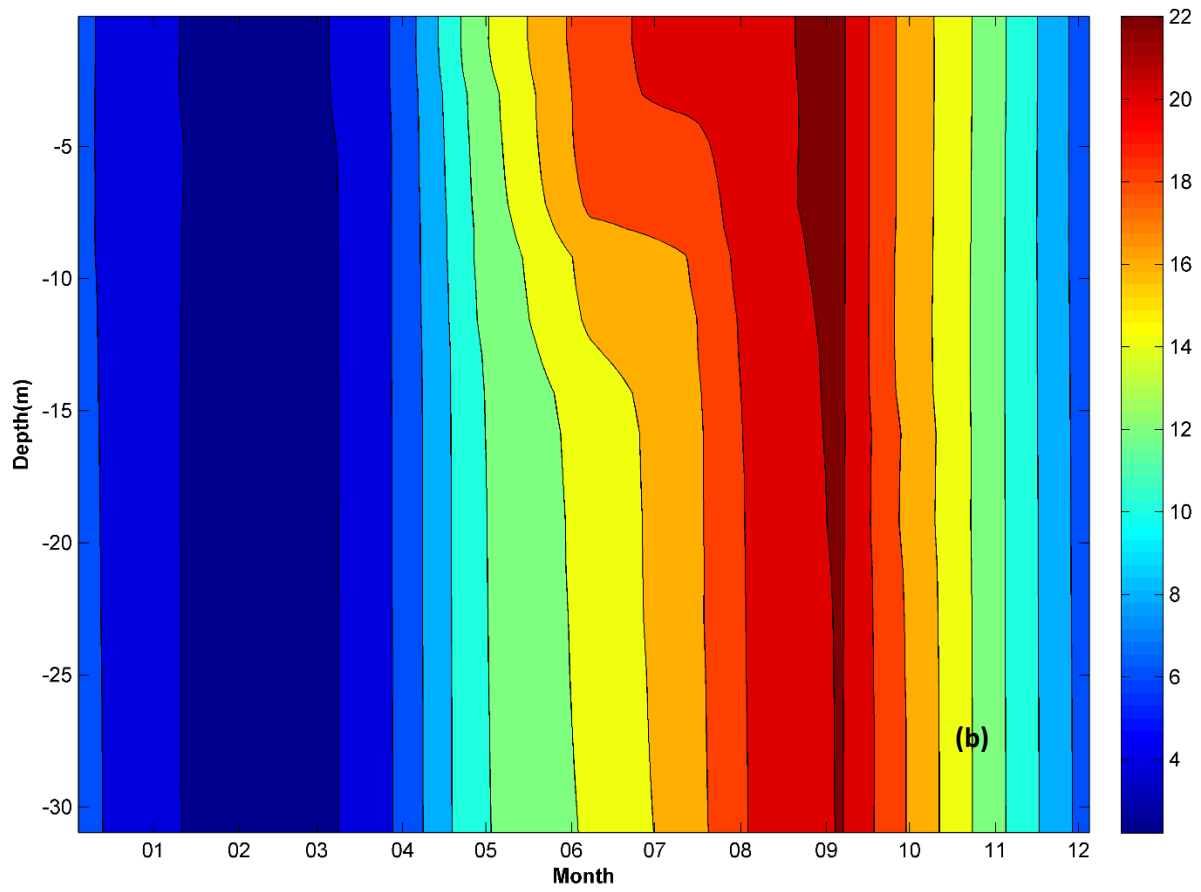


Figure 2-3. (b) Observations of vertical temperature structure (Celsius) in 2008.

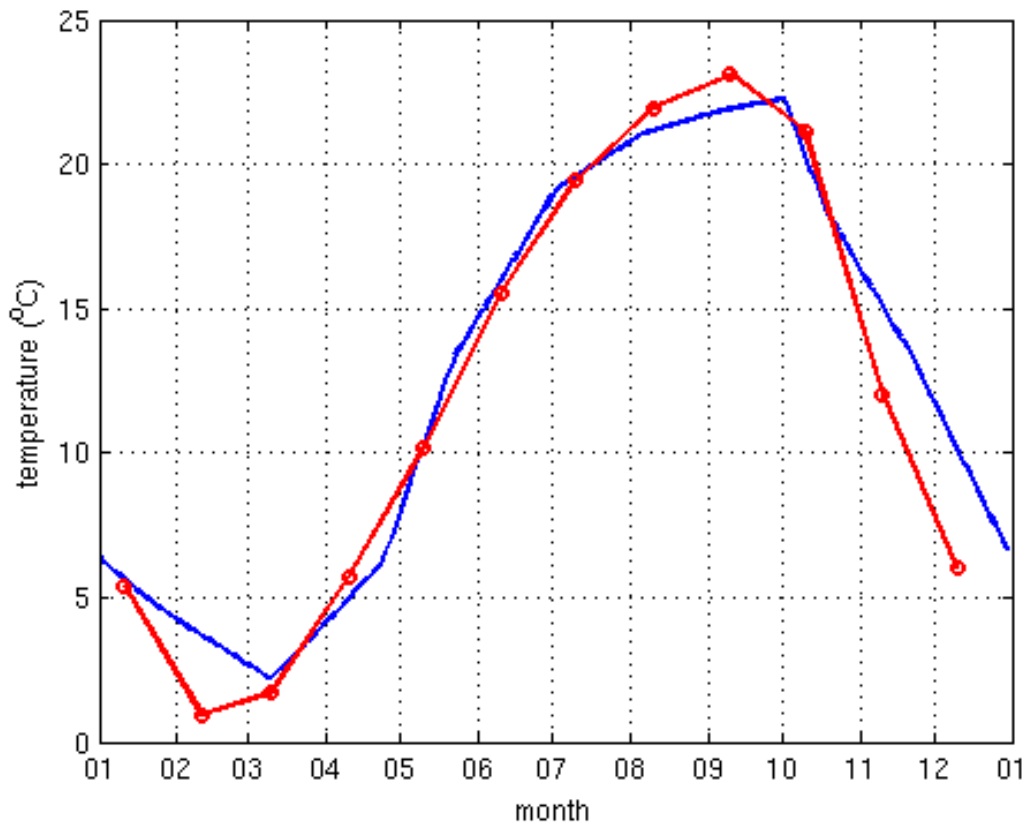


Figure 2-3. (c) Observed surface temperature in Celcius (red) compared to model simulation (blue) in 2008.

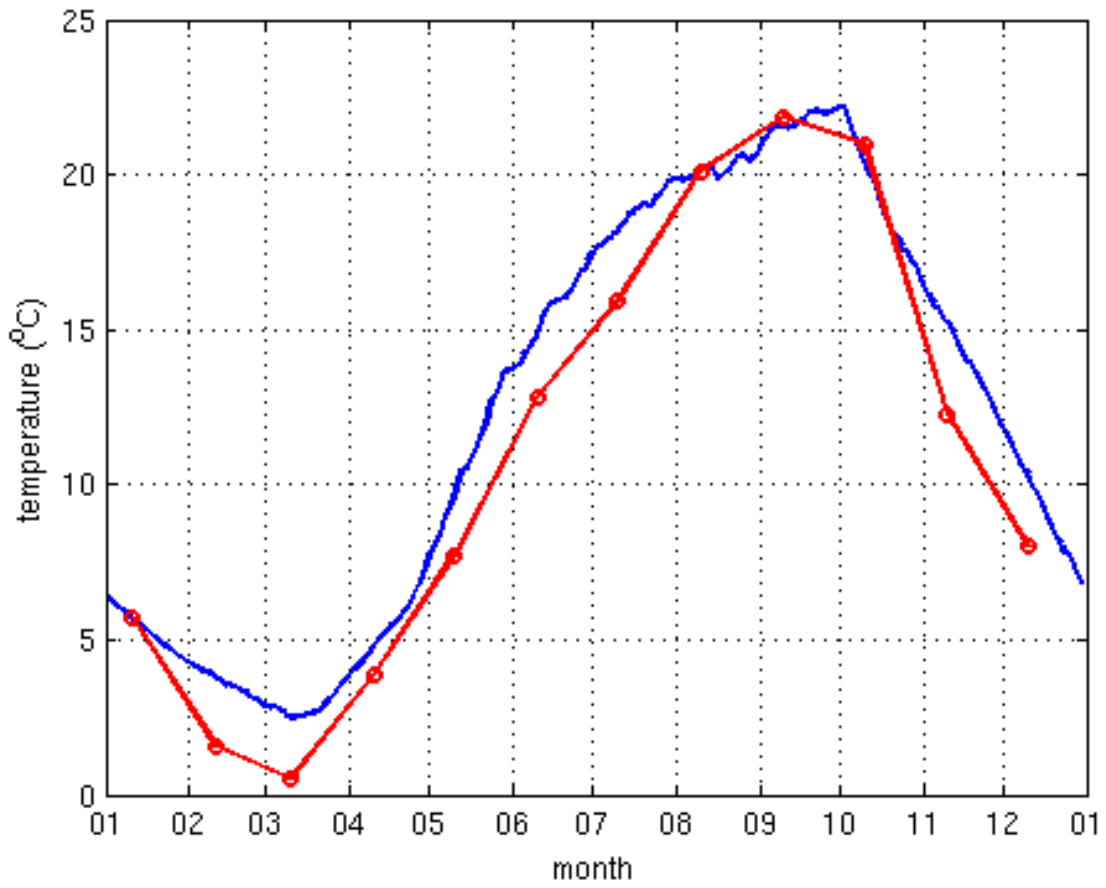


Figure 2-3. (d) Observed temperature below thermocline (red) versus model simulation (blue) in 2008.

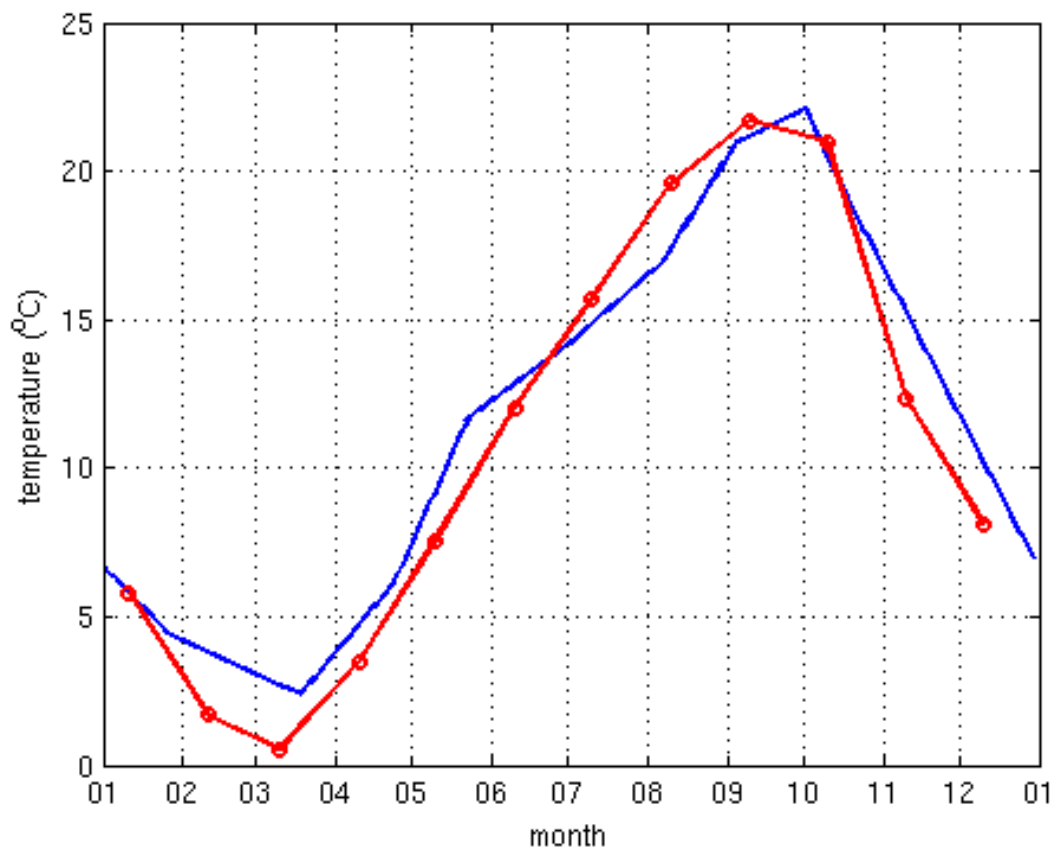


Figure 2-3. (e) Observed bottom temperature (red) compared to model simulation (blue) in 2008.

Modeled sea surface salinity (SSS) decreased from beginning of the year to reach the minimum level of 24 g/kg by the end of April (Figure 2-4a). Then it increased almost linearly to 26.25 g/kg toward early July. After that there was a small decrease to 26.15 g/kg by early August and then it increased again to reach the maximum at 26.5 g/kg by the end of September. Thereafter, the salinity kept decreasing and went below 26 g/kg by the end of the year. Modeled vertical structure of salinity differed from temperature in several aspects (Figure 2-4a). The maximum salinity difference between the surface and bottom was 1 g/kg in February, while temperature difference was 8°C. The salinity profile started to become stratified from late January, whereas thermocline started to develop from late April. The haline stratification became most intensified in February when the salinity difference between the surface and bottom was maximum. Afterwards salinity distribution became more uniform throughout the entire water column until mid-April when it began to re-stratify with relatively smaller vertical gradients, which coincided with the lower salinity value (i.e., below 25.5 g/kg). The modeled vertical salinity gradient increased as the fall season approached, i.e., the salinity difference between the surface and bottom reached 0.5 g/kg. In general, the simulated salinity variability agreed with the observations (Figure 2-4b).

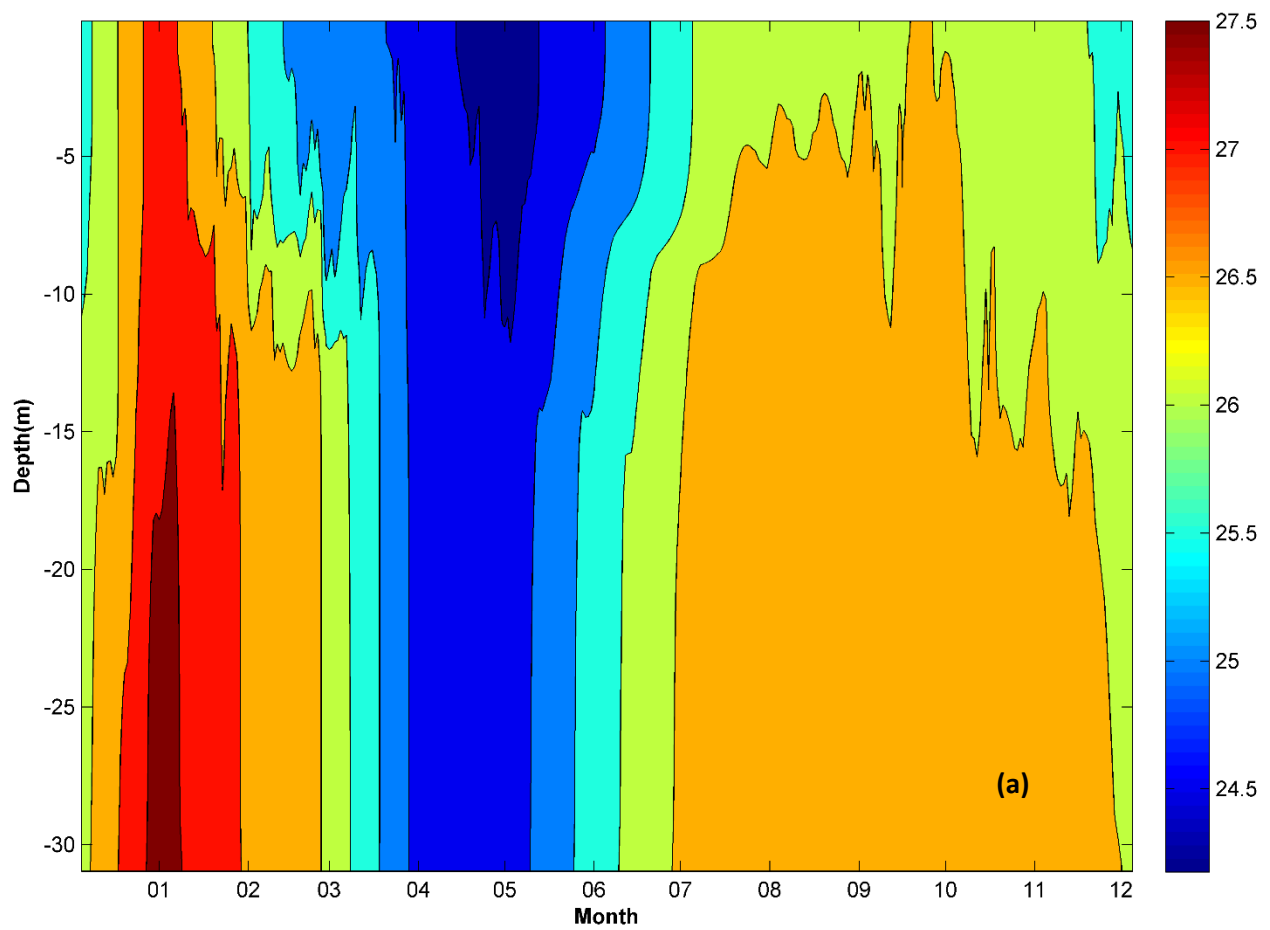


Figure 2-4. (a) Simulated seasonal variability of salinity profile (g/kg).

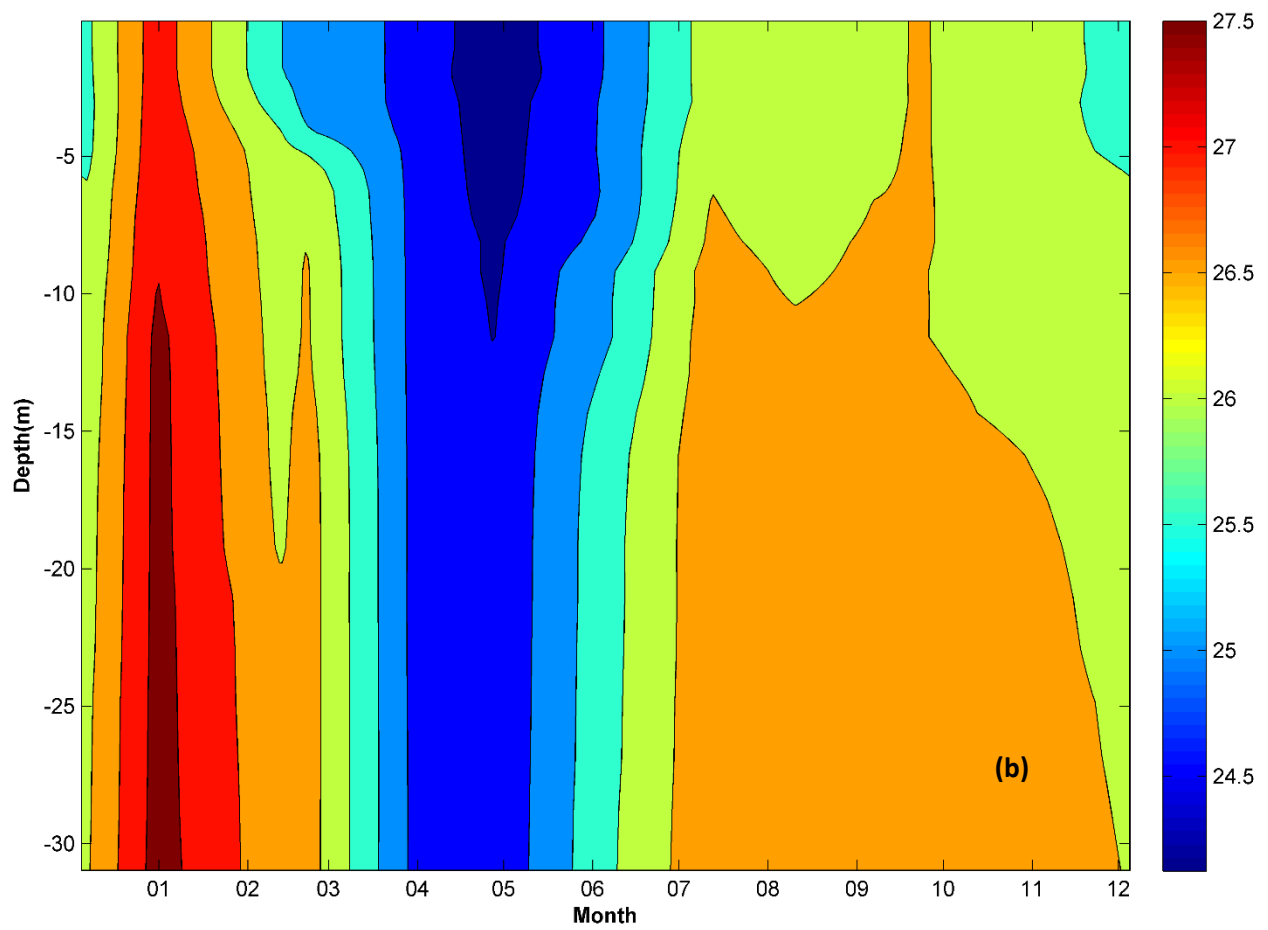


Figure 2-4. (b) Observations of vertical salinity structure (g/kg).

Modeled seasonal evolution of density structure was variable and characterized by periodic fluctuations in isopycnal distributions (i.e., with periods from two weeks to a month) (Figure 2-5), which had been previously observed in the Sound by Swanson et al. (2008). Density stratification persisted throughout the summer until early September. Between April and September, the depth of the 1018 kg m^{-3} isopycnal decreased from 14 to 7 m, below which waters were well mixed. Density stratification decreased and waters became mixed again from October through December.

The profiles of the Brunt Vaisala frequency N^2 during winter (Figure 2-6 (a)) and summer (Figure 2-6 (b)) are compared separately to the observations. The modeled N^2 agrees with the observations in terms of both magnitudes and depths of high frequency (i.e., approximately 15 m). The maximum frequency is 1.5 times higher during summer than in winter, implying stronger stratification of water column structure during summer. Richardson number is more controlled by brunt vaisala frequency in winter (Figure 2-7 (a)) due to smaller shear. In summer, the number (Figure 2-7 (b)) is dominated by vertical shear and the amplitude is approximately half of that in winter.

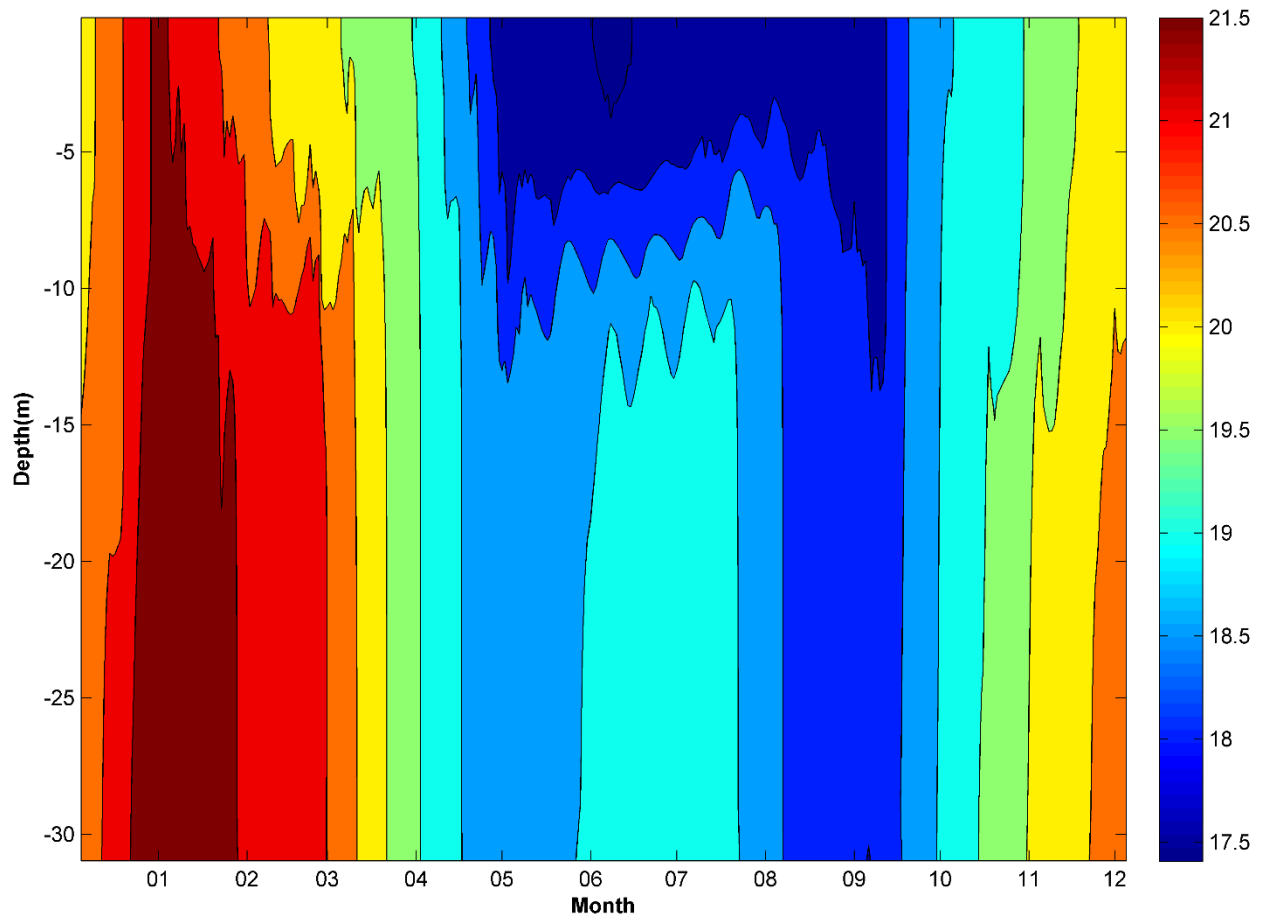


Figure 2-5. Simulated seasonal variability of the density profile (kg m^{-3}).

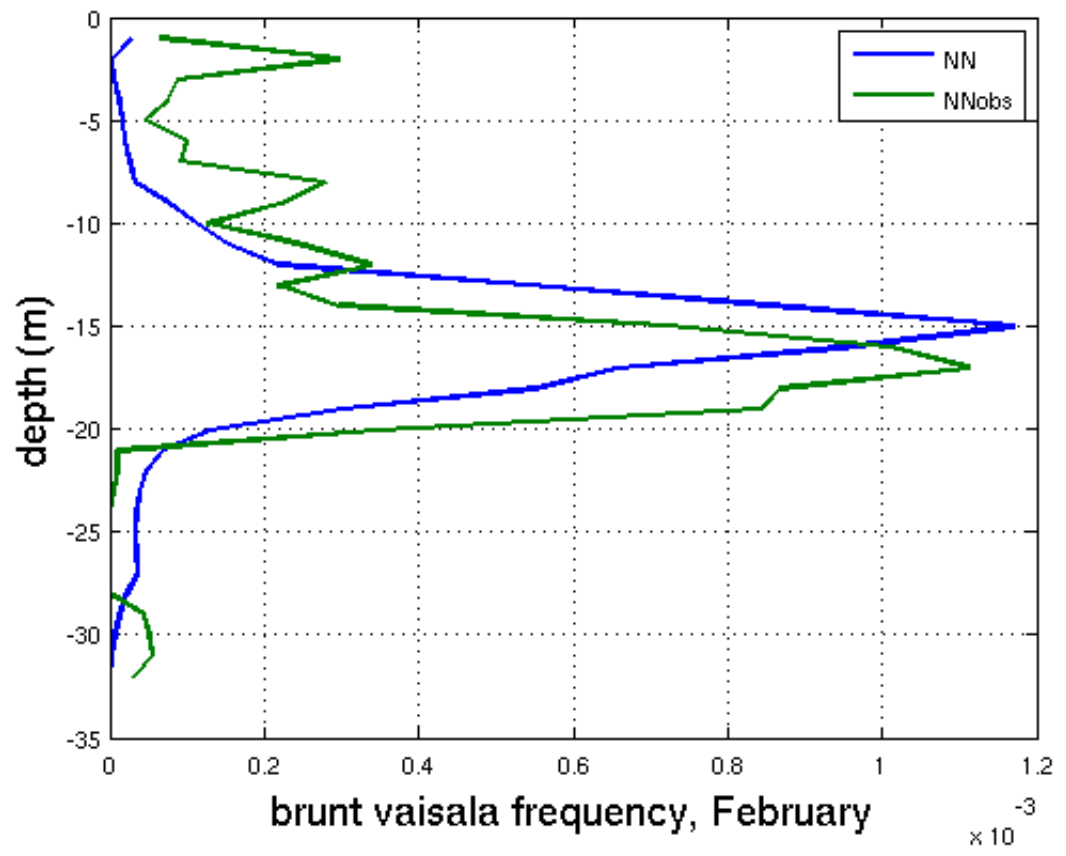


Figure 2-6 (a). Brunt Vaisala frequency profile in February.

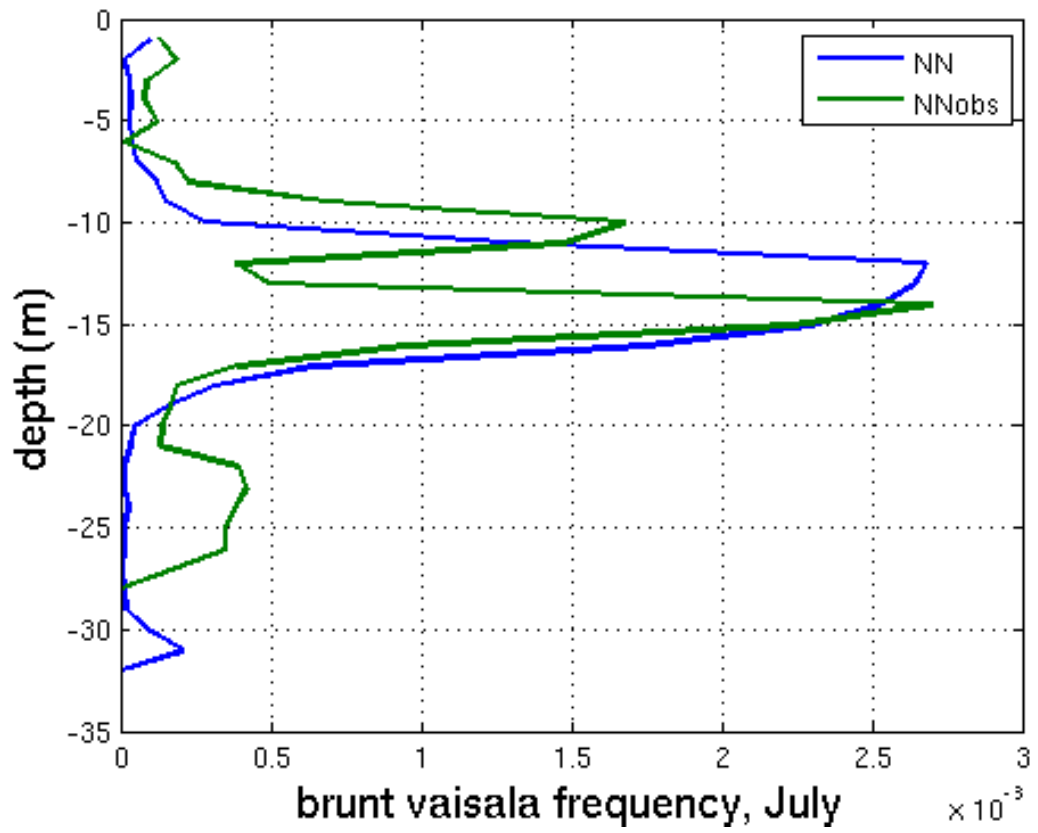


Figure 2-6 (b). Brunt Vaisala frequency profile in July.

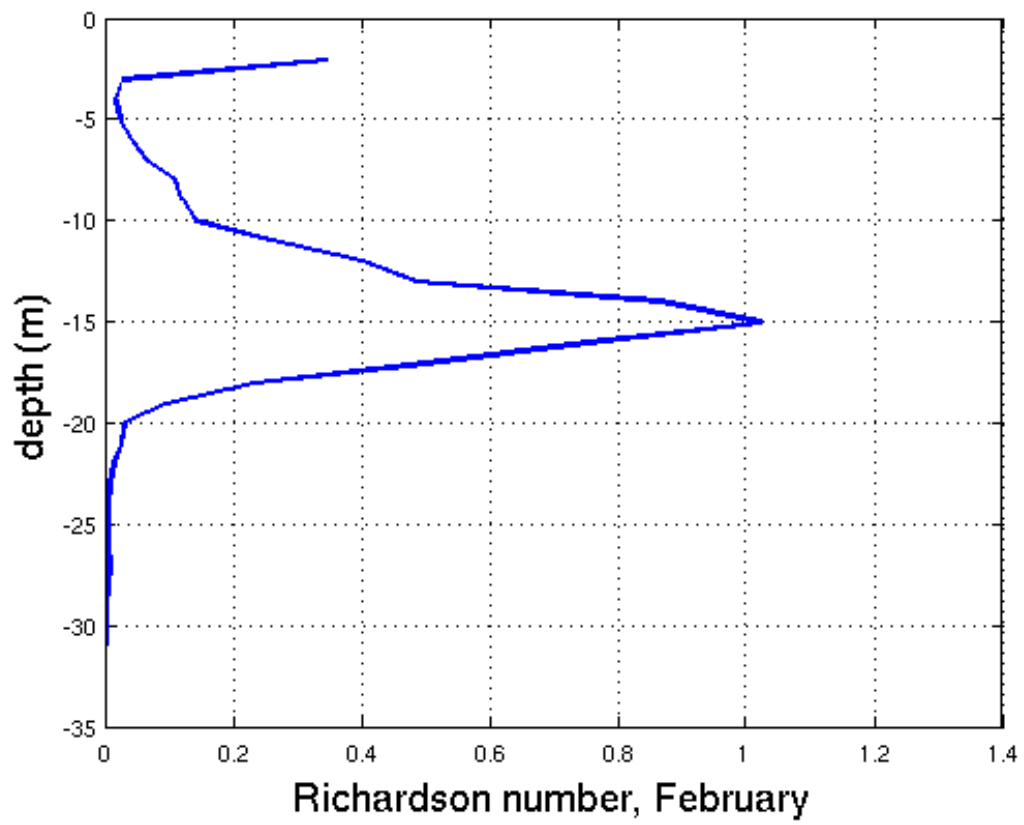


Figure 2-7 (a). Richardson number profile in February.

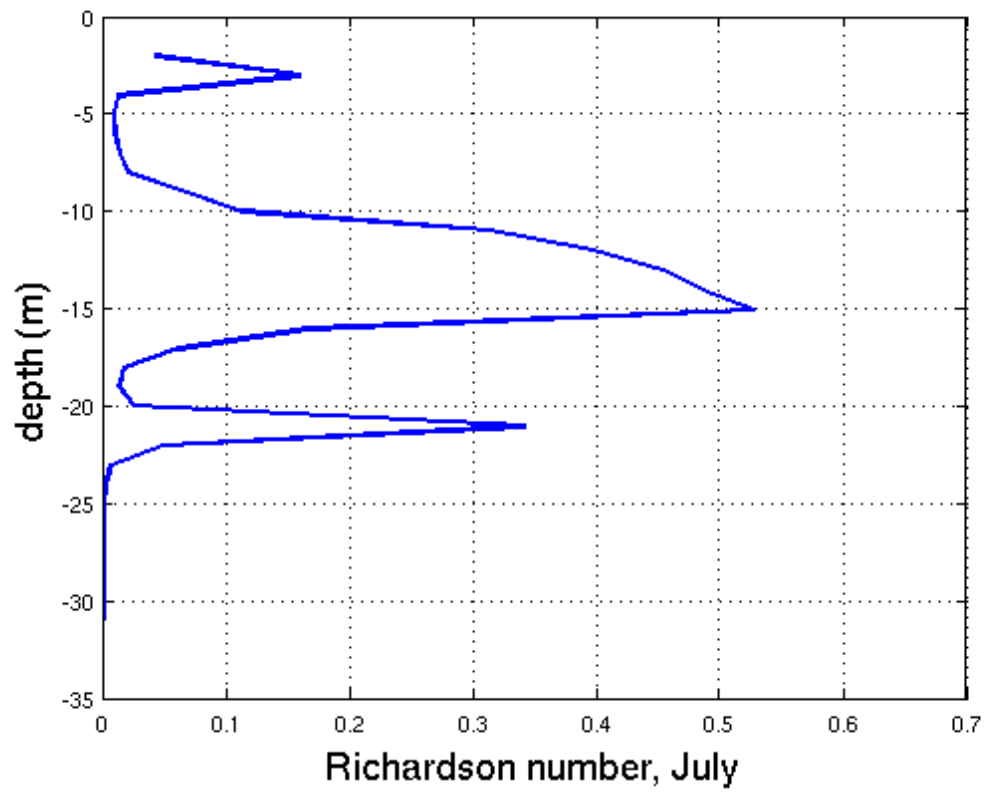


Figure 2-7 (b). Richardson number profile in July.

2.4.2 Sensitivity test of minimum k_v with respect to temperature

Physical sensitivity test of minimum k_v with respect to temperature has been done by demonstrating the statistics (i.e., RMSE and bias) on the Target diagrams. Target diagram (Taylor, 2001) is a diagram combining a set of model skill metrics (e.g., standard deviation, correlation coefficient) in one single plot (e.g., polar plot) to examine relationships between statistical properties. Target diagram includes the information about the relationship between the bias on the x-axis and the Root Mean Square Difference (RMSD) on the y-axis.

The sensitivity analysis from the Target diagram (Figure 2-8) shows that the proper k_{min} for temperature is $k_{min} = 8 \times 10^{-4}$. The smallest RMSE (x-axis) and bias (y-axis) are obtained when k_{min} was at that value. Plots of seasonal variability of temperature profiles associated with multiple k_{min} also demonstrate the best consistency with the observed temperature (Figure 2-9) as $k_{min} = 8 \times 10^{-4}$.

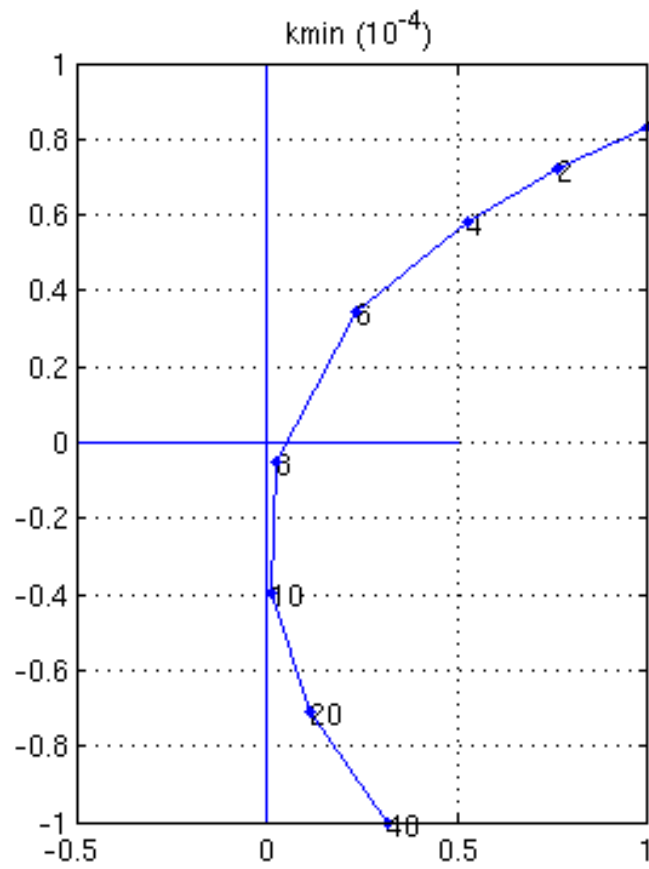


Figure 2-8. Target diagram of sensitivity test of K_{min} with respect to water temperature. X-axis shows the bias and y-axis indicates RMSE.

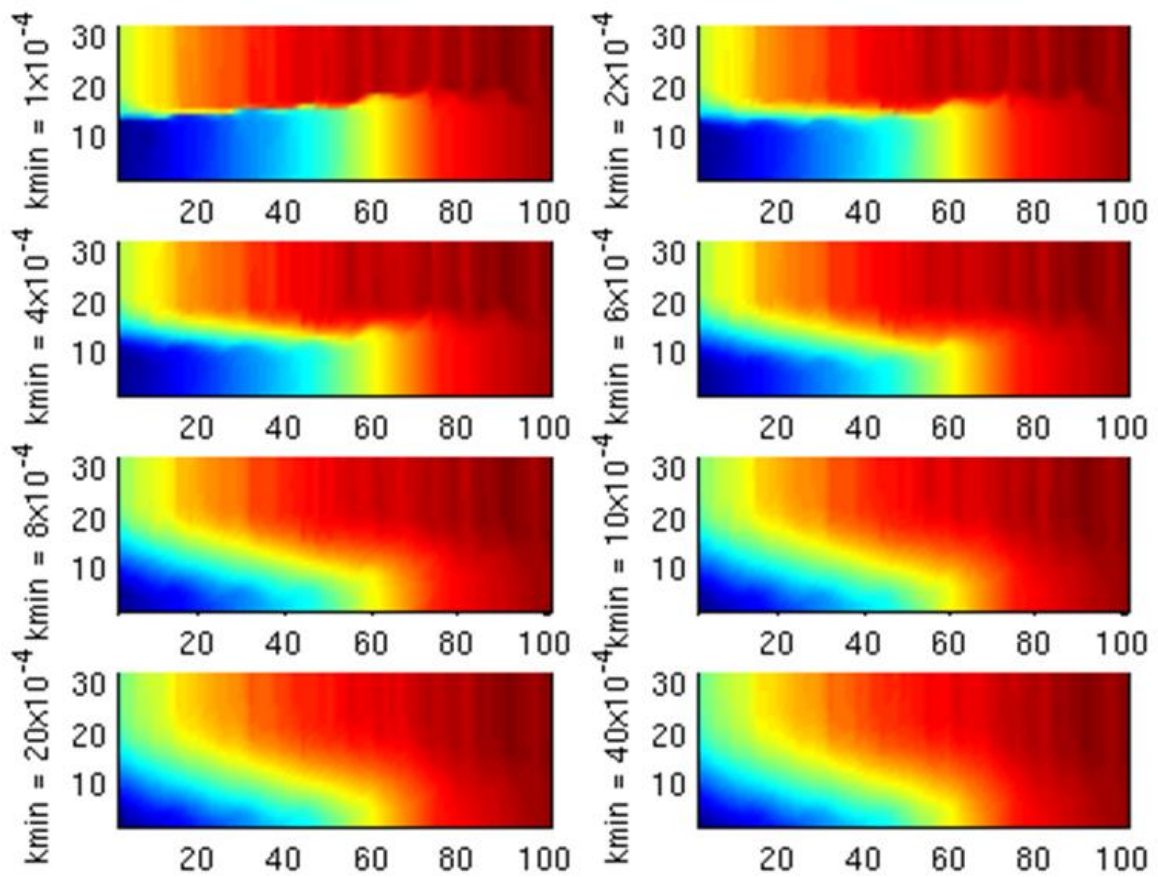


Figure 2-9. Seasonal variability of temperature profiles associated with multiple k_{min} values shown in the Target diagram by Figure 2-8

2.4.3 Seasonal variability in simulated bacterial biomass

Seasonal variations in modeled bacterial biomass density (defined to be the amount of bacterial biomass per unit volume) near the surface versus observations was shown by Figure 2-10 (a). Modeled bacterial surface biomass density was $0.25 \text{ mmol N m}^{-3}$ in early January, and increased slightly to $0.34 \text{ mmol N m}^{-3}$ in February. After a negligible drop to $0.3 \text{ mmol N m}^{-3}$ in March, biomass density gradually exceeded 1 mmol N m^{-3} in April, maintaining similar fluctuating levels throughout May, and increased linearly to $2.75 \text{ mmol N m}^{-3}$ in July. Thereafter, the biomass density declined to 2 mmol N m^{-3} in late August, then decreased gradually to $0.45 \text{ mmol N m}^{-3}$ by December. The modeled annual cycle of surface bacterial biomass captured the major variability and inventories of the observations (Figure 2-10 (a)). The seasonal variation in bacterial biomass density profile showed that between January and March concentrations within the entire water column were consistently below $0.7 \text{ mmol N m}^{-3}$ (Figure 2-10 (b)). Simulated density for the whole water column gradually increased from $0.7 \text{ mmol N m}^{-3}$ to above 1 mmol N m^{-3} from April until May. The density reached a maximum value of approximately 3 mmol N m^{-3} within the top 5 m in July and August, below which they decreased with depth to approximately $1.3 \text{ mmol N m}^{-3}$. From September onwards bacterial biomass density became uniform through the entire water column, and decreased quickly to values below $0.5 \text{ mmol N m}^{-3}$ by the end of October and remained constant until early December.

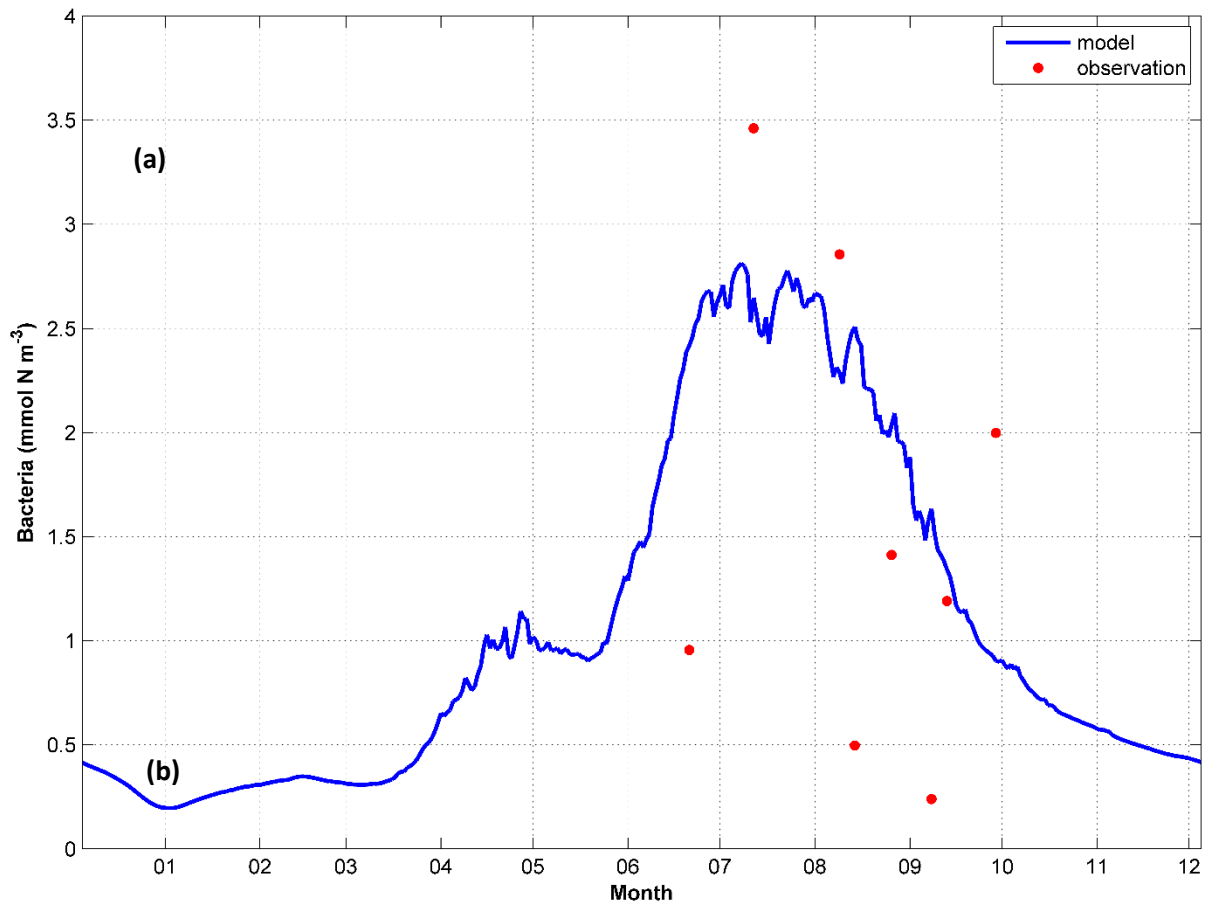


Figure 2-10 (a) Simulated seasonal evolution of surface bacteria compared to the observations.

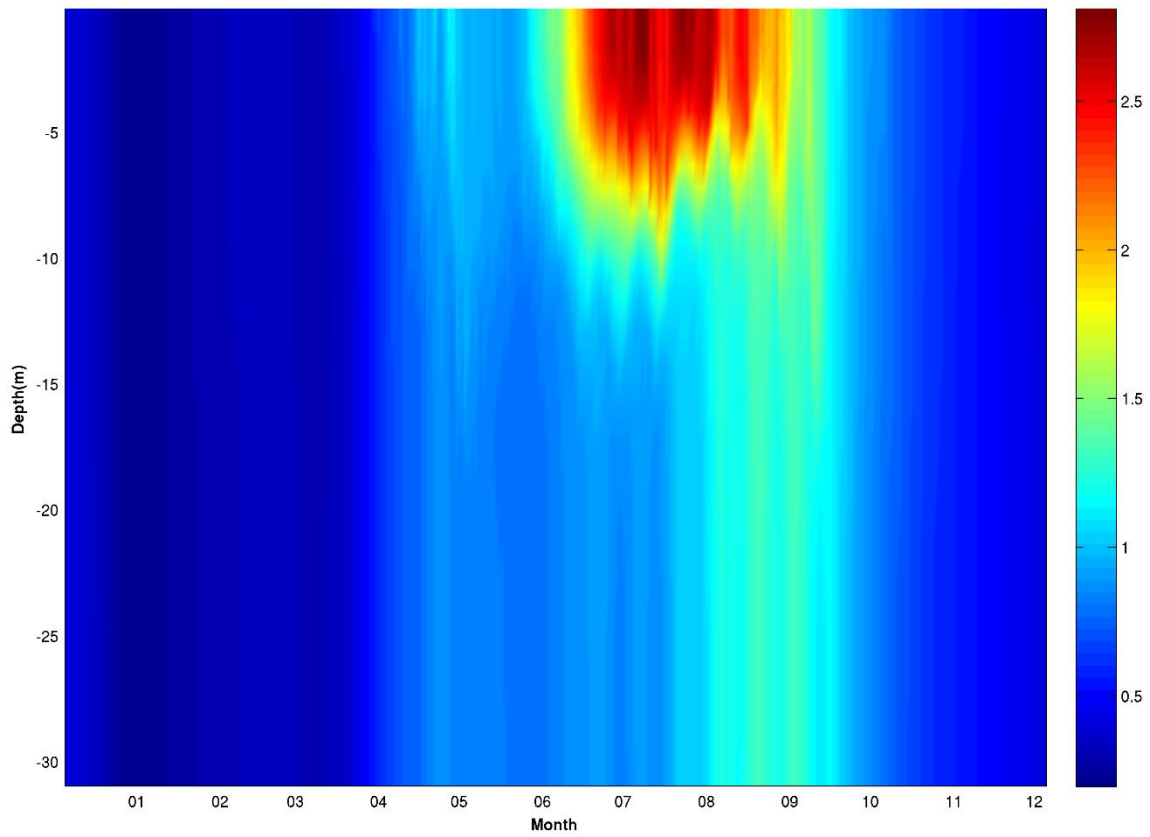


Figure 2-10 (b) Simulated seasonal variation of bacterial profile (mmol N m^{-3}).

2.4.3 Seasonal variability in DO concentration from the bacterial dynamics-included model

Inclusion of bacterial dynamics produced a simulated annual cycle of bottom DO concentrations that generally agrees with observations (Figure 2-11 (a)). Modeled bottom DO maintained relatively high levels (i.e., approximately 10.5 mg/l) from January to early April. After that concentrations decreased linearly at the rate of approximately 3 mg/l per month. Based on the 3 mg/l threshold for hypoxia (Diaz et al. 1995; NYSDEC 2000; Ritter et al. 1999), the bottom water became hypoxic in late June, which was consistent with timing of hypoxia reported by NYSDEC (2000). The concentration further decreased and reached its minimum of 0.1 mg/l in mid-August, but soon afterward the bottom water started to oxygenate and recover from hypoxia in the middle of September. The model's DO recovery rate was overestimated by 12% during the second half of September. But after September, model results agreed with the observations on recovery rate (Figure 2-11 (a)). Modeled vertical distribution of DO as it evolves with time was shown in Figure 2-11 (b). DO concentrations were high (approximately 11 mg/l) from January to May throughout the entire water column, after which the vertical DO structure became stratified, and the water column below 5 m quickly became hypoxic. DO levels in the water column between 5 and 10 m oscillated in and out of hypoxia on a weekly basis. This was consistent with the synoptic scale DO fluctuations as previously observed in the field by Anderson and Taylor (2001) and O'Donnell (2008). The water column below 10 m water depth was hypoxic throughout the whole summer until early September, after which it started to recover as the vertical DO gradient started to decrease.

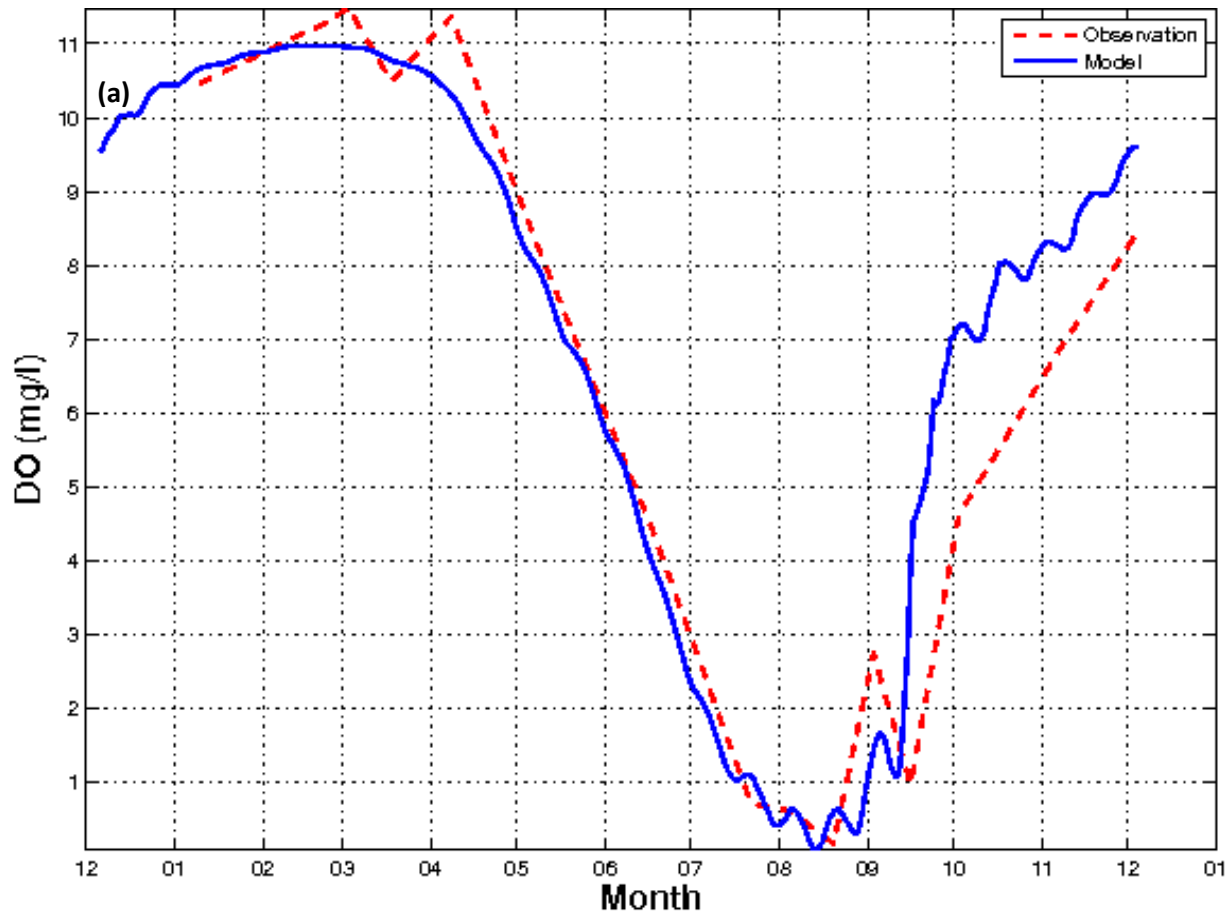


Figure 2-11 (a) Simulated Dissolved Oxygen (DO) variability with daily frequency produced by the model with hyperbolic control on bacterial growth rate in comparison to the observations.

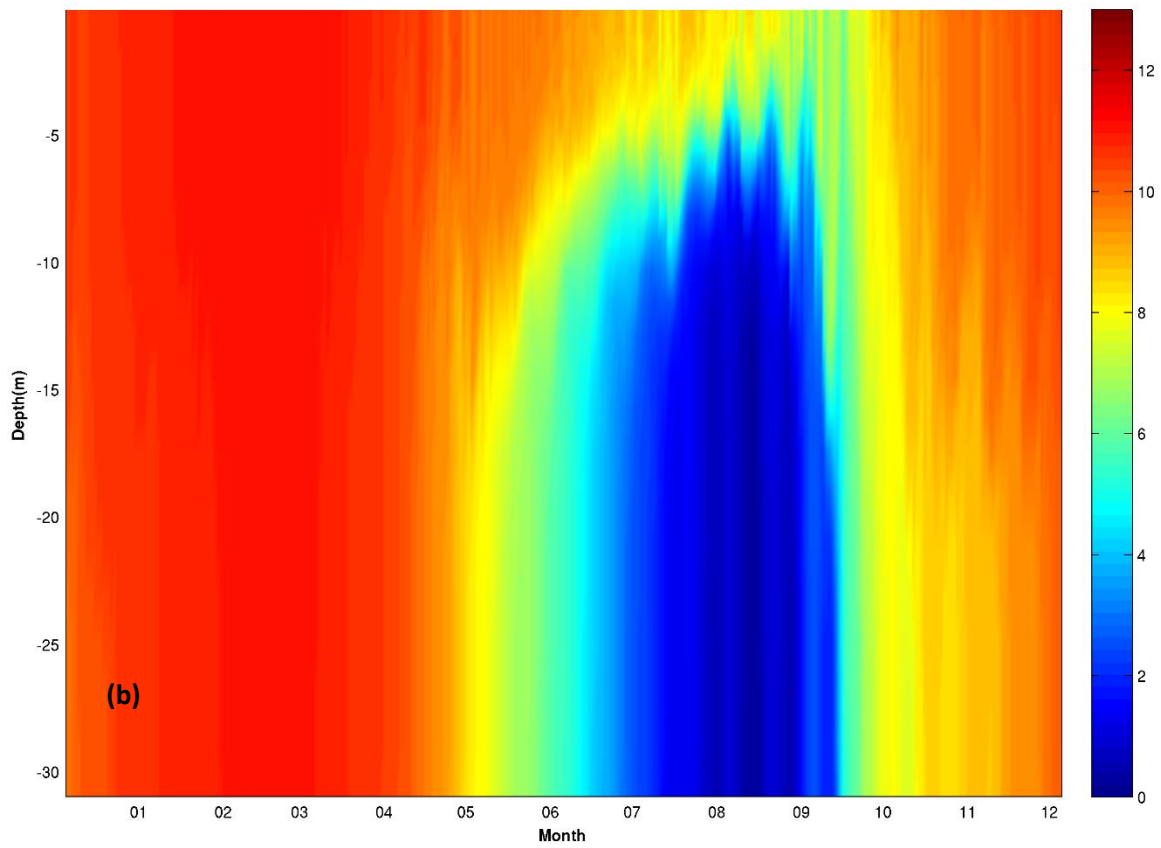


Figure 2-11 (b) Simulated seasonal variability of DO profile produced by the model with hyperbolic control on bacterial growth rates (mg/L).

To compare with DO variability produced by the model with hyperbolic thermal control on bacterial growth rate (Figure 2-11), the bottom DO dynamics from the model with Q_{10} function-controlled bacterial growth rate was shown in Figure 2-12. Observations showed that bottom waters became hypoxic (i.e., DO below 3 mg/l) in early July, whereas simulated DO became hypoxic in late July. Instead of reaching the minimum in the middle of August as observed in the field, minimum simulated DO occurred at the end of the month. Therefore, compared to observations there was a half-month delay of the simulated hypoxia associated with the Q_{10} function-controlled bacterial growth rate.

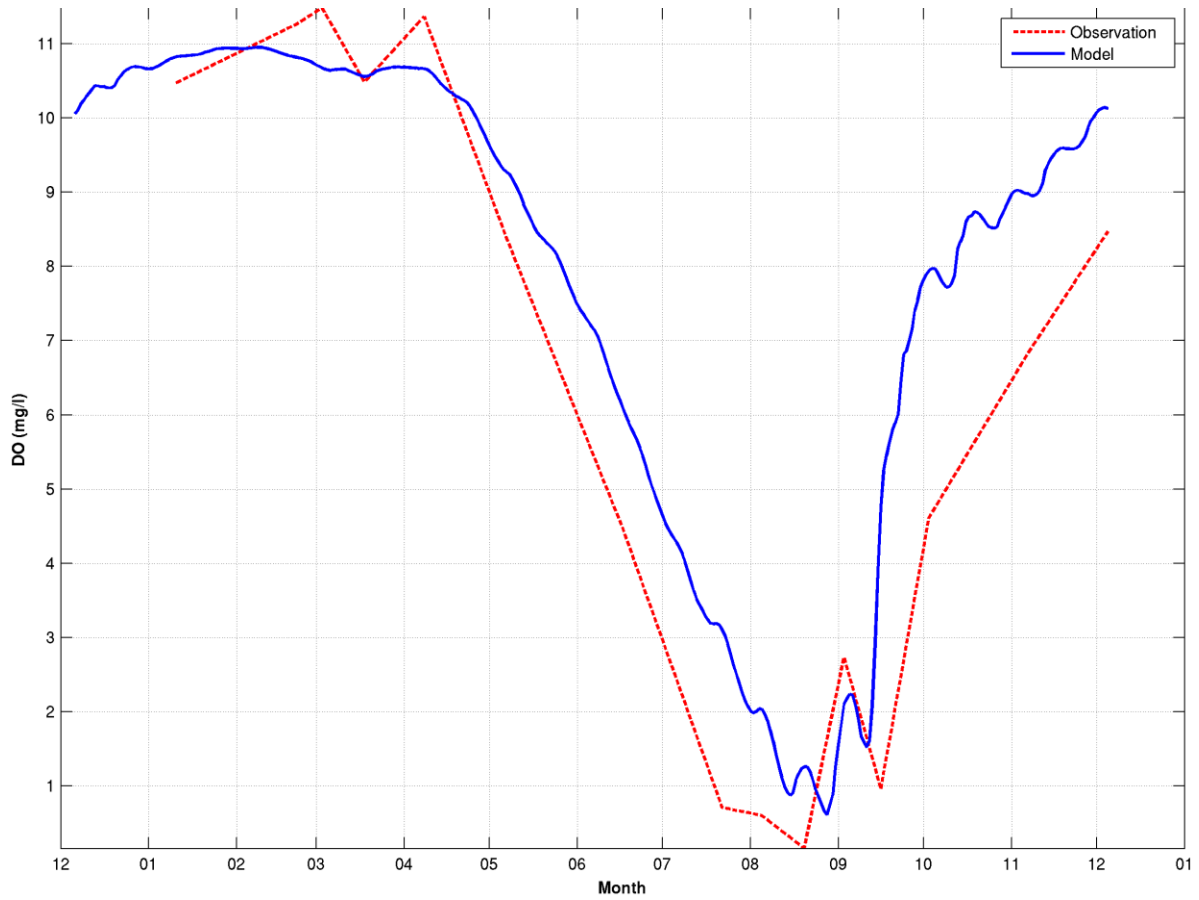


Figure 2-12. Simulated bottom DO produced by the model with Q_{10} control on bacterial growth rate in comparison to the observations (mg/l) in 2008.

2.4.4 DO variability from the bacterial dynamics-excluded model

The original ERGOM (without bacterial dynamics) produced DO variability shown in Figure 2-13. Bottom DO before May was close to 11 mg/l (Figure 2-13 (a)). From mid-April on, DO started decreasing at a rate of 1.6 mg/l per month until mid-August, when reaching its lowest value of 4 mg/l. This concentration (4 mg/l) was approximately 20 times higher than the minimum concentration of the observed DO (i.e., 0.2 mg/l). The modeled DO tendency, defined as $\frac{\partial DO}{\partial t}$ of -1.6 mg/l per month during this period was only half of the observed tendency (i.e., -3 mg/l per month). After that DO started to increase at the rate of 3 mg/l per month to the end of September. From October onwards, DO tendency decelerated to 0.75 mg/l per month. Between January and mid-April, DO simulated by the original model without bacterial dynamics was very close to the observations (Figure 2-13a). The DO profiles shown in Figure 2-13 (b) indicate high DO (i.e., approximately 11 mg/l) from January to early May throughout the water column, after which the profiles became slightly stratified. The bottom water never became hypoxic. The ratio of bottom DO from the bacterial dynamics-excluded model to the output from the bacterial dynamics-included model shown in Figure 2-13 (c) is close to 1 before early June, and then it started to increase to approximately 7 in late August. It decreased to 0.6 by early November, and then it returned to near 1 by mid-December.

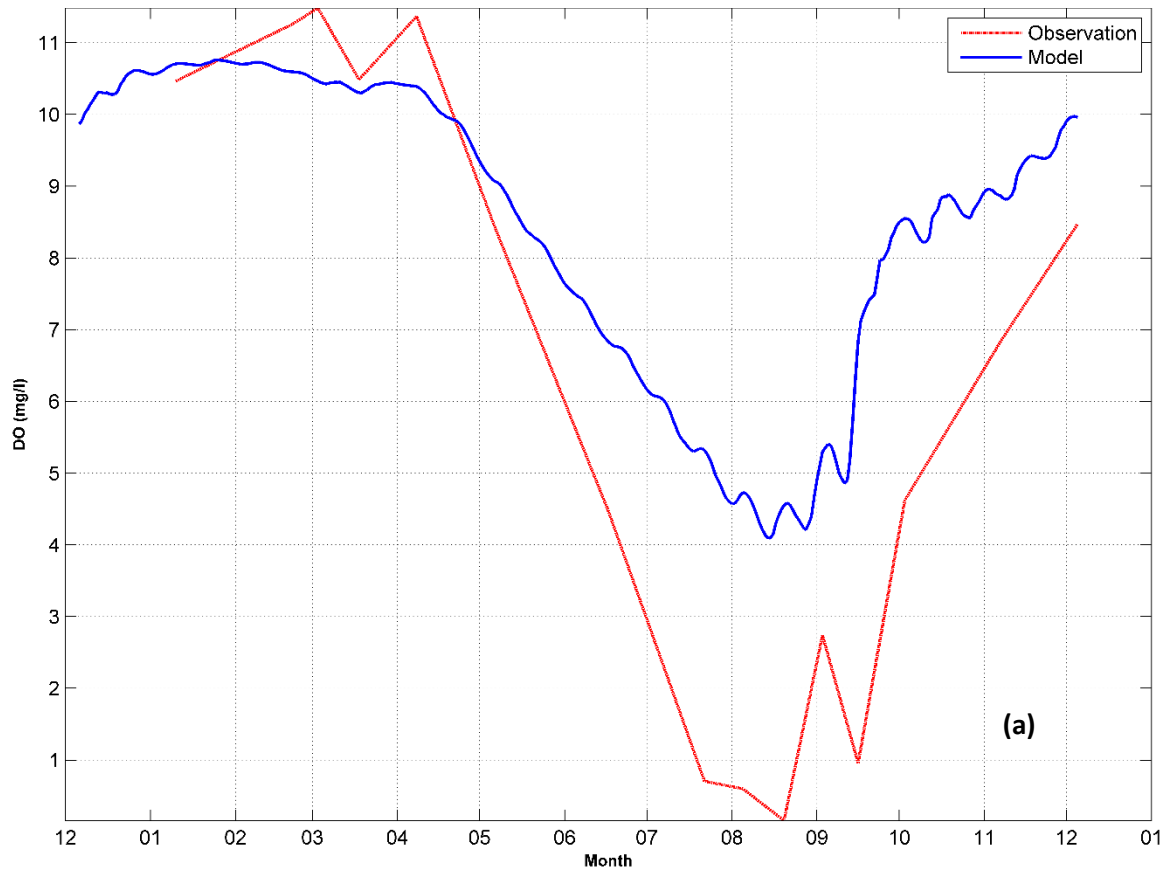


Figure 2-13. (a) Simulated bottom DO concentration from the original model without microbial loop compared to observations in 2008.

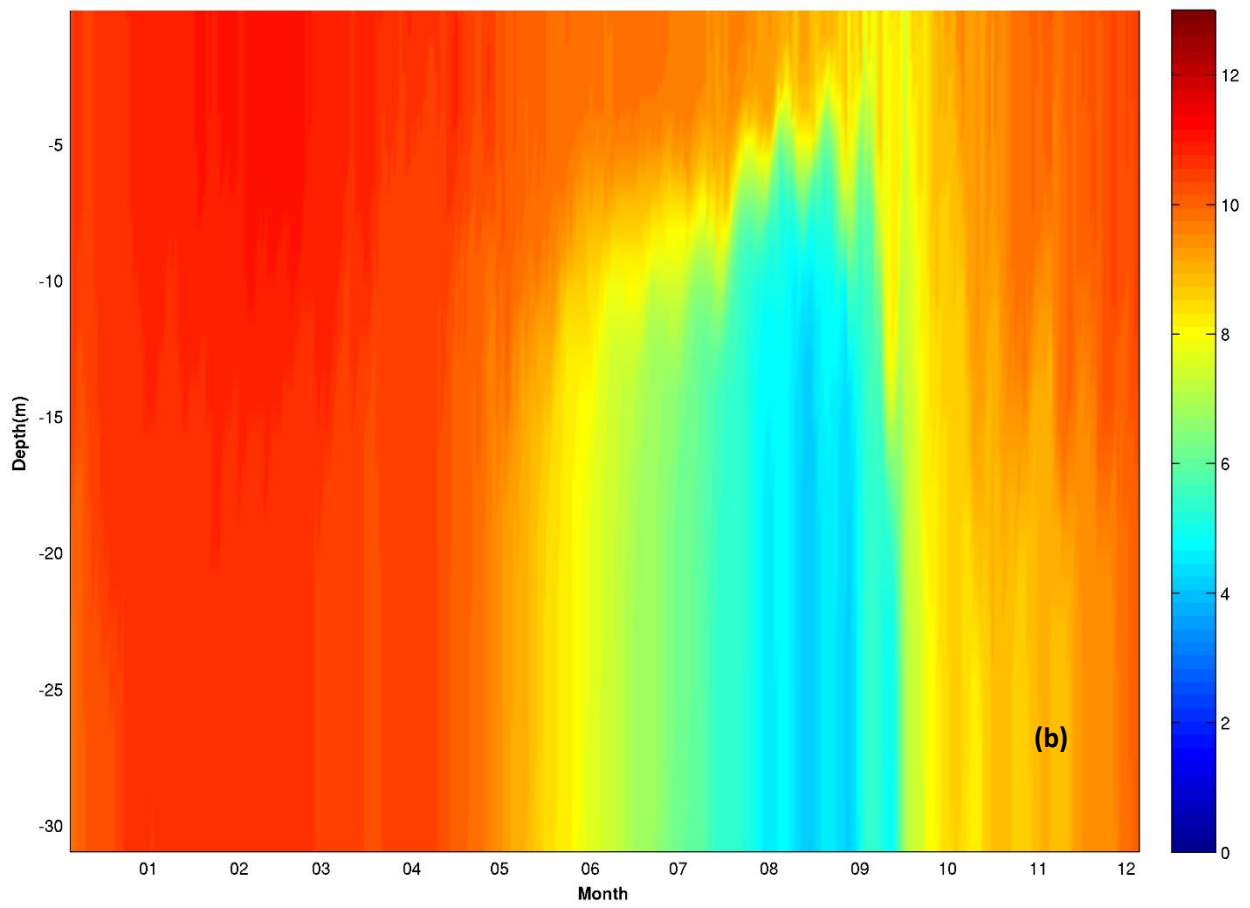


Figure 2-13. (b) Simulated seasonal variability of DO profile from the original model without bacterial activity (mg/L).

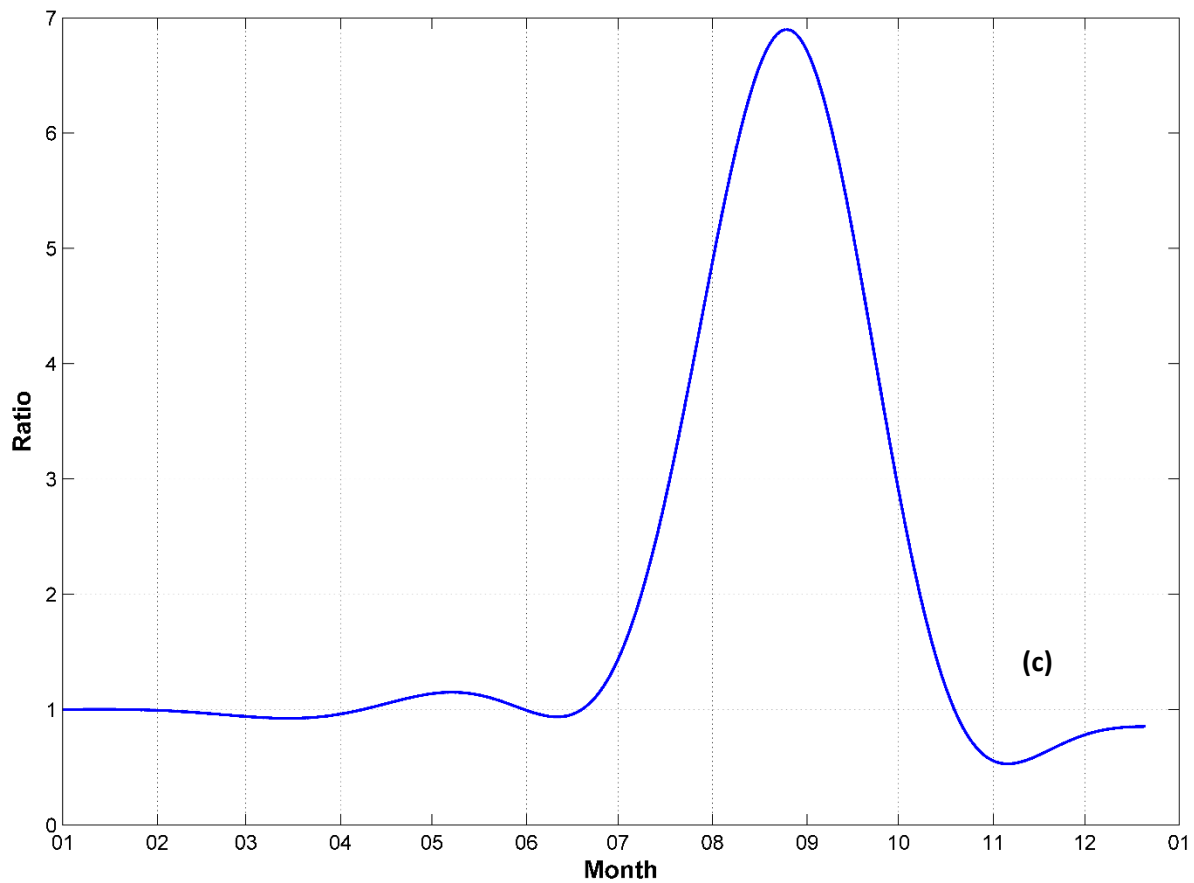


Figure 2-13. (c) Ratio of the bottom DO from the original model without microbial loop over the bottom DO from the model with microbial loop.

2.5 Discussion

2.5.1 Water column properties

Previous studies in western LIS indicated that variations in salinity were controlled by seasonal cycles of freshwater input from the East, Harlem, Connecticut and Hudson Rivers (Lee and Lwiza 2005), tidal and wind mixing, exchange with the ocean and balance between precipitation and evaporation (Lee and Lwiza 2005; O'Donnell et al. 2013; Whitney 2010). Our 1-D model accurately reproduced major variability in observed salinity, and provided reasonable representation of water column structure for DO simulation. Simulated salinity was approximately 3% lower than the observations between 5-10 m in February, whereas in July and August at the same depth the simulation exceeded the observations by only 2%. This difference was small, and most probably was caused by strong wind mixing at the air-sea interface in February and March, as well as increased tidal mixing during July and August in the model.

Welsh and Eller (1991) argued that density stratification from observations was mostly dominated by temperature in LIS. Another modeling study in LIS by Crowley (2005) showed that in 1988 the density stratification was controlled by temperature in spring, but in summer both temperature and salinity controlled stratification in western LIS. Our results showed that in winter and spring of 2008, the density structure was more dominated by salinity than temperature, whereas during that summer it was more driven by temperature (Figure 2-5).

Therefore, the control factor of the water column structure in 2008 changed with season.

O'Donnell et al. (2013) found that the onset of density stratification at A4 occurred in February, intensified in April and reached a maximum in July. Our results supported the previous study because they showed similar timing of initial stratification. The intensified stratification occurred in May, and reached the maximum at the end of July.

2.5.2 Seasonal variability in bacterial biomass

Our model was successful in estimating bacterial biomass variability accurately, and results were consistent with previous observational studies (Anderson and Taylor 2001; Capriulo et al. 2002; Larsson and Hagstrom 1982; Suter et al. 2014). For example, Anderson and Taylor (2001) found that the surface bacterial biomass increased from July through most of August in 1992 and 1993, similar to our result for the evolution of temperature during the same period in 2008. Capriulo et al. (2002) observed that bacterial abundances varied from winter lows to typical summer highs in both surface and bottom waters in the western LIS stations. To obtain correct seasonal cycle of bacterial biomass in the model, both temperature and substrate control of bacterial growth were included following the modeling studies on bacterial activity by Hall et al. (2008). Fasham et al. (1990) applied a constant maximum bacterial growth rate in their model. However, based on observations, Hall et al. (2008) showed that the growth rate is a positive-saturating function of temperature, which agrees with the fact that bacterial production peaks in summer. Our model thus included a hyperbolic saturating function in the temperature control on bacterial growth to better simulate seasonal bacterial variability. The modeled bacterial biomass with both temperature and substrate control exhibited a similar range as the observations (Figure 2-10a).

2.5.3. The importance of bacterial dynamics in simulating seasonal hypoxia

The fact that the ratio of bottom DO from the bacterial dynamics-excluded model over the bacterial dynamics-included model shown in Figure 2-13 (c) in summer increased 7-fold in summer compared to non-summer seasons suggested that bacterial activity profoundly reduced bottom DO during summer. Our analysis of DO dynamics demonstrated that bacterial decomposition of organic matter into inorganic form is the leading mechanism that controls DO consumption rate, compared to sedimentary decomposition and surface flux of DO. The added

bacterial dynamics that intensifies during summer effectively increases summer DO consumption rates by 37%, and thus reduces DO to a much lower level, which could not be achieved in the model excluding bacterial dynamics. We also posit that the inclusion of bacterial dynamics modifies the lability of dissolved organic matter (DOM) during early summer, which causes a delay in nutrient release. Reduced lability acts as ‘capacitor’ of nutrients to be used by phytoplankton in later part of summer so that more DO will be consumed through DOM remineralization.

These findings explain why it is so difficult to obtain a reasonable representation of hypoxia seasonal variability without distorting the vertical mixing or phytoplankton respiration in SWEM, RCA, ChesROMS, etc. Strong vertical mixing may significantly influence the variability of near bottom DO levels (McCardell and O'Donnell 2009; O'Donnell 2008), but microbial activity is clearly a critical control factor, which cannot be ignored for accurate prediction of bottom DO variability.

2.5.4 Comparison of DO variability produced by hyperbolic and Q10 thermal controls of bacterial metabolism

We have shown in Section 2.4.3 that there was a half-month delay of the simulated hypoxia from the model with bacterial growth rate controlled by the Q10 function. This is because the Q10 function over-emphasizes the importance of temperature in controlling bacterial growth compared to the hyperbolic temperature formulation. Therefore, bacterial growth rate under Q10 control reached the maximum at the end of August when temperature peaked. This led to a minimum bottom DO concentration in early September. However, the observed DO

concentration reached the minimum in the middle of August. As a result, DO concentrations fell below 3 mg/L at the end of July, whereas in observations this occurred one month earlier.

Therefore, with Q10-controlled bacterial growth rate, hypoxia onset is delayed by at least two weeks. The hyperbolic temperature control, on the other hand, allows for linear and gradual change of bacterial growth and as a result produces better control on DO variability.

Our interpretation of the observed departure from the classic Q10 thermal response is that our model is describing the integrated response of an ever-changing assemblage of different populations in an open ecosystem through an annual cycle. Each population is likely to have its own Q10-like response, but manifested by different thermal thresholds and optima that are favored during specific seasons. For example, winter assemblages are likely dominated by psychrotolerant (“cold tolerant”) and psychrophilic (“cold loving”) populations which are then displaced by more mesophilic (“warm loving”) populations as water temperatures warm in spring and summer. Alternatively, resident populations may possess multiple isozymes that are up-regulated or down-regulated in response to their favored temperature and thereby optimize fitness over a broad temperature range and not exhibit a Q10 response (Panigrahi et al. 2013). Even with thermal selection and adaptation, maximal bacterial metabolism of the entire assemblage will necessarily be lower at winter temperatures than during summer simply because of thermodynamic constraints. Since we are modeling an open system with structurally-complex bacterial assemblages, it is likely that those populations best adapted to current temperature-nutrient conditions will be more fit and dominate until selective pressures change. Consequently, there may be no consensus Q10 response that adequately represents a temporally-varying assemblage of diverse microbial populations in this ecosystem.

2.5.5 Missing mechanisms in the model

We want to acknowledge that the model with a sophisticated microbial loop should disaggregate zooplankton into compartments based on their body sizes with different feeding profiles, taxonomic characteristics or turnover times although there might not be fundamental distinctions between these compartments (Christian 1994; Ducklow 1994). Ducklow's, (1994) microbial loop model grouped bacteria into attached and free-living bacteria, and it is the attached bacteria that decompose detritus. Instead of protozoan, he found that the mucus-net feeders (e.g., appendicularians) are major grazers of bacteria. In addition, some detritus might be directly consumed by grazing zooplankton instead of being attached and decomposed by bacteria, and so on so forth. Therefore, linkage among detrital pathways, zooplankton food webs and microbial activity are more complicated than what current biogeochemical models have considered. Therefore, the ultimate goal is to model microbial loop by explicitly including bacterial diversity, disaggregation of zooplankton, parameterization of grazing, viral parasite processes, and other relevant microbial processes. Challenges to this endeavor include knowledge gap of the microbiology, lack of field observations to support model parameterization and validation. However, it is encouraging to note that the simple bacterial dynamics we used to represent microbial loop in our model reproduced DO dynamics with high fidelity, which means that the major drivers of microbial loop have been included for the purpose of accurately modeling DO variability.

2.6 Conclusions

This chapter emphasizes that bacterial dynamics, critical in controlling bottom DO variability and recovery from hypoxia, needs to be correctly parameterized in coastal models. Temperature dependence of metabolism by time-varying bacterial populations is better simulated by a hyperbolic temperature function than a Q10 function. Modification of a biogeochemical model to include bacterial dynamics allowed us to accurately simulate the onset and recovery from hypoxia, which have proved to be elusive in previous studies. We show that eutrophication models, in which phytoplankton biomass is used as a proxy for bacterial biomass in decomposing organic carbon, are bound to produce inaccurate estimation of DO consumption. Vertical mixing does not have to be artificially manipulated, if the bacterial dynamics is included. Accurate DO simulation requires inclusion of bacterial dynamics, which provide important feedbacks to total planktonic community processes.

References

- Anderson, T. H., 1995. Pelagic microbial processes influencing hypoxia in western Long Island Sound. M.S. Thesis. State University of New York, Stony Brook, New York.
- Anderson, T. H. and Taylor, G. T., 2001. Nutrient pulses, plankton blooms, and seasonal hypoxia in western Long Island Sound. *Estuaries*. 24(2), 228-243.
- Blumberg, A. F. and Pritchard, D. W., 1997. Estimates of the transport through the East River, New York. *J. Geophys Res-Oceans*. 102(C3), 5685-5703.
- Boon, N. A., 2008. Nutrient Dynamics of Long Island Sound. Master's thesis. Wesleyan University.
- Burchard, H., Bolding, K., Kuhn, W., Meister, A., Newmann, T. and Umlauf, L., 2006. Description of a flexible and extendable physical–biogeochemical model system for the water column. *Journal of Marine Systems*. 61, 180–211.
- Burchard, H. and Bolding, K., 2001. Comparative analysis of four second-moment turbulence closure models for the oceanic mixed layer. *J. Phys. Oceanogr.* 31, 1943–1968.
- Burchard, H., Bolding, K. and Villarreal, M.R., 1999. GOTM-a general ocean turbulence model. Theory, applications and test cases. Tech. Rep. Eur 18745 EN. European Commission.
- Capriulo, G. M., Smith, G., Troy, R., Wikfors, G. H., Pellet, J. and Yarish, C., 2002. The planktonic food web structure of a temperate zone estuary, and its alteration due to eutrophication. *Hydrobiologia*. 475(1), 263-333.
- Crowley, H. A. 2005. The seasonal evolution of thermohaline circulation in Long Island Sound. Ph.D. Thesis. Stony Brook University. Stony Brook, New York, USA.

- CTDEP. 2005. Monitoring Phytoplankton Community Composition in Long Island Sound With HPLC Photopigment Profiles. Connecticut Department of Environmental Protection, Fact Sheet. March, 2005.
- Diaz, R. J. and Rosenberg, R., 1995. Marine benthic hypoxia: A review of its ecological effects and the behavioural responses of benthic macrofauna. *Oceanography and Marine Biology: an Annual Review* 33, 245-303.
- Fasham, M. J. R., Ducklow, H. W. and McKelvie, S. M., 1990. A nitrogen based model of plankton dynamics in the oceanic mixed layer. *J. Mar. Res.*, 48, 591-639.
- Fenchel, T. 2008. Motility of bacteria in sediments. *Aquatic Microbial Ecology*. Vol. 51, 23-30.
- Hall, E. K., Neuhauser, C. and Cotner, J. B., 2008. Toward a mechanistic understanding of how natural bacterial communities respond to changes in temperature in aquatic ecosystems. *International Society for Microbial Ecology*, 2(5), 471-481.
- HydroQual, Inc. 2001. Newtown Creek Water Pollution Control Project East River Water Quality Plan / Task 10.0 System-Wide Eutrophication Model (SWEM) / Sub-Task 10.1 Construct SWEM. , Report prepared for the City of New York, Department of Environmental Protection-New York, New York under subcontract to Greeley and Hansen. 75 pp.
- Hydroqual, Inc. 2003. Presentation to the Long Island Sound Science and Technical Advisory Committee, Stony Brook University, October 23-24, 2003.
- Jahnke, R. A. and Craven, D. B., 1995. Quantifying the Role of Heterotrophic Bacteria in the Carbon-Cycle - a Need for Respiration Rate Measurements. *Limnol. Oceanogr.* 40(2), 436-441.

- Jensen, L. M., Sand-Jensen, K., Marcher, S. and Hansen, M., 1990. Plankton community respiration along a nutrient gradient in a shallow Danish estuary. *Marine Ecology Progress Series*. 61, 75-85.
- Larsson, U. and Hagstrom, A., 1982. Fractionated Phytoplankton Primary Production, Exudate Release and Bacterial Production in a Baltic Eutrophication Gradient. *Mar. Biol.* 67(1), 57-70, doi:Doi 10.1007/Bf00397095.
- Lee, Y. 2009. *Mechanisms Controlling Variability in Long Island Sound*. Stony Brook University.
- Lee, Y. J. and Lwiza, K., 2005. Interannual variability of temperature and salinity in shallow water: Long Island Sound, New York, *J. Geophys. Res-Oceans*. 110(C9), doi:Artn C09022 Doi 10.1029/2004jc002507.
- Lee, Y. J. and Lwiza, K. M. M., 2008. Characteristics of bottom dissolved oxygen in Long Island Sound, New York, *Estuar. Coast Shelf. S.*, 76(2), 187-200, doi:DOI 10.1016/j.ecss.2007.07.001.
- LISS., 2003. LISS Science and Technical Advisory Committee Meeting, Room 132, University of Connecticut - Stamford Campus Wednesday, April 2, 2003
- McCardell, G. and O'Donnell, J., 2009. A novel method for estimating vertical eddy diffusivities using diurnal signals with application to western Long Island Sound, *J. Marine Syst.*, 77(4), 397-408, doi:DOI 10.1016/j.jmarsys.2008.10.011.
- Miladinova, S. and Stips, A., 2010. Sensitivity of oxygen dynamics in the water column of the Baltic Sea to external forcing. *Ocean Sci.* 6, 461–474, 2010.

- Neumann, T., Fennel, W. and Kremp, C., 2002. Experimental simulations with an ecosystem model of the Baltic Sea: A nutrient load reduction experiment. *Global Biogeochemical Cycles*. DOI: 10.1029/2001GB001450
- NYSDEC. 2000. A Total Maximum Daily Load Analysis to Achieve Water Quality Standards for Dissolved Oxygen in Long Island Sound.
- O'Donnell, J., Dam, H. G., Bohlen, W. F., Fitzgerald, W., Gay, P. S., Houk, A. E., Cohen, D. C. and Howard-Strobel M. M., 2008. Intermittent ventilation in the hypoxic zone of western Long Island Sound during the summer of 2004. *Journal of Geophysical Research: Oceans* DOI: 10.1029/2007JC004716.
- O'Donnell, J., Dam, H. G., McCardell, G. and Fake, T., 2010. Long Island Sound Study EPA Assistance Award Final Report.
- O'Donnell, J., Wilson, R. E., Lwiza, K., Whitney, M., Bohlen, W. F., Codiga, D., Fake, T., Bowman, M., and Varekamp, J., 2013. The Physical Oceanography of Long Island Sound, in Swanson, R.5 yarish, C. and Latimer, J. (eds), "Long Island Sound". Springer-Verlag Publishing company.
- Officer, C. B., Biggs, R. B., L. T. J, Cronin, L. E., Tyler, M. A., and Boynton, W. R., 1984. Chesapeake Bay anoxia: Origin, development, and significance., *Science* 223, 22-27.
- Panigrahi, S., Nydahl, A., Anton, P. and Wikner, J. Strong seasonal effect of moderate experimental warming on plankton respiration in a temperate estuarine plankton community. *Estuarine coastal and shelf science*. 135: 269-279. DOI: 10.1016/j.ecss.2013.10.029

- Pokryfikil, L. and Randall, R. E., 1987. Nearshore hypoxia in the bottom water of the northwestern Gulf of Mexico from 1981 to 1984, *Marine Environmental Research* 22:75-90.
- Rabalais, N. N., Turner, R. E., Wiseman, W. J. and Boesch, D. F., 1991. A brief summary of hypoxia on the northern Gulf of Mexico continental shelf: 1985-1988, p. 35-47. In R. V. Ritter, C. and Montagna, P. A., 1999. Seasonal hypoxia and models of benthic response in a Texas bay, *Estuaries* 22:7-20.
- Schumann, U. and Gerz, T., 1995. Turbulent Mixing in Stably Stratified Shear Flows, *J. Appl. Meteorol.* 34, 33–48.
- Science and Technical Advisory Committee., 2003. Systemwide Eutrophication Model (SWEM) Workshop Summary, Long Island Sound Study.
- Suter, E., Lwiza, K. M. M., Rose, J., Gobler, C., and Taylor, G. T., 2014. Nutrient and phytoplankton regime shifts in an urbanized estuary. *Marine Ecology Progress Series* 497:51-67.
- Suter, E. 2011. Plankton Dynamics, Nutrient Stoichiometry, and Oxygen Utilization in Western Long Island Sound. Master's Thesis, SUNY Stony Brook University.
- Swanson, R.L., Wilson, R.E., Crowley, H.A., 2008. Perspectives on long-term variations in hypoxic conditions in western Long Island Sound. DOI: 10.1029/2007JC004693.
- Taylor, A.H., Geider, R.J., Gilbert, F.J.H., 1997. Seasonal and latitudinal dependencies of phytoplankton carbon-to-chlorophyll a ratios: results of a modeling study. *Marine Ecology Progress Series* 152: 51-66.
- Taylor, G.T., 1982. The role of pelagic protozoa in nutrient cycling: A review. *Ann. Inst. Oceanogr.*, (Suppl.), Paris, 58:227-241.

- Umlauf, L., Burchard, H. and Bolding, K., 2005. General Ocean Turbulence Model. Scientific documentation. Marine Science Reports no. 63. Baltic Sea Research Institute Warnemünde, Warnemünde, Germany. 274 pp.
- US Environmental Protection Agency. 1998. Long Island Sound Study: Phase III Actions of Hypoxia Management. Report No. EPA 902-R-98-002, United States Environmental Protection Agency. Stamford, CT, USA.
- Vieira, M. E. C. 1990. Observations of Currents, Temperature and Salinity in Long Island Sound, 1988. A Data Report. , Data Report #6. Marine Sciences Research Center, State University of New York, Stony Brook, New York.
- Vieira, M. E. C. 2000. The long-term residual circulation in Long Island Sound, *Estuaries*, 23(2), 199-207, doi:10.2307/1352827.
- Welsh, B. L. and Eller, F. C., 1991. Mechanisms Controlling Summertime Oxygen Depletion in Western Long-Island Sound, *Estuaries*, 14(3), 265-278.
- Whitney, M. M. 2010. A study on river discharge and salinity variability in the Middle Atlantic Bight and Long Island Sound, *Continental Shelf Research*, 30(3-4), 305-318, doi:10.1016/j.csr.2009.11.011.
- Wilson, R. E. and Swanson, R. L., 2005. A perspective on bottom water temperature anomalies in Long Island Sound during the 1999 lobster mortality event. *J. Shellfish Res.* 24(3), 825-830.

Chapter 3

Estimation of exchange transport in the East River and the western Narrows in LIS with high-resolution 3-D model

Abstract

Physical processes including advection and mixing play important roles in hypoxia development in coastal waters. It is thus critical to have an accurate estimation of the horizontal exchange transport with a high resolution 3-D modeling approach, so that its impact on the development of seasonal hypoxia in the East River and the western LIS can be quantified. Estimations from previous studies show large discrepancies in estimating exchange transport. A three-dimensional numerical hydrodynamic model for Long Island Sound is applied to examine the spatial structure of the tidal and residual circulation in Long Island Sound and the East River. We quantify the exchange transport between the western LIS and the East River with high resolution model grid (up to 30 grid points across the East River), and find large seasonal variability of exchange transport in this region, which differs from previous studies. In order to understand mechanisms driving the transport variability in the East River and the Narrows, we analyze the Ekman number and momentum balance across four transects in this area. We find that the current structure is controlled by both the gravitational circulation and surface wind. The momentum balance analysis shows that barotropic pressure gradient and surface stress dominate the momentum balance. Advection and baroclinicity play secondary roles. Coriolis force plays a more important role as water depth increases.

3.1 Introduction

Previous studies show that physical process including advection and mixing play an important role in hypoxia development in coastal waters. For example, buoyancy advection has a major responsibility for hypoxia formation in the bottom boundary layer over northern Gulf of Mexico (Zhang et al. 2015). Seasonal expansion of Low Oxygen Water in the southern Benguela ecosystem during its upwelling season (i.e., summer and fall) is affected by coupled effect of advection and phytoplankton decay, while vertical mixing ventilates the water column during winter time (Lamont et al. 2015). Another study conducted by Pitcher et al. (2014) over the same region further indicates that the shoreward advection of the bottom pool of oxygen-depleted water influenced DO levels in the near-shore area of the southern Benguela. Yu et al. (2015) suggests that the combination of physical processes including advection and vertical diffusion, as well as sediment oxygen consumption determine the spatial extent and dynamics of hypoxia on the Louisiana shelf. A hypoxia study conducted by Silva et al. (2014) on the large estuarine system, *i.e.*, Chilean Patagonian Fjords, reveals that horizontal advection of adjacent well oxygenated waters is the main source of DO in the deep Fjord. Over the Eastern tropical Pacific oxygen minimum zone, DO variability associated with physical processes including advection was found to be on one order of magnitude larger than that associated with the biogeochemical processes (Montes et al. 2014).

In LIS, physical processes also have a big impact on hypoxia in LIS. For example, Wilson et al. (2008) suggest that summer wind variability affects the seasonal hypoxia development. Back in the early 1990's, Valle-Levinson et al., (1995) and Torgersen et al., (1997) suggest that advection of bottom waters has an impact development of seasonal hypoxia in the western LIS.

However, O'Donnell et al. (2008) and (2013) argue that the majority of physical DO transport to the bottom waters of western LIS is due to vertical mixing across the pycnocline, rather than the horizontal advection. O'Donnell et al. (2010) further report that 9 out of 11 observed events associated with ventilation at the Execution Rocks station in the western LIS resulted from enhanced vertical mixing instead of horizontal advection.

In order to understand the exchange transport processes and their impacts on seasonal hypoxia, there have been intensive studies using both observational and modeling approaches in LIS. The history of estimating transport in LIS can be traced back to 1956. Riley (1956) used observational data to estimate current transport in LIS. He obtained $1100 \text{ m}^3\text{s}^{-1}$ and $1400 \text{ m}^3\text{s}^{-1}$ net transport rates in the western and eastern end of the Sound, respectively, with a gradual increase toward the east throughout the Sound. Blumberg and Pritchard (1997) combined current measurements and a 3-D modeling approach to estimate the net mean rate of exchange transport and they obtained a westward $310 \text{ m}^3\text{s}^{-1}$ transport rate between the East River and LIS with $100 \text{ m}^3\text{s}^{-1}$ monthly fluctuations. Compared to their results, Riley (1956) overestimated the net transport in the west because he ignored the shear dispersion. Gay and O'Donnell (2004) applied inverse method to solve conservation equation of salt and water. They found that approximately 90% of the exchange transport in eastern LIS is due to dispersion, with less than 10% due to gravitational circulation. Crowley (2005) estimated the open boundary condition by calculating barotropic velocity at the open boundary and applying Orlanski radiation condition for the baroclinic velocity. Her study found a consistent exchange transport of $650 \text{ m}^3\text{s}^{-1}$ toward the west throughout the Sound from her warm season experiment in 1988. This result differs from the $310 \text{ m}^3\text{s}^{-1}$ westward transport rate estimated by Blumberg and Pritchard (1997) by a factor of two.

She attributed the difference to local effects of river discharge and different water storage between sections.

These modeling results have laid foundation for the study of transport in LIS, but the relatively low resolution of these models did not allow for further examination of current structure and the seasonal variation of exchange transport across the western Narrows of LIS and the East River, which is a very narrow area (with the narrowest width at 183 m) and has complex topography. Therefore, it is important to apply a high resolution model configuration in the western LIS and the East River, so that an accurate estimation of exchange transport and its impact on development of seasonal hypoxia in this narrow area in LIS can be achieved.

In previous modeling studies, efforts have been made to understand mechanisms controlling the dynamics and exchange transport in LIS. Crowley (2005) estimated the individual contributions of the terms of the momentum equations. This is the first study that thoroughly analyzes the dynamics in LIS with the major focus on the main water body of LIS. The model domain Crowley (2005) applied extends from the eastern end of the Eastern River in the western LIS to the Block Island in the east of LIS. The study focused on summertime hydro-thermal dynamics derived from five major transects between the Execution Rocks Station in the western LIS and the Greenport Station in the eastern of the Sound. She found that in the middle-eastern of LIS, the advective acceleration was directed toward the west and was balanced by the eastward accelerations associated with a barotropic pressure gradient. Their sum was directed toward the west and nearly balanced by the eastward contribution from vertical viscosity. Based on Crowley's (2005) work, Hao (2008) estimated the momentum balance of the tidal flow and the residual flow for a middle transect in LIS separately. She found that during the tidal period the local acceleration was mainly balanced by the pressure gradient acceleration and the friction; and

the lateral residual momentum was in geostrophic balance. Both studies examined the mechanisms of momentum variations in LIS, but their focus was on the area to the east of the Execution Rocks Station in LIS. Fribois et al. (2013) examined the observation-based momentum balance in the western LIS. They suggested that advection is more important to along-estuary momentum than across-estuary momentum. When compared to observed values at sampling locations, the along-estuary advection was overestimated in previous model simulations. In order to understand the current structure and dynamics in the narrow area across the western Narrows of LIS and the East River, it is thus important to apply a high resolution model configuration.

This chapter is organized in the following manner. Section 3.2 describes the study area and background information. Section 3.3 introduces the 3-D high resolution model, the model setup and configuration. The model results are shown in Section 3.4. Section 3.4.1 will show the tidal results validation, Section 3.4.2 and 3.4.3 show the model results of exchange transport and the terms of the momentum balance in the East River and the western Narrows of LIS. Section 3.5 discusses the seasonal variation of water transport and the mechanisms leading to the variation. Conclusions from this Chapter are presented in Section 3.6.

3.2 Study area

LIS is a 20x150 km estuary with an average depth of 20 m. The western end of LIS is connected to the lower Hudson River via the East River, where tidal currents exceed 1 m/s (Blumberg and Pritchard 1997; O'Donnell et al. 2013). LIS is made up of four major basins (i.e., the Eastern Basin, the Central Basin, the Western Basin and the Narrows) separated by several sills and shoals (Figure 1). Among those four major basins, the western Basin, with a deep channel

continuing to the eastern part of the Narrows, is separated by Cable and Anchor Reef (Vieira 2000). Tidal currents are strong in LIS, ranging from 0.5 m/s in the Central Basin to 1 m/s at the eastern end, which is consistent with the magnitude of the East River tidal currents (Vieira 1990). The major tidal component in the Sound is M2, the principal lunar semi-diurnal tide with approximately 12.42 hr period. The amplitude of its major tidal ellipse axis near surface is 0.9 m/s. The lunar elliptic and primary solar semi-diurnal tide, i.e., N2 and S2 are the other two major tidal components in LIS, and the amplitudes of their near surface major tidal axes are 0.19 and 0.12 m/s, respectively (O'Donnell et al. 2013). There are very few observational studies of residual flow in LIS, but model predictions showed westward motion at depth and eastward motion at the surface (Vieira 2000). In addition, Schmalz et al. (1994) in his modeling study proposed that there is a westward motion on the north side of the Sound and eastward motion along the Long Island shore dominating the central basin. To the west of LIS, the East River is a narrow channel system connecting LIS with New York Harbor. The width of the river is between 183m and 1,219 m. The East River extends from the Battery at the New York Harbor to the Willets Point at the western end of LIS with an approximate length of 25 km. The approximate mean water depth in the river is below 10 m, with complicated bottom topography in certain sections. The East River has impacts on both the water quality and the gravitational circulation in the western LIS.

3.3 Methods

3.3.1 Model configuration

The numerical model applied for the transport study is the Regional Ocean Model System (ROMS), which is a free-surface, hydrostatic, terrain-following, primitive equations ocean model

(e.g., Haidvogel et al., 2000; Di Lorenzo, 2003; Dinniman et al., 2003; Budgell, 2005; Warner et al., 2005; Wilkin, 2006). The model domain extended from the western end of the East River in the west to Plum Island in the east. The model grid included 40 by 300 grid cells with 16 evenly-spaced sigma levels in the vertical direction. In the East River, there were as many as 25 grid cells (e.g., between Hunts point and College point) with approximately 70 m resolution on average and a maximum resolution of 40 m near College point (Figure 3-1), in comparison to less than 10 grid points of previous modeling studies for this area. The high resolution 3-D model configuration was enabled to run relatively fast on Gordon supercomputer operated in San Diego Supercomputer Center, as a cluster member of the Extreme Science and Engineering Discovery Environment (XSEDE). Gordon supercomputer consists of 1024 compute nodes and 64 I/O nodes. The network topology of Gordon is a 3D torus. The topography of the model construction was based on the 30-second resolution bathymetry data and sub-sampled from the National Geophysical Data Center (NGDC) Coastal Relief Model, and interpolated onto the model grid (Figure 3-2). The minimum water depth was set to be 5 m. The surface elevation and transport of five tidal constituents (M2, S2, N2 and O1), obtained from an Advanced Circulation (ADCIRC) model tidal database, were prescribed along the open boundary in the east using free surface Chapman condition and 2-D velocity Flather condition. An Orlanski radiation boundary condition is applied to the 3-D velocity and tracers.

Temperature and salinity were nudged with one-month relaxation time period in order to ensure correct gravitational circulation. The data of temperature and salinity climatology was derived from the Connecticut Department of Energy & Environmental Protection (CTDEEP) monitoring data of temperature and salinity sampled in 2008 (see Figure 3-3). The temperature and salinity data were interpolated into the entire model domain with 16 sigma-levels. Initial and boundary

conditions were also created based on the monthly climatological fields. Hourly wind data (speed and direction) were obtained from MYSound buoy stations operated by UCONN in LIS (Figure 3-3), and then decomposed into east-west and north-south components. Wind stress was estimated according to

$$\tau_{wind} = \rho_{air} C_D U_h^2 \quad (3.1)$$

where ρ_{air} is the density of the air; C_D is the wind-drag coefficient. U_h is the wind speed at 10 m level above the ocean surface. Surface atmospheric variables including relative humidity, air temperature, and surface pressure were obtained from the buoys, and then averaged daily in order to calculate surface heat flux terms in the model.

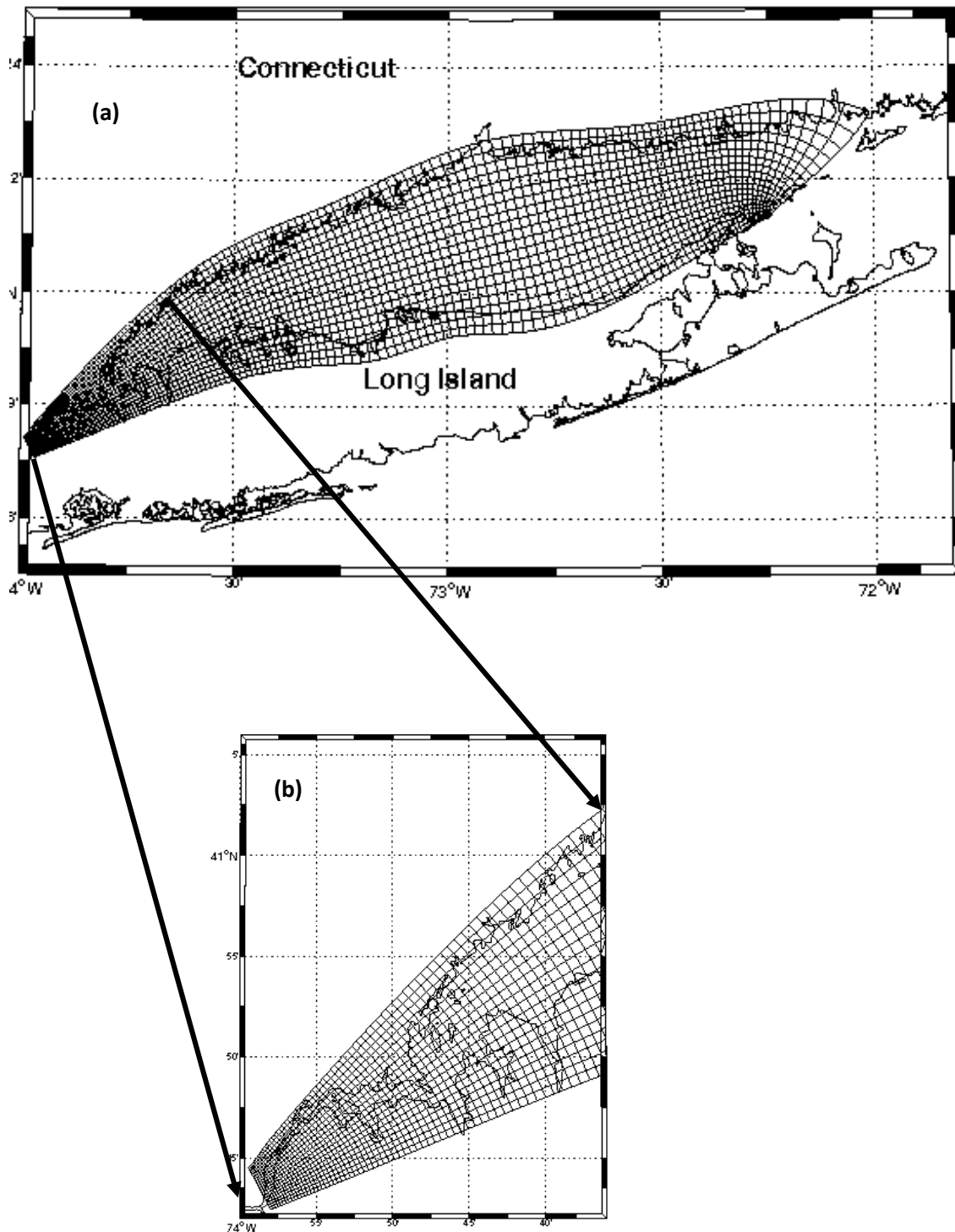


Figure 3-1. (a) Grid points in the model domain (sub-sampled by 2 grid points). (b) zooming-in view of the highlighted section.

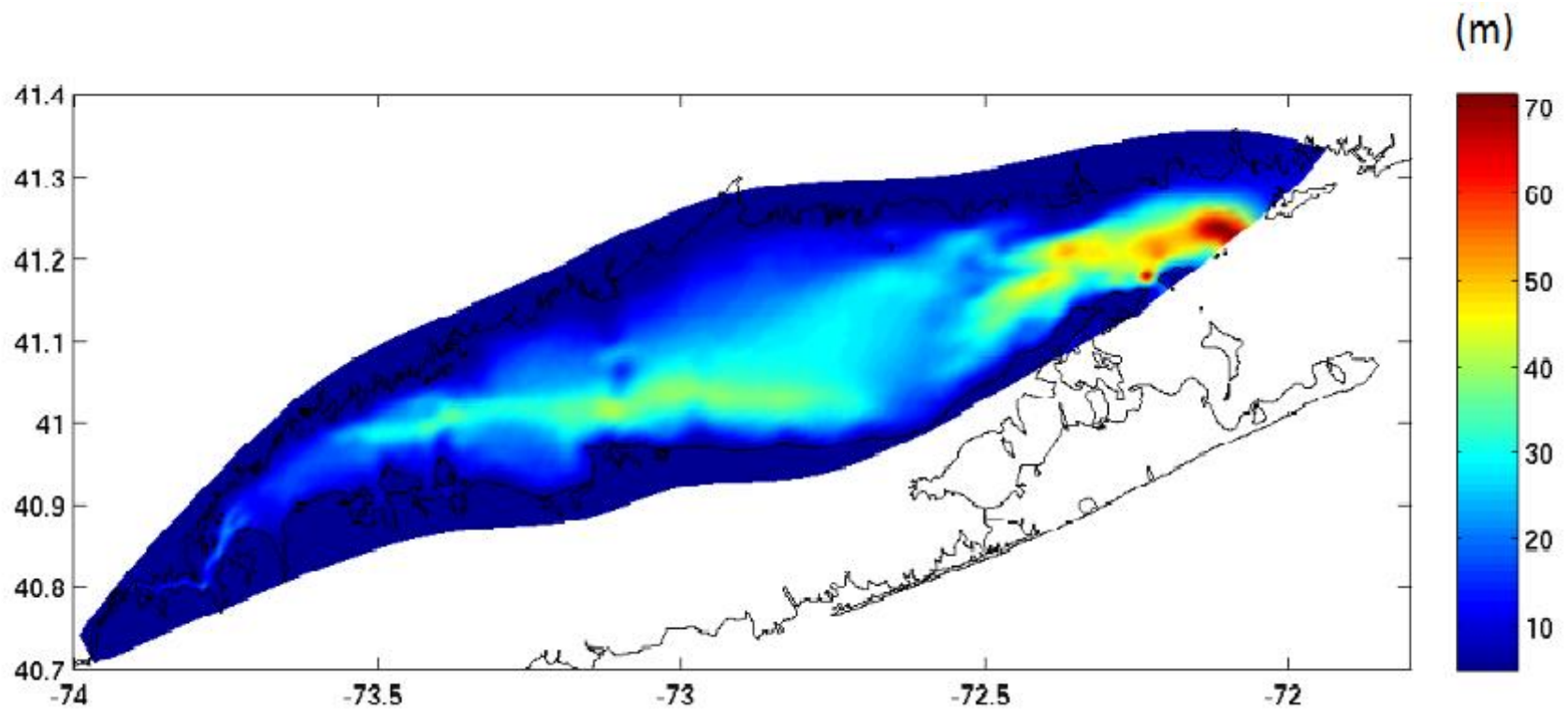


Fig 3-2. Topography of model domain.

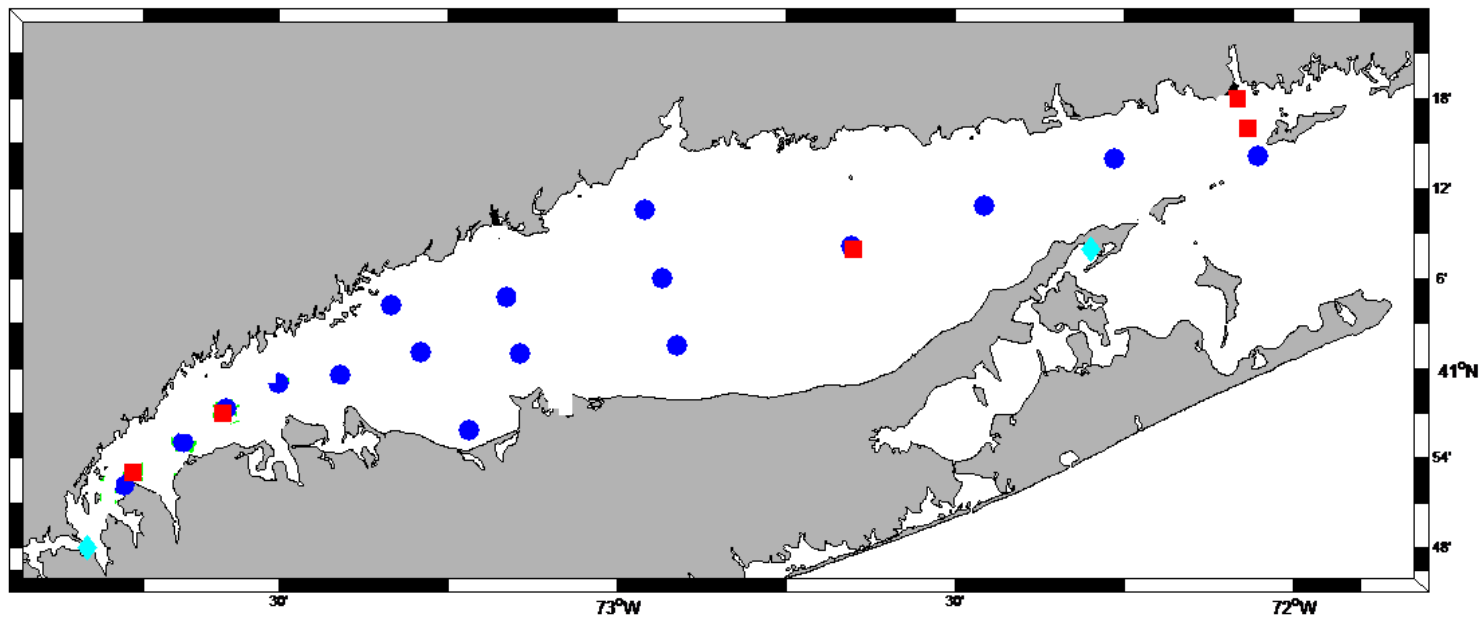


Figure 3-3. Buoy stations in LIS with wind and climatology observations. Blue dots indicate CTDEEP all-year round water quality monitoring stations. Red squares show MYSound buoy stations operated by UCONN.

3.3.2 Tidal validation

NOAA Center for Operational Oceanographic Products and Services (CO-OPS) provides the coastal tidal water level product for public access. The CO-OPS data of water levels for 14 tidal stations located in the western LIS (see Figure 3-4 for the locations) were used to calculate the major tidal constants listed in Table 3.1, i.e., tidal amplitudes and the phase lags (Greenwich epoch) of the major tidal constituent principal lunar semidiurnal M2. The ferry (i.e., P.T. Barnum) based marine observing system which operated along a central LIS transect from Bridgeport, CT to Port Jefferson, NY between 6 AM and 10 PM daily from July 26 to August 11 were applied to validate the tidal constants derived from the modeled tidal currents (Figure 3-5). Optimal interpolation method was used to estimate the u, v components of amplitudes and phases of the tidal currents of the major tidal constituent M2 of the ferry-borne ADCP data. The tidal constants including the semi-major and semi-minor axis, phases and inclination angles were derived from the tidal amplitudes and phases by using the matlab function ap2ep.m. For the modeled current velocities, both the longitudinal and lateral components of the amplitudes and phases for the M2 tidal constituent were estimated based on the least-squares harmonic analysis following Moody et al. (1984). The modeled tidal constants (i.e., semi-major and semi-minor axis, tidal inclination, phase lag) for 9 locations along the P.T. Barnum ferry track were compared to the observations in Table 3.2. In order to validate simulated tidal elevation in the East River, tidal elevations and phases of 5 tidal stations with locations indicated by blue stars in Figure 3-4 were extracted from ADCIRC tidal data base.

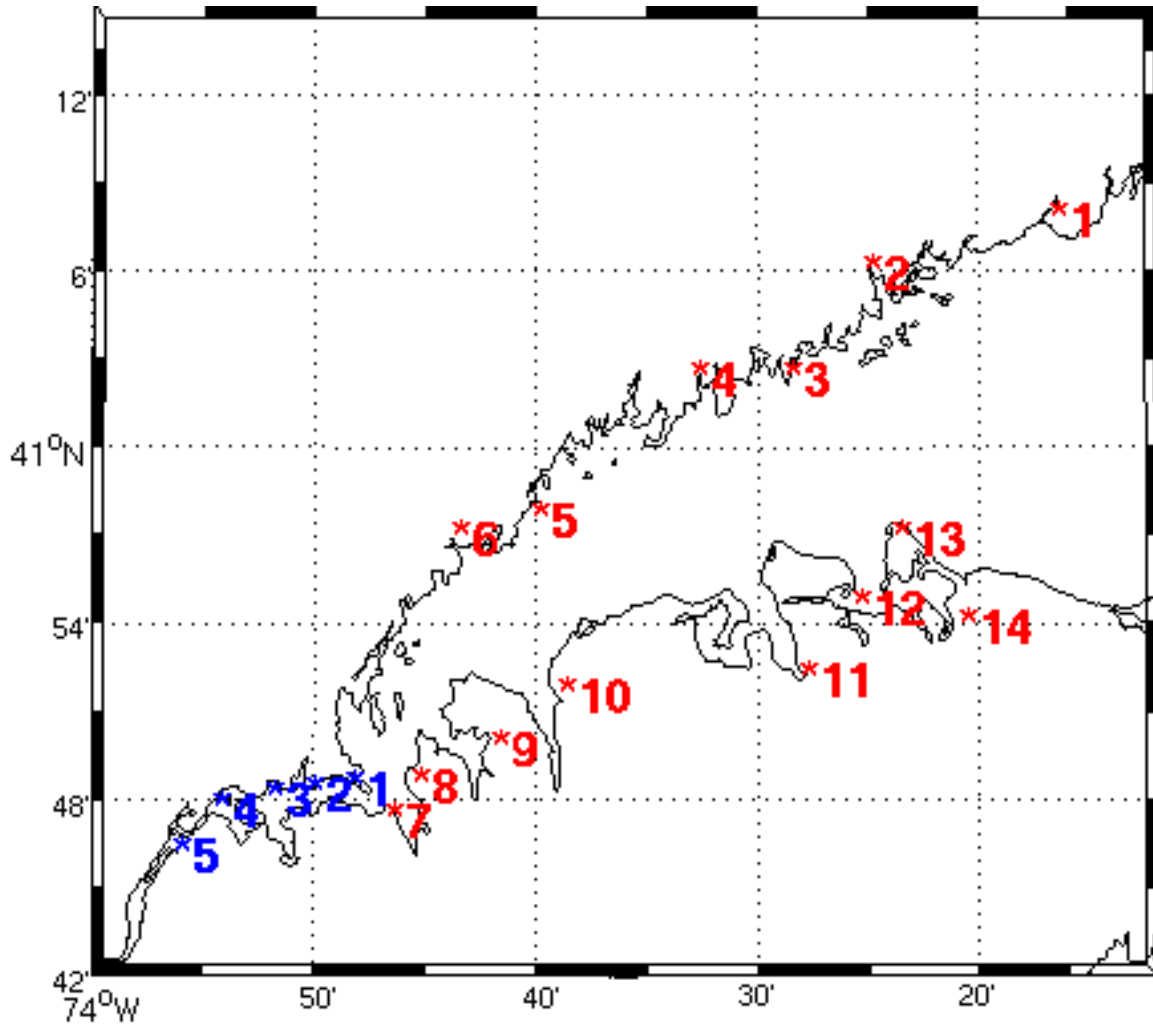


Figure 3-4. Locations of 14 tidal stations in the western LIS operated by CO-OPS are indicated by red star and numbers. Blue stars indicate tidal stations extracted from ADCIRC tidal data base. The stations are labeled the same as in Table 3.1

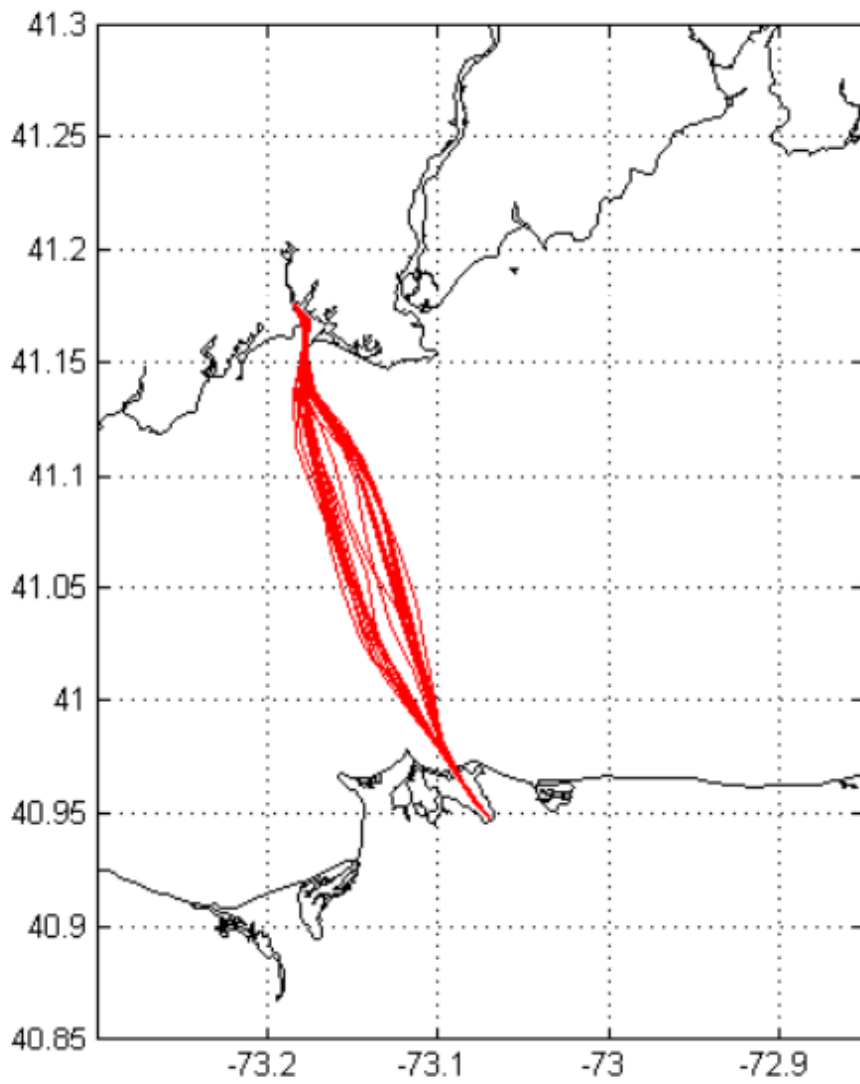


Figure 3-5. P.T. Barnum ferry LIS transects for ADCP observations between Port Jefferson, NY and Bridgeport, CT between July 20 and August 11, 2008 (after Wilson 2007).

3.3.3 Estimation of exchange and net transports

Four transects between the western end of the Eastern River and the Execution Rocks Lighthouse in the western LIS were selected in order to estimate the mean current velocity and the water transport within the domain (Figure 3-6). The net transport mentioned in this Chapter was defined as the net difference between the westward and eastward transport. The modeled net transport across four transects (shown by Figure 3-13) were estimated by multiplying the depth-averaged residual current velocity (Figure 3-12) normal to each of the four transects (Figure 3-6) at each cell by the cell area. The time series of the net transports were obtained by applying a 34-hour lowpass filter to the depth-averaged longitudinal residual current velocity in order to remove the tidal signal, and the time series plots of the estimated net transport are shown in Figure 3-13.

Since the estimation of net transport itself is insufficient for understanding the exchange transport pattern, it is also important to examine the westward and eastward transports separately, so that the variability of the exchange transport can be assessed. The calculated month-to-month variability of the westward and eastward transports is shown by the bar charts in Figure 3-14. The positive part of the bars stand for the eastward transport, and the negative part stands for the westward transport.

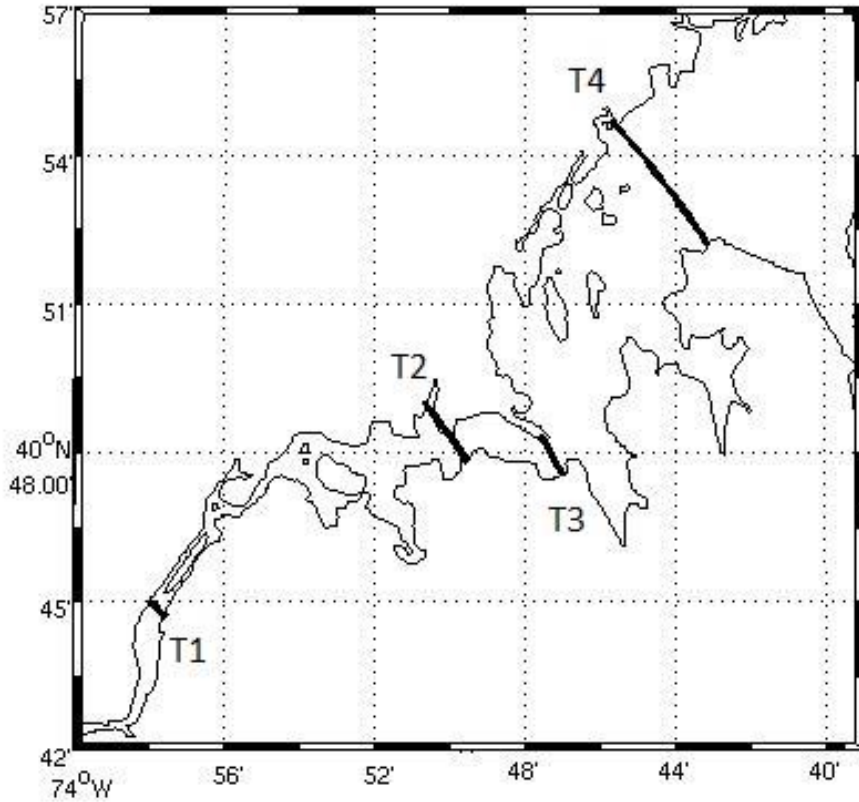


Figure 3-6. Transects T1, T2, T3 and T4 between the western end of the East River in the west and Sands Point in the Narrows of western LIS in the east. Transects T1, T2 and T3 are located in the East River, and T4 is the transect in the western LIS. Transect T1 lies to the south of Belmont Island; Transect T2 is across the Bronx-Whitestone Bridge; Transect T3 is close to the Throgs Neck Bridge; Transect T4 goes through the Execution Rocks lighthouse located in the western LIS.

3.3.4 Momentum balance analysis

The dynamic terms in the momentum balance equation along the longitudinal and lateral directions in ROMS could be written as:

$$\begin{aligned}\frac{\partial u}{\partial t} &= -g \frac{\partial \eta}{\partial x} - \frac{g}{\rho} \int_z^\eta \frac{\partial \rho}{\partial x} dz + \frac{1}{\rho} \frac{\partial \tau_{xz}}{\partial z} + fv - \left(u \frac{\partial u}{\partial x} + v \frac{\partial u}{\partial y} + w \frac{\partial u}{\partial z} \right) \\ \frac{\partial v}{\partial t} &= -g \frac{\partial \eta}{\partial y} - \frac{g}{\rho} \int_z^\eta \frac{\partial \rho}{\partial y} dz + \frac{1}{\rho} \frac{\partial \tau_{yz}}{\partial z} + fu - \left(u \frac{\partial v}{\partial x} + v \frac{\partial v}{\partial y} + w \frac{\partial v}{\partial z} \right)\end{aligned}\quad (3.2)$$

The momentum balance equation states that the local velocity acceleration is induced by barotropic pressure gradient due to sea level slope, baroclinic pressure gradient generated by the density gradient advection, divergence of vertical stress (i.e., vertical viscosity in this case), Coriolis force, as well as total advection.

In order to examine the mechanisms controlling the dynamics in the East River and western Narrows of LIS, time series of depth-averaged and low-pass filtered momentum terms during the 30 day experiment for the four transects described above were calculated. The depth-averaged form of equation (3.2) was represented by:

$$\begin{aligned}\frac{\partial \bar{u}}{\partial t} &= -\frac{1}{H + \eta} \int_{-H}^\eta \left(u \frac{\partial u}{\partial x} + v \frac{\partial u}{\partial y} + w \frac{\partial u}{\partial z} \right) dz - g \frac{\partial \eta}{\partial x} - \\ &\quad \frac{1}{H + \eta} \int_{-H}^\eta \left(\frac{g}{\rho} \int_z^\eta \frac{\partial \rho}{\partial x} dz \right) dz + \frac{\tau_{sx}}{\rho(H + \eta)} - \frac{\tau_{bx}}{\rho(H + \eta)} + f\end{aligned}$$

$$\frac{\partial \bar{v}}{\partial t} = -\frac{1}{H + \eta} \int_{-H}^\eta \left(u \frac{\partial v}{\partial x} + v \frac{\partial v}{\partial y} + w \frac{\partial v}{\partial z} \right) dz - g \frac{\partial \eta}{\partial y} -$$

$$\frac{1}{H + \eta} \int_{-H}^{\eta} \left(\frac{g}{\rho} \int_z^{\eta} \frac{\partial \rho}{\partial y} dz \right) dz + \frac{\tau_{sy}}{\rho(H + \eta)} - \frac{\tau_{by}}{\rho(H + \eta)} + f \quad (3.3)$$

in which \bar{u} and \bar{v} are depth-averaged velocity in longitudinal and lateral directions, H is the undisturbed water depth, and η is the sea surface elevation; vertical stress term is represented by longitudinal surface and bottom stresses in this form.

3.3.5. Estimation of Ekman number

Kasai et al. (2000) shows that the circulation pattern is strongly dependent on the Ekman number E, which is a dimensionless number representing the ratio between viscous force to Coriolis force, with the formulation,

$$E = \frac{A_z}{fH^2} \quad (3.4)$$

in which,

A_z is the eddy viscosity, H stands for water depth, and f is the Coriolis parameter. We calculated the spatial variation of Ekman number for LIS with vertical viscosity A_z derived from the model.

The result is shown by Figure 3-18.

3.4 Results

3.4.1 Tidal validation results

The modeled amplitude and phase lag of M2 tidal component in LIS are shown by Figure 3-7. The tidal amplitude (Figure 3-7 (a)) decreased toward the west, with the maximal amplitude of 1.3 m in the East River in the west, and the minimum of approximately 0.2 m in the eastern end of the model domain. The modeled M2 phase (Figure 3-7 (b)) had a maximal value of 120 degree in the East River and reached the minimum of approximately 30 degree in the eastern end of the domain. In the east of the Sound, the M2 tidal phase increased from approximately 30 degree from the east to 85 degree at 72.3°N, and it tends to become constant toward the west of LIS, which implied a standing tidal wave toward the middle and western LIS (Crowley 2005 and Hao 2008).

Modeled M2 tidal amplitudes and phase lag in western LIS are compared to measurements from 14 harmonic stations operated by NOAA Center for Operational Oceanographic Products and Services (NOAA/NOS/CO-OPS) in Table 3-1. The modeled M2 tidal amplitudes are close to the observed values from the 14 harmonic stations with the minimum percent difference of 0.2% of underestimation at Station 11 Cold Spring Harbor station. The largest overestimation of modeled tidal amplitude is 7% at Station 7 Willet Point. The maximum overestimation of the phase is at Station 5 Rye Beach by approximately 6.5%. In general, the modeled phases agree well with the observations.

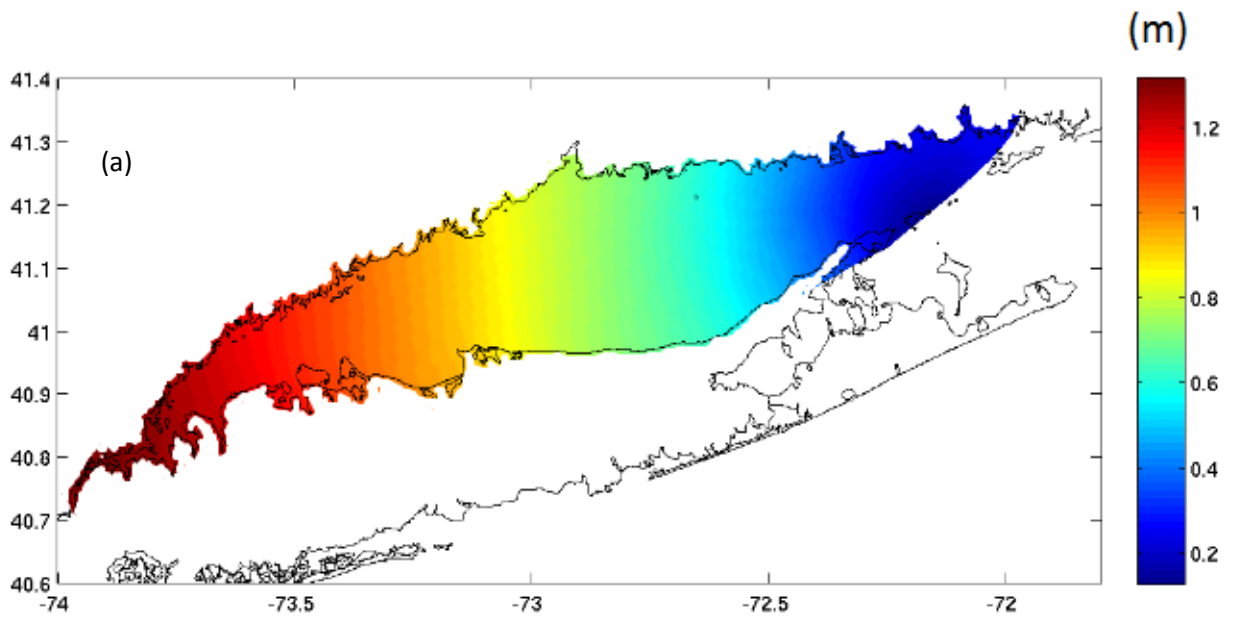


Figure 3-7. (a) M2 tidal amplitude from the 3-D model.

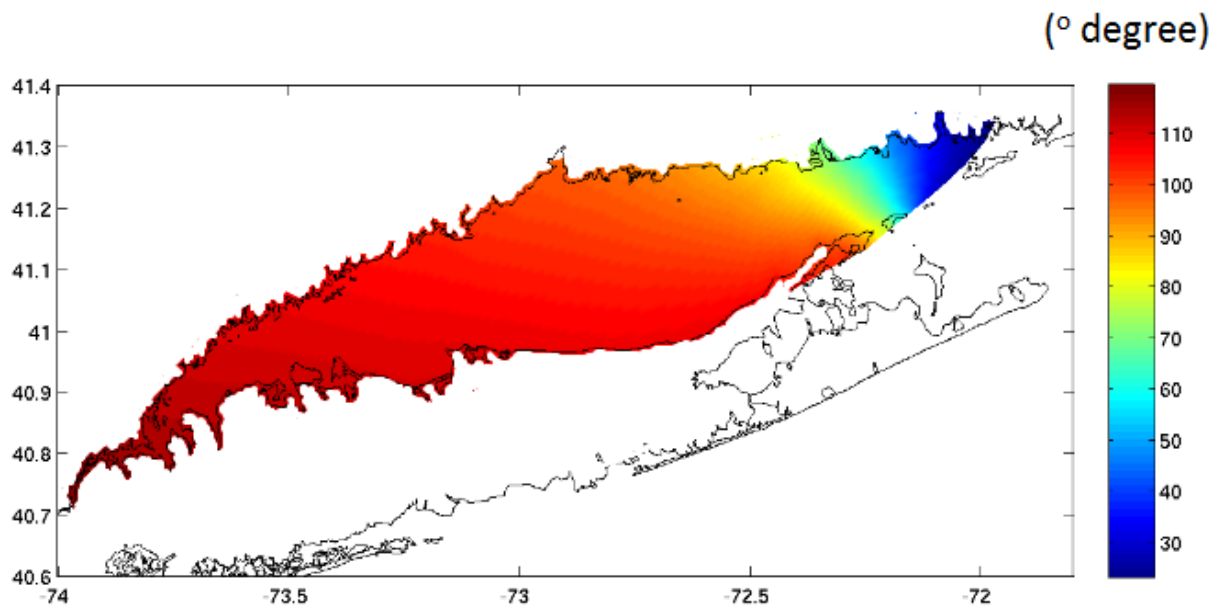


Figure 3-7. (b) Modeled M2 phase from the 3-D model

Tidal gauges	Longitude (° degree)	Latitude (° degree)	Observed amplitude (m)	Modeled amplitude (m)	Observed phase (° degree)	Modeled phase (° degree)
1.Southport Harbor	-73.28	41.13	1.023	0.980	110.15	106.75
2.South Norwalk	-73.42	41.10	1.073	1.056	113.44	106.91
3.Long Neck Point	-73.48	41.04	1.052	1.084	111.38	108.05
4.Stamford	-73.55	41.04	1.066	1.120	114.19	110.18
5.Rye beach	-73.67	40.96	1.146	1.173	112.70	119.98
6.New Rochelle	-73.73	40.95	1.193	1.197	108.24	112.27
7.Willet Point	-73.78	40.79	1.137	1.224	116.75	113.25
8.Kings Point	-73.76	40.81	1.187	1.222	116.65	113.31
9.Port Washington	-73.70	40.83	1.201	1.211	117.93	113.27
10.Glen Cove	73.65	40.86	1.169	1.193	113.68	117.49
11.Cold Spring Harbor	-73.47	40.87	1.129	1.127	114.83	114.55
12.Lloyd Harbor	-73.43	40.91	1.053	1.092	113.43	113.44
13.Eatons Neck	-73.40	40.95	1.099	1.064	117.73	112.02
14.Northport	-73.35	40.90	1.099	1.051	114.80	113.47
ADCIRC tidal stations	Longitude (° degree)	Latitude (° degree)	ADCIRC amplitude (m)	Modeled amplitude (m)	ADCIRC phase (° degree)	Modeled phase (° degree)
ADCIRC Station 1	-73.81	40.808	1.2284	1.2306	133.84	116.89
ADCIRC Station 2	-73.84	40.805	1.2293	1.2310	133.90	117.01
ADCIRC Station 3	-73.87	40.801	1.2303	1.2410	133.96	117.17
ADCIRC Station 4	-73.91	40.795	1.2316	1.2516	134.05	117.21
ADCIRC Station 5	-73.94	40.77	1.2435	1.2629	134.07	118.65

Table 3-1. Tidal amplitude and phase comparison with tidal gauges.

The modeled tidal current properties are validated by comparing the M2 tidal current amplitude (Figure 3-8(a)) and phase lag (Figure 3-9(a)) across the Port Jefferson ferry transection between Port Jefferson, NY and Bridgeport, CT to the measured amplitude (Figure 3-8(b)) and phase lags (Figure 3-9(b)) of tidal current derived from the Port Jefferson ferry-borne ADCP data measured between July, 19th and August, 13th of 2008 (Figure 3-5 shows the ship track). Also compared are the tidal ellipses derived from both the modeled and observed current velocities along the ferry track transects (Figure 3-10). The model results are in good agreement with the observations. Both the model and observational results indicate the existence of a two-core system in the vertical tidal current structure, although there are small discrepancies between the model and the observations (Figure 3-8 and 3-9). Both the model and the observations show that the M2 amplitude was approximately 15% higher between 40.98°N and 41.02°N above 15 m water depth, as well as between 41.05°N and 41.09°N above 10 m water depth, than the other area of the vertical structure, which indicated that there is an approximately 15% of faster tidal transport in the upper water column than the lower water column. The modeled and observed tidal current amplitudes had small disagreement between 41.05°N and 41.09°N above 10 m: the model over-estimated the amplitude by 10% compared to the same area in the observations (Figure 3-8(a) and (b)). The simulated phase (Figure 3-9(a)) captures the general structure of what existed in the observed pattern (Figure 3-9(b)), which has a larger phase change in the upper water column compared to the lower part. And both the model and the observations have very similar values of the maximum phase lag, *i.e.*, approximately -3.2 radians. We noticed there was a difference between the modeled and observed tidal current phase lag along the edges of the vertical structure, however, it does not alter the fact that the model captured the most features of the observed patterns.

Also compared are the tidal ellipses derived from the modeled and observed depth-averaged current velocities along the ferry transects (Figure 3-10). The model and observations are in general agreement. The tidal ellipses tend to go counter-clockwise near the north coast of LIS and clockwise near the southern coast. Both the modeled and observed tidal ellipses generally tend to align themselves approximately parallel to the shoreline.

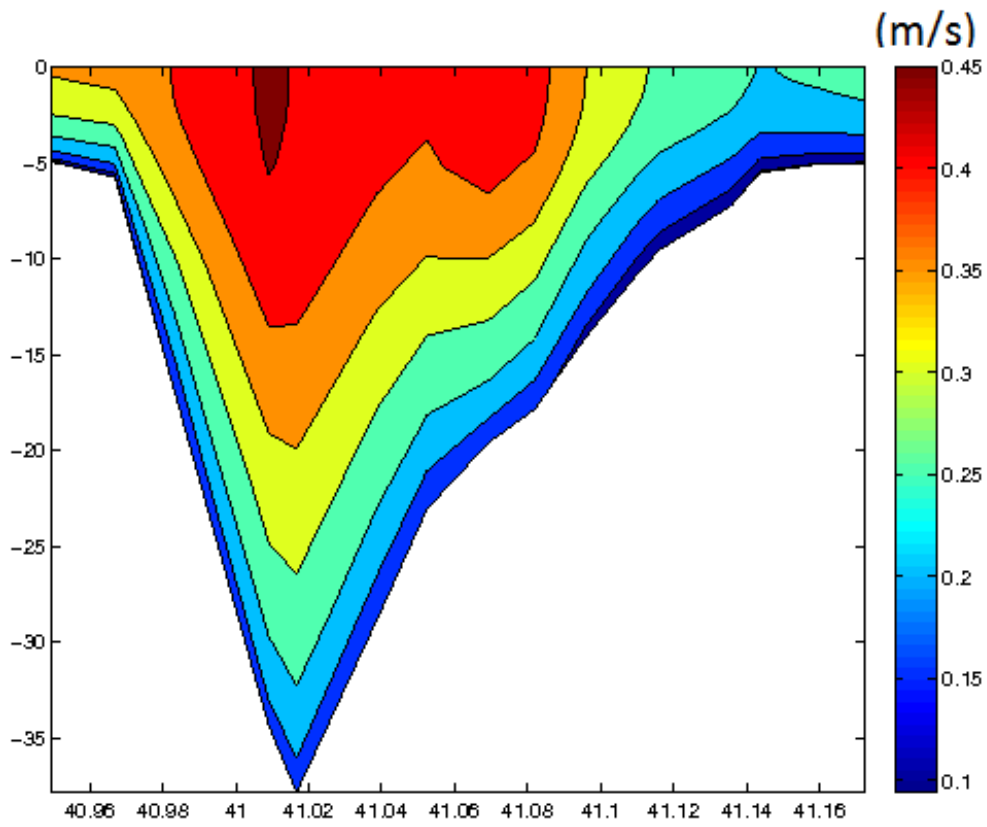


Figure 3-8. (a) Simulated M2 amplitude of the current velocity.

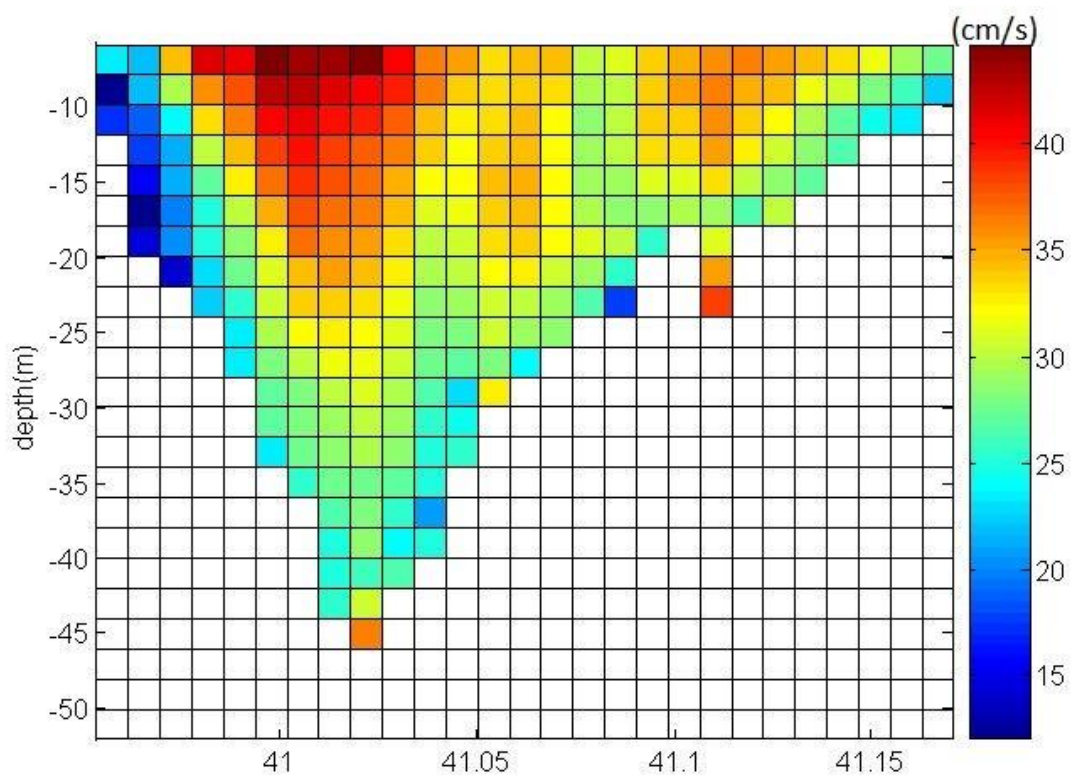


Figure 3-8. (b) M2 amplitude derived from the ferry observations.

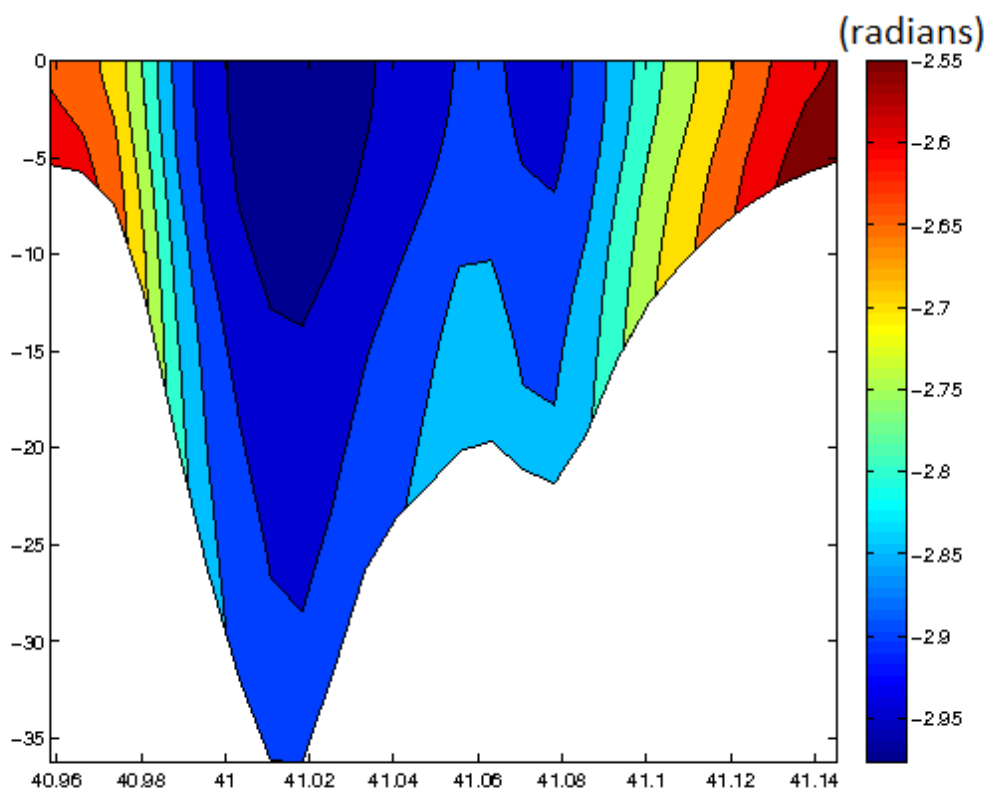


Figure 3-9. (a) Modeled M2 phase lag of current velocity in radians.

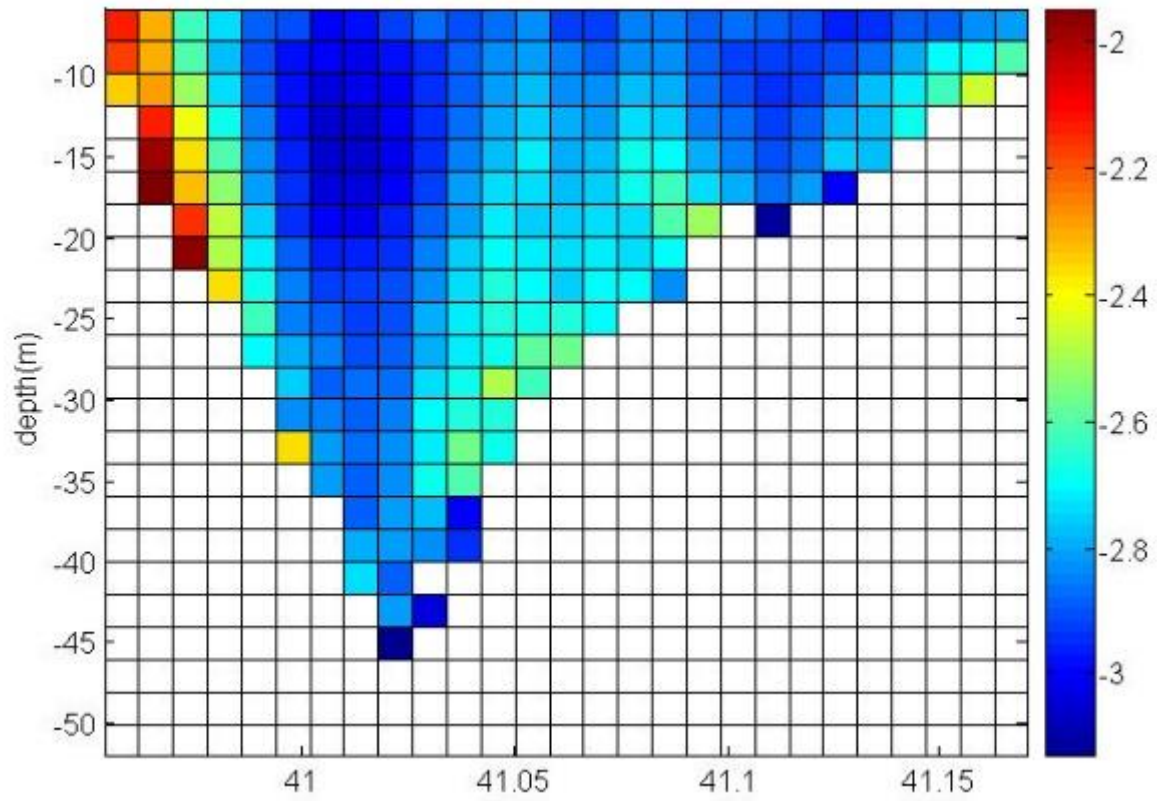


Figure 3-9. (b) M2 Phase derived from the ferry observations in 2008.

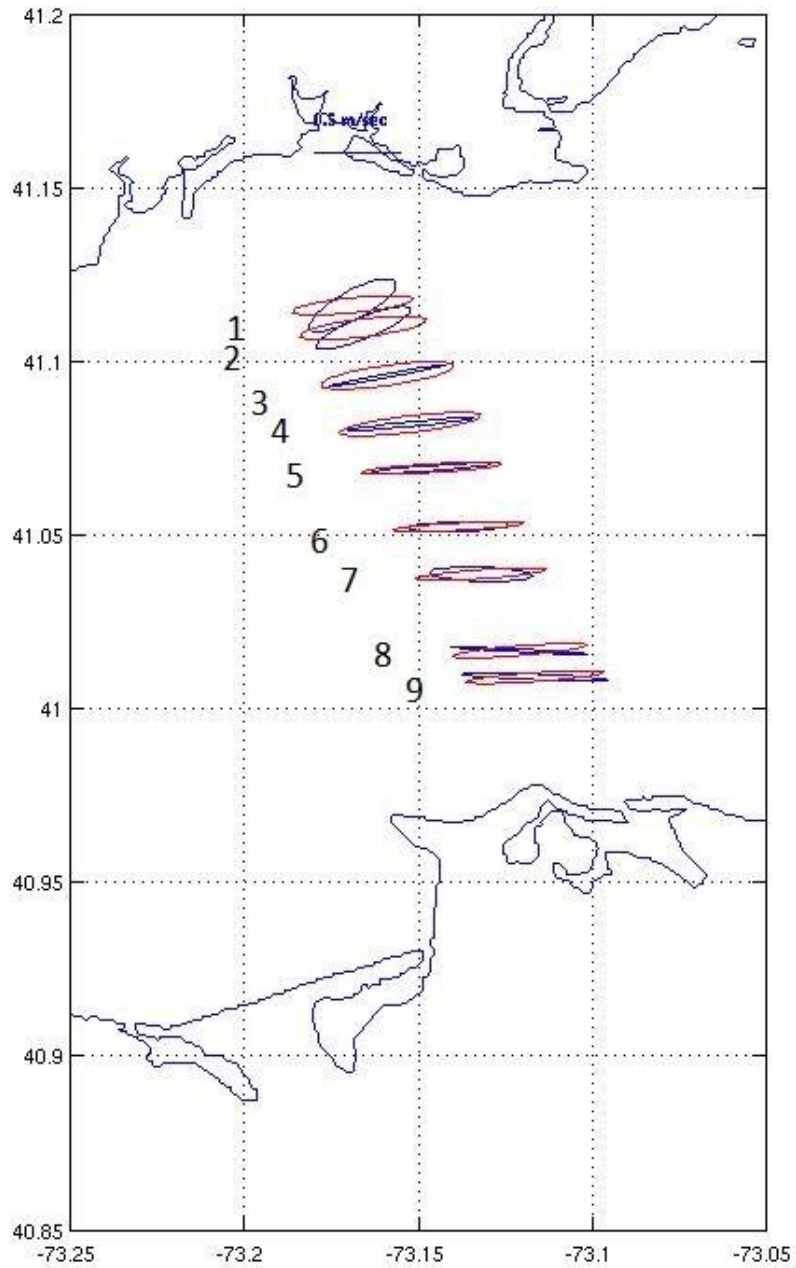


Figure 3-10. Tidal ellipses comparison between model (red) and observations (blue). Stations are labeled according to Table 3-1 Site numbers.

3.4.2 Water transport across the western Narrows of LIS and the East River

In order to calculate the exchange transport across the western Narrows of LIS and the East River, it is essential to have an estimate of the spatial distribution of the cross-transect longitudinal momentum of the depth averaged residual current, which is shown in Figure 3-11. The range of the residual current is within a $[-0.12, 0.12]$ m/s window, with the largest magnitudes appearing in the eastern end of the model domain, where the tidal signal propagates from. The residual current close to the eastern end of the domain indicates strong current shear, which might be an artifact of the boundary effect. The mean flow starts to increase the amplitude toward the western Narrows of the Sound because of the Bernoulli effect as it flows through a narrower channel. Most of the water within the narrow channel has a westward residual current, with the magnitude increasing from approximately 2.5 cm/s between Hempstead Bay and Mamaroneck, to approximately 5.5 cm/s in the Narrows across Sands Point and Whitestone. However, within the Hempstead Bay, Manhasset Bay and Little Neck Bay, the residual currents are toward the east, which tends to balance the westward flow in the middle of the narrow channel. The vector plot in the figure shows that there is a westward mean flow in the western LIS. In the eastern LIS, flows are mainly toward the west in the Connecticut shoal and are eastward toward the Long Island shore.

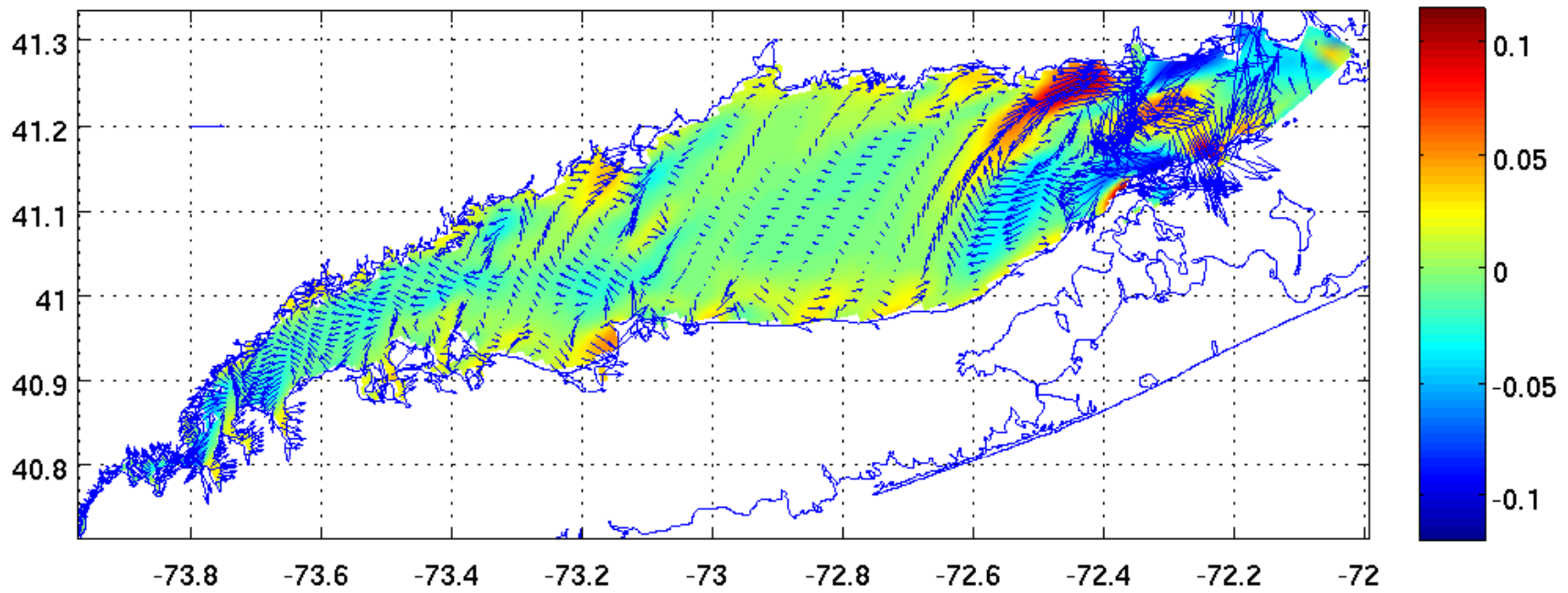


Figure 3-11. Plot of depth-averaged horizontal residual current velocity in LIS. Color plot represents the depth-averaged longitudinal residual current velocity u .

Four transects between the western end of the East River and the Execution Rocks Station in the western LIS were selected to analyze the current structure and residual flow (Figure 3-6). The vertical and lateral structure of residual current velocity across Transects T2, T3 and T4 are shown in Figure 3-12. In general, the residual flow structure was stratified in the upper East River (i.e., across T2), and both vertically and laterally stratified in the Narrows of LIS (i.e., across T3 and T4). There was a major eastward mean flow in the upper layer across T2 with the maximum magnitude of 6 cm/s (Figure 3-12(a)). Below 4 m water depth, the mean flow turned toward the west with the maximal magnitude of 6 cm/s. The mean flow across T3 (Figure 3-12(b)) and T4 (Figure 3-12(c)) propagated westward in the north shore of LIS, and in the southern part of LIS the flow was toward the east, and the flow intensity decreased with depths. For example, in the north part of the section T3, the magnitude of the westward mean flow decreased from approximately 8 cm/s at the surface to 4 cm/s near the bottom. In the southern part of T3, the eastward mean flow decreased from 2 cm/s near surface to about 0 near bottom. The mean flow across T4 demonstrated that in the south, there was a eastward flow in the upper layer (up to 1 cm/s) and a westward flow in the lower layer (1 cm/s). In the deeper section of the north, the flow was toward the west with the intensity up to 3.5 cm/s, but turned to the east as the water shoals. The mean flow structure across T4 (Figure 3-12(c)) is compared to the cross-section structure of long-term residual current isotachs in cm/s across same transect as T4 in Vieira (2000) (Figure 3-12(d)), and the two patterns are in general agreement.

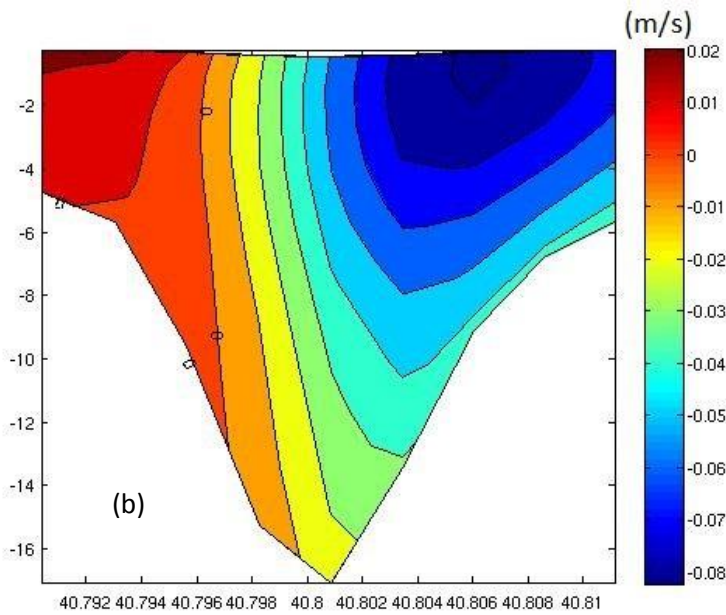
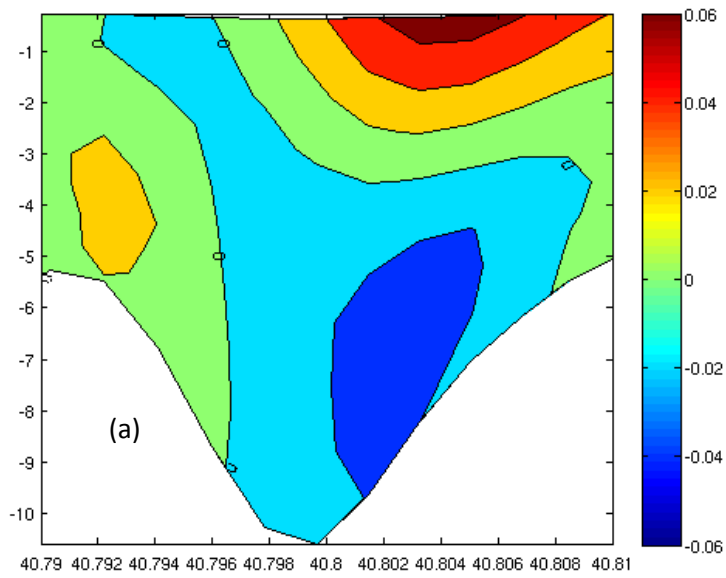


Figure 3-12. (a) Vertical structures of longitudinal residual current across T2 (Whitestone), (b) Vertical structures of longitudinal residual current across T3 (Willet Point) transect

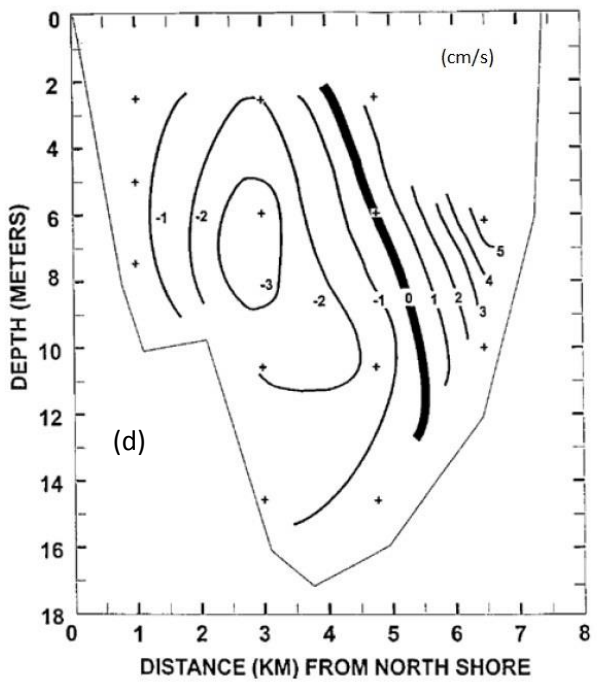
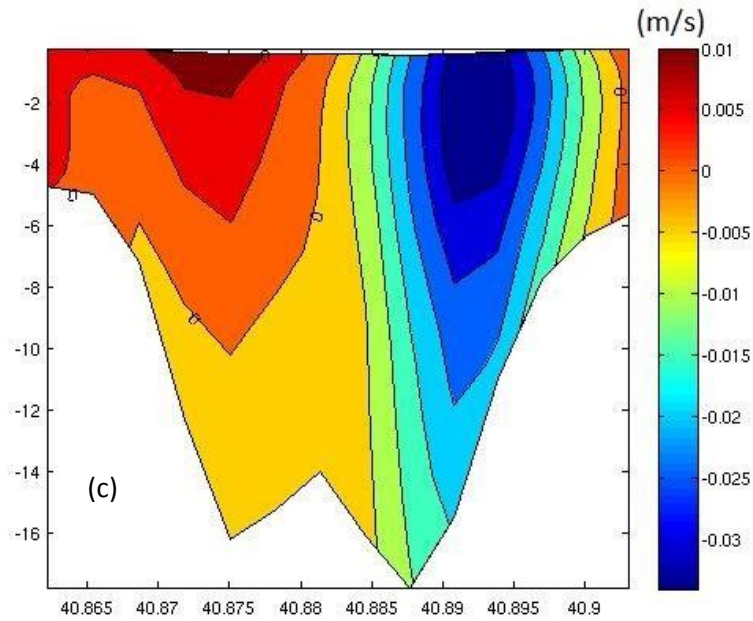


Figure 3-12. (c) Vertical structures of longitudinal residual current across T4 (Execution Rocks) transect in Long Island Sound. (d) Cross-section structure of long-term residual current isotachs in cm/s across same transect as T4 in Vieira (2000).

Water volume transport was calculated at the four transects mentioned above. In order to avoid the Stokes drift complications, the transport is calculated by multiplying the instantaneous non-tidal residual velocity by instantaneous total depth (mean depth plus water level variation). The conservation of mass constrains that the net water transport does not vary significantly at the different locations (Figure 3-13 (a) and (b)). The sectionally-integrated transport shown by Figure 3-13 is much weaker than the circulating exchange flow (Figure 3-14) during year 2008. The net westward transport is as low as $200 \text{ m}^3 \text{ s}^{-1}$ throughout three transects during warm season when wind is weak, in winter the net westward transport reaches as high as $750 \text{ m}^3 \text{ s}^{-1}$. The temporal variability of the net transport is also spatially coherent (Figure 3-13). The differences in the various time series may be due to localized effects of river discharge and to the different storage of water between sections. This result is different from an estimate of $-310 \text{ m}^3 \text{ s}^{-1}$ without large seasonal variation by Blumberg and Pritchard (1997) for the net transport of water between Long Island Sound and the East River.

To better understand the monthly variation of the exchange transport (i.e., the westward and eastward transport), the monthly mean of the exchange transport is shown by Figure 3-14. The bars with positive values indicate the eastward transport and the bars with negative values stand for the westward transport. In general, T1 had the largest seasonal variability of the exchange transport, although the transport intensity was the weakest among all four transections. For this transect, the largest exchange transport (both westward and eastward) occurred in winter seasons, whereas the smallest transport was evident in summer. Both T2 and T4 demonstrated relatively large seasonal variations, with intensified exchange transport during winter and weakened transport in summer. The exchange transport across T3 shows relatively weaker seasonal change.

Also the westward transport for all transects also increased between April and May due to intensified freshwater input.

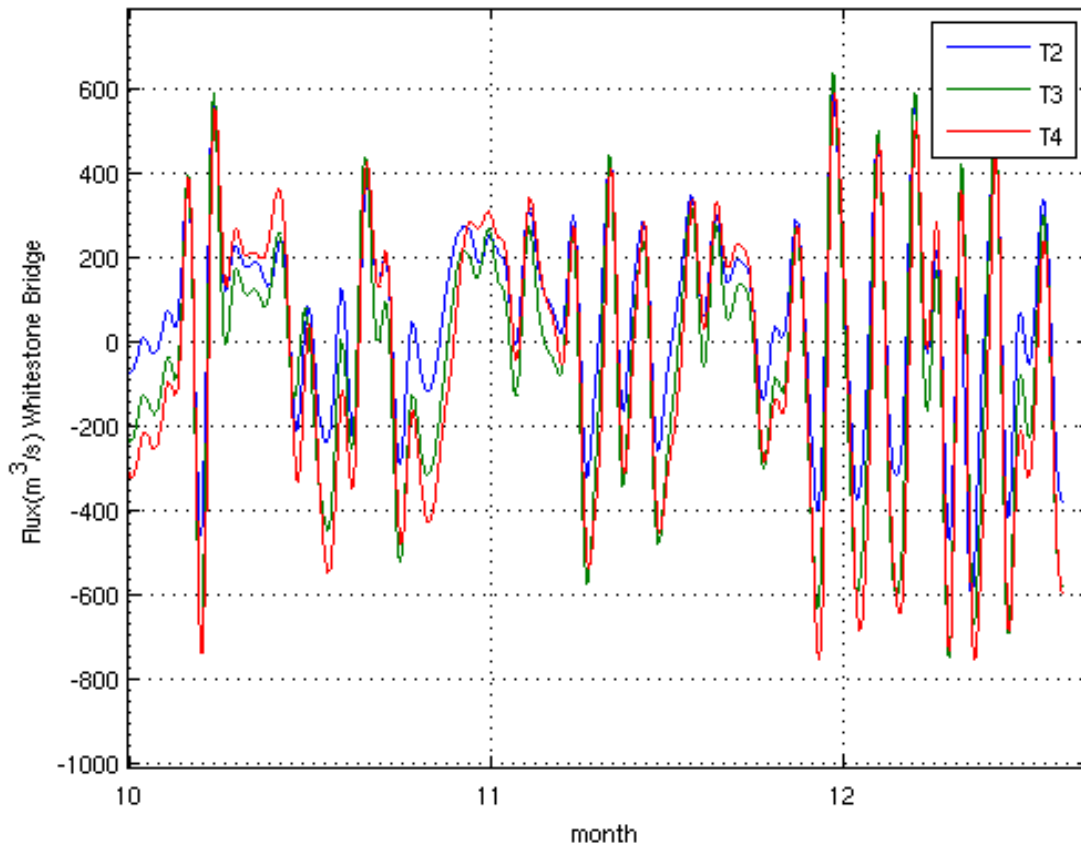


Figure 3-13 (a). The net transport integrated for the component of residual currents perpendicular to T2, T3 and T4 in Long Island Sound for winter, 2008

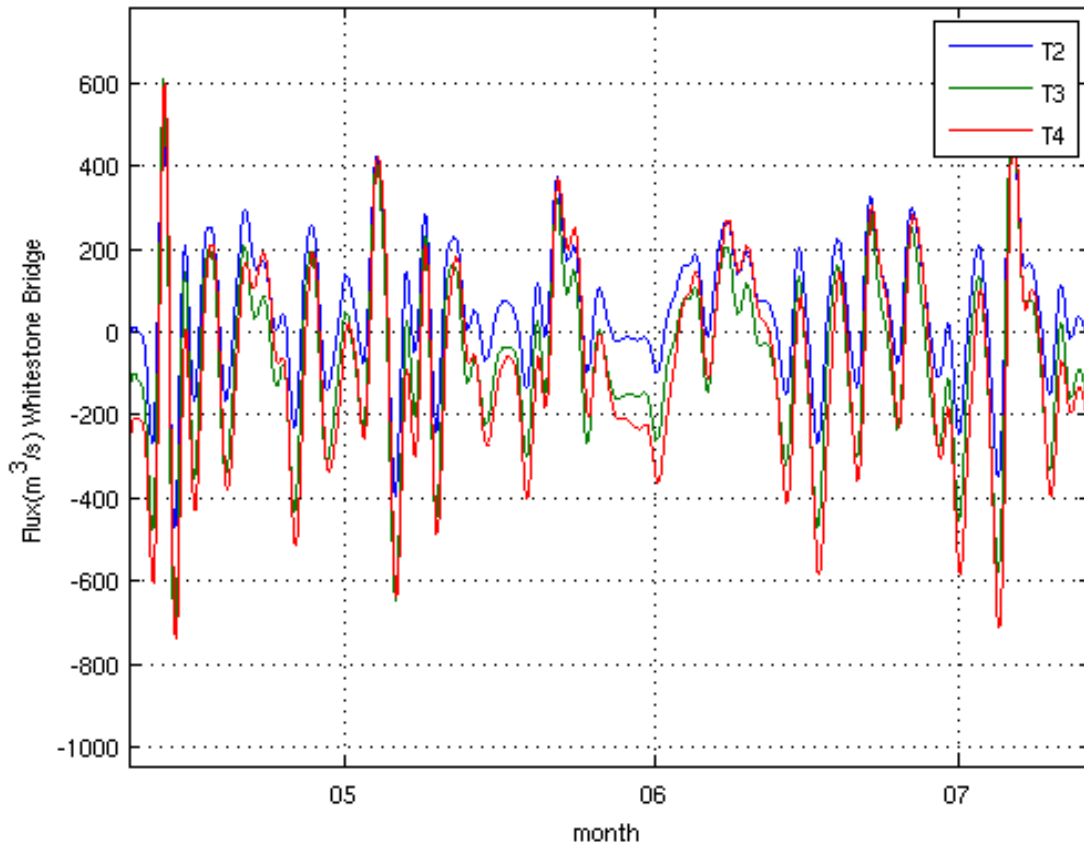


Figure 3-13 (b). The net transport integrated for the component of residual currents perpendicular to T2, T3 and T4 in Long Island Sound for summer, 2008.

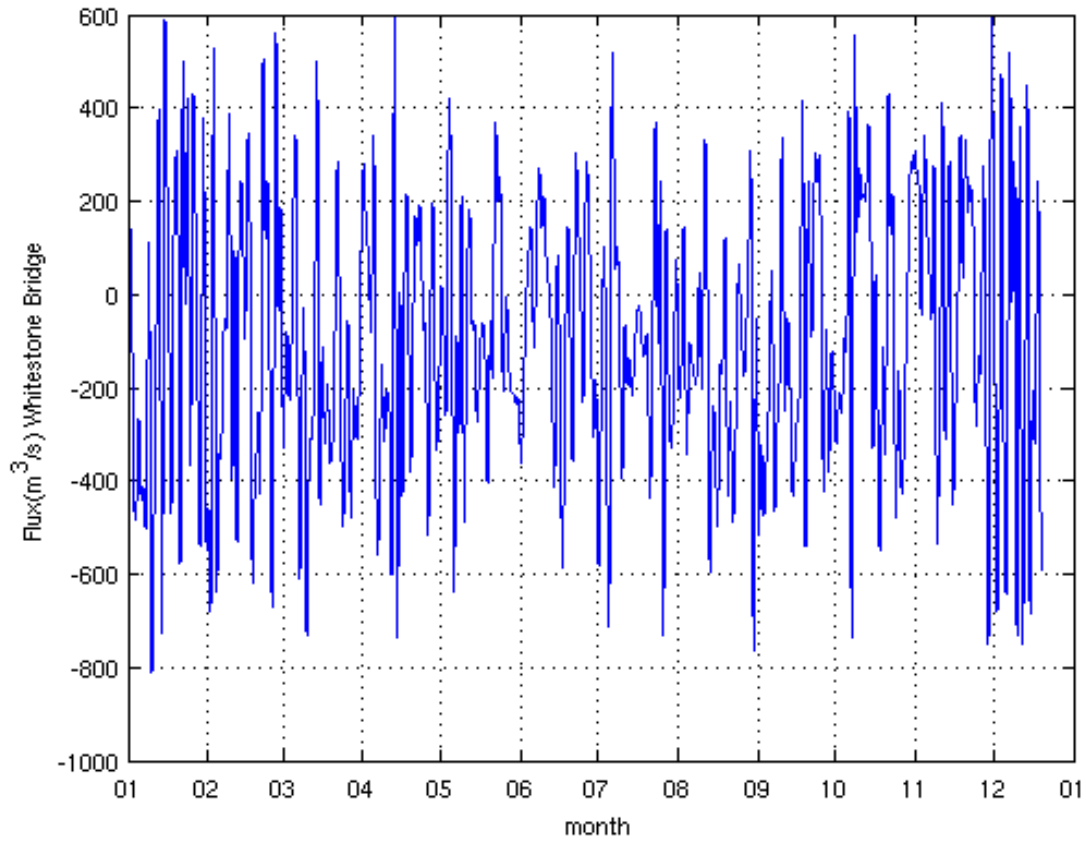


Figure 3-13 (c). The net transport integrated for the component of residual currents perpendicular to T4 in Long Island Sound for 2008.

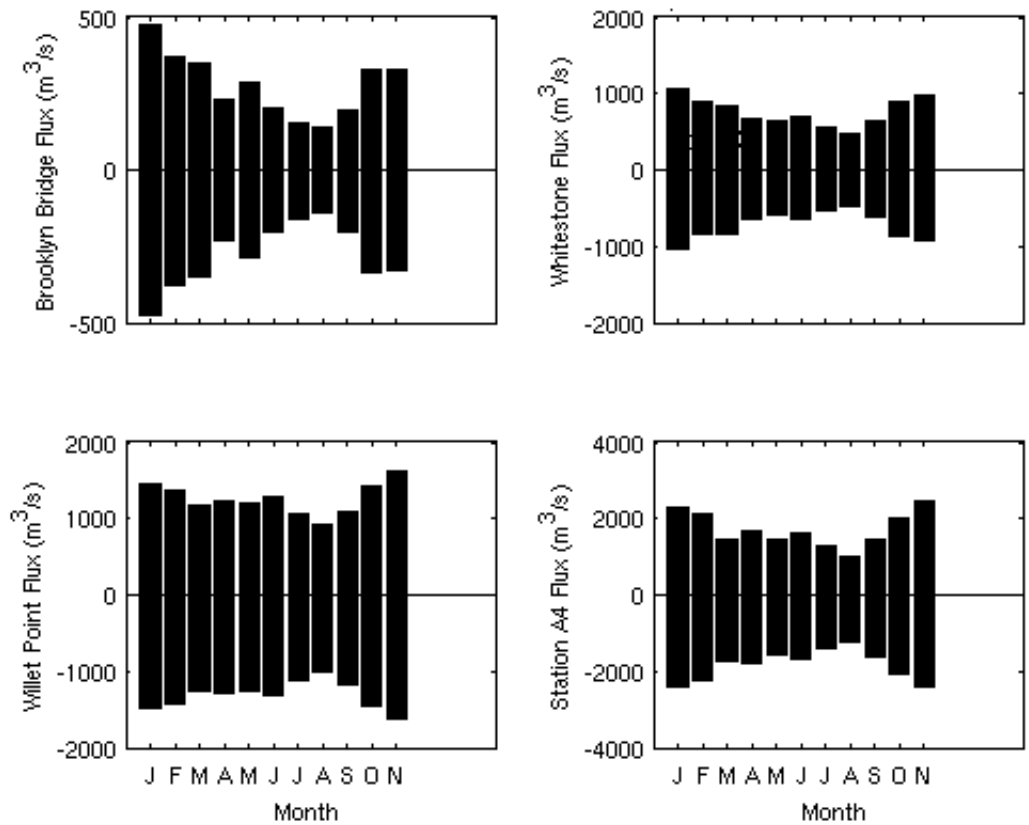


Figure 3-14. Mean exchange transport in the East River and the Narrows in LIS. Positive values stand for eastward flow; Negative values are westward transport.

3.4.3 Vertical eddy viscosity and Ekman number

In order to examine the relative importance between rotation and wind stress to the flow structure, we then show the spatial distribution of the vertical eddy viscosity and the Ekman number. The vertical viscosity derived from ROMS are between 0 and 0.01 m²/s (Figure 3-15). The viscosity tends to increase from the western LIS toward the east as water depth deepens. In the East River and western Narrows, the viscosity was below 0.002 m²/s. It increases to approximately between 0.004 and 0.005 m²/s range in the western LIS. Toward the middle of the Sound, viscosity increases gradually in the center of the channel to approximately 0.008 at about -73.25°N, and drops slowly to approximately 0.003 toward -72.5°N in the eastern LIS. The Ekman number along the thalweg of the Sound tends to be more uniformly distributed (Figure 3-16). In the deep middle channel, the number is below 0.1, indicating strong Coriolis effect on the circulation (i.e., geostrophic flow in lateral direction). The Ekman number increases toward the boundary of the domain to approximately 0.5. This is due to decreased Coriolis effect associated with reduced water depth. In the western Narrows and the East River, Ekman number is approximately 0.2 along the thalweg, and increases to be 0.5 along the northern and southern boundary.

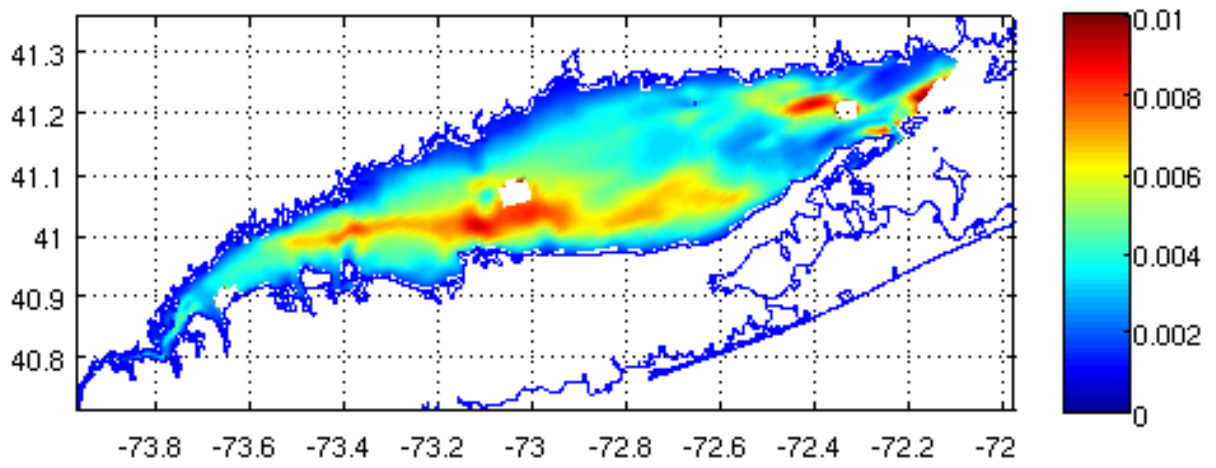


Figure 3-15. Vertical eddy viscosity for LIS derived from ROMS.

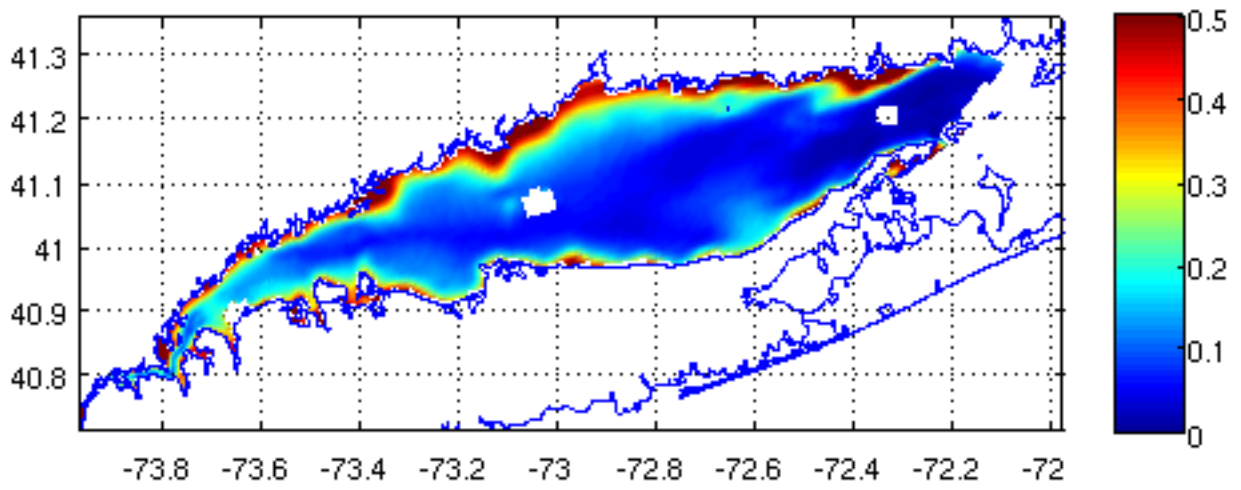


Figure 3-16. Ekman number for LIS estimated from vertical viscosity shown by Figure 3-17 and Eq 3.4.

3.4.4 Momentum balance analysis

The longitudinal momentums across four transects shown by Figure 3-17, 3-18, 3-19, and 3-20 are primarily dominated by the barotropic pressure gradient force and the surface stress. For T1 (Figure 3-16), it is the sum of surface and bottom stress, and advection being balanced by the sum of barotropic pressure gradient, acceleration and baroclinic pressure gradient. Barotropic pressure gradient force and surface stress dominate the balance. Bottom stress and acceleration play secondary roles. Advection, baroclinic pressure gradient force and Coriolis force are relatively smaller than the other terms in the longitudinal direction. We do acknowledge that Coriolis force might play more important role in the geostrophic flow along lateral direction according to Ekman number analysis in Section 3.4.4.

Figure 3-17 shows that across T2 it is mainly the sum of positive barotropic pressure gradient force and surface stress balanced by the negative acceleration, bottom stress and baroclinic pressure gradient force. Baroclinic pressure gradient and Coriolis force is relatively small terms and plays least important role across this transect. Advective acceleration across T2 is approximately two times larger than that across T1, and plays more important role compared to T1.

The major momentum balance across T3 (Figure 3-18) is in general agreement with that across T2. The mean of advective acceleration term increases from T2 (i.e., approximately $0.7 \times 10^{-5} \text{ m/s}^2$) to T3 (i.e., approximately $1 \times 10^{-5} \text{ m/s}^2$) by approximately 40%, with the range being reduced from $0.6 \times 10^{-5} \text{ m/s}^2$ to $0.35 \times 10^{-5} \text{ m/s}^2$. Across T4 (Figure 3-19), Coriolis force starts to become larger than previous two transects due to the widening of the basin and the turning effect of the current.

In the lateral direction, the balance is dominated by positive barotropic pressure gradient force and negative Coriolis force (Figure 3-21, 3-22, 3-23 and 3-24), which suggests that the flow is in geostrophic balance. Coriolis acceleration is important in lateral direction, which is consistent with Ekman number results in Section 3.4.4. The secondary terms in the lateral direction are advection, surface stress and baroclinicity. Our results indicate that baroclinic pressure gradient plays a bigger role than longitudinal direction.

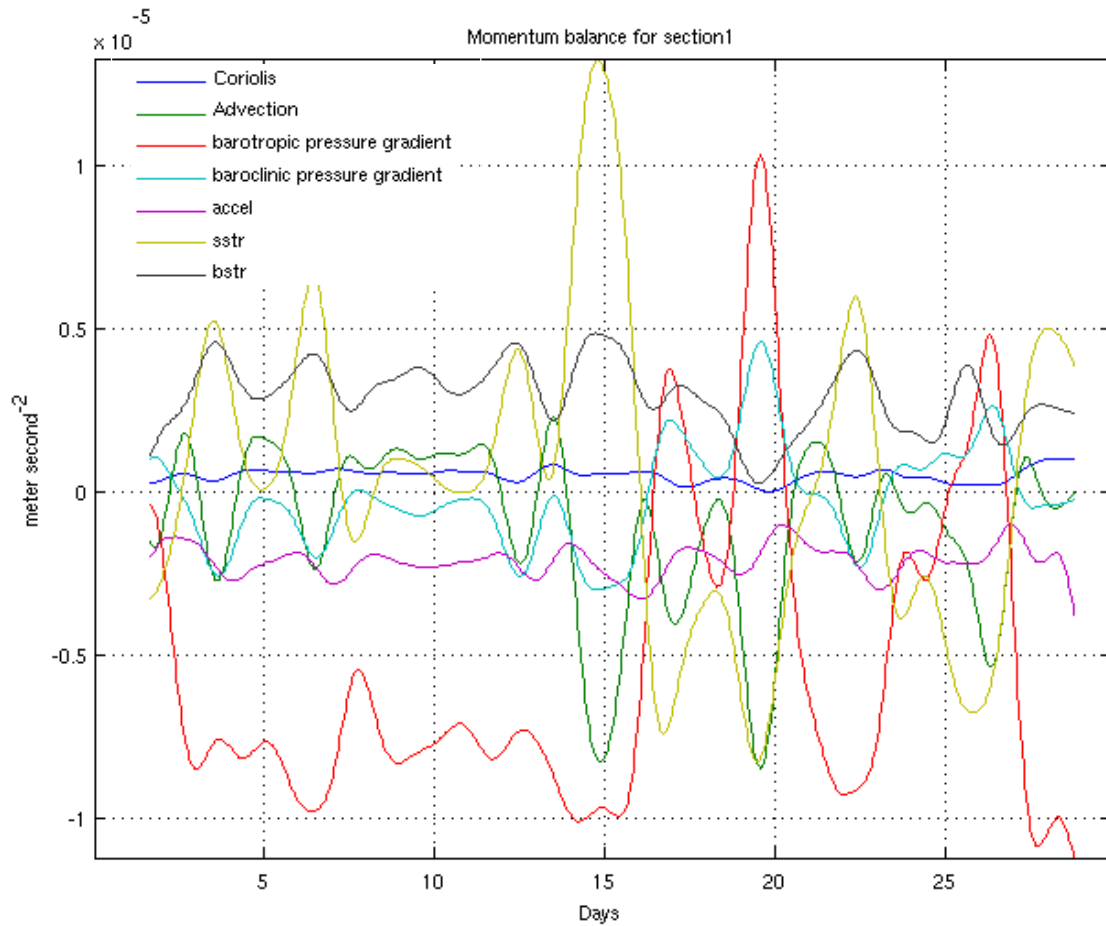


Figure 3-17. Longitudinal momentum terms derived from the momentum balance equation 3.3 in ROMS for transect T1, July, 2008. Blue line indicates the variability of the Coriolis acceleration term; Green line shows the variability of the advection term; Red line represents the barotropic pressure gradient; Cyan indicates baroclinic pressure gradient; Magenta line is the local acceleration; Yellow and black lines show surface and bottom stress, respectively

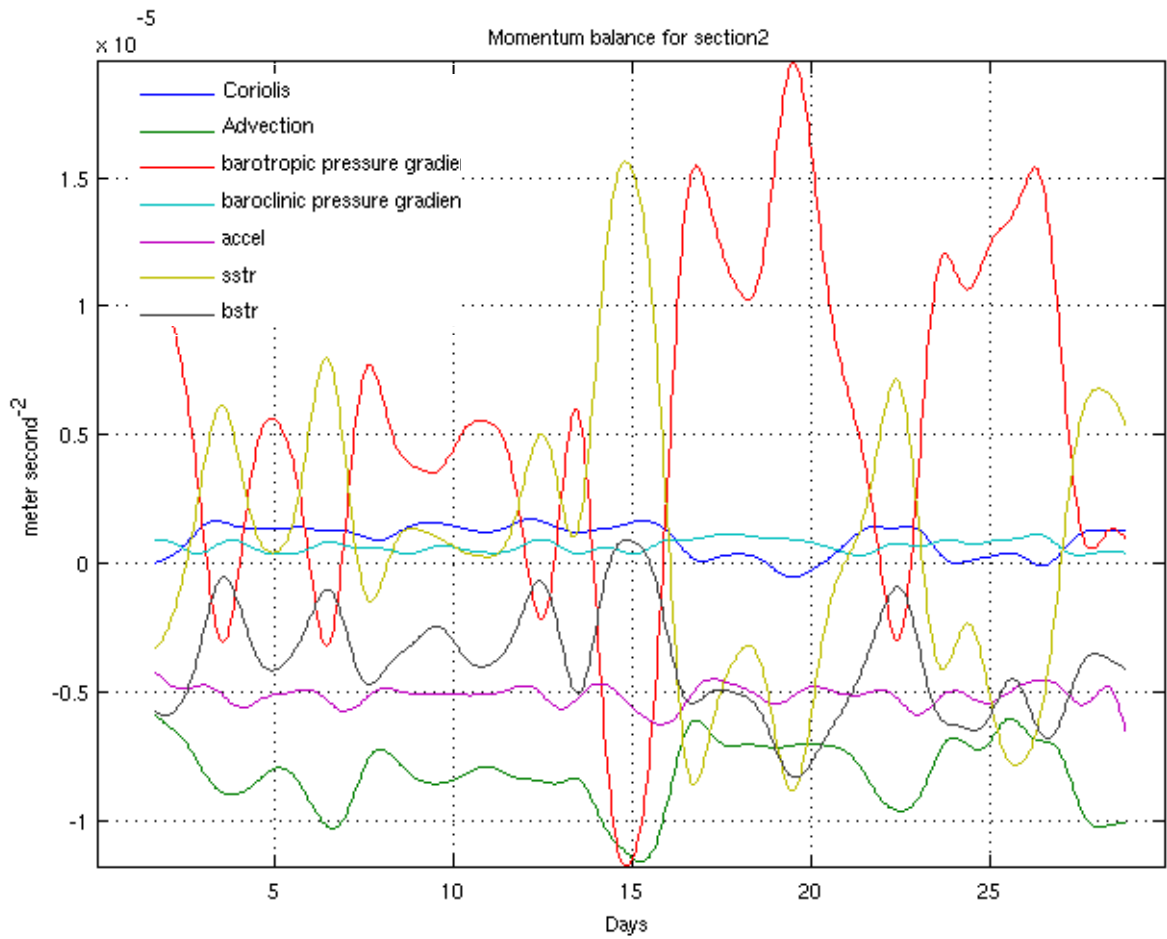


Figure 3-18. Longitudinal momentum terms derived from the momentum balance equation 3.3 in ROMS for transect T2, July, 2008. Line colors indicate the same terms as Figure 3-17.

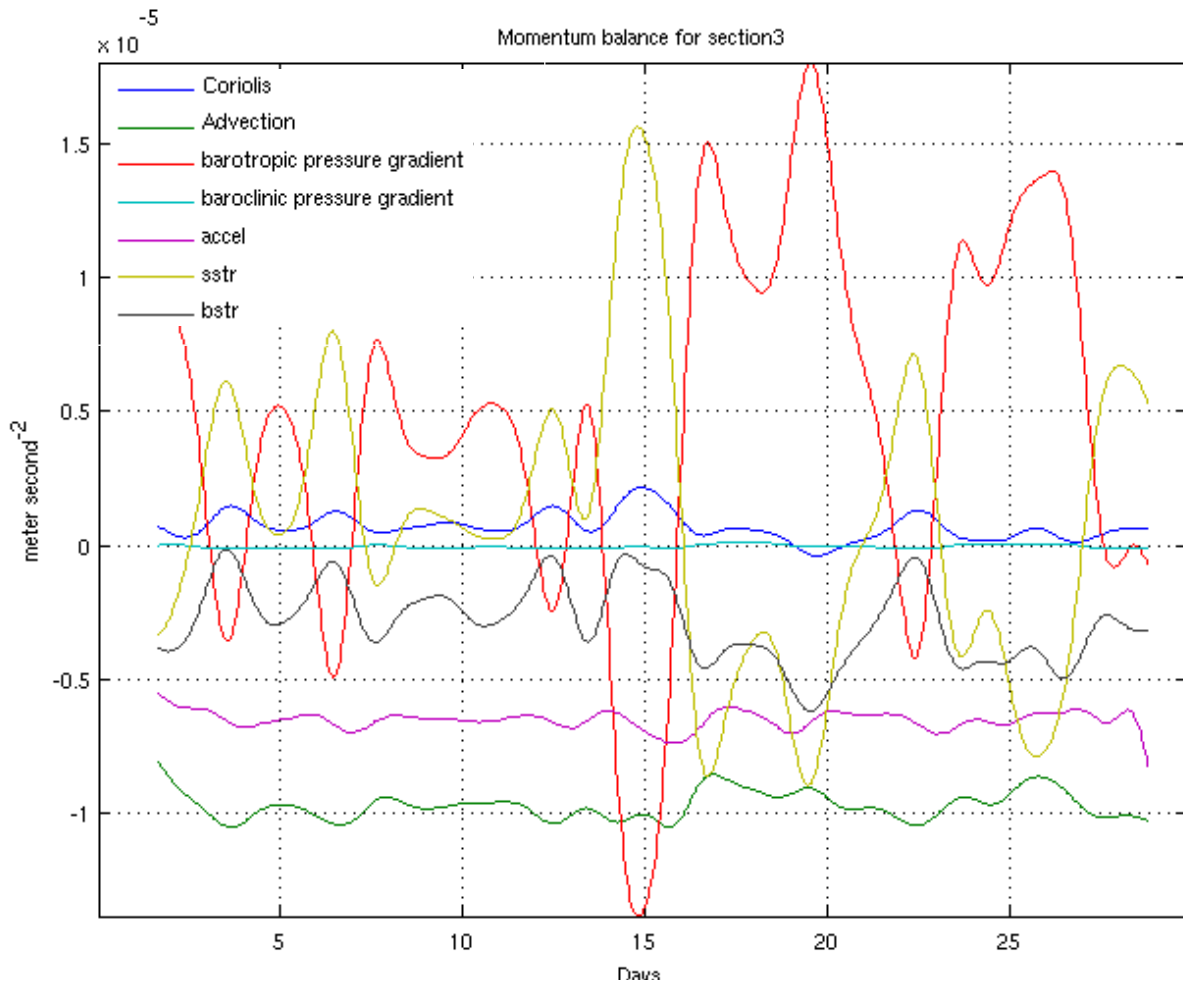


Figure 3-19. Longitudinal momentum terms derived from the momentum balance equation 3.3 in ROMS for transect T3, July, 2008. Line colors indicate the same terms as Figure 3-17.

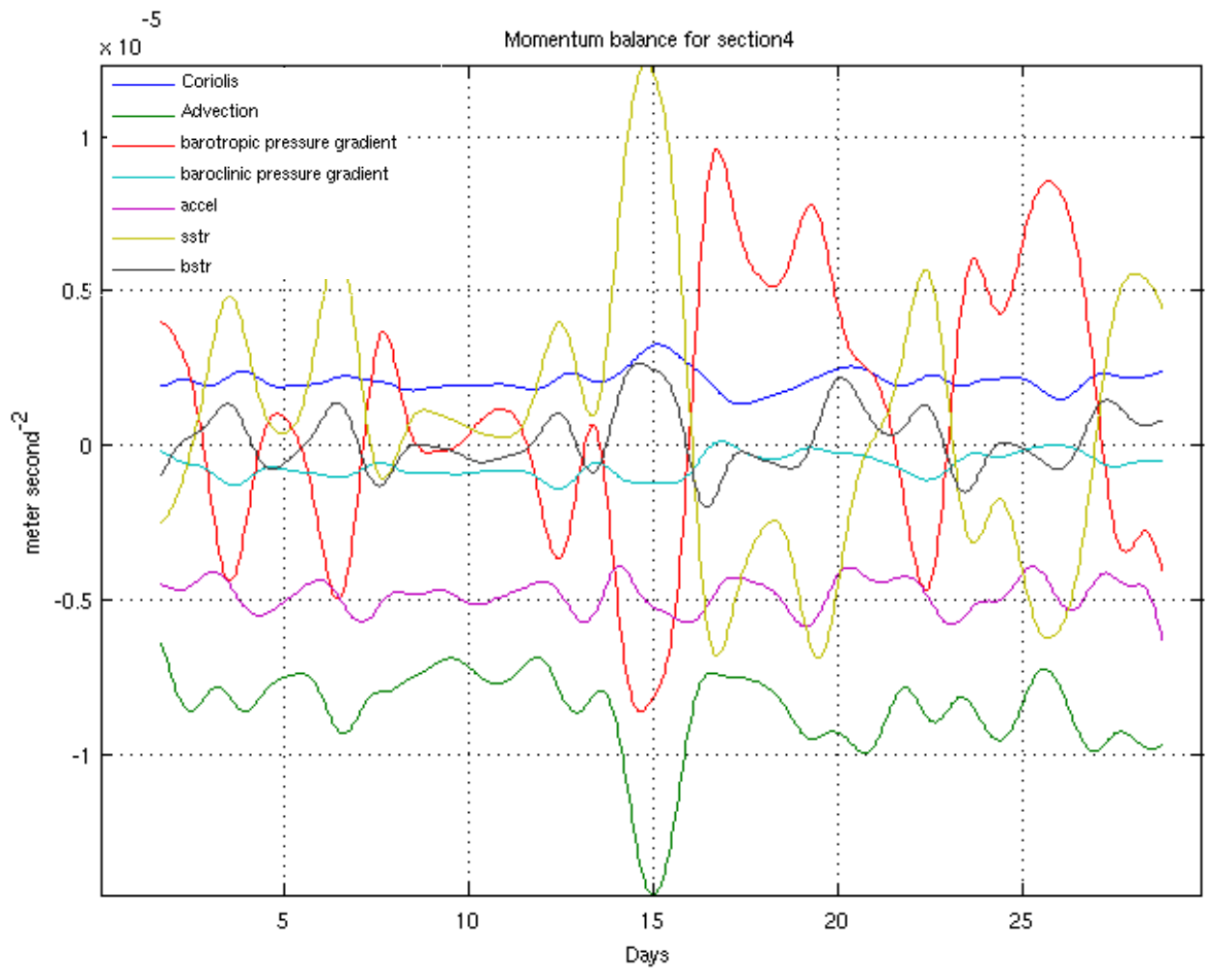


Figure 3-20. Longitudinal momentum terms derived from the momentum balance equation 3.3 in ROMS for transect T4, July, 2008. Line colors indicate the same terms as Figure 3-17.

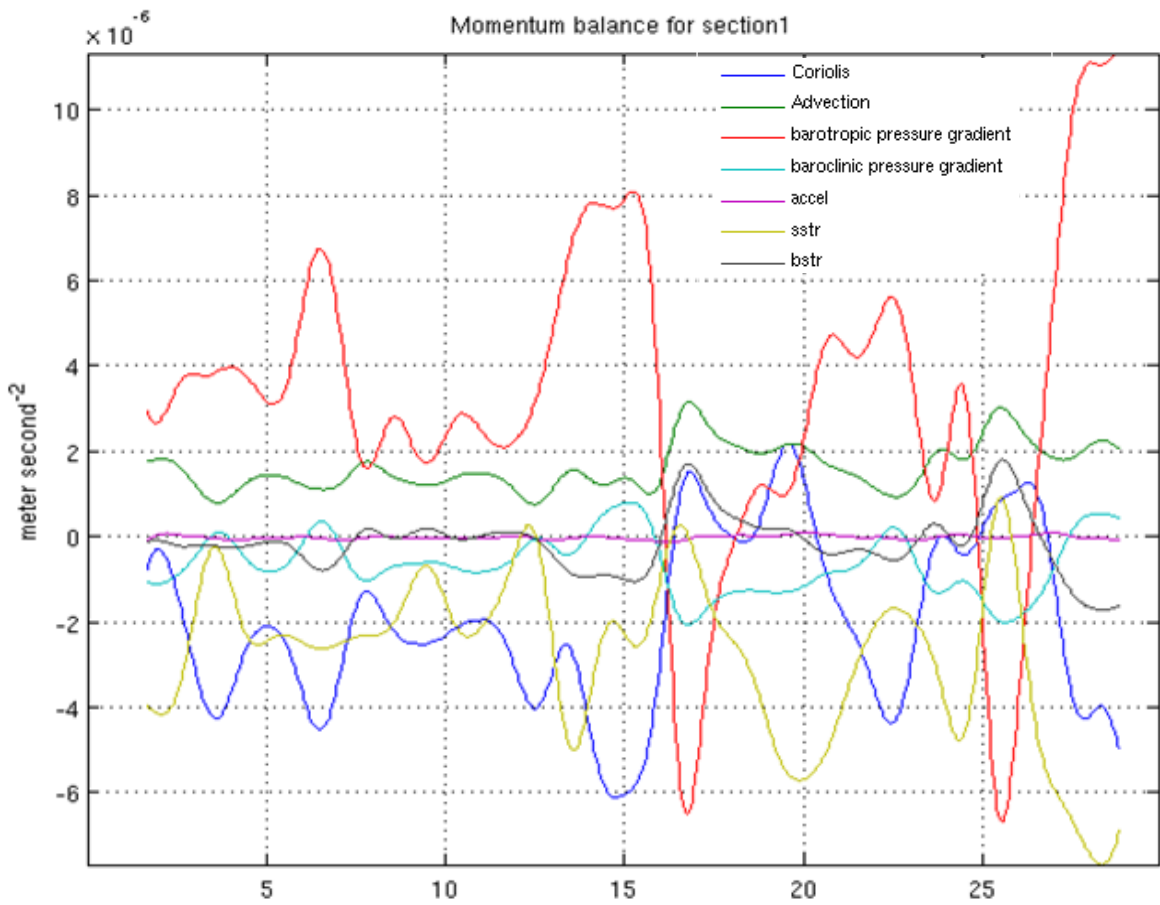


Figure 3-21. Lateral direction momentum terms derived from the momentum balance equation 3.3 in ROMS for transect T1, July, 2008. Line colors indicate the same terms as Figure 3-17.

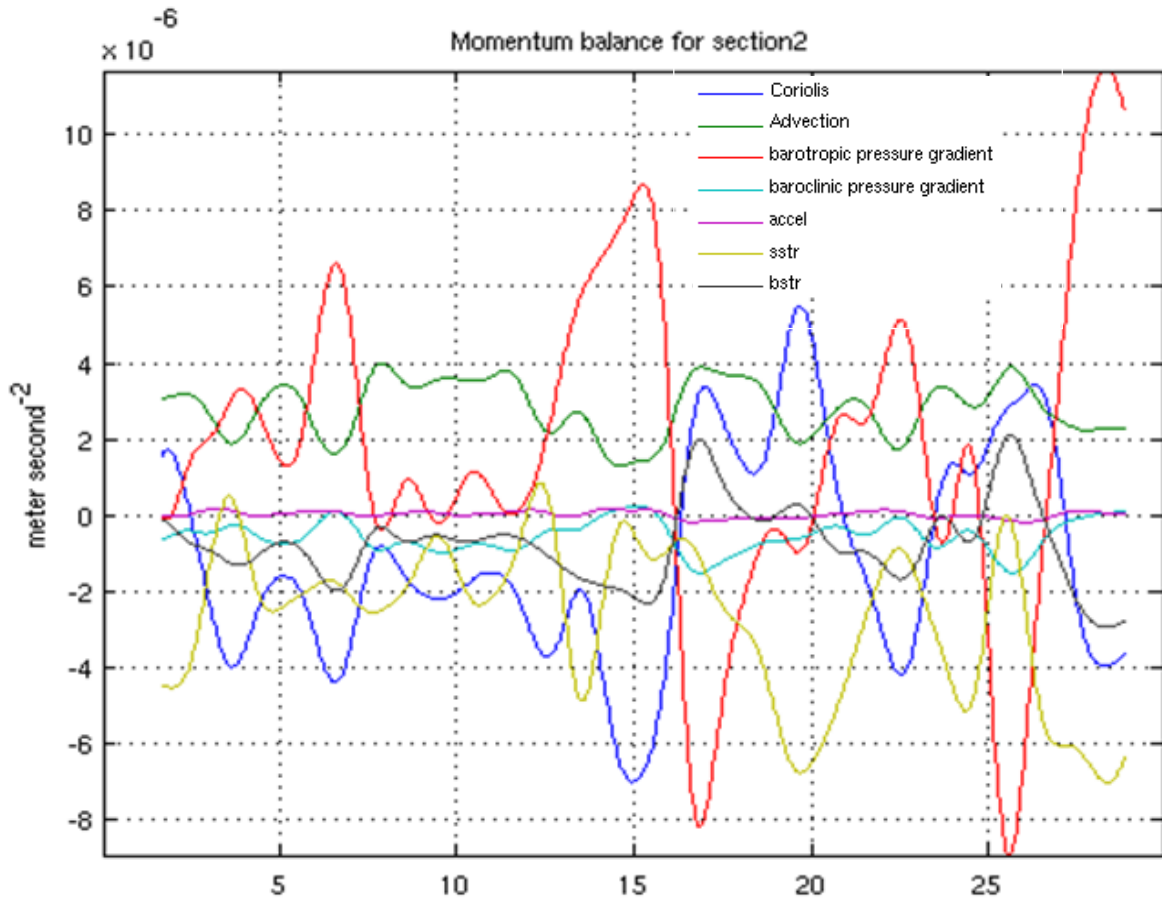


Figure 3-22. Lateral direction momentum terms derived from the momentum balance equation 3.3 in ROMS for transect T2, July, 2008. Line colors indicate the same terms as Figure 3-17.

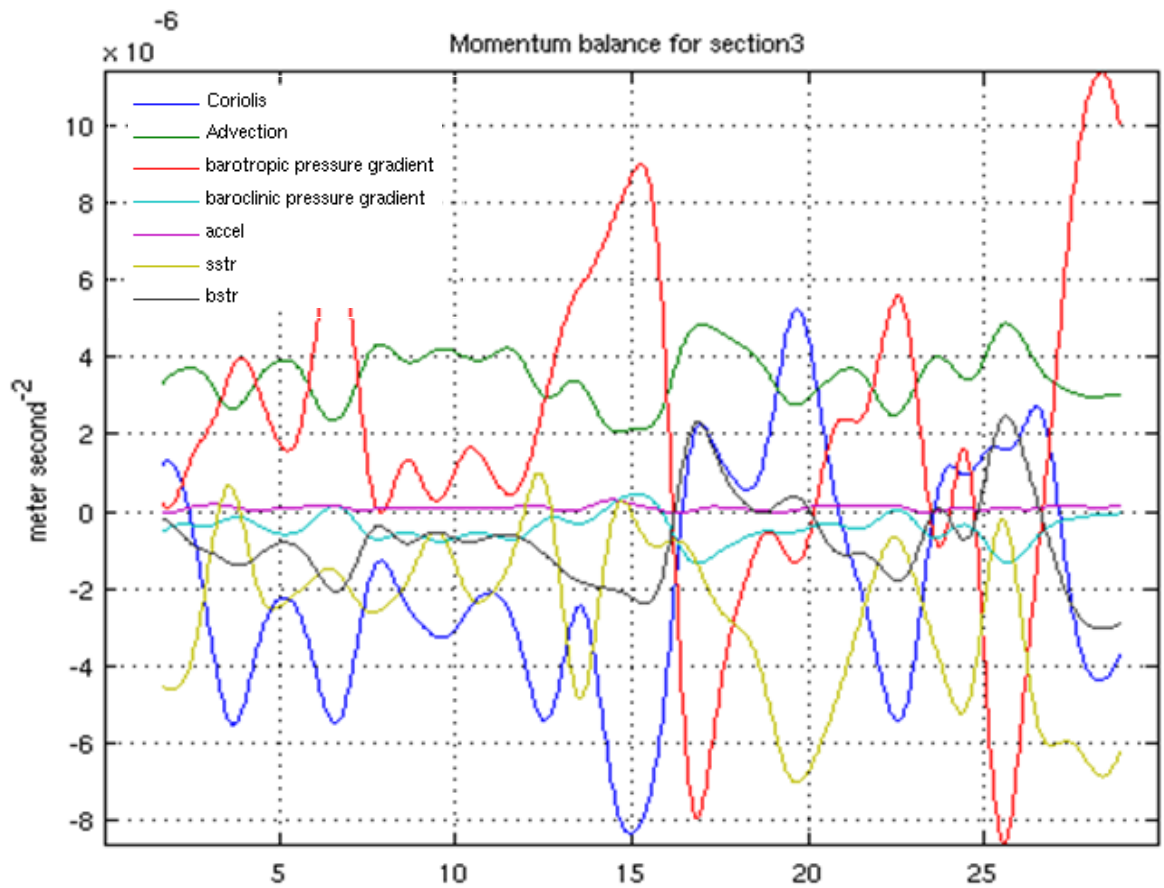


Figure 3-23. Lateral direction momentum terms derived from the momentum balance equation 3.3 in ROMS for transect T3, July, 2008. Line colors indicate the same terms as Figure 3-17.

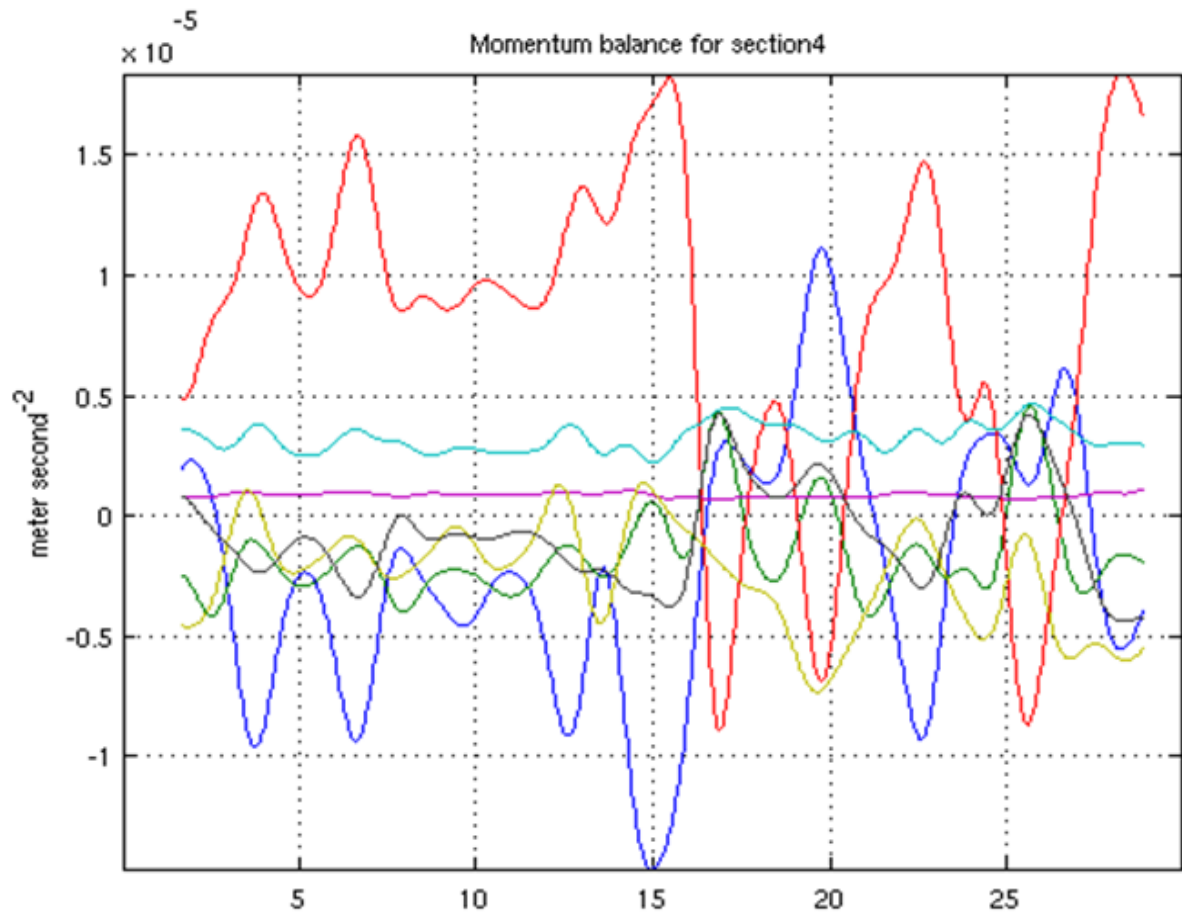


Figure 3-24. Lateral direction momentum terms derived from the momentum balance equation 3.3 in ROMS for transect T4, July, 2008. Line colors indicate the same terms as Figure 3-17.

3.5 Discussion

3.5.1 Current structure analysis

Csanady (1973), Signell (1990), Glorioso and Davies (1995) proposed that in an rectangular, flat-bottom basin, under steady wind forcing, along the longitudinal direction, a typical two-layer vertical shear developed. They also noted that in basins with lateral-varying bathymetry, laterally sheared currents were generated with down-wind currents above shallower areas and up-wind currents in the deeper channel. Across the triangular transects, Wong (1994), Valle and Lwiza (1995), Li and O'Donnell (1997) show that, the lateral variability of residual circulation pattern is generated by the river discharge, gravitational effect, and topography. Wind forcing and local topography may interact and generate lateral residual current variability. For example, local wind forcing generates downwind flows along the shores where the water is shallow and an upwind return flow concentrated in the deep channel. Wong (1994) indicated that wind forcing also interacts with the gravitational effect in generating lateral current variability. Upward local wind may counteract the gravitational circulation through the cross-sections of the estuaries and reduce the transverse residual current shear.

Our results suggest that the residual circulation in the East River and western Narrows is controlled mainly by interactions between the wind stress and the topography, indicating reduced impact of the Harlem River discharge. For example, the longitudinal residual current across T2 transect shown by Figure 3-12 (a) demonstrates a down-wind currents over the shallower area and an up-wind currents over the deeper channel. In western LIS, the wind stress (Figure 3-25) tends to have the opposite direction to the mean transport (Figure 3-12), which is a result of much stronger up-wind transport than the down-wind transport. Our results of the long-term mean current across transects T3 and T4 demonstrated both strong lateral and vertical shear.

There is an up-wind current transport in the northern half section of LIS, and a down-wind current transport in the southern section of LIS. Current structure across T3 demonstrates other complexity: along the shallow north shore area of LIS, there is a down-wind current transport, which is consistent with both Signell (1990) and Wong (1994)'s theory that the gravitational circulation is dominated by a transverse structure with negative inflow concentrating in the deep channel and positive outflow in the shoals. Wong (1994) attributed this current structure to the depth-dependent nature of baroclinic pressure gradient force. In addition, the mean current structure across Transect T4 in Figure 3-12 (c) is very similar to the long term residual longitudinal current isotachs across the Matinlcock Point Section shown by Vieira et al. (2000) (Figure 3-12 (d)), which demonstrates a westward residual flow in the northern half of the transect and a eastward flow in the southern half. The existence of this structure is supported by Schmalz et al. (1994) and Murphy (1979), both of which show that the dominant pattern in both models had a westward motion on the north side of the Sound and eastward motion along the Long Island shore with a cyclonic (counter clockwise) circulation dominating the basin of LIS, as was once proposed by Riley (1956).

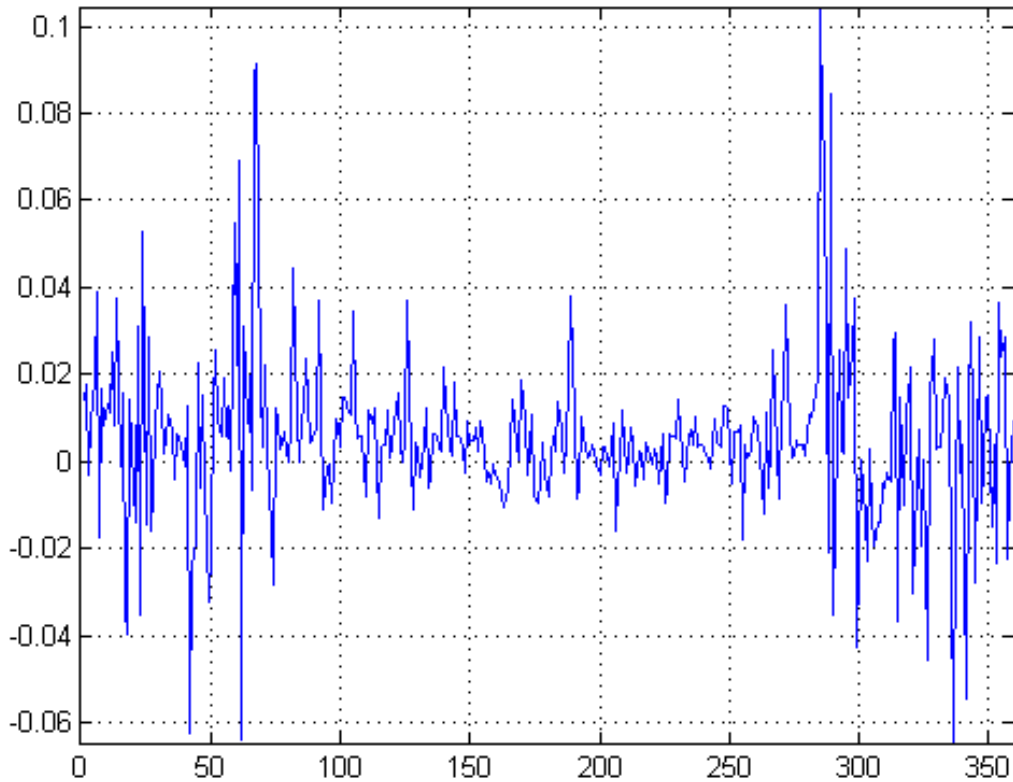


Figure 3-25. Wind stress variation of the Execution Rocks station during year 2008.

3.5.2 Exploration of dynamics controlling the general current structure

Our analysis of Ekman number shows that along the middle channel of LIS, the number is below 0.1, indicating a non-negligible Coriolis effect on the circulation pattern in this area. The Ekman number increases toward the boundary of the domain to approximately 0.5, most likely due to decreased Coriolis effect associated with reduced water depth. In the western Narrows and the East River, Ekman number is approximately 0.2 along the thalweg, and increases to be 0.5 along the northern and southern boundary. Kasai et al. (2000) suggests that with an intermediate Ekman number ($E \sim 0.1$), the inflow of Ise Bay in the Pacific coast of Japan tends to concentrate in the lower layer where the viscosity plays an important role. The flow in the upper layer is determined by geostrophic balance. Our results of Ekman number in the western Narrows of LIS and the East River between 0.2 and 0.5 implies that Coriolis force is important to the circulation pattern in the lateral direction.

3.5.3 Exchange transport

Our results of the exchange transport across the East River and the western Narrows transects were different from previous studies in this area. First, the net transport across this area shown by Figure 3-13 indicates that there is a strong seasonal variability of water transport between the East River and the Narrows, which disagreed with what was found by Blumberg and Pritchard (1997), who suggested that there was very little monthly variability at the Willets Point Section, which was close to the Transect T3 in this Chapter. This chapter suggests that the major mechanism driving to large variation of exchange transport was the wind forcing. This differs

from the result of Blumberg and Pritchard (1997) which indicated that the flux direction and magnitude in the East River were primarily depending on the water elevation differences. Wind forcing had a significant impact on the non-tidal longitudinal residual current structure, which was one of the key components of estimating the long-term exchange transport.

3.5.4 Momentum analysis

Crowley (2005) suggested that in the middle-eastern LIS the non-tidal advective accelerations were directed toward the west and balanced by the eastward accelerations associated with a barotropic pressure gradient in the longitudinal direction. Their sum was directed toward the west and was nearly balanced by the eastward contribution from vertical viscosity. Our results of momentum balance in the East River and western Narrows of LIS show that the momentum balance in this area differs from the middle and eastern of LIS found by Crowley (2005) (Figure 3-17 - Figure 3-20). First, the dominant longitudinal momentum terms over this region are the barotropic pressure gradient force and the surface stress term. Advection, bottom stress and acceleration are the secondary momentum term, which are also important. Coriolis force tends to increase toward transects with deeper water depth, but is less important than the other factors in the longitudinal direction. The Ekman number analysis indicates that Coriolis force play a big role in determining the lateral direction current structure in western LIS. The momentum balance analysis for the lateral direction confirms this: Along the lateral direction, the balance is between barotropic pressure gradient and Coriolis, which suggests that the lateral currents are in geostrophic balance. Coriolis acceleration is dominant term in lateral direction, which is consistent with what the Ekman number suggests. The secondary momentum terms in the lateral direction are advection, surface stress and baroclinicity. Baroclinic pressure gradient plays bigger

role than longitudinal direction. Second, the longitudinal advection term is negative, indicating a westward advection. The advection term derived from our analysis across the East River and western Narrows transects (i.e., within $[0.5 \text{ } 1] \times 10^{-5} \text{ m/s}^2$ range) is larger than that estimated by Fribance et al. (2013) for the Execution Rocks Station and the western LIS station (less than $0.5 \times 10^{-5} \text{ m/s}^2$). This implies a more important role advection might play in the East River and western narrows, compared to the western LIS. Third, Li and O'Donnell (1997) found that the residual mean elevation tends to increase toward the head of the weakly stratified water channel, which set up a seaward residual pressure gradient causing a seaward return flow. Our results of the spatial variation of residual current and the momentum balance analysis tend to agree with this finding. For example, the momentum analysis shows a strong spatial variation of the pressure gradient force, which decreases from inside of the East River toward the western LIS (Figure 3-18, 3-19 and 3-20). This is caused by the net westward residual transport that setup a high pressure in the head of the East River, where the westward residual transport reached the maximum (Figure 3-12).

3.5.5 Model error analysis

This setup of the 3-D model have potential sources of errors. For example, the eastern boundary of model domain is close to the eastern end of LIS, which may affect the tidal prediction in the eastern LIS. However, since western LIS is the focus of this study, the tidal signals in western LIS are reasonably predicted according to Figures 3-7 to 3-10, as well as Tables 3-1 and 3-2. The western boundary of the domain was set along the western end of the East River, which might affect model prediction of current and transport close to this boundary. However, we found it difficult to extend the model domain further to the west without sacrificing the model resolution

in the very narrow East River. We examined current structures far from the western boundary to avoid errors due to the boundary effect. Along the western open boundary, there is no tidal signal prescribed, which is not true in reality. In reality, tide also comes from New York Harbor into the East River. However, the modeled tidal elevation and phases in the East River are in general agreement with the tidal data from the ADCIRC tidal base, which suggests that the tide from the New York Harbor may not play a dominant role in the East River and LIS. Salinity in the model domain is weakly nudged with CTDEEP salinity data, which do not contain sufficient information for the East River. For example, the Harlem River carries relatively low salinity water into the East River, which might have an impact on the water column structure. The model thus might not be able to resolve that impact.

3.6 Conclusion

The response of the East River and western Narrows' water to the wind is controlled by interactions between the surface wind stress and the topography. In general, the residual flow structure was stratified in the upper East River, and both vertically and laterally stratified in the Narrows of LIS. There was a major eastward mean flow in the upper layer of the upper East River. In the lower layer of the water, the mean flow turned toward the west. The mean flow in the western Narrows propagated westward in the north shore of LIS, and in the southern part of LIS the flow was toward the east, and the flow intensity decreased with depths. Across the Execution Rocks Station transect (i.e., T4), there is a westward motion on the north side of the Sound and eastward motion along the Long Island shore, and therefore forms a cyclonic (counter clockwise) gyre in the western Narrow of LIS. The wind stress tends to have an opposite direction to the mean transport due to much stronger up-wind transport than the down-wind

transport. There is a large seasonal variability in the exchange transport in the East River and western Narrows of LIS, with stronger transport during the winter than the summer. The Ekman number in the East River and western Narrows is between 0.2 and 0.5, indicates that Coriolis forcing is important in determining the current flow. The lateral direction momentum balance analysis also indicates that Coriolis force plays a big role in determining the lateral direction current structure in western LIS, which suggests that the lateral currents are in geostrophic balance. The longitudinal momentum balance over the East River and Narrows is dominated by the barotropic pressure gradient force and the surface stress. The advection and baroclinicity are important secondary momentum terms. Coriolis force plays more important role as water deepens. Baroclinity is more important in the lateral direction than the longitudinal direction.

References

- Banas, N. S. and Hickey, B.M. 2005. Mapping exchange and residence time in a model of Willapa Bay, Washington, a branching, macrotidal estuary. *Journal of Geophysical Research*. Vol. 110, C11011.
- Blumberg, A. F. and Pritchard, D. W., 1997. Estimates of the transport through the East River, New York. *J. Geophys Res-Oceans*. 102(C3), 5685-5703.
- Budgell, W.P., 2005: Numerical simulation of ice-ocean variability in the Barents Sea region, *Ocean Dynamics*, DOI 10.1007/s10236-005-0008-3.
- Crowley, H. A. 2005. The seasonal evolution of thermohaline circulation in Long Island Sound. Ph.D. Thesis. Stony Brook University. Stony Brook, New York, USA.
- Csanady, G. T., 1973. Wind-Induced Barotropic Motions in Long Lakes. *Journal of Physical Oceanography*, Volume 3, Pages 429 - 438
- Di Lorenzo, E., 2003: Seasonal dynamics of the surface circulation in the southern California Current System, *Deep-Sea Res., Part II*, 50, 2371-2388.
- Dinniman, M. S., J. M. Klinck, and W. O. Smith Jr. (2003), Cross shelf exchange in a model of the Ross Sea circulation and biogeochemistry, *Deep-Sea Res., Part II*, 50, 3103-3120.
- Fribance, D. B., James O'Donnell and Adam Houk. 2013. Residual circulation in western Long Island Sound. *Journal of Geophysical Research: Oceans*. Vol. 118, 4727–4745, doi:10.1002/jgrc.20329, 2013
- Gay, P. S., J. O'Donnell and C. A. Edwards. 2004. Exchange between Long Island Sound and adjacent waters. *Journal of Geophysical Research* 109, C06017, doi:10.1029/2004JC002319.

- Glorioso, P. and Davies A., 1995. The Influence of Eddy Viscosity Formulation, Bottom Topography, and Wind Wave Effects upon the Circulation of a Shallow Bay. *Journal of Physical Oceanography*. Volume 25, Pages 1243 – 1264.
- Haidvogel, D. B., H. G. Arango, K. Hedstrom, A. Beckmann, P. Malanotte-Rizzoli, and A. F. Shchepetkin (2000), Model evaluation experiments in the North Atlantic Basin: Simulations in nonlinear terrain-following coordinates, *Dyn. Atmos. Oceans*, 32, 239-281.
- Hao, Y., 2008. Tidal and Residual Circulation in Long Island Sound. Ph.D. thesis, School of Marine and Atmospheric Sciences, Stony Brook University, New York.
- Lamont, T., Hutchings, L., van den Berg, M. A. 2015. Hydrographic variability in the St. Helena Bay region of the southern Benguela ecosystem. *Journal of Geophysical Research-Oceans*. Volume: 120 Issue: 4 Pages: 2920-2944
- Lee, Y. 2009. Mechanisms Controlling Variability in Long Island Sound. Stony Brook University.
- Li, C. and O'Donnell, J. 1997. Tidally driven residual circulation in shallow estuaries with lateral depth variation. *J. of Geophysical Research*. 102. C13.
- McCardell, G. and O'Donnell, J., 2009. A novel method for estimating vertical eddy diffusivities using diurnal signals with application to western Long Island Sound, *J. Marine Syst.*, 77(4), 397-408
- Montes, Ivonne, Dewitte, Boris, Gutknecht, Elodie. 2014. High-resolution modeling of the Eastern Tropical Pacific oxygen minimum zone: Sensitivity to the tropical oceanic circulation *Journal of Geophysical Research-Oceans*. Volume: 119 Issue: 8 Pages: 5515-5532

- Moody, J.A., Butman, B., Beardsley, R.C., Brown, W.S., Daifuku, P., Irish, J.D., Mayer, D.A., Mofield, H.O., Petrie, B., Ramp, S., Smith, P., Wright, W.R., 1984. Atlas of Tidal Elevation and Current Observations on the Northeast American Continental Shelf and Slope. U.S. Geological Survey Bulletin 1611, 122.
- Murphy, D.L., 1979. A Numerical Investigation into the Physical Parameters which Determine the Residual Drift in Long Island Sound. Ph.D. Dissertation, Dept. of Marine Sciences, The University of Connecticut.
- O'Donnell, J., Dam, H. G., Bohlen, W. F., Fitzgerald, W., Gay, P. S., Houk, A. E., Cohen, D. C. and Howard-Strobel M. M., 2008. Intermittent ventilation in the hypoxic zone of western Long Island Sound during the summer of 2004. *Journal of Geophysical Research: Oceans* DOI: 10.1029/2007JC004716.
- O'Donnell, J., Dam, H. G., McCardell, G. and Fake, T., 2010. Long Island Sound Study EPA Assistance Award Final Report.
- O'Donnell, J., Wilson, R. E., Lwiza, K., Whitney, M., Bohlen, W. F., Codiga, D., Fake, T., Bowman, M., and Varekamp, J., 2013. The Physical Oceanography of Long Island Sound, in Swanson, R.5 yarish, C. and Latimer, J. (eds), "Long Island Sound". Springer-Verlag Publishing company.
- Pitcher, Grant C., Probyn, Trevor A., du Randt, Andre. 2014. Dynamics of oxygen depletion in the nearshore of a coastal embayment of the southern Benguela upwelling system. *Journal of Geophysical Research*. Volume: 119 Issue: 4 Pages: 2183-2200

- Riley, G. A. 1956. Oceanography of Long Island Sound, 1952-1954. II. Physical Oceanography. Bulletin of the Bingham Oceanographic Collection 15:15-46.
- Schmalz, R.A., Devine, M.F., and Richardson, P.H., 1994. Residual circulation and thermohaline structure, Long Island Sound Oceanography Project Summary Report, Volume 2, NOAA Technical Report NOS-OES-003, National Oceanic and Atmospheric Administration, Rockville, MD, 199 pages.
- Schumann, U. and Gerz, T., 1995. Turbulent Mixing in Stably Stratified Shear Flows, J. Appl. Meteorol. 34, 33–48.
- Scully, Malcolm E.; Geyer, W. Rockwell; Lerczak, James A., 2009. The Influence of Lateral Advection on the Residual Estuarine Circulation: A Numerical Modeling Study of the Hudson River Estuary. J. Phys. Oceanogr., 39, 107–124.
- Signell, R. P., Beardsley, R. C., Graber, H. C., Capotondi, A., 1990. Effect of Wave-Current Interaction on Wind-Driven Circulation in Narrow, Shallow Embayments. Journal of Geophysical Research, Volume 95, No. C6, Pages 9671-9678
- Signell, R. P. and Geyer W. R., 1991. Transient eddy formation around headlands. Journal of Geophysical Research, Volume 96, Issue C2, Pages 2561–2575
- Silva, Nelson; Vargas, Cristian A. Hypoxia in Chilean Patagonian Fjords. 2014. Progress in Oceanography. Volume: 129, Special Issue: SI Pages: 62-74
- Swanson, R.L., Wilson, R.E., Crowley, H.A., 2008. Perspectives on long-term variations in hypoxic conditions in western Long Island Sound. DOI: 10.1029/2007JC004693.

- Torgersen, T., Deangelo, E., O'Donnell, J., 1997. Calculations of horizontal mixing rates using ^{222}Rn and the controls on hypoxia in western Long Island Sound, 1991. *Estuaries* 20, 328–345.
- Valle-Levinson, A. and R. E. Wilson. 1998. Effects of rotation and vertical mixing on volume exchange in eastern Long Island Sound. *Estuarine Coastal and Shelf Science*, 46:573-585.
- Vieira, M. E. C. 1990. Observations of Currents, Temperature and Salinity in Long Island Sound, 1988. A Data Report. , Data Report #6. Marine Sciences Research Center, State University of New York, Stony Brook, New York.
- Vieira, M. E. C. 2000. The long-term residual circulation in Long Island Sound, *Estuaries*, 23(2), 199-207, doi:10.2307/1352827.
- Vigil, H. L. 1991. The fate of dissolved oxygen in Long Island Sound bottom waters, M.S. Thesis, State University of New York, Stony Brook.
- Warner, J.C, C.R. Sherwood, H.G. Arango, and R.P. Signell, 2005a: Performance of four Turbulence Closure Methods Implemented using a Generic Length Scale Method. *Ocean Modelling*, 8, 81-113.
- Welsh, B. L. and Eller, F. C., 1991. Mechanisms Controlling Summertime Oxygen Depletion in Western Long-Island Sound, *Estuaries*, 14(3), 265-278.
- Whitney, Michael M.; Jia, Yan; McManus, Pearse M.; et al. 2014. Sill effects on physical dynamics in eastern Long Island Sound. *Ocean Dynamics*.
Volume: 64 Issue: 3 Pages: 443-458

- Wong, K.-C. 1994. On the nature of transverse variability in a coastal plain estuary. *Journal of Geophysical Research* 99:14,209-14,222. *Journal of Geophysical Research* 99:14,209-14,222.
- Wilkin, J.L., H.G. Arango, D.B. Haidvogel, C.S. Lichtenwalner, S.M. Durski, and K.S. Hedstrom, 2005: A regional Ocean Modeling System for the Long-term Ecosystem Observatory. *J. Geophys. Res.*,110, C06S91, doi:10.1029/2003JC002218.
- Wilson, R. E. and Swanson, R. L., 2005. A perspective on bottom water temperature anomalies in Long Island Sound during the 1999 lobster mortality event. *J. Shellfish Res.* 24(3), 825-830.
- Wilson, R.E. 2007. Final Report of Project: Ferry Based Marine & Atmospheric Observing System.
- Wong, K.-C., The effect of East River on the barotropic motions in Long Island Sound, *J. Mar. Res.*, 49, 321-337, 1991.
- Yu, L., Fennel, K., Laurent, A. 2015. Numerical analysis of the primary processes controlling oxygen dynamics on the Louisiana shelf. *Biogeosciences*. Volume: 12 Issue: 7 Pages: 2063-2076
- Zhang, Wenxia, Hetland, Robert D., DiMarco, Steven F. 2015. Processes controlling mid-water column oxygen minima over the Texas-Louisiana shelf. *Journal of Geophysical Research-Oceans*: Volume: 120 Issue: 4 Pages: 2800-2812

Chapter 4

Exploration of physical and biological mechanisms affecting seasonal hypoxia using the enhanced 1-D and 3-D model results

Abstract

Bacterial dynamics is one of the most important processes in determining the development of seasonal hypoxia in eutrophication models. The approach of adding bacterial dynamics includes adding control equations standing for bacterial growth, respiration, grazing by zooplankton, and consumption of DO during remineralization. With the added bacterial module, eutrophication models are enabled to simulate seasonal DO variability more accurately than those without considering the bacterial dynamics. Along with the importance of the bacterial dynamics, it is instructive to conduct a thorough examination of other mechanisms influencing hypoxia. These mechanisms may include DO production by plankton growth and surface oxygen supply, DO consumption by organic matter remineralization both in the water column and the sediment, DO transport by vertical mixing and horizontal advection. In order to explore these mechanisms and quantify their individual impacts on seasonal hypoxia, we analyze the rates of DO consumption/production, which include the surface flux of DO, detritus remineralization or bacterial consumption, sedimentary DO consumption, as well as horizontal advection of DO. By quantifying these dynamic terms in DO control equation, we are able to demonstrate that DO consumption rate associated with bacterial activities has significantly the largest influence. We also find that perturbing wind mixing contributes at most 30% to the late summer DO variability. Advection plays a non-trivial role in hypoxia development. Ignoring horizontal advection leads to up to 23% of under-estimation of DO during low DO season. DO variability was sensitive to

horizontal advection during low DO season. An examination of DO consumption/ventilation rates indicates that horizontal advection has same order of impact as planktonic photosynthesis in terms of oxygen generation, but it is on three orders less than bacterial DO consumption. We assess the effect of nudging surface nutrient concentration and find that nudging does not generate spurious surface fluxes, which implies this approach could be applied to study biological processes in coastal waters, especially in the cases that the exact nutrient fluxes are unknown.

4.1 Introduction

Interactions among physical and biogeochemical processes have big impacts on the seasonal evolution of DO variation in coastal and estuaries. These processes include air-sea exchange, nutrient input, vertical mixing, horizontal advection, primary productivity, sedimentation and organic matter decomposition, as well as sediment DO demand. The traditional understanding of hypoxia is that bottom DO becomes under-saturated when water density stratification in the overlying water is enhanced. At the same time, wind speeds decline to their minimum, and organic matter decomposition fuels biological oxygen demand (BOD) consuming DO. The recovery of DO from minimum levels is primarily driven by increased mixing (McCardell and O'Donnell 2009; O'Donnell et al. 2008; Welsh and Eller 1991).

Mechanisms controlling oxygen depletion in coastal waters have been studied by using both observational and modeling approaches. Testa et al. (2014) applied the coupled model ROMS/RCA to study the control factors of hypoxia in Chesapeake Bay. They found that nitrogen loading had a large non-linear impact on hypoxia, and identified the importance of phytoplankton growth in connecting nitrogen loading and hypoxic volume. Justic et al. (2014) studied the patterns of temporal and spatial variability in hypoxia on the Inner Louisiana-upper-Texas (LaTex) with the unstructured hydrodynamic model FVCOM. They found the dynamics of hypoxia is controlled by advection of bottom hypoxic water over the mid-continental shelf, frequency of cold fronts and tropical storms, and the bathymetric feature of the shelf. In general, increasing temperature caused by climate warming will reduce solubility of oxygen, thus increasing the occurrence of hypoxia in both lakes and estuaries (Stefan and Fang, 1994; Jankowski et al., 2006). Locally, however, global change may produce opposite effects. For

example, wind speed increase due to global warming may enhance mixing in both marine and freshwater systems, which might relax hypoxic condition. Alterations in the freshwater balance may also reduce density gradients (Neumann, 2010). An observational research in oxygen variability in the Strait of Georgia conducted by Johannessen et al. (2014) found that the advection of anoxic bottom water supplied to the Strait is a much stronger driver than increasing temperature in driving hypoxia. Anthropogenic nutrient loading, on the other hand, is relatively unimportant to hypoxia formation in that area.

In Long Island Sound, Welsh and Eller (1991) found that biological uptake of DO (i.e., mainly through biological respiration activity) in combination with physical re-ventilation are the major mechanism that controls seasonal hypoxia in LIS. Later on, Wilson et al. (2008) argued that the changes of long-term physical processes have a bigger impact on hypoxia in LIS than previously thought. Their analysis of relationship between bottom DO concentration and water column structure indicated that the long-term change of summer winds have an impact on the seasonal hypoxia development. McCardell and O'Donnell (2006) and O'Donnell et al (2007) demonstrated that the majority of physical DO transport to the bottom waters of western LIS is due to vertical mixing across the pycnocline, rather than the lateral mixing. O'Donnell et al. (2008) also reported that 9 out of 11 observed hypoxic events associated with ventilation at the Execution Rocks station in LIS resulted from enhanced vertical mixing instead of horizontal advection, and they attributed over 80% of the ventilation events during hypoxia to vertical mixing in western LIS. Even though O'Donnell's study emphasized the importance of vertical mixing on the DO ventilation, Lee and Lwiza (2008) found that DO recovery was not associated with increased wind mixing alone, and they proposed that it might be induced by enhanced horizontal exchange or reduced microbial activity.

In Chapter 2, we developed a 1-D coupled physical-biogeochemical model to simulate the bacterial dynamics by adding a new module representing the bacterial dynamics, so that the impact of bacterial activity on the DO dynamics could be evaluated for the western LIS. This module includes equations standing for the aerobic bacterial biomass growth, respiration, regeneration of inorganic nitrogen and phosphate, and zooplankton grazing on bacteria. Also added are the equations representing the contributions of bacterial remineralization and zooplankton excretion to inorganic nutrient regeneration. With the enhanced model, we show that with bacterial dynamics, the simulated DO variation during year 2008 is much closer to the observations, compared to the model without bacterial dynamics. The relative difference of DO concentration before and after adding bacterial dynamics may be up to 7 fold. Therefore, we conclude that the bacterial dynamics is a necessary component in the biogeochemical model in order to simulate development of seasonal hypoxia in western LIS properly. In addition, by including the bacterial dynamics, we eliminate the need of artificially modifying vertical mixing or phytoplankton respiration rate to simulate observed seasonal variability in DO as was done in the past.

In this chapter, the mechanisms responsible for this change will be examined further by analyzing the individual dynamic terms standing for respective dynamic processes from the DO governing equation. These processes include the DO consumptions/production through the phytoplankton growth and respiration, sedimentary remineralization, bacterial remineralization of organic matter, and surface oxygen flux. Also important in this chapter, the role of wind induced vertical mixing in DO variability is quantified in the way that DO variations driven by the observed wind forcing and lagged wind forcing are compared. In addition, the horizontal advection of momentum flux derived from Chapter 3 with the 3-D ROMS, together with the

horizontal DO advection are used in the 1-D coupled model (i.e., GOTM/ERGOM) in order to examine the role of horizontal advection in affecting seasonal hypoxia in western LIS.

This chapter is organized in the following manner. Section 4.2 introduces the study area. Section 4.3 describes the approaches applied to analyze the effects that bacterial dynamics have on seasonal DO variation, to examine the role of wind forcing and the importance of addition of horizontal advection to DO variation. The results of the mechanism analysis are presented in Section 4.4. A comprehensive discussion of physical and biological mechanisms leading to seasonal hypoxia is shown in Section 4.5. At the end of Section 4.5, implications on future coastal hypoxia modeling are provided. Conclusions from this Chapter are presented in Section 4.6.

4.2 Study area

LIS is a 20x150 km estuary with an average depth of 20 m. LIS is made up of four major basins (i.e., the Eastern Basin, the Central Basin, the Western Basin and the Narrows) separated by several sills and shoals (Figure 4-1). Among these four major basins, the western Basin, with a deep channel continuing to the eastern part of the Narrows, is separated by Cable and Anchor Reef (Vieira 2000). Freshwater enters the Sound from runoff and drainage along the coast of Long Island, New York, and Connecticut. Freshwater discharge reaches its maximum during the spring freshet. Up to 90% of the freshwater input into the Sound comes from the discharge of three major rivers, namely, Thames River, Housatonic River, and Connecticut River, among which Connecticut River contributes 74% of the total freshwater discharge. Sewage treatment plants also contribute approximately 1% of the total annual freshwater input (Boon 2008). Since the early 1970s, the western Narrows of LIS has exhibited seasonally developed hypoxia in the bottom waters (Anderson et al. 2001). Figure 4-2 shows the percent of hypoxia between 1991 and 2011 in Long Island Sound. The western LIS exhibited the most percent of occurrence of hypoxia. The location of the Execution Rocks Lighthouse Station A4 is highlighted in Figure 4-1, and this is the location that the 1-D coupled model runs for.

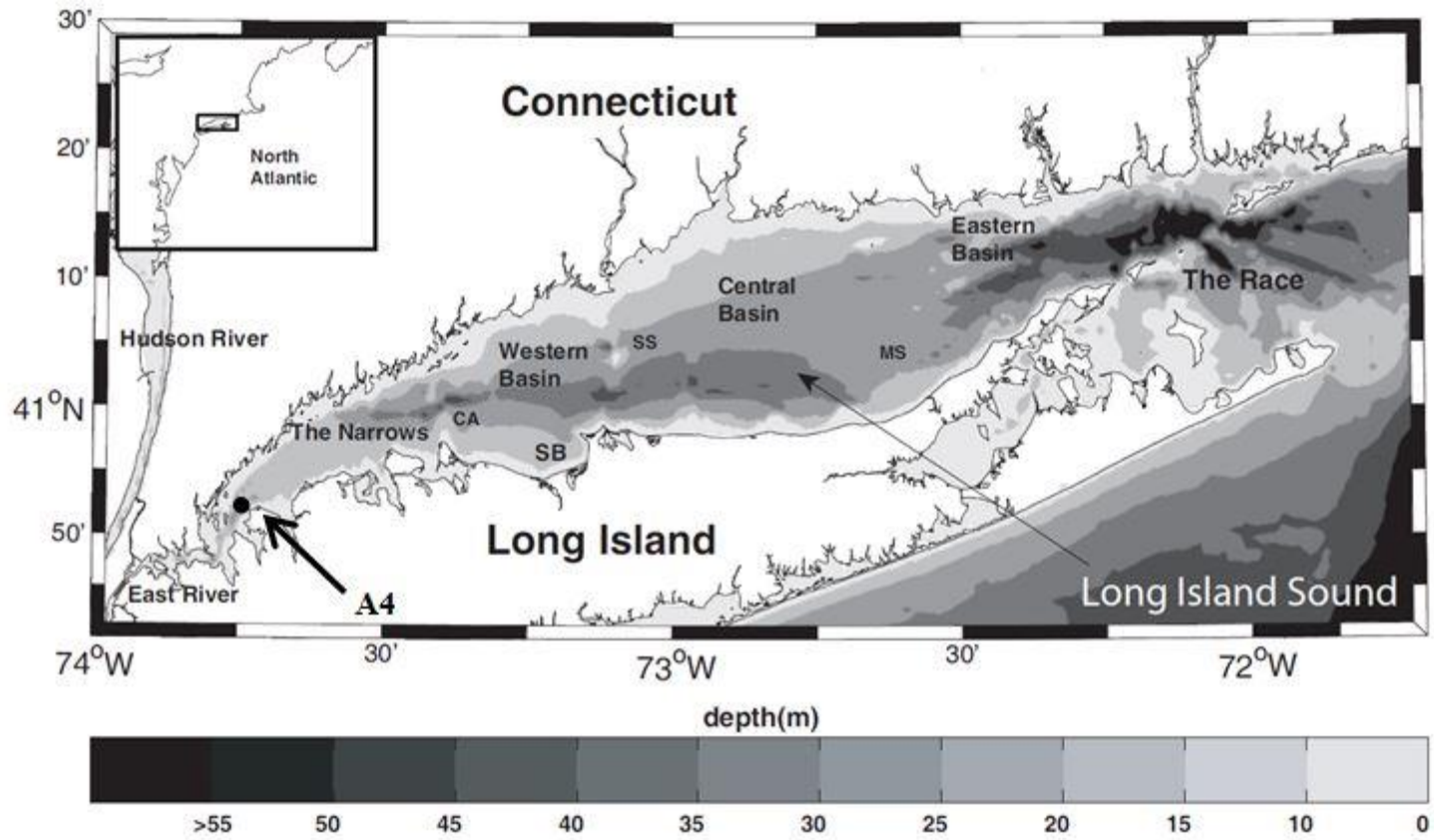


Figure 4-1. Long Island Sound Bathymetry (Lee 2009).

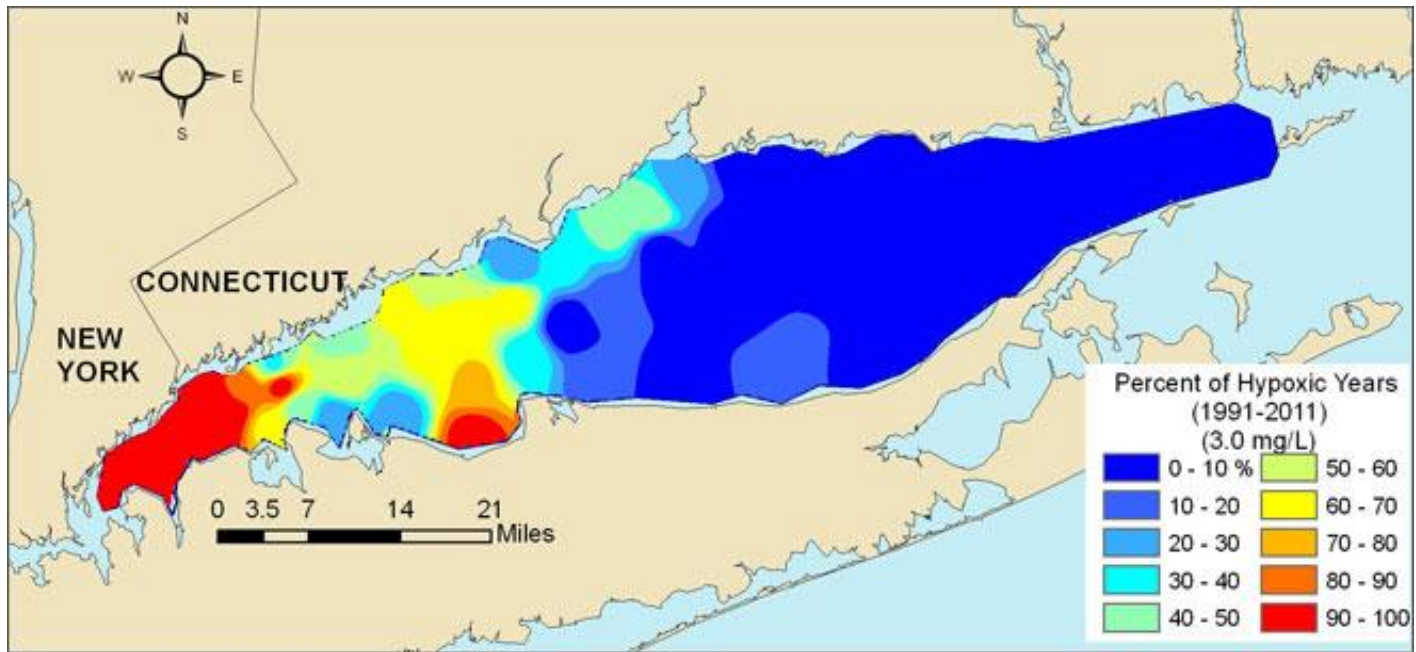


Figure 4-2. Percent of Hypoxia between 1991 and 2011 in Long Island Sound (Long Island Sound Study).

4.3 Methods

4.3.1 Examination of mechanisms leading to further DO reduction due to added bacterial dynamics

In order to examine how variability in bottom DO is influenced by bacterial dynamics, DO variability from the original model without bacterial dynamics is compared to results from the bacterial dynamics-inclusive model. The ratio between bottom DO concentrations from the bacterial dynamics-excluded model divided by the output from the bacterial dynamics-included model has been shown and analyzed in Chapter 2. The terms in the model that determine DO dynamics are extracted to assess the model's sensitivity to drivers of DO variability. These terms stand for the rates of DO consumption/production and surface oxygen flux with a unit of $\text{mmol O m}^{-3} \text{ hr}^{-1}$. Figure 4-3 shows the DO dynamics from the model with the bacterial dynamics included. In comparison, the DO dynamics from the model without the bacterial dynamics is shown by Figure 4-4.

4.3.2 Examination of the role of wind-induced vertical mixing

There are basically two schools of thought about the mechanism of hypoxia recovery in late summer or early fall. The generally accepted one is that recovery results from increased wind mixing (McCardell and O'Donnell 2009; O'Donnell et al. 2008; Welsh and Eller 1991).

However, there are other studies indicating that increased wind mixing is not the only factor leading to oxygen recovery. Oxygen recovery can also be caused by reduced microbial activity or enhanced horizontal advection (Lee and Lwiza 2008). We hypothesize that the timing of DO recovery is driven by increased wind forcing, and test this hypothesis by conducting twin

experiments: (i) in the first, the model is forced by the normal wind speed, (ii) in the second experiment, the wind speed is lagged one month behind observations to drive the model during the same period. We then compare wind speed and DO pattern from both experiments. The impact of horizontal advection on DO variability is also added into the 1-D coupled model and compared to the effect of vertical mixing. The approach of examining the impact of wind-induced horizontal momentum flux on DO variation is discussed in the next Section (Section 4.3.3). The results and discussion of the impact are described in Section 4.4.4 and 4.5.2, respectively.

4.3.3 Exploring the importance of horizontal advection to DO variation

In order to explore the impact of horizontal advection on seasonal hypoxia in western LIS, the 1-D GOTM was modified to be able to read the u and v components of the horizontal advection from an ASCII file from ROMS. The following equations represent horizontal momentum flux,

$$\frac{dU}{dt} = D_U - g \frac{\partial \zeta}{\partial x} + \int_z^{\zeta} \frac{\partial B}{\partial x} dz' - \frac{1}{\tau_R} (U - U_{obs}) - C_f U \sqrt{U^2 + V^2} \quad (4.1)$$

$$\frac{dV}{dt} = D_V - g \frac{\partial \zeta}{\partial y} + \int_z^{\zeta} \frac{\partial B}{\partial y} dz' - \frac{1}{\tau_R} (V - V_{obs}) - C_f V \sqrt{U^2 + V^2} \quad (4.2)$$

Where $\frac{dU}{dt}$ and $\frac{dV}{dt}$ denotes the material derivative of U and V , ζ the free surface elevation and

B the mean buoyancy. $D_{U/V}$ is the sum of the turbulent and viscous transport terms modelled according to,

$$D_U = \frac{\partial}{\partial z} ((\nu_t + \nu) \frac{\partial U}{\partial Z} - \overline{\tau_U}) \quad (4.3)$$

and,

$$D_V = \frac{\partial}{\partial z} ((\nu_t + \nu) \frac{\partial V}{\partial Z} - \overline{\tau_V}) \quad (4.4)$$

In the equations (4.3) and (4.4), ν_t and ν are the turbulent and molecular diffusivities of momentum, respectively, and $\overline{\tau_{U/V}}$ denotes the non-local flux of momentum. $\overline{\tau_{U/V}}$ in GOTM was modified and enabled to be read from an ASCII file, in which the u, v components of the total advection derived from the 3-D ROMS (Chapter 3) were included.

In addition to the inclusion of the non-local momentum flux, we also added horizontal DO advection term $\vec{V} \nabla c_i$ (i.e., $u \frac{\partial DO}{\partial x}$, mainly longitudinal advection) into the oxygen control

equation in ERGOM, which is,

$$\frac{\partial oxy}{\partial t} + \frac{\partial}{\partial z} (m_i * oxy - K_V \frac{\partial oxy}{\partial z}) = P(oxy) - D(oxy) \quad (4.5)$$

The addition of horizontal advection modified the control equation to be:

$$\begin{aligned} \frac{\partial oxy}{\partial t} + \left\{ \vec{V}_{B2 \rightarrow A4} \frac{(oxy_{B2} - oxy_{A4})}{X_{B2} - X_{A4}} + \vec{V}_{A3 \rightarrow A4} \frac{(oxy_{A3} - oxy_{A4})}{X_{A3} - X_{A4}} \right\} \\ + \frac{\partial}{\partial z} (m * oxy - K_V \frac{\partial oxy}{\partial z}) = P(oxy) - D_i(oxy) \end{aligned} \quad (4.6)$$

where $\vec{V}_{B2 \rightarrow A4}$ and $\vec{V}_{A3 \rightarrow A4}$ are the eastward and westward longitudinal velocity at Station A4 estimated by the model. $\frac{(oxy_{B2} - oxy_{A4})}{X_{B2} - X_{A4}}$ and $\frac{(oxy_{A3} - oxy_{A4})}{X_{A3} - X_{A4}}$ are the eastward and westward gradients of oxygen concentration, respectively.

We quantify the relationship of oxygen gradients between A3 and A4, and between A4 and B2 based on survey results of New England Interstate Water Pollution Control Commission (NEIWPCC). We then estimate the eastward oxygen transport between A3 and A4 based on this relationship and O'Donnell et al. 2008's measurement of the westward transport between WS (close to Station B2) and EX (at A4) (Figure 4-3).

Figure 4-5 (result from Chapter 3) shows that between A3 and A4, there is an eastward non-tidal transport, which potentially transports oxygenated/non-oxygenated water eastward from the west of A4. Between A4 and B2, there is a westward transport from the east to A4.

Mid-July NEIWPCC Survey results (Figure 4-4 (a)) show that DO gradient between A3 and A4 is very weak (almost zero). For late-July survey (Figure 4-4 (b)), DO gradients are similar between A3 and A4, and between A4 and B2 (i.e., Station WS in O'Donnell et al. 2008). DO level is lower at A4 (<3.0 mg/L), and higher at A3 and B2 (3-3.99 mg/L). Due to a net eastward transport between A3 and A4 (Figure 4-5), and a westward transport between B2 and A4 (Figure 19), the increasing rate of DO production at Station A4 due to horizontal advection is expected to double in late July.

In August, there is a stronger (i.e., 25% stronger) eastward gradient between A3 and A4 than the westward oxygen gradient between B2 and A4 (Figure 4-4 (c)). In early September, gradient between A3 and A4 is zero (Figure 4-4 (d)). During mid-September (Figure 4-4 (e)), there is a westward transport of oxygenated water from B2 to A4, and an eastward transport of less oxygenated water from A3 to A4, the oxygen gradients have same magnitude and direction between A3 and A4, and between A4 and B2 (i.e., all toward the west).

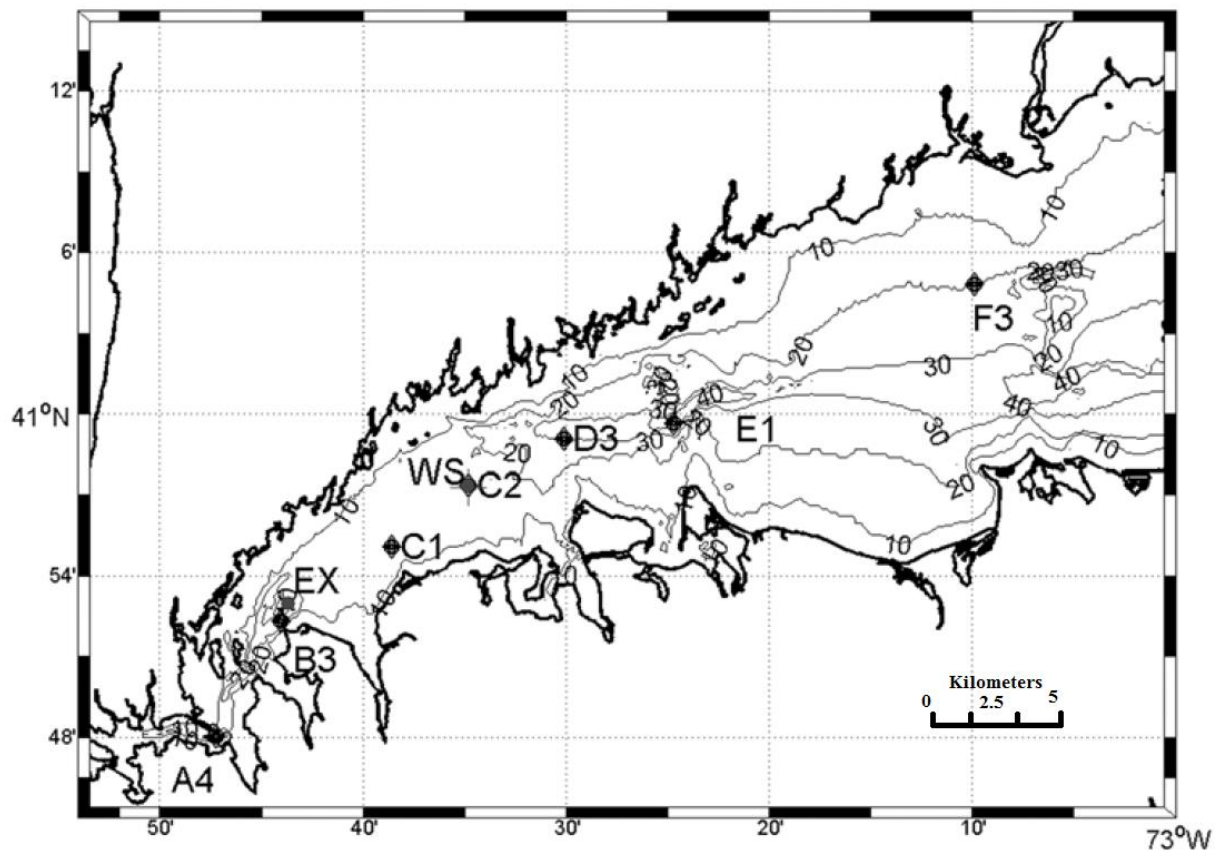
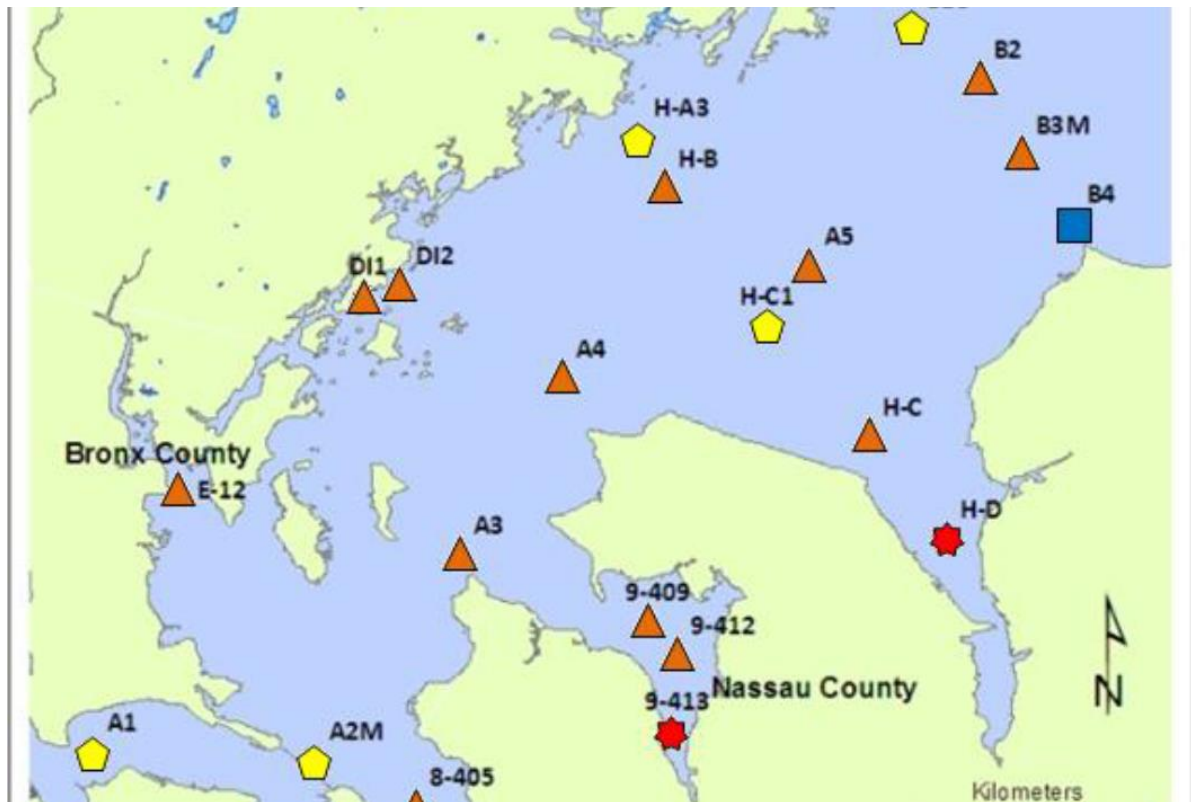


Figure 4-3. Map of the shoreline of western Long Island Sound showing the location of the Execution Rocks Buoy and western LIS Station (EX and WS on the map) used to estimate horizontal DO gradient (O'Donnell et al. 2008).



**NEIWPCC-IEC DISTRICT
2014 WLIS SAMPLING STATIONS**

Survey #3 Dissolved Oxygen Concentration in Bottom Waters






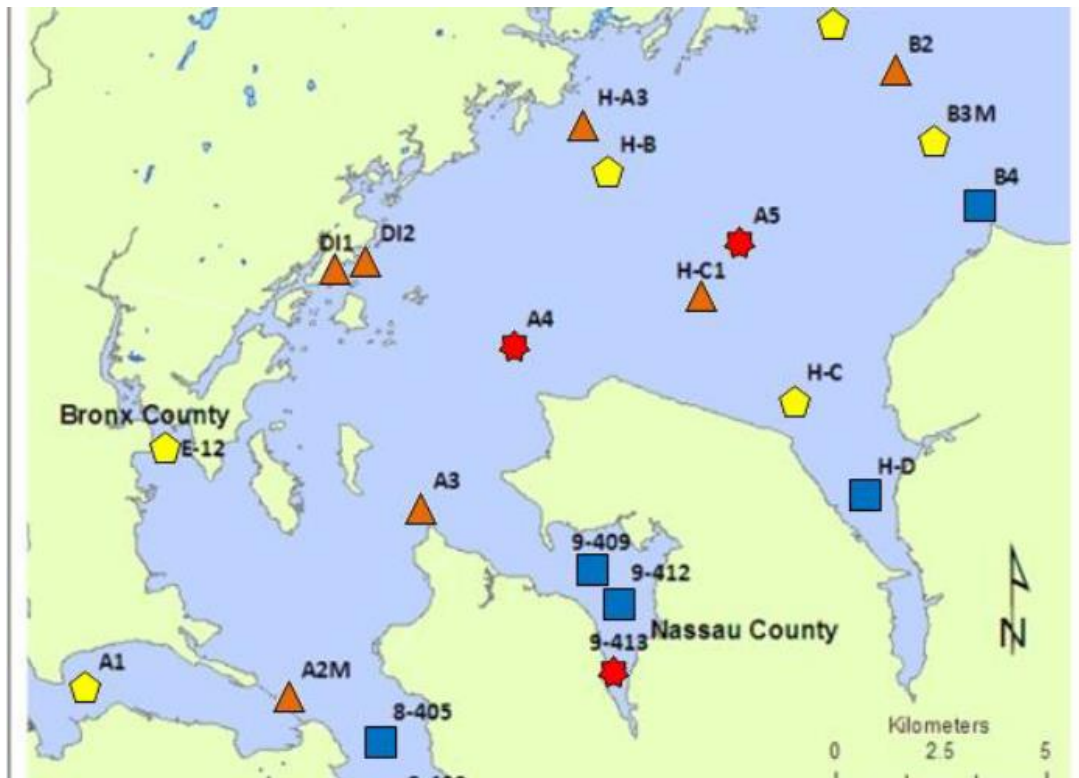
-  < 3.0 mg/L (Severe-Moderately Severe)
-  3.0 mg/L - 3.99 mg/L (Marginal)
-  4.0 mg/L - 4.79 mg/L
-  4.8 mg/L - 5.00 mg/L
-  > 5.0 mg/L (Excellent)

Figure 4-4 (a). NEIWPCC-IEC District western LIS sampling stations. Levels of oxygen were estimated from Mid-July Survey of 2014 (NEIWPCC 2014)



**NEIWPC-IEC DISTRICT
2014 WLIS SAMPLING STATIONS**

Survey #3 Dissolved Oxygen Concentration in Bottom Waters






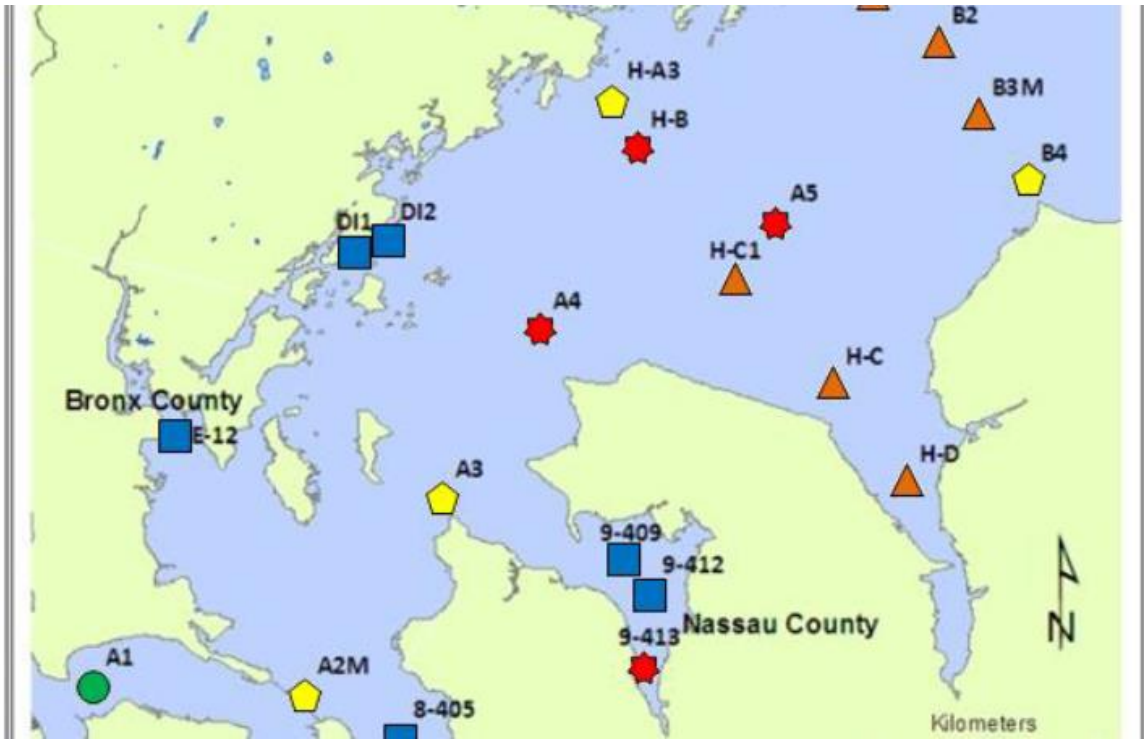
-  < 3.0 mg/L (Severe-Moderately Severe)
-  3.0 mg/L - 3.99 mg/L (Marginal)
-  4.0 mg/L - 4.79 mg/L
-  4.8 mg/L - 5.00 mg/L
-  > 5.0 mg/L (Excellent)

Figure 4-4 (b). NEIWPC-IEC District 2014 western LIS sampling stations. Levels of oxygen were estimated from Late-July (NEIWPC 2014)



**NEIWPCC-IEC DISTRICT
2014 WLIS SAMPLING STATIONS**

Survey #3 Dissolved Oxygen Concentration in Bottom Waters






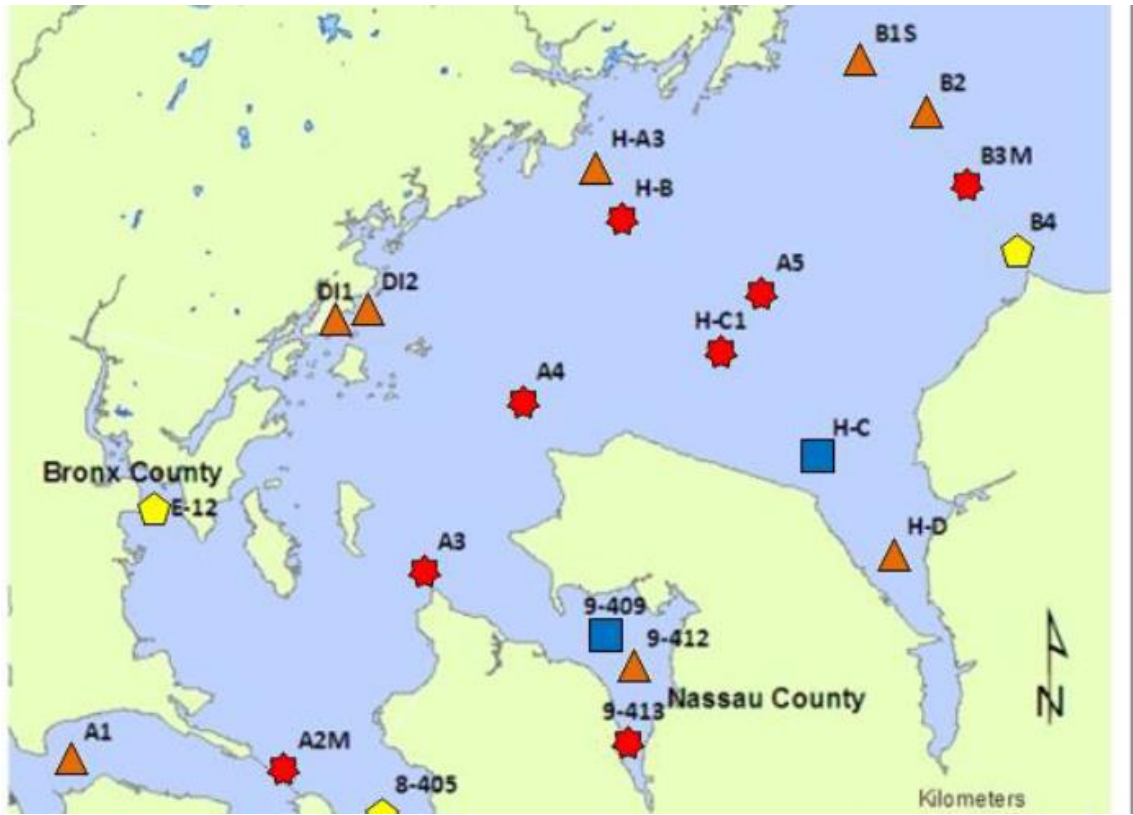
-  < 3.0 mg/L (Severe-Moderately Severe)
-  3.0 mg/L - 3.99 mg/L (Marginal)
-  4.0 mg/L - 4.79 mg/L
-  4.8 mg/L - 5.00 mg/L
-  > 5.0 mg/L (Excellent)

Figure 4-4 (c). NEIWPCC-IEC District 2014 western LIS sampling stations. Levels of oxygen were estimated from August (NEIWPCC 2014)



**NEIWPC-IEC DISTRICT
2014 WLIS SAMPLING STATIONS**

Survey #3 Dissolved Oxygen Concentration in Bottom Waters






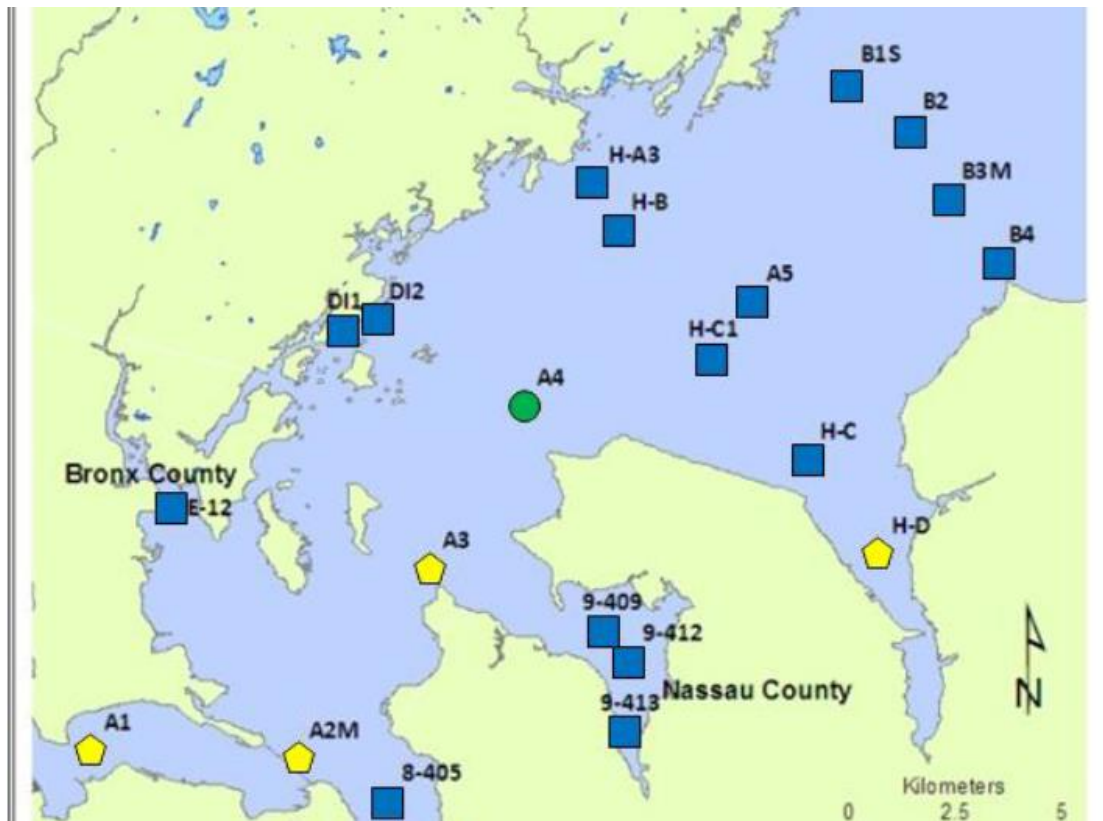
-  < 3.0 mg/L (Severe-Moderately Severe)
-  3.0 mg/L - 3.99 mg/L (Marginal)
-  4.0 mg/L - 4.79 mg/L
-  4.8 mg/L - 5.00 mg/L
-  > 5.0 mg/L (Excellent)

Figure 4-4 (d). NEIWPC-IEC District 2014 western LIS sampling stations. Levels of oxygen were estimated from Early September (NEIWPC 2014)



**NEIWPC-IEC DISTRICT
2014 WLIS SAMPLING STATIONS**

Survey #3 Dissolved Oxygen Concentration in Bottom Waters






-  < 3.0 mg/L (Severe-Moderately Severe)
-  3.0 mg/L - 3.99 mg/L (Marginal)
-  4.0 mg/L - 4.79 mg/L
-  4.8 mg/L - 5.00 mg/L
-  > 5.0 mg/L (Excellent)

Figure 4-4 (e). NEIWPC-IEC District 2014 western LIS sampling stations. Levels of oxygen were estimated from Middle of September (NEIWPC 2014)

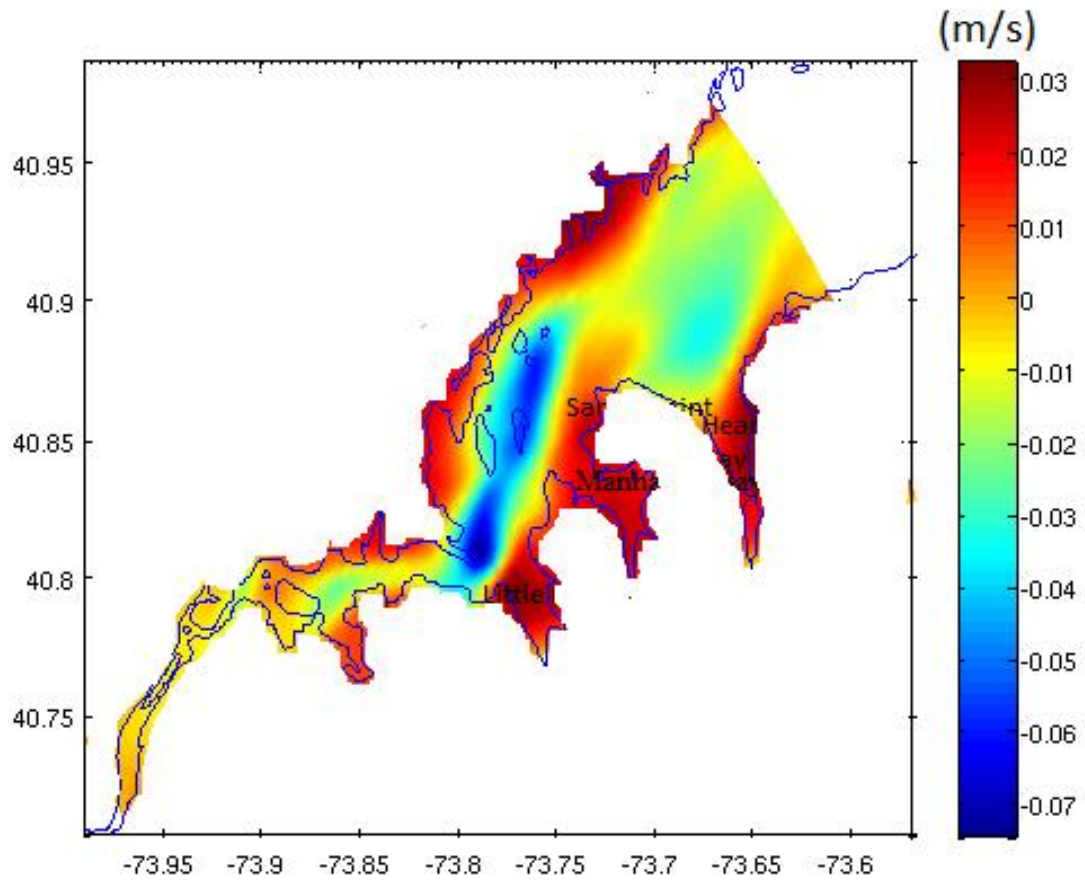


Figure 4-5. Along channel non-tidal transport estimated from the u momentum equation. Positive transport is toward the east.

4.3.4. Estimating the nutrient flux due to surface nudging of nutrient concentration

In order to examine the impact of nutrient nudging at the surface, we estimated the nutrient flux due to surface nudging. This was achieved by approximating the flux difference between the experiments with and without nudging. Because we do not know the surface nutrient flux in western LIS, we set it as a function of monthly change of surface nutrient concentration (CTDEEP) with an average value of $6 \text{ mmol N m}^{-2} \text{ d}^{-1}$, and allowed the physics to mix it throughout the water column. The relaxation time scale of nudging is one month. We conducted two cases of experiments and analyzed results from the experiments, namely (i) Case I: microbial loop on, and (ii) Case II: microbial loop off. Then the percentage of nutrient concentration difference between nudging and no-nudging experiments for both cases was plotted in Figure 4-17. The nutrient flux generated by nudging was calculated as the nutrient concentration difference within one unit time and depth level. The individual components of fluxes calculated as nutrient difference between nudging and no-nudging experiments for both cases were shown by Figure 4-18 (a) and (b). Finally, Figure 4-19 shows the sum of nutrient fluxes due to nudging.

4.4 Results

4.4.1 Mechanisms controlling DO variability

In order to examine the effect of microbial activity on DO levels, we examined the dynamics of non-linear DO production and consumption in $\text{mmol O m}^{-3} \text{ hr}^{-1}$ from the model with bacterial activity in Figure 4-5. In comparison, Figure 4-6 shows these processes without the microbial activity. Both Figure 4-6 and 4-7 indicate that the DO dynamics are determined by processes of

surface flux of DO, detritus remineralization (which inherently includes a non-parameterized bacterial dynamics) or bacterial consumption (a model that explicitly includes bacterial dynamics), and sedimentary DO consumption. There are three major processes in controlling DO variability with two to three orders higher of magnitudes than the other rates in Figure 4-6 and 4-7. Comparison of these three terms between the model run without (Figure 4-6) and with (Figure 4-7) bacterial dynamics show that sedimentary DO consumption and surface flux did not change significantly. However, water column DO consumption rate obtained by including the bacterial dynamics is significantly larger than that produced by the model with only detritus remineralization without any artificial tuning of parameters.

Figure 4-8 also shows the contributions of water and sedimentary oxygen consumption. Without bacterial activity, oxygen consumption in the water column is up to approximately 40% of sedimentary oxygen consumption. With bacterial activity, oxygen consumption within water column reached as high as 75% of the consumption in the sediment.

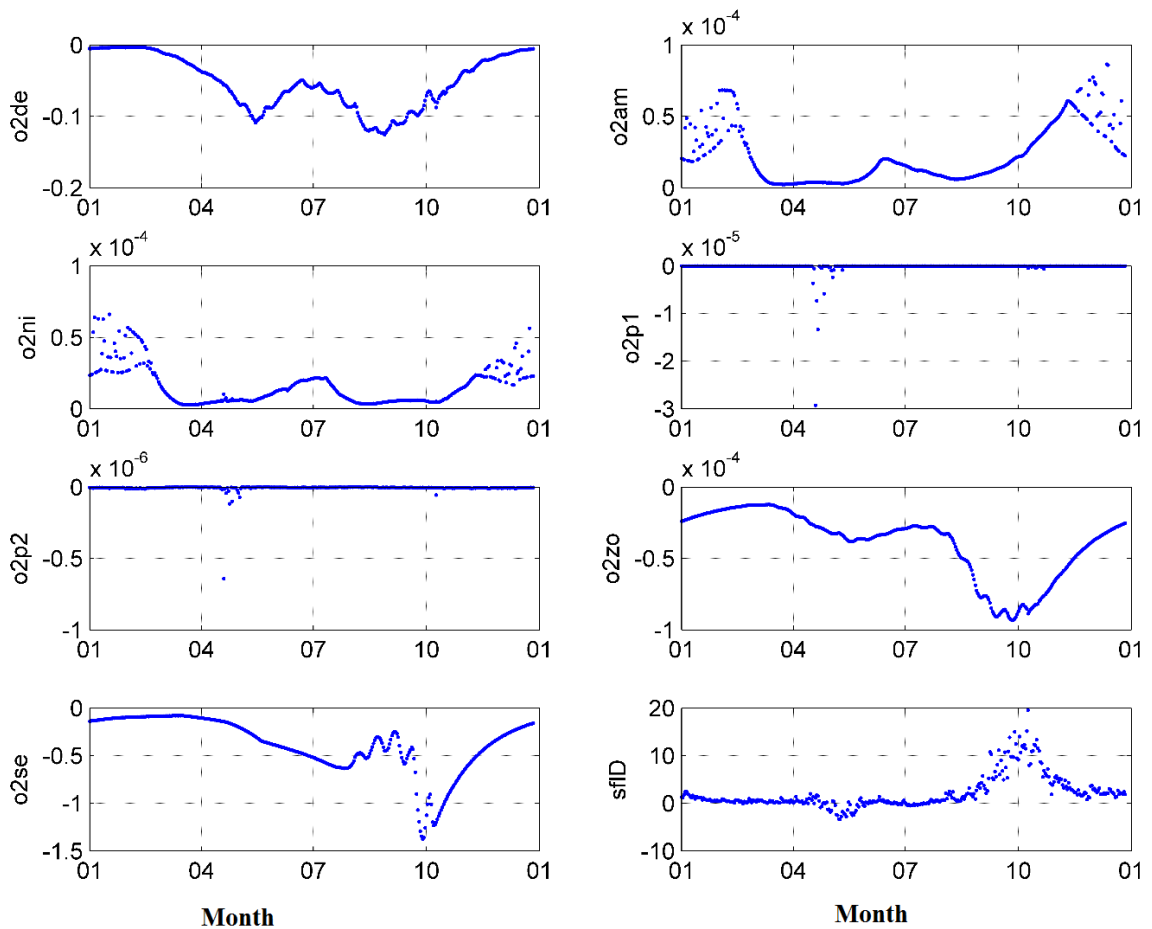


Figure 4-6. DO dynamics from a model excluding bacterial dynamics in $\text{mmol O m}^{-3} \text{ hr}^{-1}$ for the Execution Rocks Station in 2008. From top to bottom and left to right, are rates of DO consumption by detritus remineralization, DO production due to nutrient uptake by phytoplankton, DO consumption due to respiration of phytoplankton and zooplankton, sedimentary DO consumption and surface oxygen flux, respectively. Surface flux, detritus remineralization and sedimentary DO consumption, are three major processes in controlling DO variability.

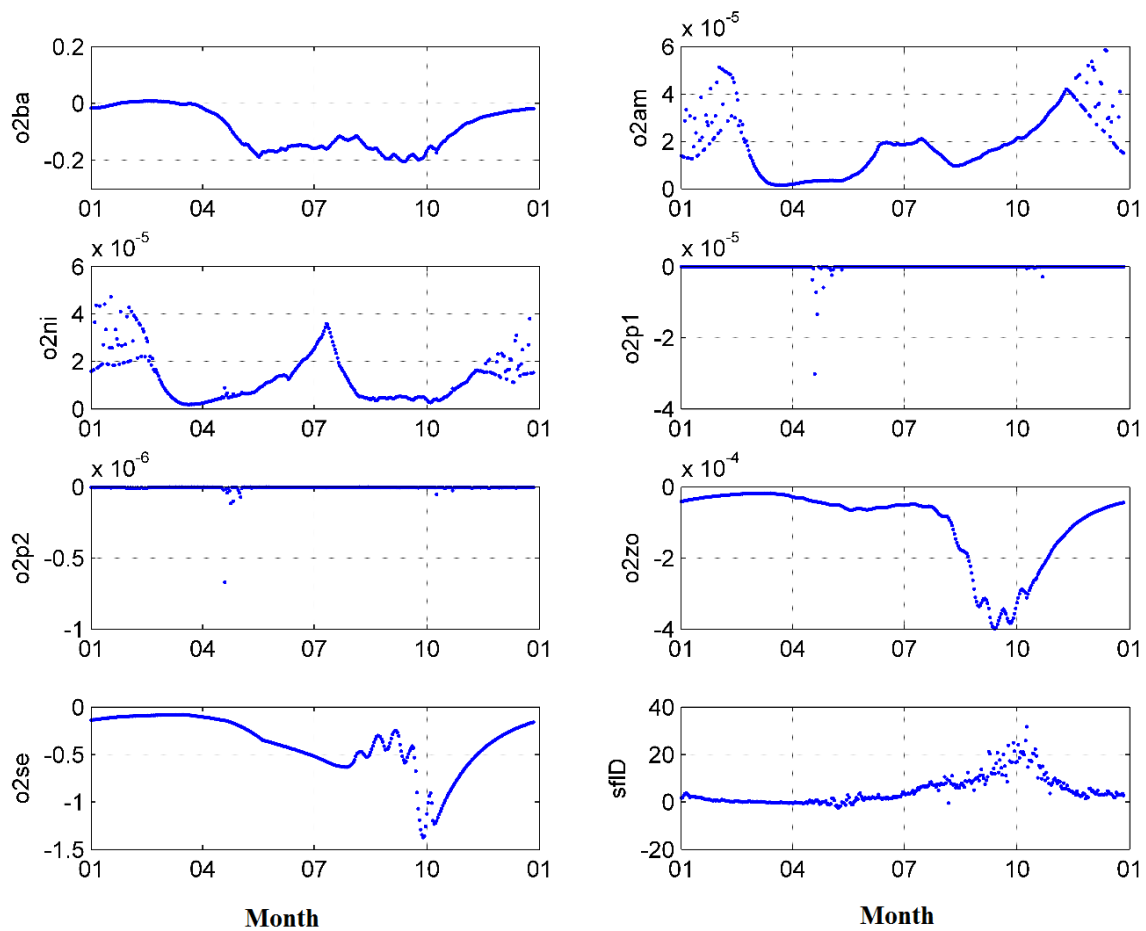


Figure 4-7. DO dynamics from a bacterial dynamics-included model in $\text{mmol O m}^{-3} \text{ hr}^{-1}$ for the Execution Rocks Station in 2008. From top to bottom and left to right are rates of DO consumption by bacteria decomposition of detritus, DO production due to nutrient uptake by phytoplankton, DO consumption due to respiration of phytoplankton and zooplankton, sedimentary DO consumption and surface oxygen flux, respectively.

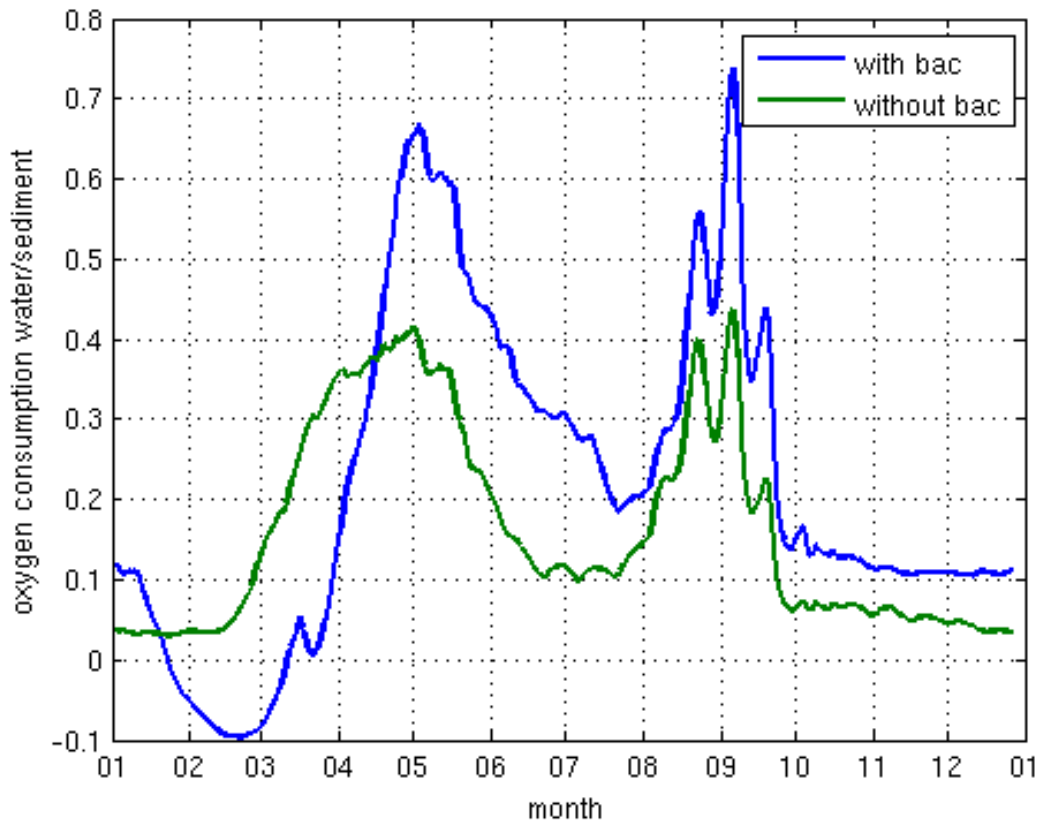


Figure 4-8. Ratio of oxygen consumption rate within the water column and the sediment in the models with and without bacterial dynamics in 2008.

4.4.2 Roles of vertical mixing on the recovery of hypoxia

The role of wind induced vertical mixing on the recovery from hypoxia was examined using the modified 1-D model and conducting twin experiments. Figure 4-9 shows results of the first experiment, in which wind forcing was obtained from observations. Figure 4-10 shows results of the second, in which the wind forcing was artificially lagged behind the observations by one month. The wind speed shown in Figure 4-9 reached its minimum in early June, and started to increase slightly into mid-August. In Figure 4-10, however, the wind speed reached its minimum in early July before rebounding slightly, and a significant increase occurred after mid-September. Bottom DO evolution, however, did not exactly reflected the change of wind speed as expected. Under the observed wind forcing, DO reached its minimum in mid-August, and started to increase from late August. The main issue to examine here is what happens to bottom DO if the wind does not increase. When wind forcing was postponed by one month, DO still reached its minimum in mid-August even though wind speed did not increase significantly in mid-August, then DO started to increase at the same time as in the original wind case. Therefore, seasonal evolution of DO under lagged wind forcing is not significantly different from that is simulated under the original wind forcing. The DO ratio between the original and the lagged wind speed experiments shown in Figure 4-11 was very close to 1 between February and May, and then increased to approximately 1.3 (130%) between the middle of July and August. After that it decreased to approximately 0.75 in early September. This decrease of DO ratio was due to the fact that DO recovered slightly faster under normal wind than lagged wind, but not fast enough to alter the timing of the recovery. After that, the ratio rose back to 1 by early October and maintained that value until the end of October. Therefore, this shows that perturbing the wind speed contribute up to 30% to the DO seasonal variability.

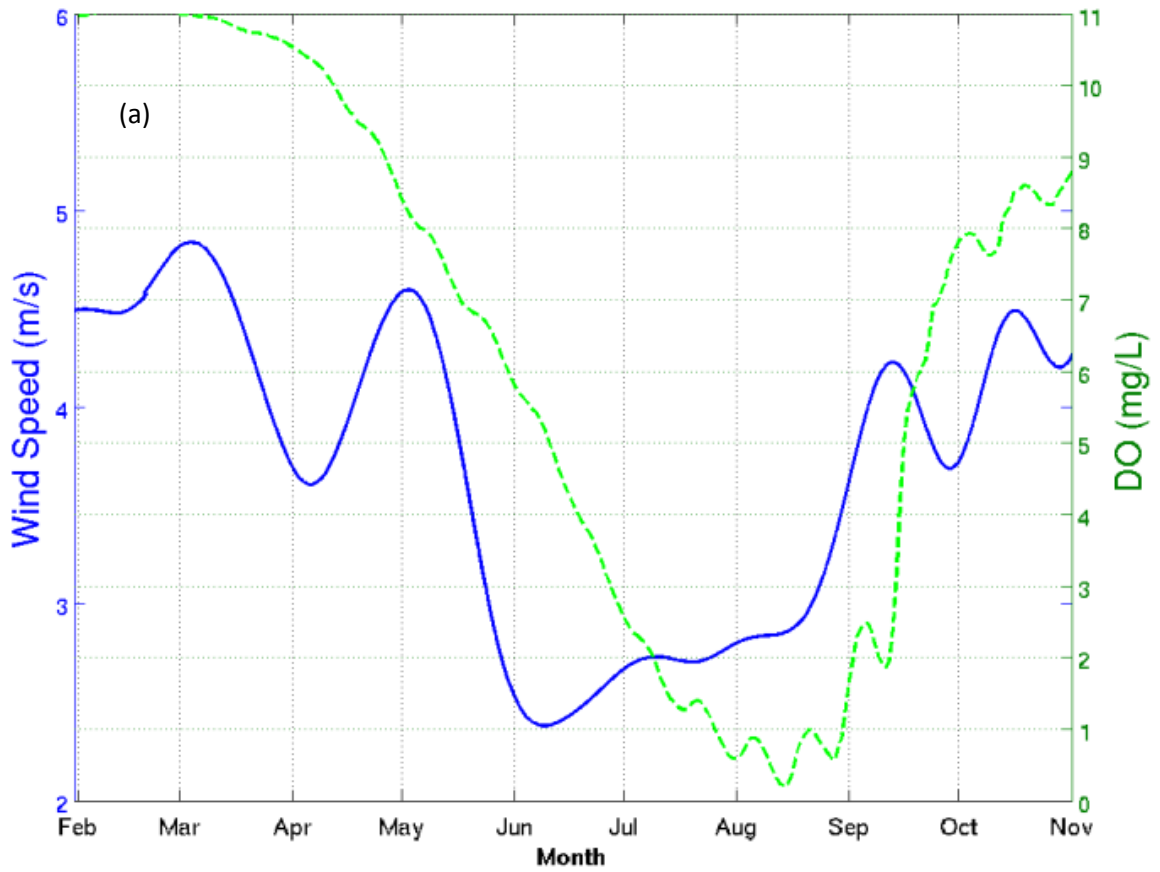


Figure 4-9. Simulated bottom DO (dashed green) forced by the observed wind speed (solid blue) between February and October, 2008, at the Execution Rocks Station.

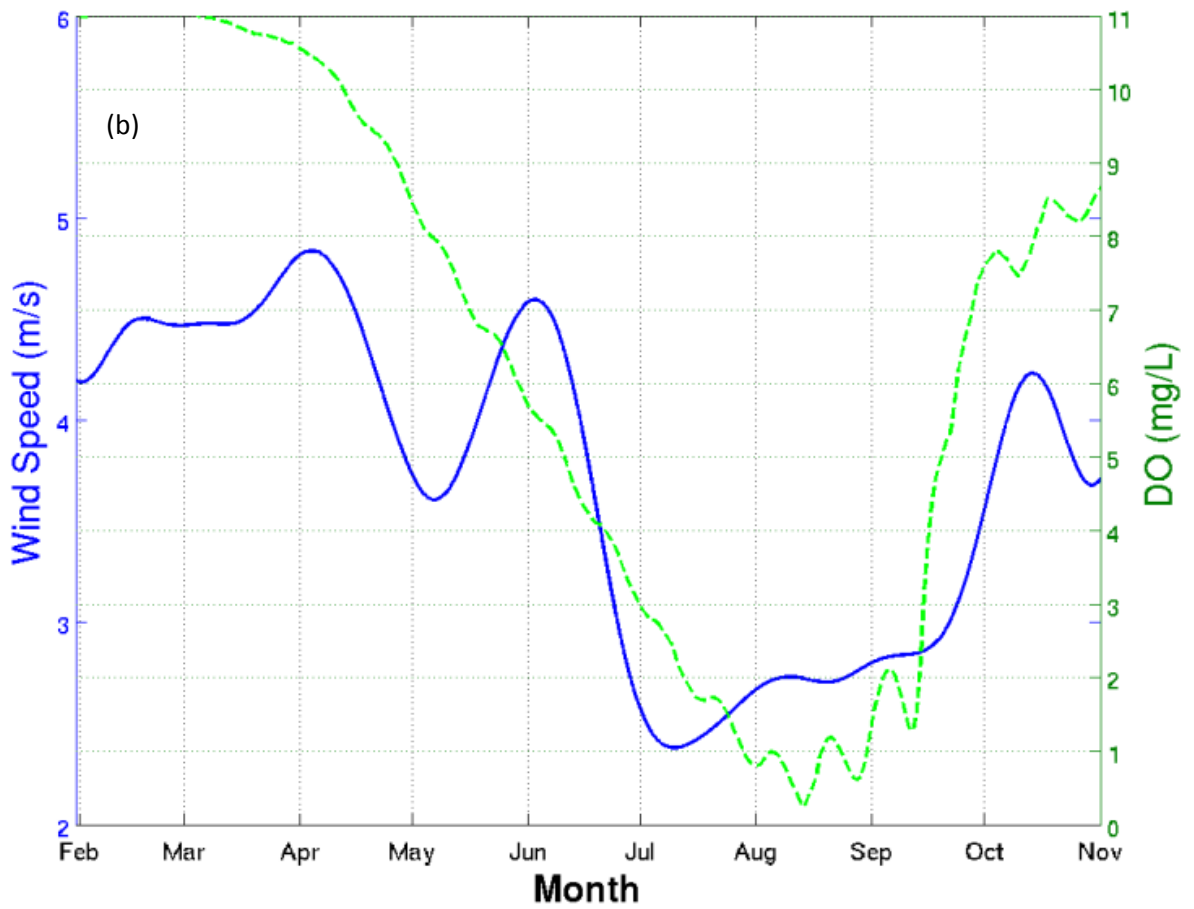


Figure 4-10. Simulated bottom DO (dashed green) under the wind speed lagged behind observations for one month (solid blue) for year 2008, at the Execution Rocks Station.

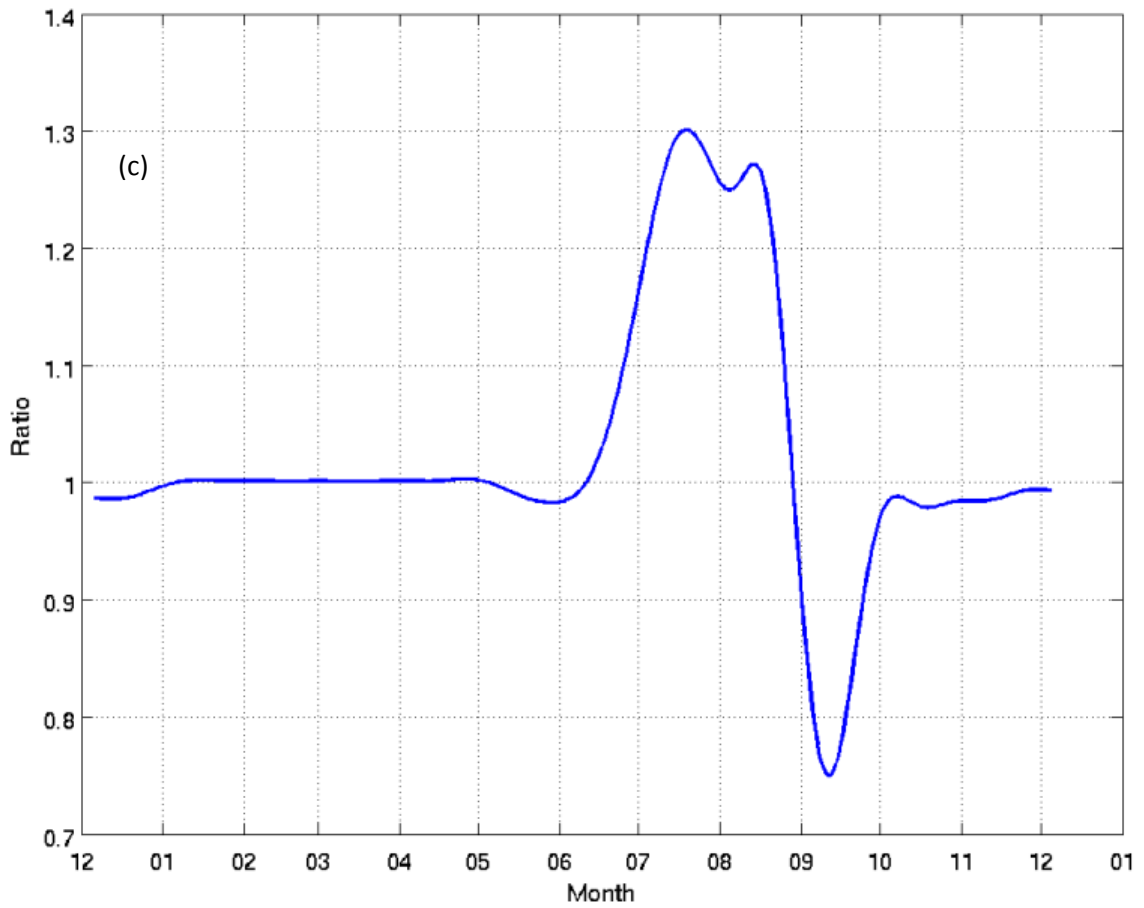


Figure 4-11. The ratio of bottom DO forced with the lagged wind forcing (Figure 4-5) divided by DO forced by observed wind forcing (Figure 4-6). It shows that perturbing wind forcing contributes to at most 30% of the total DO variability.

4.4.3 Roles of horizontal advection on hypoxia development

In general, the addition of horizontal advection does not alter the seasonal variation of DO concentration significantly (see Figures 4-12 and 4-13). The rate of DO reduction between April and July decreased slightly with added advection acceleration, especially in June and July (Figure 4-13). Figure 4-13 also shows that there was a relatively higher DO concentration with added horizontal advection during the minimum DO time (i.e., August). The increase of DO starting in September in the case with advection had similar rate as the case without advection (Figure 4-12 and 4-13). The later increasing rate of DO between early October and late November with advection was approximately 20% lower than the case without advection. The ratio between DO concentration from the model without horizontal advection and the DO from the model with horizontal advection is also shown by Figure 4-14. The difference of DO concentration was small (i.e. ratio close to 1) before June, and then the ratio started to decrease in July and reached the minimum of 57% in late August, and then started to increase to approximately 120% until the beginning of October. It suggested that without the addition of horizontal advection, DO concentration was under-estimated by at most 43% in August, and over-estimated by at most 15% between September and October.

In order to analyze the mechanism of horizontal advection leading to increased DO levels during low DO season, we show the rates of the non-linear DO variability in $\text{mmol O m}^{-3} \text{ hr}^{-1}$ from the model with horizontal advection in Figure 4-15. In general, there was a positive DO increasing rate between July and August. Between September and early October, the DO increasing rate became negative during most of the time, but fluctuated in the positive range in early and late September. This explains why there was a large increase of the ratio (Figure 4-14) in July and

August, and also explains the reason that in September this ratio decreased and fluctuated around 1. In the other words, between July and August, the model with horizontal advection brought extra DO (ratio shown by Figure 4-14 decreased) from western LIS to the Execution Rocks Station area, and led to a positive DO increasing rate. In September, the model with horizontal advection brought water more depleted in DO (ratio shown by Figure 4-14 increased) from the western LIS westward to the Execution Rocks Station area, and led to a negative DO increasing rate. The late half of August with almost zero DO change rate coincided with the turning point of the DO ratio from decreasing trend to increasing in Figure 4-14, when the added horizontal advection had the smallest impact to DO variability.

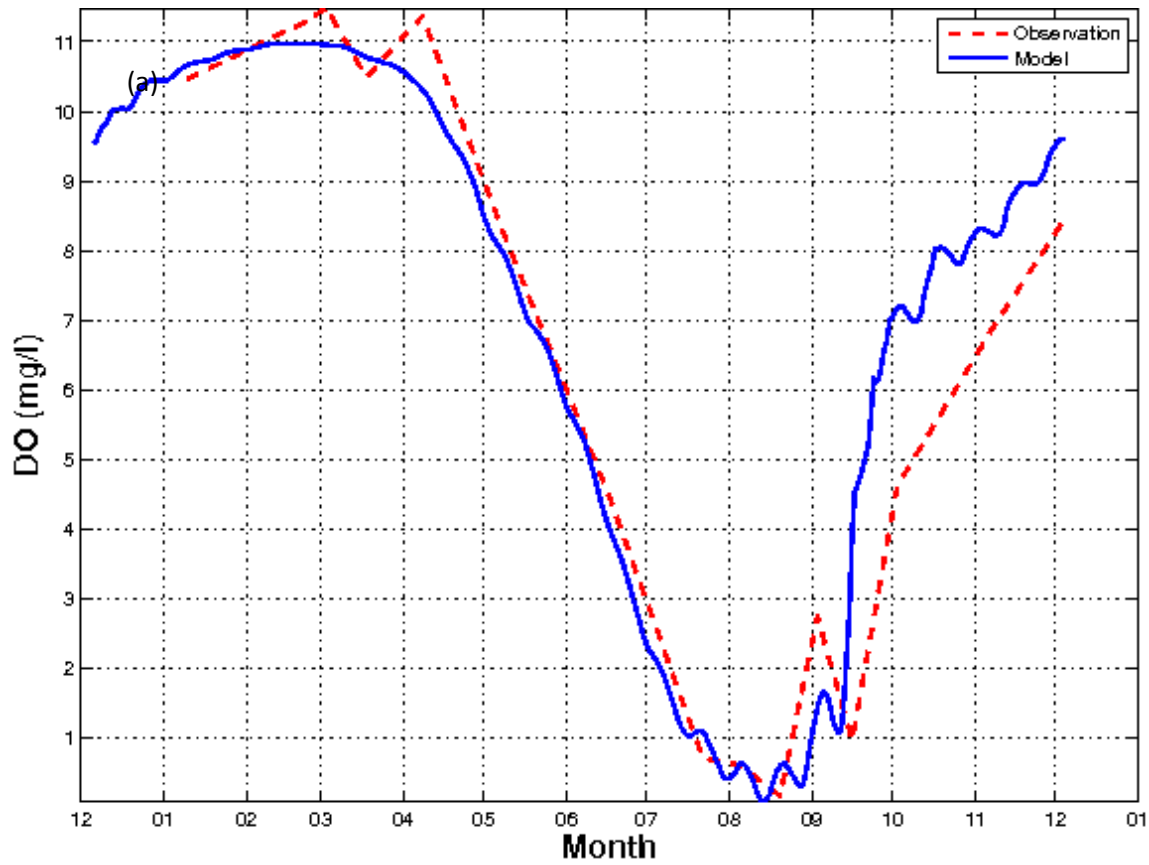


Figure 4-12. Modeled DO variation plotted against the observations. This figure shows time series of DO concentration before adding advection for year 2008, at Execution Rocks Station.

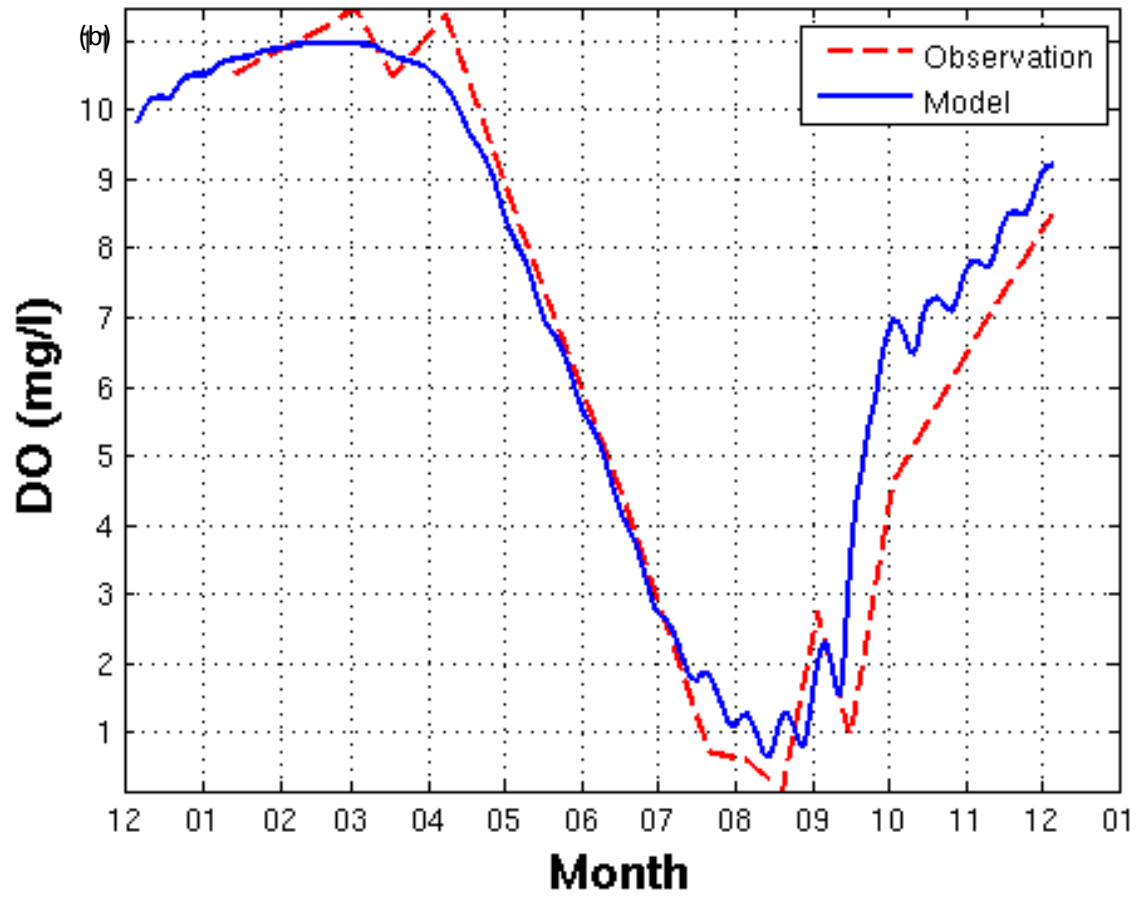


Figure 4-13. Modeled DO variation plotted against the observations. This figure shows seasonal variability of DO concentration after adding advection for year 2008, at Execution Rocks Station.

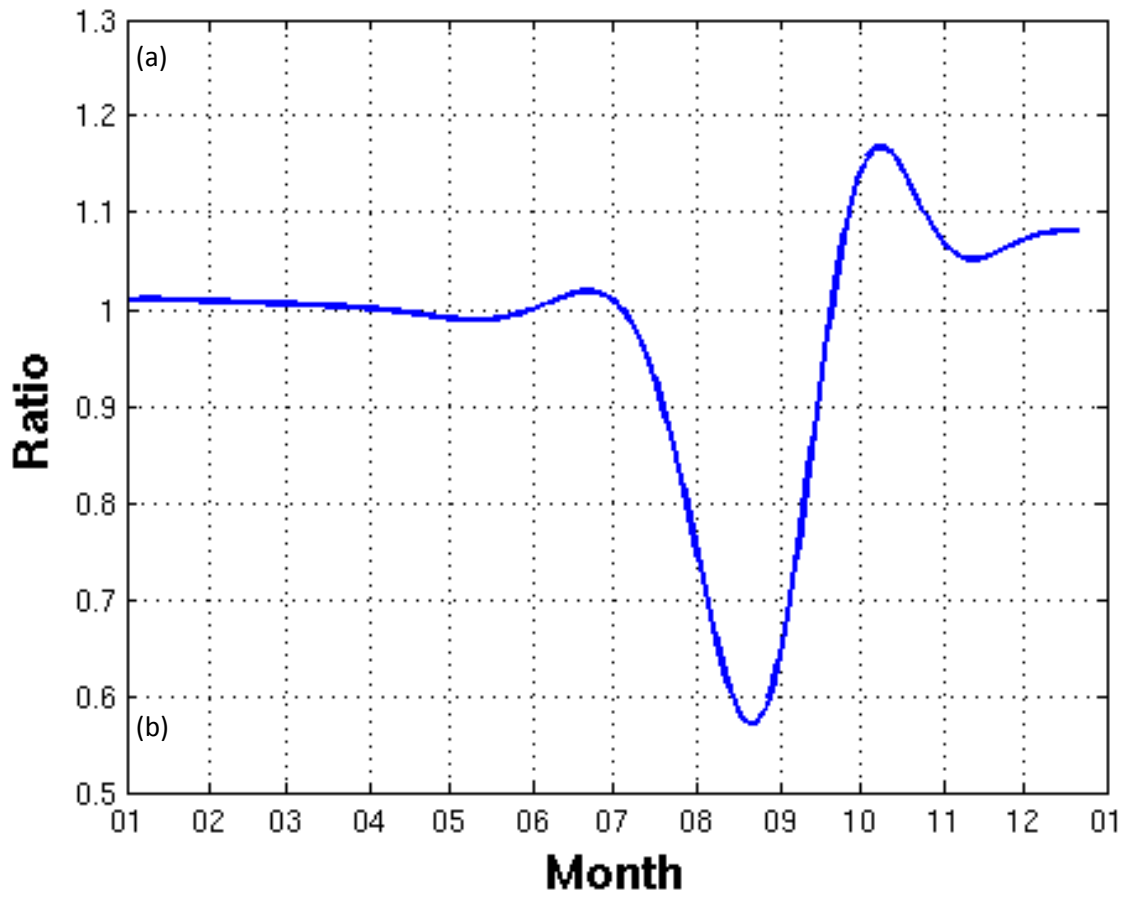


Figure 4-14. The ratio between the seasonal DO variation from the model without the horizontal DO advection and the seasonal DO variation from the model with the horizontal DO advection.

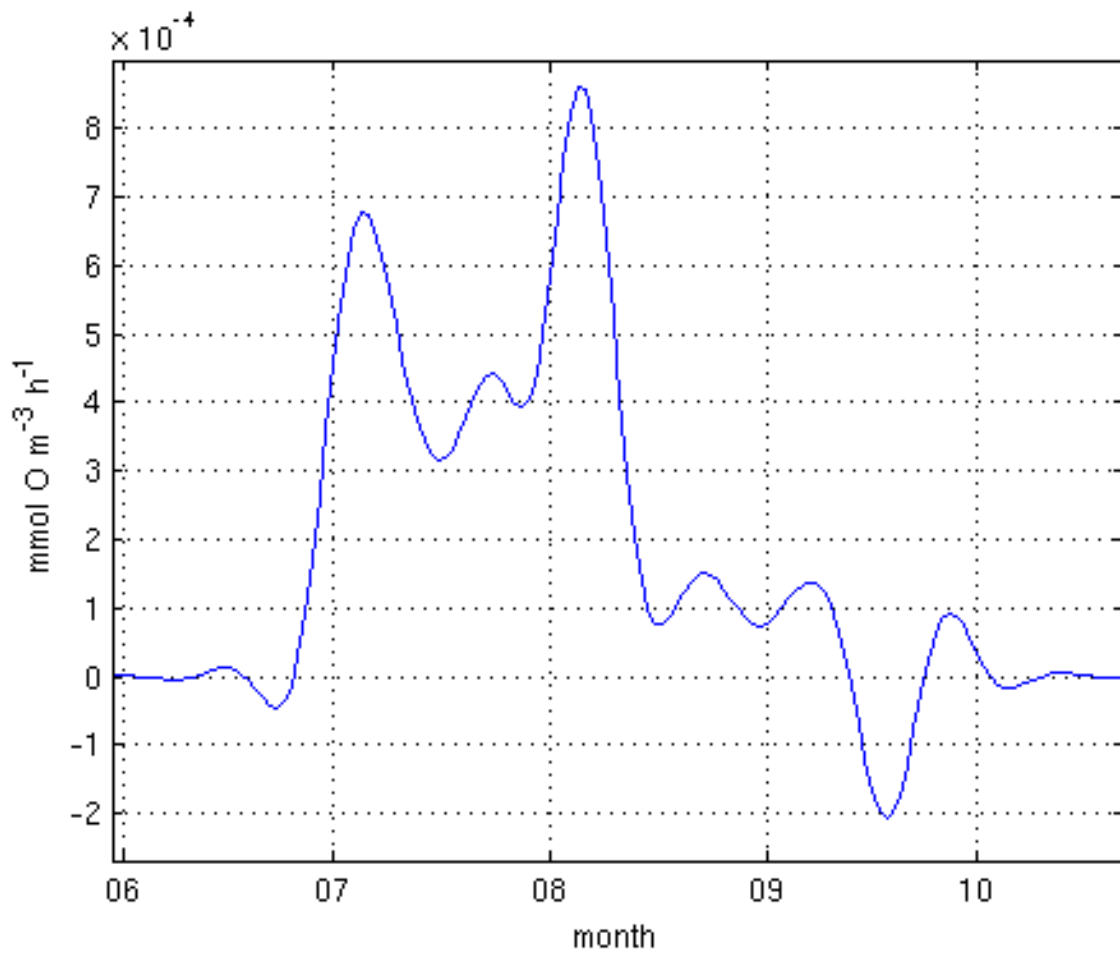


Figure 4-15. The rate of DO increase (positive sign) due to horizontal advection in 2008. The time shown in this figure is when the measured horizontal DO gradient is available from O'Donnel et al. 2008.

4.4.4. Estimating nutrient flux generated by nudging surface nutrient

We described in Section 4.3.4 that we conducted two cases of experiments, namely (i) Case I: microbial loop on, and (ii) Case II: microbial loop off. We also showed the approach to generate results shown by Figure 4-16, 4-17 and 4-18 and 4-19. These results indicated that, in both cases, the nutrient concentration was close to the concentration without nudging during most time of the year, although small discrepancies were observed (Figure 4-16). Comparison of percentage of the nutrient difference between experiments with and without nudging in Cases I and Case II was shown by Figure 4-17. The difference was approximately 10% on average, with the peak value of 25% in May due to low nutrient concentration (Figure 4-17). The difference was negative during most of the time, but it became positive during the summer time in Case I. The individual nutrient component fluxes due to nudging in Case I and II were isolated as shown in Figure 4-18 (a) and (b), which show that the flux was negative during most time of the year, but between August and September, it fluctuated to become positive in Case II experiment. The total fluxes generated by nudging surface nutrient concentration for both Case I and Case II shown by Figure 4-19 had similar variability as the nutrient concentration difference due to nudging for both cases shown in Figure 4-17. This is because the nutrient flux was calculated as a linear function of nutrient concentration difference between nudging and non-nudging experiments.

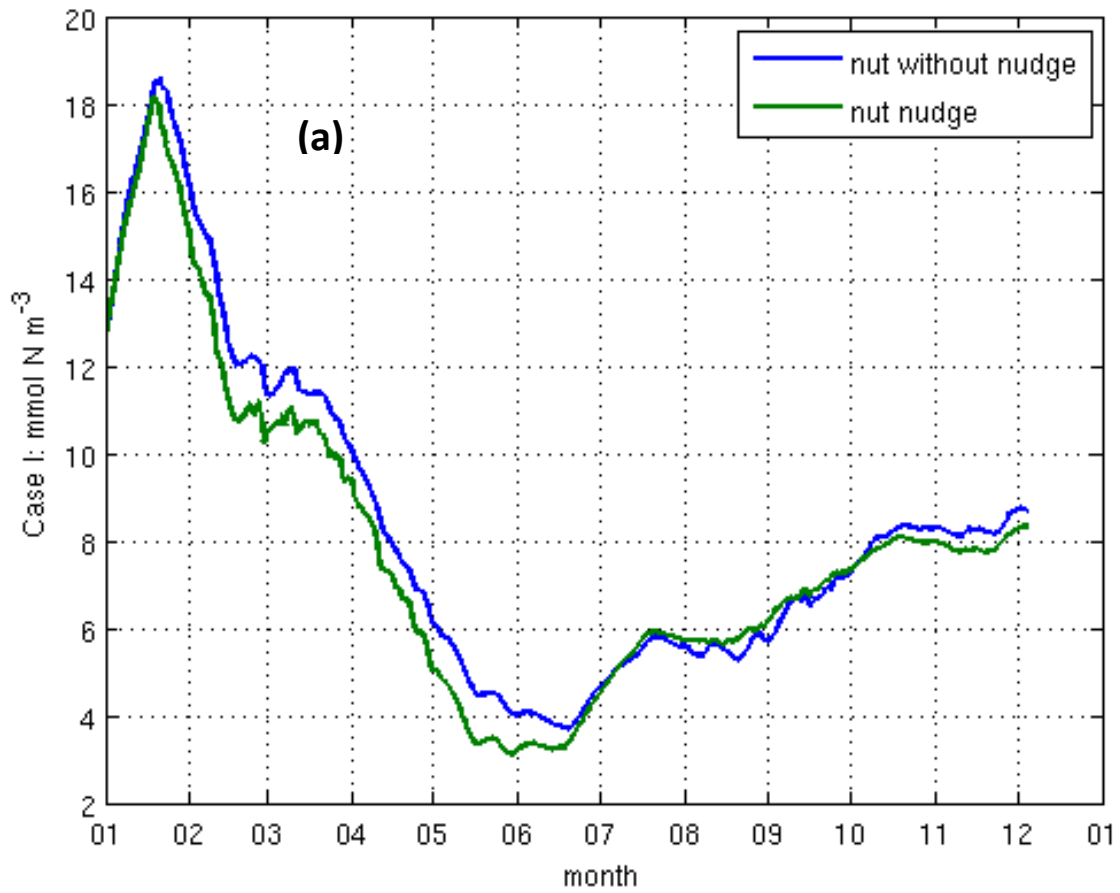


Figure 4-16. (a) Case I experiment results with microbial loop. Figure shows the nutrient concentration comparison between nudging and no-nudging experiments (mmol N m⁻³) for 2008.

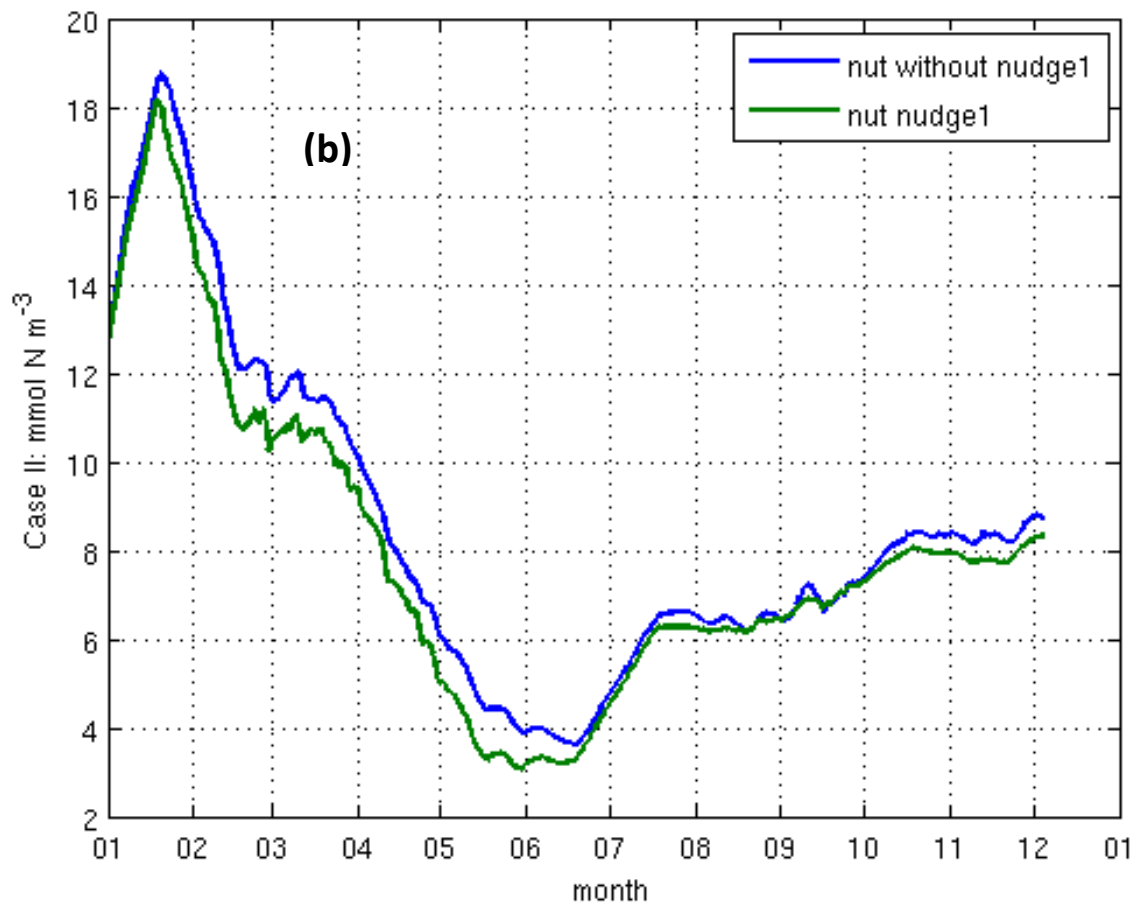


Figure 4-16. (b) The comparison between nudging and no-nudging of nutrient concentration (mmol N m⁻³) for Case II (without microbial loop) for 2008.

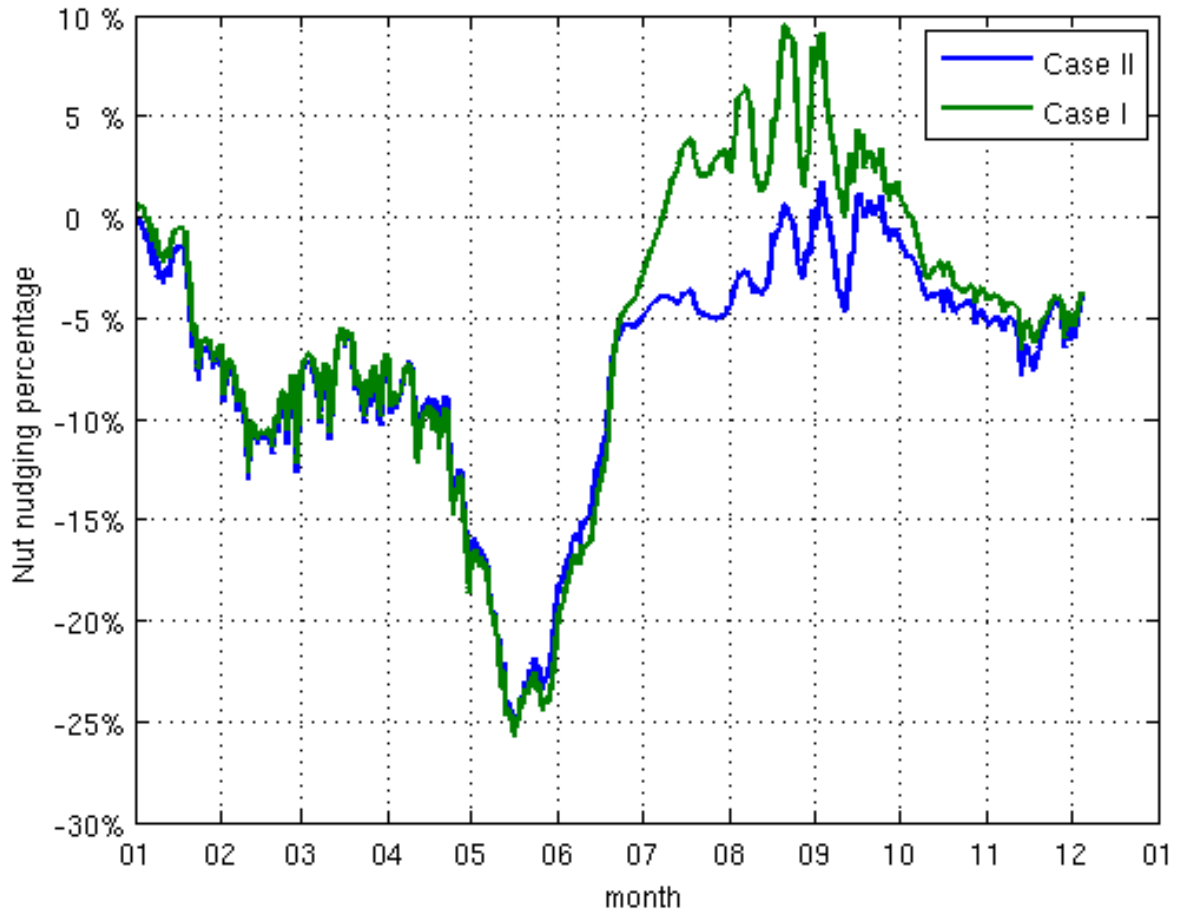


Figure 4-17. Percentage of nutrient concentration difference due to nudging compared for Case I: with microbial loop, and Case II: without microbial loop, for 2008.

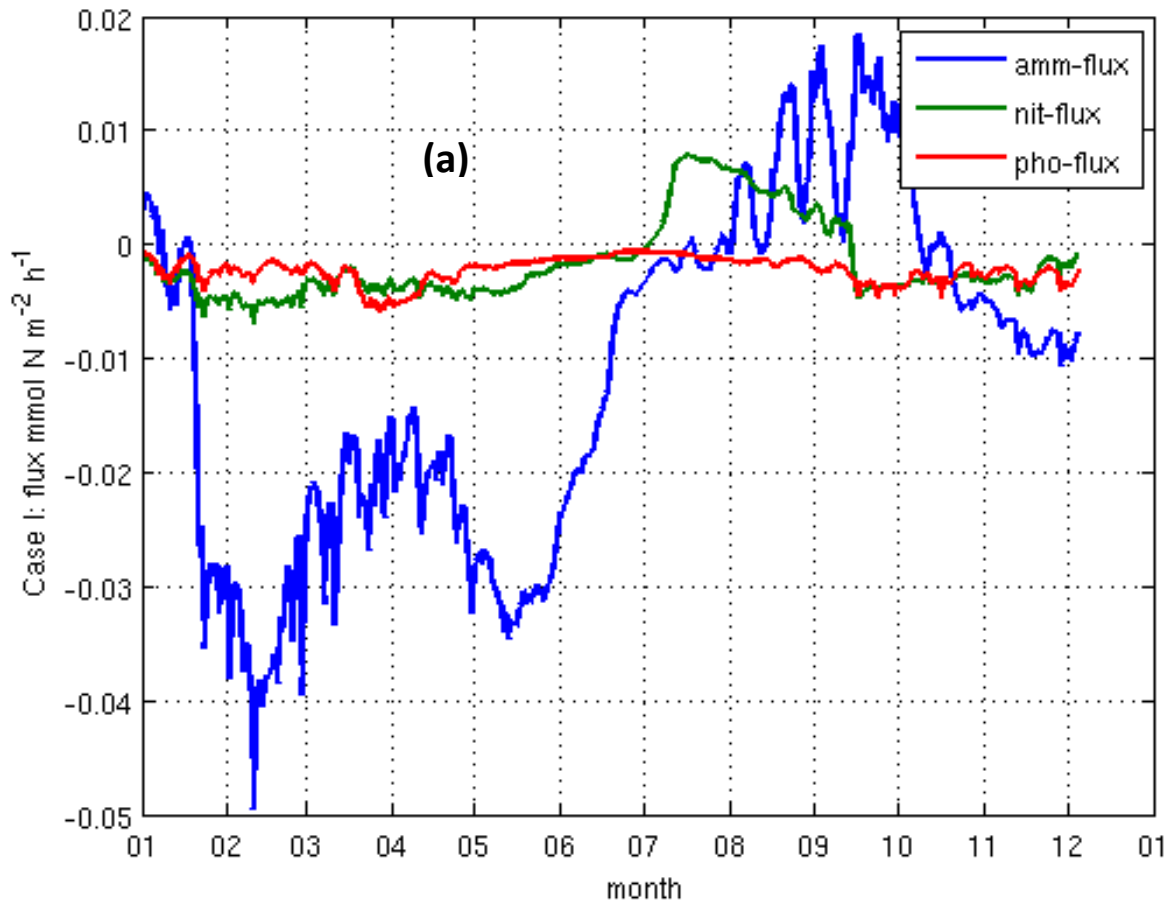


Figure 4-18. (a) Individual nutrient component flux ($\text{mmol N m}^{-2} \text{ h}^{-1}$) due to nudging in Case I experiment with microbial loop for 2008.

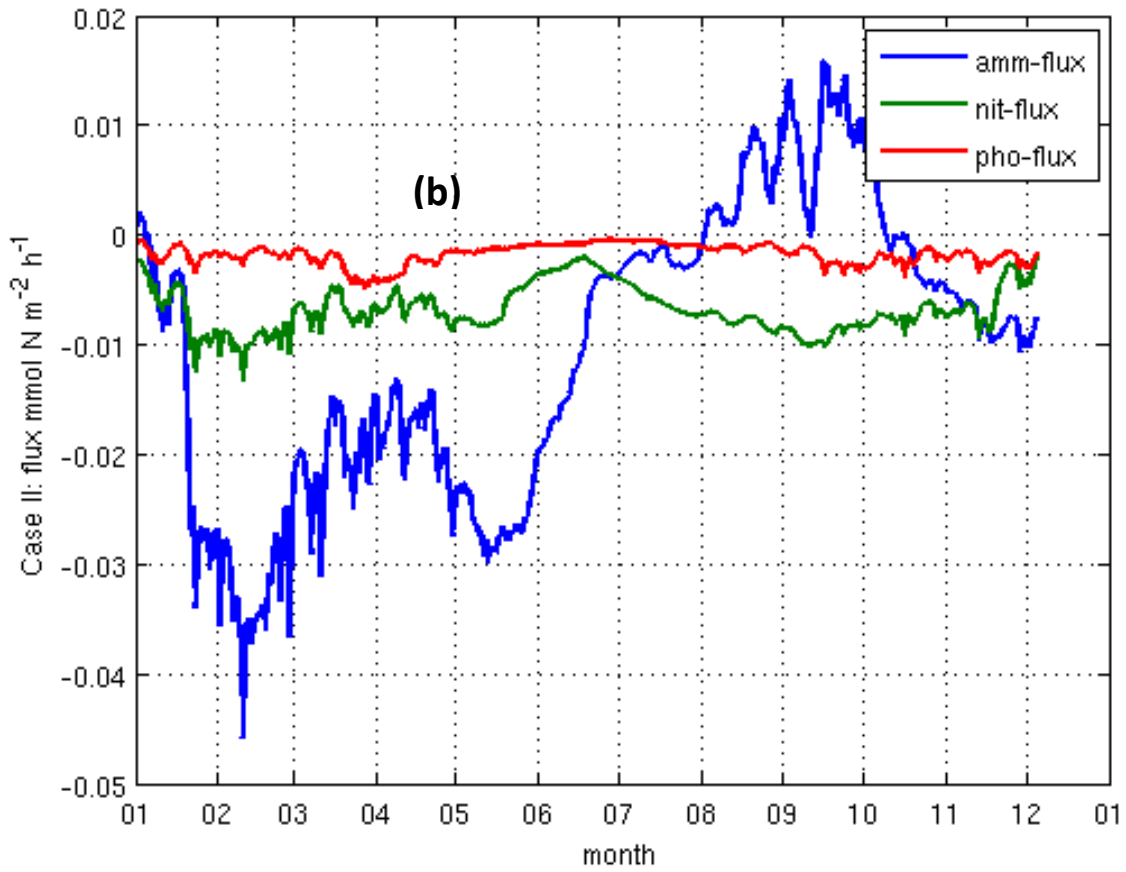


Figure 4-18. (b) Individual nutrient component flux ($\text{mmol N m}^{-2} \text{h}^{-1}$) due to nudging in Case II experiment without microbial loop for 2008.

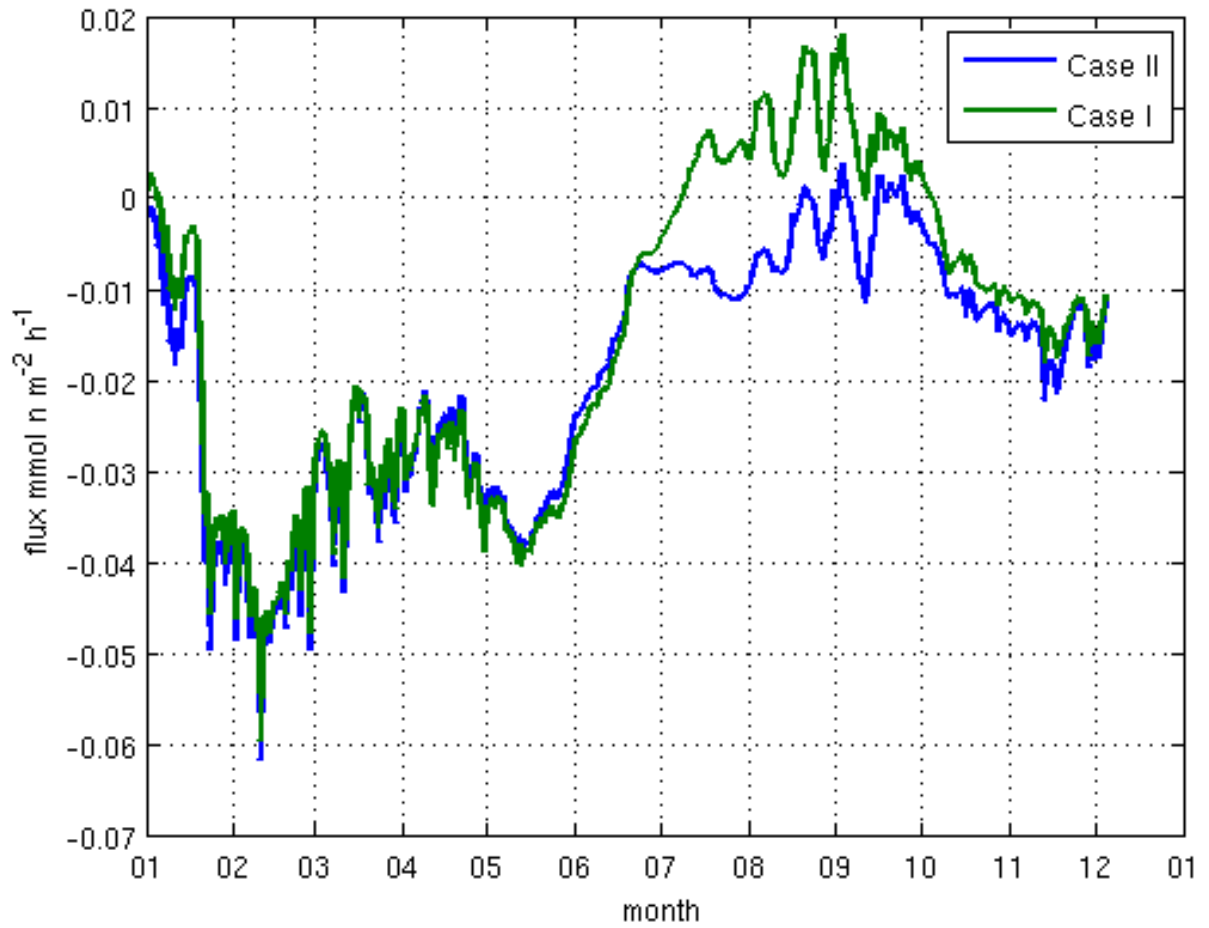


Figure 4-19. Comparison of total nutrient flux ($\text{mmol n m}^{-2} \text{h}^{-1}$) due to nudging between Cases I and Case II.

4.5 Discussion

4.5.1 The mechanisms leading to DO reduction with added bacterial dynamics

Our results in Section 4.4.1 indicate that DO variability was linked to non-linear dynamical processes including surface oxygen flux, sedimentary remineralization, bacterial growth, respiration, mortality, and zooplankton grazing, as well as bacterial decomposition of labile detritus into inorganic matter. It is thus not easy to tease out the contribution of individual components to DO variation and seasonal hypoxia. Our results of comparison between different dynamic terms determining DO variability demonstrate that bacterial decomposition of organic matter into inorganic form was the leading mechanism that controls DO consumption rate, compared to sedimentary decomposition and surface flux of DO.

In order to further understand the mechanisms that lead to strong microbially induced DO reduction, DO consumption through bacterial decomposition (the first subplot in Figure 4-7) is assessed by two processes: (i) decomposition of labile detritus (top panel of Figure 4-20) and (ii) production of ammonium (middle panel). Detritus remineralization in the model without explicit bacterial dynamics (bottom panel of Figure 4-20) and DO consumption during bacterial decomposition of detritus have similar rates, peaking at $0.15 \text{ mmol O m}^{-3} \text{ hr}^{-1}$ in May and August. However, bacteria induced inorganic matter production during summer leads to further increase of the rates by $0.07 \text{ mmol O m}^{-3} \text{ hr}^{-1}$ (middle panel) in the bacterial dynamics-including model, which is approximately 37% of the total DO consumption rate. This is the source of additional increase of DO consumption compared to the model without bacterial dynamics.

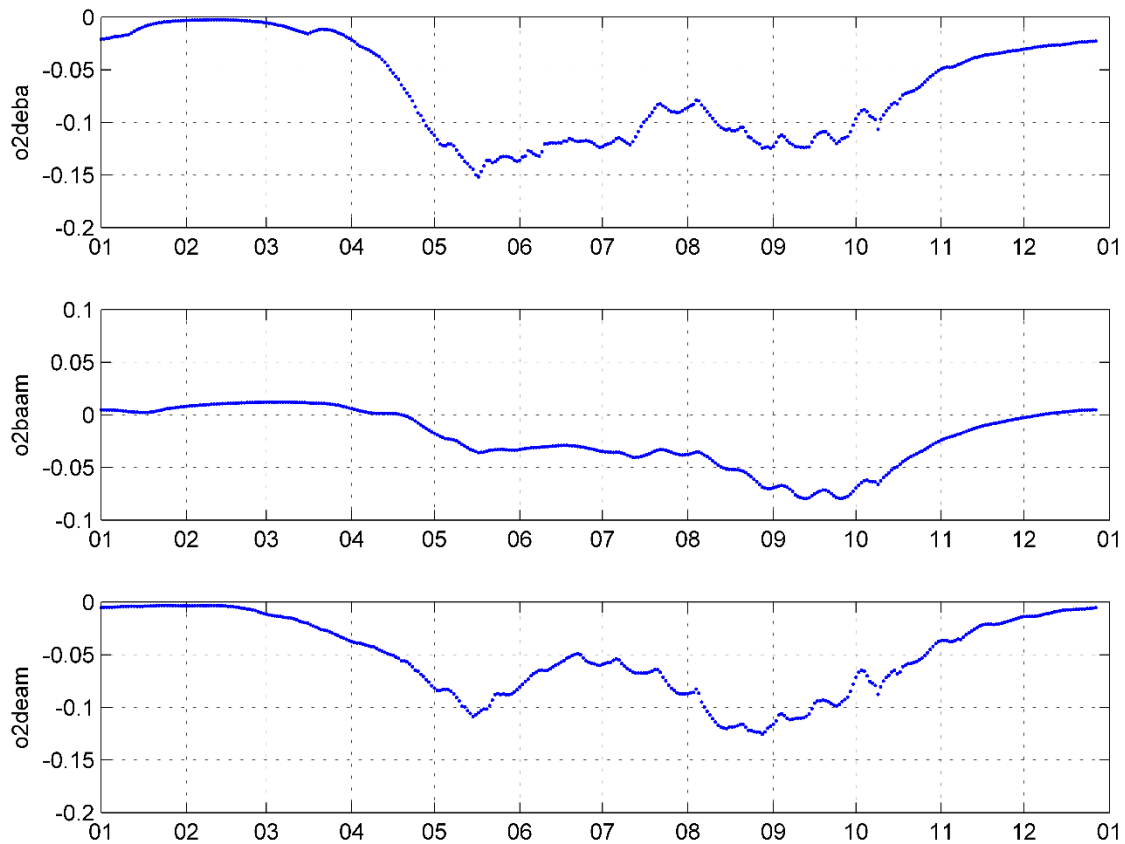


Figure 4-20. DO consumption rates in $\text{mmol O m}^{-3} \text{ hr}^{-1}$ as bacterial decomposing labile detritus into inorganic nitrogen (top and middle panel) from the bacterial dynamics-included model. For comparison, bottom panel shows the rates during detritus remineralization from the bacterial dynamics-excluded model. Bacteria induced inorganic matter production during summer leads to further increase of the rates by $0.07 \text{ mmol N m}^{-3} \text{ hr}^{-1}$ (middle panel) in the bacterial dynamics-included model, which is approximately 37% of the total DO consumption rate.

4.5.2 The importance of vertical mixing in simulating seasonal hypoxia

Hypoxia is known to be caused by intensified stratification induced by increased insolation and input of low-salinity surface water, as well as relaxation of wind mixing during summer (Vigil 1991; Welsh and Eller 1991). In addition, biological activity in the water column above the hypoxic layer can remove DO, which would otherwise diffuse downward through a relatively weak pycnocline (Welsh and Eller 1991). Despite the importance of microbial activity, several studies have overemphasized the significance of wind mixing in controlling DO ventilation, and some have argued that the duration of and recovery from hypoxia in LIS is controlled by the spatial and temporal variability of stratification and vertical mixing (e.g., O'Donnell 2008; Welsh and Eller 1991). For example, O'Donnell et al. (2008) argued from their observational results that intermittent ventilation of the deep waters by vertical mixing of DO was the principal DO source at the study site near Execution Rocks during the summer of 2004. McCardell and O'Donnell (2009) estimated the magnitude of the vertical flux across the pycnocline in LIS using buoy observations, and argued that it was comparable to the vertically integrated respiration rates within the water column estimated by Goebel and Kremer (2007). Despite of these findings, we have shown in Section 4.3.2 that ventilation is only part of the story.

In this section, the one-dimensional coupled model without horizontal advection was applied to isolate and quantify the impact of wind-induced vertical mixing to DO variability. We hypothesized that the timing of DO recovery is driven by increased wind forcing, and tested this hypothesis by conducting twin experiments. The DO ratio between the original and the lagged wind speed experiments (Figure 4-11) being close to 1 suggested that bottom DO under lagged wind stress is close to the one under normal wind stress during most of the time. Analysis of the relationship between wind stress and bottom DO (Figure 4-5 and 4-6) shows that when wind

stress escalation was lagged by one month, hypoxic condition still occurred in late August, and the timing of DO recovery was unchanged. This clearly shows that the contribution of wind to recovery of hypoxia is relatively small. In addition, perturbing wind forcing leads to at most 30% of DO variability. Therefore, recovery from late summer hypoxia might not be as sensitive to the change of wind mixing as previously thought.

4.5.3 The importance of horizontal advection in simulating seasonal DO variability

The change of ratio between DO concentrations without and with horizontal advection indicated that ignoring horizontal advection leads to approximately 40% of under-estimation of DO during low DO season. This result implied that DO variability was sensitive to horizontal advection during low DO season. Previous studies have emphasized the importance of horizontal advection in producing ventilation in LIS, but most of them do not quantify the impact of advection on DO variability. For example, Wilson et al. (2008) showed that lateral advection was the most important mechanism producing ventilation in LIS rather than simple longitudinal or lateral straining. Lee and Lwiza (2008) hypothesized that horizontal advection might be an important factor leading to oxygen recovery. On the other hand, O'Donnell et al. (2008) counted the number of observed ventilation events associated with horizontal advection and vertical mixing during summer of 2004, and reported that less than 20% of the observed hypoxic events associated with ventilation at the Execution Rocks station in LIS resulted from horizontal advection during low-oxygen season, and over 80% of the ventilation intervals were associated with vertical mixing in year 2004. Our model results showed that without adding horizontal advection, the DO variability may be under-estimated by approximately 40%. It also demonstrated a time-varying impact of horizontal advection on DO variation during summer

time. The impact of horizontal advection in DO variability increased from less than 5% at the end of June to approximately 40% in the middle of August with an increasing rate of 20% per month, and then decreased to zero in the middle of September. From September on to the end of the year, there was an over-estimation of DO up to 17% without horizontal advection.

The fact that the DO level is more controlled by horizontal advection than vertical mixing is evident in other coastal regions. For example, Resplandy et al. (2012) found that oxygen variability was modulated by lateral advection in the coast of Arabian sea. Along the western coast, the Somali Current transported waters rich in oxygen from the south during summer. Within the oxygen minimum zone off the eastern coast of the Arabian Sea, it was the Indian coastal undercurrent that advects southern oxygenated waters during summer. A study in the Sea of Japan conducted by Kasai (2014) also argued that during low oxygen season, very little oxygen-sufficient water would be supplied to the bottom layer through vertical mixing. Horizontal advection played an important role for re-supply of oxygen when oxygen was depleted in the stagnant bottom water. Xue et al. (2014) conducted data denial experiments to study DO variability in the Mass Bay. They found that by only including horizontal advection of the western Gulf of Maine coastal currents, simulated seasonal DO variation could almost reproduce the observed DO variability in Mass Bay, which implied that horizontal advection played a dominant role in controlling DO variability in the Mass bay. On the other hand, removing oxygenation by horizontal advection could lead to a 1–1.5 mg/l difference throughout almost the whole year, which accounted for up to 30–50% of the total DO seasonal variation. A comparison between Figure 4-15 and Figure 4-7 (i.e., DO consumption rates in $\text{mmol O m}^{-3} \text{ hr}^{-1}$ from the bacterial dynamics-included model) also shows that horizontal advection has the same order of impact as the total rate of DO regeneration via phytoplankton/zooplankton

photosynthesis/growth. However, horizontal-advection generated DO variability is three orders less than bacterial consumption of DO, which implies a much smaller impact of horizontal advection on DO variation compared to bacterial activity.

4.5.4 Impact of nudging surface nutrient

Nudging is usually used to assure that material and energy fluxes are consistent with time-rate changes of the variables within the model domain. There are previous modeling studies applying nudging technique in their models. For instance, Ray et al. (2015) nudged the sea surface temperature and analyzed the possibility of reconstruction deeper ocean variability with nudging. Astitha et al. (2012) applied nudging technique to simulate both the global and regional desert dust emission. Their estimation shows that nudging might lead to up to 20% of reduction of global dust emission. In this study, surface nutrient nudging was applied in the biological model ERGOM. The purpose of nudging in this study is to ensure seasonal development of the major nutrient drivers and phytoplankton biomass responses more closely replicate observations so that the role of bacterial dynamics in determining DO variability could be examined correctly. However, it is still important to know how much of surface nutrient flux could be generated due to surface nutrient nudging. We have shown in Section 4.4.4 that the generated flux due to nudging is very small in both cases of experiments. It leads to at most 10% of surface nutrient flux when comparing with the total surface nutrient flux. Despite of this, conduction of these experiments provides important insights. First, the minus sign in Figure 4-17 indicate nutrient concentrations tend to be over-estimated without nudging during most of the time, which might be caused by a lack of nutrient advection in the 1-D model. Second, the summer-time discrepancy for Case I switched sign to become positive, indicating that the model with

microbial loop (i.e., Case I) tends to under-estimate the nutrient concentration without nudging. This time happens to be when there is a strong bacterial activity, which tends to reduce the surface nutrient level, but the nutrient flux prevents the nutrient from being depleted even if without nudging. Third, the amplitude of ammonium flux generated by nudging surface ammonium concentration is approximately 2-3 times larger than nitrate and phosphate fluxes generated by nitrate and phosphate nudging (indicated by Figure 4-18). This relatively large ammonium flux generated by nudging ammonium concentration suggests that ammonium concentration is more difficult to simulate accurately without nudging. This is because ammonium concentration is controlled by more dynamic processes in the model than other nutrient components, this becoming more difficult to constrain. For example, ammonium, nitrate and phosphate are all consumed by phytoplankton for growth, but only ammonium is utilized for bacterial growth in addition to detritus in the model due to the fact that ammonium is the primary source of dissolved nutrient for bacteria. The utilization amount of ammonium by bacteria is determined by multiple non-linear factors including temperature and C:N ratio of detritus. In reality, for example, ammonium might be utilized if detritus is rich in carbohydrates, but if detritus is rich in proteins, bacteria may not need ammonium for growth (Anderson 1995). In addition to these ammonium consumption processes, ammonium is also produced through bacterial remineralization processes in both the water column and sediment, which is a non-linear function of temperature, bacterial biomass and detritus concentration (Hall et al. 2008).

4.5.5 Implications on coastal hypoxia modeling

The Long Island Sound Study (LISS) has been using SWEM to establish nitrogen reducing levels of TMDL and predict coastal hypoxia for management purposes in the Sound since 1998. In SWEM/RCA, organic carbon decomposition is assumed to be mediated by temperature and bacterial biomass, but bacterial biomass and its associated activity are not explicitly simulated. Instead, phytoplankton biomass is used to fulfill the role of bacterial biomass by default (Miller and Wands 2009). According to our results, however, organic matter decomposition cannot be controlled properly under realistic forcing without adding terms for the bacterial dynamics. Evidently, the bacterial dynamics is essential in accurately predicting hypoxia because detrital remineralization modulated by microbial activity is not tightly coupled to phytoplankton dynamics and has a large impact on seasonal DO excursions.

Another model to consider is ChesROMS, which is a community ocean model adapted to the Chesapeake Bay region developed by NOAA, University of Maryland, Chesapeake Research Consortium (CRC) and Maryland Department of Natural Resources (MD DNR). The model is used to provide nowcast and forecast of 3D hydrodynamic circulation, temperature and salinity, sediment transport, and biogeochemical states. Similar to SWEM, ChesROMS does not explicitly include bacterial parameterization (Fennel et al. 2006; Prasad et al. 2011). Although it is designed to include the effects of temperature control on organic matter remineralization (Luettich et al. 2012), it may still have difficulty predicting DO variability accurately because it does not include microbial activity that control organic matter remineralization and DO variability.

Our results show that bacterial dynamics is required for accurate DO simulation, which provide necessary feedbacks to the planktonic activity. In summary we note that exclusion of the

bacterial dynamics from eutrophication models leads to underestimation of respiration and in some cases the need to artificially reduce vertical mixing. In addition, the way that phytoplankton biomass is used to parameterize bacterial biomass in decomposing organic carbon, leads us to question if phytoplankton biomass and organic matter decomposition process could be modeled properly. The models described above may involve remineralization, but exclusion of explicit bacterial interactions compromises skill in simulating remineralization. Errors in simulating remineralization most likely accumulate and propagate through computations of DO dynamics because of their direct cause and effect relationship.

For management purpose, it is important for an eutrophication model to be able to predict the areal coverage of hypoxia volume and duration. Maximum seasonal hypoxic volume in some of the most affected areas, e.g., Gulf of Mexico, the Chesapeake Bay and Long Island Sound, has been increasing nowadays. The success of GOTM coupled with the modified ERGOM suggests that the next logical step in this direction is to apply ERGOM in the General Estuarine Turbulence Model (GETM) (Stips et al. 2004), a 3-D version of GOTM, in order to understand factors that control the hypoxic volume, and in turn improve its predictability.

4.5.6 Missing mechanisms and future direction

We have mentioned in Chapter 2 that there are missing mechanisms in the 1-D coupled model that need to be fulfilled in future studies. In addition to the coarse representation of bacterial activity, the horizontal advection is artificially added into the 1-D coupled model by controlling only the DO dynamic equation. This neglects the impact that horizontal advection might have on the other processes of the system, e.g., phytoplankton bloom, nutrient flux, sedimentary

transport, etc. The DO gradient derived from O'Donnell et al. (2008) is also limited to summer time period, which does not provide insight into seasonal variability of DO horizontal advection. The eastward DO gradient between Station A4 and A2 is estimated by making comparison to the westward gradient based on the NEIWPCC bi-monthly investigation, which may not take into consideration of the tidal impact. Because it usually takes time for observational data to come along, it is important to apply a fully coupled 3-D physical-biological model to thoroughly examine the impact of wind-induced horizontal advection to biogeochemical processes in Long Island Sound. With a 3-D model approach, hypoxia volume could be quantified over LIS, and the seasonal and spatial change of DO variability in the Sound could also be resolved. Before applying the 3-D coupled model, it is also wise to apply the current 1-D model to multiple stations in the western and middle LIS, so that the horizontal hypoxia extent could be quantified.

4.6 Conclusions

In contrast to previous studies, our results of western LIS show that wind mixing increase alone is insufficient to explain late summer hypoxia recovery. It explains 30% of the DO variability due to physical transport. In addition to vertical mixing, horizontal advection in western LIS has a non-trivial impact on hypoxia development. Our results indicate that ignoring horizontal advection leads to up to 40% of under-estimation of DO during low DO season. This result implied that DO variability is sensitive to horizontal advection during low DO season.

Temperature and substrate-responsive microbial activity are the primary mechanism controlling DO dynamics. The impacts of planktonic activity and horizontal advection on seasonal DO variability are second order effects. The source of additional increase of DO consumption with bacterial dynamics-included model compared to the bacterial dynamics-excluded model is

attributed to the bacteria induced inorganic matter production during summer, which leads to further increase of the rates by approximately 37% of the total DO consumption rate. Therefore, there is strong evidence showing that explicitly adding bacterial dynamics could lead to stronger DO reduction during summer. Nudging surface nutrient concentration generates relatively small nutrient flux due to nudging, which is negligible for the western LIS case.

References

- Anderson, T. H., 1995. Pelagic microbial processes influencing hypoxia in western Long Island Sound. M.S. Thesis. State University of New York, Stony Brook, New York.
- Astitha, M., Lelieveld, J., Kader, M., Pozzer, A. 2012. Parameterization of dust emissions in the global atmospheric chemistry-climate model EMAC: impact of nudging and soil properties. *Atmos. Chem. Phys.*, 12, 11057–11083
- Boon, N. A., 2008. Nutrient Dynamics of Long Island Sound. Master's thesis. Wesleyan University.
- Christian, R. R. 1994. Aggregation and disaggregation of Microbial Food Webs. *Microb Ecol* 28:327-329
- Ducklow, H. W. 1994. Modeling Microbial Food Web. *Microb Ecol* 28:303-319
- Fennel, K., Hetland, R., Feng, Y. and DiMarco, S., 2011. A coupled physical-biological model of the Northern Gulf of Mexico shelf: model description, validation and analysis of phytoplankton variability. *Biogeosciences*. 8, 1881–1899, 2011, doi:10.5194/bg-8-1881-2011.
- Fennel, K., Wilkin, J., Levin, J., Moisan, J., O'Reilly, J. and Haidvogel, D., 2006. Nitrogen cycling in the Middle Atlantic Bight: Results from a three-dimensional model and implications for the North Atlantic nitrogen budget. *Global Biogeochem. Cy.*, 20(3). doi:Artn Gb3007 Doi 10.1029/2005gb002456.
- Goebel, N.L., Kremer, J.N., 2007. Temporal and spatial variability of photosynthetic parameters and community respiration in Long Island Sound. *Marine Ecology Progress Series* 329, 23–42.

- Grant McCardell and James O'Donnell. Department of Marine Sciences, University of Connecticut. Long Island Sound Research Conference Proceedings 2006.
- Hall, E. K., Neuhauser, C. and Cotner, J. B., 2008. Toward a mechanistic understanding of how natural bacterial communities respond to changes in temperature in aquatic ecosystems. *International Society for Microbial Ecology*, 2(5), 471-481.
- Jankowski, T., Livingstone, D. M., Bührer, H., Forster, R., and Niederhauser, P. 2006. Consequences of the 2003 European heat wave for lake temperature profiles, thermal stability, and hypolimnetic oxygen depletion: implications for a warmer world. *Limnol. Oceanogr.*, 51, 815–819, 2006.
- Kasai, A. 2014. Hypoxia Controlled by Hydrodynamics. *Aqua-BioScience Monographs*, Vol. 7, No. 4, pp. 117–145 (2014).
- Lee, Y. J. and Lwiza, K. M. M., 2008. Characteristics of bottom dissolved oxygen in Long Island Sound, New York, *Estuar. Coast Shelf. S.*, 76(2), 187-200, doi:DOI 10.1016/j.ecss.2007.07.001.
- Luetlich, R., Wright, L. D., and Smith, E., 2012. U.S. IOOS Coastal Modeling Testbed: A Super-Regional Testbed to Improve Models of Environmental Processes on the U.S. Coasts.
- McCardell, G.M. and J. O'Donnell, 2009. A novel method for estimating vertical eddy diffusivities using diurnal signals with application to Western Long Island Sound. *J. Mar. Systems.* 77, 397–408
- Miladinova, S. and Stips, A., 2010. Sensitivity of oxygen dynamics in the water column of the Baltic Sea to external forcing. *Ocean Sci.* 6, 461–474, 2010.

- Miller, R. E. L. and Wands, J. R., 2009. Applying the System Wide Eutrophication Model (SWEM) for a Preliminary Quantitative Evaluation of Biomass Harvesting as a Nutrient Control Strategy for Long Island Sound.
- New England Interstate Water Pollution Control Commission (NEIWPCC), 2014. Hypoxia in far western Long Island Sound and upper East River
- O'Donnell, J., W. F. Bohlen, and H. G. Dam, 2006. Wind stress and the ventilation of the hypoxic zone of western Long Island Sound. Proc. 8th Biennial Long Island Sound Research Conference, Conn. Sea Grant Program, New London, Conn.
- O'Donnell, J., Dam, H. G., Bohlen, W. F., Fitzgerald, W., Gay, P. S., Houk, A. E., Cohen, D. C. and Howard-Strobel M. M., 2008. Intermittent ventilation in the hypoxic zone of western Long Island Sound during the summer of 2004. *Journal of Geophysical Research: Oceans* DOI: 10.1029/2007JC004716.
- O'Donnell, J., Dam, H. G., McCardell, G. and Fake, T., 2010. Long Island Sound Study EPA Assistance Award Final Report.
- O'Donnell, J., Wilson, R. E., Lwiza, K., Whitney, M., Bohlen, W. F., Codiga, D., Fake, T., Bowman, M., and Varekamp, J., 2013. The Physical Oceanography of Long Island Sound, in Swanson, R.5 yarish, C. and Latimer, J. (eds), "Long Island Sound". Springer-Verlag Publishing company.
- Prasad, M. B. K., Long, W., Zhang, X. S., Wood, R. J. and Murtugudde, R., 2011. Predicting dissolved oxygen in the Chesapeake Bay: applications and implications. *Aquat. Sci.* 73(3), 437-451, doi:DOI 10.1007/s00027-011-0191-x.

- Ray, Sulagna; Swingedouw, Didier; Mignot, Juliette; et al. 2015. Effect of surface restoring on subsurface variability in a climate model during 1949-2005. *Climate Dynamics*. Volume: 44 Issue: 9-10 Pages: 2333-2349
- Resplandy, L., Levy, M., Bopp, L., Echevin, V., Pous, S., Sarma, V.V.S.S. and Kumar, D. 2012. Controlling factors of the oxygen balance in the Arabian Sea's OMZ. *Biogeosciences*, 9, 5095–5109, 2012.
- Stefan, H. G. and Fang, X. 1994. Model simulations of dissolved oxygen characteristics of Minnesota lakes: past and future, *J. Environ. Manage.*, 18, 73–92, 1994.
- Stips, A. , Bolding, K. , Pohlman, T. , and Burchard, H., 2004. Simulating the temporal and spatial dynamics of the North Sea using the new model getm (General Estuarine Transport Model), *Ocean Dynamics*, 54, 266-283.
- Torgersen, T., E. DeAngelo and J. O'Donnell, 1997. Calculations of horizontal mixing rates using ^{222}Rn and the controls on hypoxia in western Long Island Sound. *Estuaries* 20: 328-343.
- Vigil, H. L. 1991. The fate of dissolved oxygen in Long Island Sound bottom waters, M.S. Thesis, State University of New York, Stony Brook.
- Welsh, B. L. and Eller, F. C., 1991. Mechanisms Controlling Summertime Oxygen Depletion in Western Long-Island Sound, *Estuaries*, 14(3), 265-278.
- Wilson, R.E., R.L. Swanson and H.A. Crowley , 2008. Perspectives on long-term variations in hypoxic conditions in Western Long Island Sound. *Journal of Geophysical Research*, 113, C12011, doi:10.1029/2007JC004693.

Xue, P., Chen, C., Qi, J., Beardsley, R. C., Tian, R., Zhao, L., Lin, H. 2014. Mechanism studies of seasonal variability of dissolved oxygen in Mass Bay: A multi-scale FVCOM/UG-RCA application. *Journal of Marine Systems* 131 (2014) 102–119.

Chapter 5

Conclusion

Bacterial dynamics, critical in controlling bottom DO variability and recovery from hypoxia, needs to be correctly parameterized in coastal models. Modification of a biogeochemical model to include bacterial dynamics allowed us to accurately simulate the onset and recovery from hypoxia, which have proved to be elusive in previous studies. However, we first had to model the bacterial metabolism correctly. We found that temperature dependence of metabolism by time-varying bacterial populations is better simulated by a hyperbolic temperature function than a Q10 function. This study shows that eutrophication models, in which phytoplankton biomass is used as a proxy for bacterial biomass in decomposing organic carbon, are bound to produce inaccurate estimation of DO consumption. Vertical mixing does not have to be artificially manipulated, if the bacterial dynamics is included. Accurate DO simulation requires inclusion of bacterial dynamics, which provide important feedbacks to total planktonic community processes (Chapter 2).

The 3-D model results from Chapter 3 indicate that the response of the East River and western Narrows of LIS's to the wind is controlled by interactions between the surface wind stress and the topography. In general, the residual flow structure is stratified in the upper East River, and both vertically and laterally stratified in the Narrows of LIS. There is a distinct eastward mean transport/flux with an annual mean of $120 \text{ m}^3/\text{s}$ in the upper layer of the upper East River. In the lower layer of the water, the mean flow turns toward the west, and the annual mean transport is approximately $400 \text{ m}^3/\text{s}$. The mean flow in the western Narrows propagates westward in the north shore of LIS, and in the southern part of LIS the flow is toward the east, and the flow intensity decreases with depth. Across the Execution Rocks Station transect (i.e., T4), there is a

westward motion on the north side of the Sound and eastward motion along the Long Island shore, and therefore forms a cyclonic (counter clockwise) circulation cell in the western Narrows of LIS. The wind stress tends to have an opposite direction to the mean transport due to much stronger up-wind transport than the down-wind transport because of the barotropic pressure gradient force. There is a large seasonal variability in the exchange transport in the East River and western Narrows of LIS (i.e., 200-750 m³/s), with stronger transport during the winter (i.e., maximum of 800 m³/s) than the summer (i.e., as low as 100 m³/s). The Ekman number in the East River and western Narrows is between 0.2 and 0.5, indicating that Coriolis forcing is important in determining the current flow. The lateral direction momentum balance analysis also indicates that Coriolis force plays a big role in determining the lateral direction current structure in western LIS, which suggests that the lateral flow is in geostrophic balance. The longitudinal momentum balance over the East River and Narrows is dominated by the barotropic pressure gradient force and the surface stress. The advection and baroclinicity are important secondary momentum terms. Coriolis force plays more important role as water deepens, and baroclinity is more important in the lateral direction than the longitudinal direction.

Analysis of contributions of vertical mixing, horizontal transport and planktonic activity to the DO variability in Chapter 4 shows that wind mixing increase alone is insufficient to explain late summer hypoxia recovery. It explains only 30% of the DO variability due to physical transport. In addition to vertical mixing, horizontal advection in western LIS has a non-trivial impact on hypoxia development. Our results indicate that ignoring horizontal advection leads to up to 40% of under-estimation of DO during low DO season in late summer. This result implies that DO variability is sensitive to horizontal advection during low DO season. Temperature and substrate-responsive microbial activity are the primary mechanism controlling DO dynamics. The impacts

of planktonic activity and horizontal advection on seasonal DO variability are second order effects. The source of additional increase of DO consumption in the model with bacterial dynamics compared to the model without bacterial dynamics is attributed to the bacteria induced inorganic matter production during summer, which leads to further increase of the rates by approximately 37% of the total DO consumption rate. Therefore, there is strong evidence showing that explicitly adding bacterial dynamics could lead to stronger DO reduction during summer.

There are remaining challenges for this modeling study. For example, the eastern boundary of the 3D model domain is close to the eastern end of LIS, which may affect the tidal prediction in the eastern LIS. The western boundary of the domain was set along the western end of the East River, which might affect model prediction of current and transport close to this boundary.

However, we found it difficult to extend the model domain further to the west without sacrificing the model resolution in the very narrow East River. We examined current structures far from the western boundary to avoid errors due to the boundary effect. Salinity in the model domain is weakly nudged with CTDEEP salinity data, which do not contain sufficient information for the East River. For example, the Harlem River carries relatively low salinity water into the East River, which might have an impact on the water column structure. To overcome these shortcomings of the model, the model domain needs to be extended further so that the study place of interest is inside the domain in order to avoid the boundary errors. In addition, salinity information to the west of Station A4 should be applied into the model configuration, so that the water column structure prediction could be refined.

Another challenge with the 1D model with added horizontal advection is that, the horizontal advection is artificially added into the 1-D coupled model by controlling only the DO dynamic

equation. This neglects the impact that horizontal advection might have on the other processes of the system, e.g., phytoplankton bloom, nutrient flux, sedimentary transport, etc. The DO gradient derived from O'Donnell et al. (2008) is limited to summer time period, which does not provide insight into seasonal variability of DO horizontal advection. The eastward DO gradient between Station A4 and A2 is estimated by making comparison to the westward gradient based on the NEIWPC bi-monthly investigation, which may not take into consideration of the tidal impact.

Besides the challenges of this study, there are remaining scientific issues that need to be addressed in future studies. The relative importance of eddy diffusivity and bacterial dynamics on seasonal hypoxia development needs to be quantified. In addition to the one-dimensional seasonal oxygen variation, it is also important to examine the spatial distribution of oxygen variability. This could be achieved by applying the 1-D model (i.e., GOTM/ ERGOM) to multiple stations (e.g., A3, A4, B3, C1, C2, D3, E1, F2) across western and middle sections of LIS so that the oxygen variability at those locations will be simulated and validated by station observations. With this information, the seasonal variation of spatial oxygen gradient could be estimated. However, a 3-D model is still a necessary approach to examine the temporal change of the flow structure and hypoxia volume. The impacts of gravitational circulation, wind stress and friction on the 3-D flow structure need to be fully accessed after salinity information to the west of Station A4 (e.g., salinity of the Harlem River) is incorporated into model simulation. The hypoxia extent in the western LIS should be examined in full dimension with a 3-D coupled physical and biological model, so that the mechanisms leading to temporal variation of spatial distribution of hypoxia volume in estuaries could be further explored.